INTRAVESICULAR SOLIDS IN CHEMICAL AND BIOLOGICAL SYSTEMS

A thesis submitted in partial
fulfilment of the requirements
for the Degree of
Doctor of Philosophy
in the
University of Oxford
by

Stephen Mann

Jesus College
Oxford

Hilary Term
1982

ABSTRACT

INTRAVESICULAR SOLIDS IN CHEMICAL AND BIOLOGICAL SYSTEMS

Thesis submitted for the Degree of Doctor of Philosophy

by Stephen Mann

Hilary Term 1982

Jesus College.

This thesis is concerned with the formation and nature of intravesicular solids in chemical and biological systems. The precipitation of Ag_2O within unilamellar vesicle micro-volumes is described in detail. Formation of small (<10nm) single-domain cubic Ag_2O crystallites occurs on membrane diffusion of hydroxide ions. Nucleation initiates at a single site on the inner membrane surface followed by slow crystal growth. No precipitation is observed below an extravesicular pH (pH_{OUT}) of ca. 11.0. Permeable intravesicular nitrate ions permit hydroxide influx only when a critical membrane potential gradient is surpassed. Above a pH_{OUT} of 11.0 rate of precipitation is dependent on the rate of crystal growth. Kinetics are first-order with respect to intravesicular Ag(I) concentration and approximately first-order with respect to hydroxide concentration below a pH_{OUT} of 12.0. Solubility equilibria for intra-and extravesicular Ag_2O formation are the same.

Further in situ intravesicular precipitation reactions are described for FeO(OH) (crystalline), FeO(OH) (amorphous), Ag_2SiO_3 (crystalline), $CoSiO_3$ (amorphous), $Co(OH)_2$ (amorphous), Ag_2S

(crystalline), CoS (amorphous), and AgI (crystalline). Precipitation of single oxidation state compounds is the same in vesicle space as for normal aqueous solution. For a mixed valency state solid, Fe_3O_4, intravesicular precipitation results in an amorphous material compared with a crystalline material prepared in aqueous solution. Inclusion of pre-formed Fe_3O_4 into vesicles is of potential use as a magnetic drug carrier system and n.m.r. relaxation probe.

Intravesicular silica deposition in Stephenaoeca diplocostata Ellis is investigated. Siliceous costal strips are found to be extremely amorphous in structure, have surfaces active to Co(II) and Fe(III) ions, and demineralise from their centre of axis. T-joins of costal strips in intact loricae are found to be joined by a connective material containing amorphous silica centred around a filamentous material of unknown composition. Sectioned material indicates that silicification possibly initiates on an organic preformer laid down within an elongated intracellular vesicle.

Potential EM stains, $K_5SiPhGeW_{11}O_{39}$, $Gd(fod)_3$, and $t\text{-}BuNH_3[(nC_{22}H_{45}PO_3)_2Mo_5O_{15}]$ interact with vesicle bilayers resulting in observable images in the EM. Binding of $K_5SiPhGeW_{11}O_{39}$ can be followed by ^1H n.m.r. spectroscopy. $Gd(fod)_3$-loaded vesicles are potential n.m.r. probes for protein - membrane binding studies.

To my parents and to Cindy.

ACKNOWLEDGEMENTS

I thank my supervisor, Professor R.J.P. Williams F.R.S. for the opportunity to carry out the work presented in this thesis, and for his enthusiasm, insight and continual help during its course.

I also wish to express my thanks to Dr. A.J. Skarnulis for introducing me to the art of electron microscopy, and for his valuable discussions concerning electron microscopy experiments.

Many thanks are due to Dr. B.S.C. Leadbeater whose understanding and knowledge of the organism *Stephanoeca diplocostata* Ellis has helped me greatly in appreciating the complexity and beauty of biology.

Many colleagues have helped with the contribution of materials and time. I am specially indebted to Dr. B.S.C. Leadbeater for supplying cultures of *Stephaneoca diplocostata* Ellis, Dr. M.T. Pope for supplying samples of $K_5SiPhGeW_{11}O_{39}$ and $t\text{-}BuNH_3[(n\text{-}C_{22}H_{45}PO_3)_2Mo_5O_{15}]$, Dr. R.G. Ratcliffe and Mr. M.J. Kime for help with ^{31}P n.m.r. spectroscopy, Dr. A.P. Boswell for help with ^{1}H n.m.r. spectroscopy, and Mr. M. Pye for help with T_1 experiments.

Thanks are also due to many people who have used their skills on my behalf, in particular; Mrs. A. Stoker and Dr. A.J. Skarnulis for watching over the EM in troubled times, Messrs K. Waters and J. Broad for photography, Mrs C. Palmer for drawing diagrams, Mr J. Kench for atomic absorption spectroscopy and Mrs L. Woods for typing in the middle of decorating her kitchen.

Finally, I thank Cindy for reading and correcting the manuscript and the Science Research Council and I.C.I. for providing me with financial support throughout the course of this work.

CONTENTS

CHAPTER 1

INTRODUCTION

This thesis is concerned with the formation and nature of intravesicular inorganic solids in chemical and biological systems. The formation of such deposits is a central aspect of biomineralisation, in which biological systems concentrate and localise elements in the form of biosolids which are adapted to some functional role. The storage of these deposits in biology is usually achieved by cells having intracellular compartments into which specific elements can be directed. These compartments are usually in the form of membrane-bounded vesicles and in any one cell type there may be many different types of vesicle ranging in size and function. Generally, intracellular vesicles are spherical in shape and can be of diameters 10nm up to the size of the cell (e.g. a plant vacuole is essentially a very large vesicle) although elongated vesicles can be made (chapter 4). These vesicles may be used to store not only biomineralised materials but also concentrated solutions of organic molecules such as acetyl choline in synaptic vesicles (1) and adrenalin in chromaffin granules of the adrenal gland (2). However, for the purpose of this thesis it is the role of vesicles as a biomineral-forming structure which is important.

Many different types of inorganic solids have been located as biomineralised deposits but in general the substances stored are $CaCO_3$ (calcite and aragonite), $Ca_2(OH)PO_4$ (hydroxyapatite), SiO_2 (hydrated silica) and Fe-oxides (magnetite, lepidocrocite) Selection of these types of materials (with simple anions) can be achieved not only by compartmentalization but by the process

of precipitation. Complex formation of ions such as Ca(II), Fe(II), would not be as selective unless the counter anion (the complexing agent) was made more complicated. Thus the solids are then associated with polymers. The function of these deposits can be structural (bones, shells), as gravity devices (otoconia, otoliths), as direction-finding devices (magnets), or as storage centres to regulate cytoplasmic concentrations (e.g. Ca granules (3)), or as waste collection centres (e.g. Cd 'pollution' in mussels (4)).

The chemistry of formation of these materials may be very different from the corresponding precipitation reactions investigated in inorganic chemistry. Firstly, these biosolids are formed in small confined spaces so that it is the chemistry of this microenvironment which must be studied and not the corresponding reaction in free solution. Secondly, precipitation in biological compartments is controlled by cellular activity; thus the solids formed may bear little resemblance to their non-biological counterparts because they have been intricately sculptured for some functional use. Ion precipitation in biological systems often occurs through nucleation by organic residues in a matrix of protein and polysaccharide. The resulting crystals or particulates may remain small due to inhibitory effects of the vesicle environment, or may be allowed to grow in particular orientations by cellular control. The resulting morphology may then be very different from that of crystals allowed to grow in free solution. Thus the formation of biomaterials illustrates the interplay between inanimate molecular forces which tend towards a minimum-energy configuration and the organisational capacity of the living cell.

It is the process of ion precipitation on an organic

substance within a microenvironment to which this thesis is addressed. The solid state principles involved in this process are obviously very important in relating the descriptive investigations of biosolids to the general phenomenon of biomineralisation. For instance, a wide range of knowledge has been collected about the intricate relationship between the organic matrix and mineral phases in bones, shells and teeth and the role the matrix plays as a bonding medium between crystals and crystal layers, as an agent in initiating crystal nucleation, controlling crystal orientation and limiting crystal growth, and as a factor in altering the physical properties such as mechanical strength (5). Similar descriptive knowledge is known of the crystallographic nature of such deposits. However, there appears to be only a limited understanding of the solid state principles involved in mineral deposition on organic substrates. It is the attempt to understand these processes in terms of the solid state mechanisms involved that has resulted in the work presented in the following chapters.

In order to investigate the chemistry of precipitation in confined spaces a suitable model system has to be established since an _in vivo_ study would be extremely complicated. A suitable system is that formed by preparing small (25nm diameter), unilamellar phosphatidylcholine vesicles by sonicating dispersions of the lipid in aqueous solution. The advantage of this system is that it has two compartments, internal and external phases, with a small internal compartment (_ca_ 10^{-17} cm^3) into which ions can be encapsulated. By diffusing suitable materials across the bilayer membrane from the external phase, intravesicular precipitation reactions can be investigated under

different conditions.

The development of such a model system is described in detail in chapter 3. There are two essential questions which have been investigated in these model systems;

(a) Is the chemistry different within the vesicle to that in normal aqueous solution? An approach to answering this question has been made by characterising the intravesicular reaction products by analytical electron microscopy techniques and comparing the results with those obtained for similar non-vesicular precipitates.

(b) Can the thermodynamic and kinetic properties of these reactions be investigated? It is important to determine these properties since the smallness of the intravesicular crystallites may result in different solubility characteristics from crystals formed in aqueous solution. In general, the storage of an inorganic solid in a biological system will depend on the (energised) rate of uptake and the thermodynamic equilibria established. Hence an important related question is, what control does the lipid membrane have over the rate of intravesicular precipitation in these model systems?

Several of the intravesicular solids chosen for study here bear relationships with biological systems; for example, Fe-oxide precipitation and Fe biomineralisation (chapter 5), silicate precipitation (chapter 6) and biological silica deposition (chapter 4). Other model systems may have important chemical/biochemical applications such as in catalysis (chapter 3) and magnetic drug carriers (chapter 5).

In relation to the work described for model vesicle systems, a biological system in which silica deposition occurs was also studied and is described in chapter 4. Biomineralisation is a complex process involving many interrelated steps including uptake and transport of ions, biochemical control, bioenergetics, mineral deposition and rejection (figure 1.1). Abundance and availability of the elements to be stored is obviously an important factor in controlling selectivity but there must be other factors involved since diatoms concentrate SiO_2 whereas other sea creatures prefer $CaCO_3$ to build their shells. Uptake must then be dependent on the ion transport mechanisms available in the organism.

The energy requirements for transport and solid deposition will be important factors in biomineralisation processes. Energy will be required whenever ions are 'pumped', i.e. transported against an energy barrier, and to initiate mineralisation through changes of intravesicular concentrations until the solubility product of the ions is exceeded. The presence of an organic matrix at the mineralisation site will assist deposition if the binding constant of the ion at the organic surface is high resulting in a favourable energy transformation. However, in biological systems, kinetic factors are more likely to control the biomineralisation process than thermodynamic considerations since the overall rate of deposition could be controlled by many factors; element availability, transport rates, cellular activity, nucleation rates, and crystal growth rates.

The biological control of mineralisation is often adapted to the control of crystal shape, size and conformation. For instance, in the growth of $CaCO_3$ spicules in the sea urchin (6)

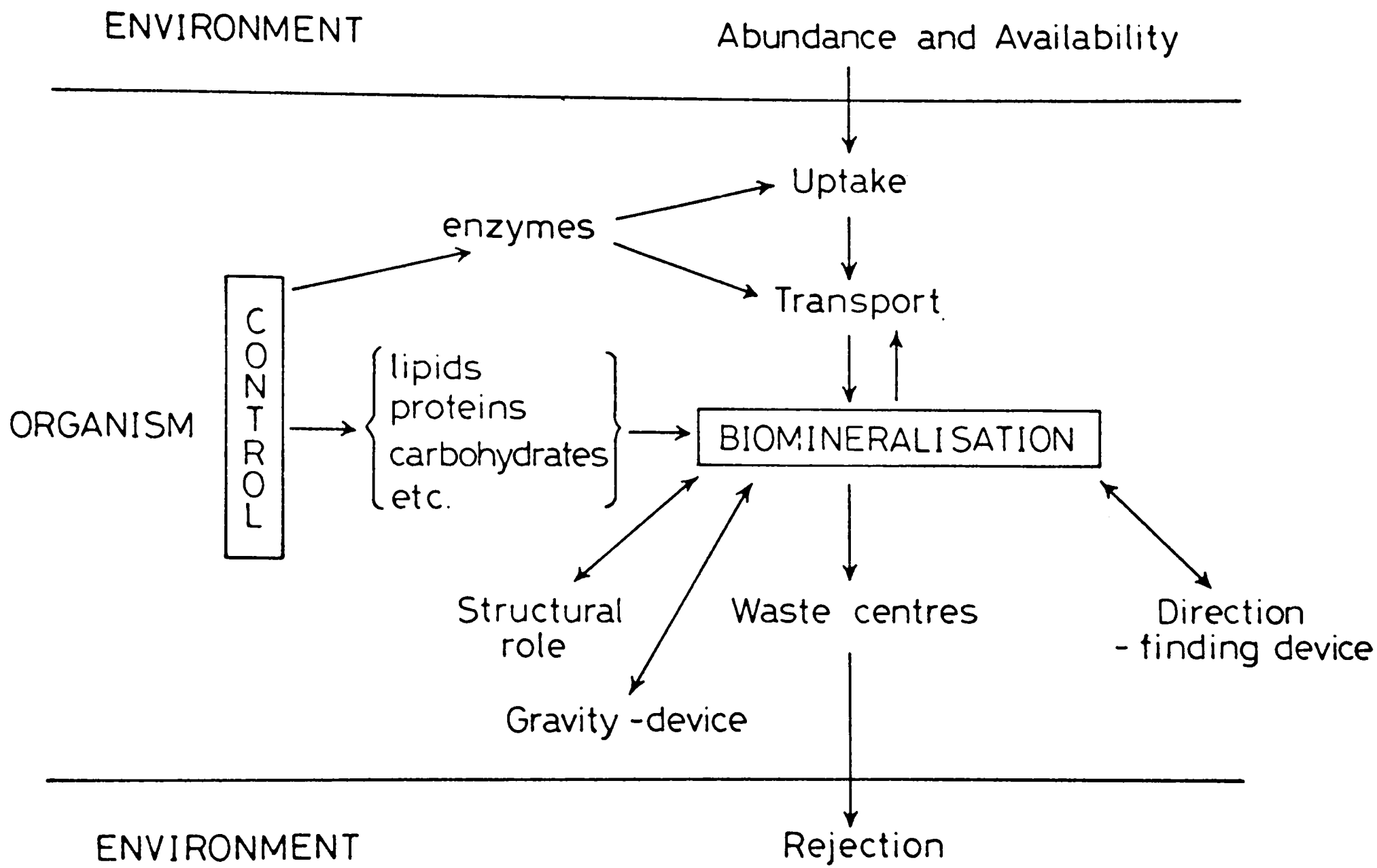

Figure 1.1 Simplified schematic representation of mineralisation within a biological system.

the resulting biomineralised structures consist of crystalline $CaCO_3$, but do not conform to non-biological calcite in external morphology due to the inhibition of growth of particular crystal faces by mesenochyme cells. The crystallographic structure deposited will tend towards the lowest energy configuration unless metastable states can be stabilised by kinetic factors (chemically or biochemically induced). Thus silica is biomineralised in an amorphous form for chemical reasons (chapter 4) whereas the stability of the aragonite shell of Nautilus pompilius appears to be the result of acidic amino-acids forming a protective overgrowth on the aragonite surface via carboxylate groups (5).

In chapter 5 silicification in the organism Stephanoeca diplocostata Ellis is investigated. Amorphous hydrated silica is found in many unicellular sea creatures such as diatoms, siliceous sponges and silico-flagellates and in plants such as grasses where it is deposited in the form of opaline pearls. Although silicon is, next to oxygen, the most abundant element in the earth's crust, the concentration of free monosilicic acid ($Si(OH)_4$), the only species thought to be available to biology due to the impermeability of silicate and polysilicate ions through biological membranes, rarely exceeds 0.2mM in most rivers, lakes and oceans. For precipitation of amorphous SiO_2 at room temperature, a concentration of ca. 2mM must be reached (7). Thus the hydrosphere is unsaturated with respect to dissolved silica implying that a 'pumping' mechanism might be required by biological systems. Solubility equilibria for calcite in sea water is very different and supersaturation is usually reached in the surface layers. This disequilibrium state is attributed to the presence of a series of inhibitors,

most notably magnesium and dissolved organic matter that interfere with the nucleation of a $CaCO_3$ crystal seed (5). At depths of 3000-4000m the ocean usually becomes unsaturated with respect to $CaCO_3$; in rivers and lakes concentrations of $CaCO_3$ are usually below supersaturation levels.

Silica itself is a trace element and essential for basic physiological processes ranging from DNA synthesis to bone formation (8). Most biological research on Si mineralisation has been derived from diatom studies. It is known that there are specific active transport systems in these organisms one of which seems to be related to a Na^+ gradient that is generated and maintained across the diatom membrane (9).

The silica shell of diatoms contains an organic coating comprised of sugars and amino acids in a complex arrangement (10). The initial SiO_2 deposition appears to take place in minute vesicles which then extend until theentire new valve is complete. This mineralisation process, being subject to biological control results in the beautifully formed species so often seen in electron micrographs. The degree of sophistication of the design mechanism involved in this process can be seen in figure 1.2. These electron micrographs show the ultra-structure across pores in two different species of diatom imaged at high resolution on a JEOL 200CX electron microscope. Within the pores are secondary silica structures which are characteristic of the species. The diameter of the pores are ca. 0.3μm which shows the fineness of control the cell has over silicification.

In chapter 5 several model systems of intravesicular Fe-oxide deposition are described. The importance of Fe-oxide biomineralisation has been increasingly recognised over the last few years due to the discovery of the role of magnetic

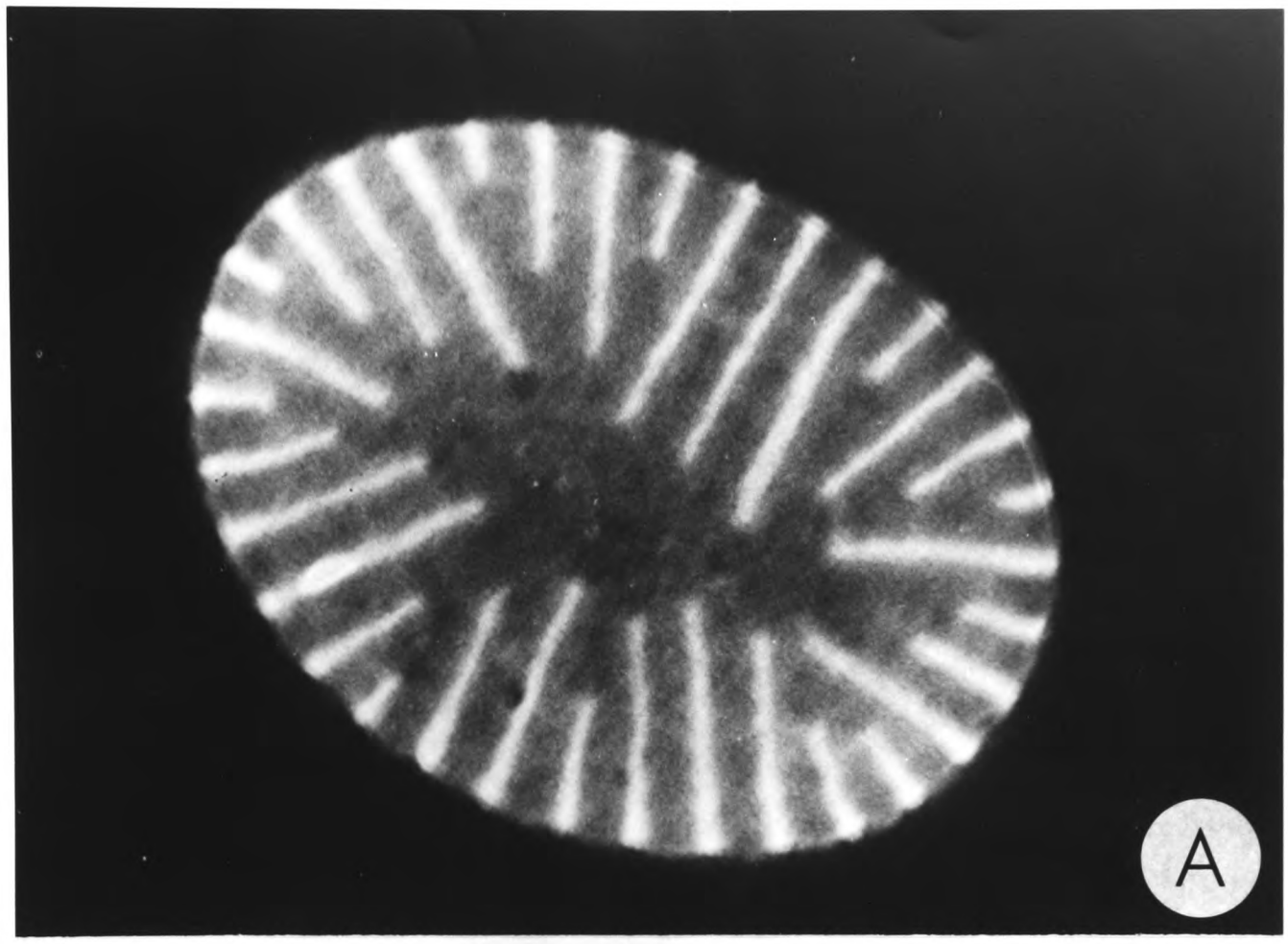

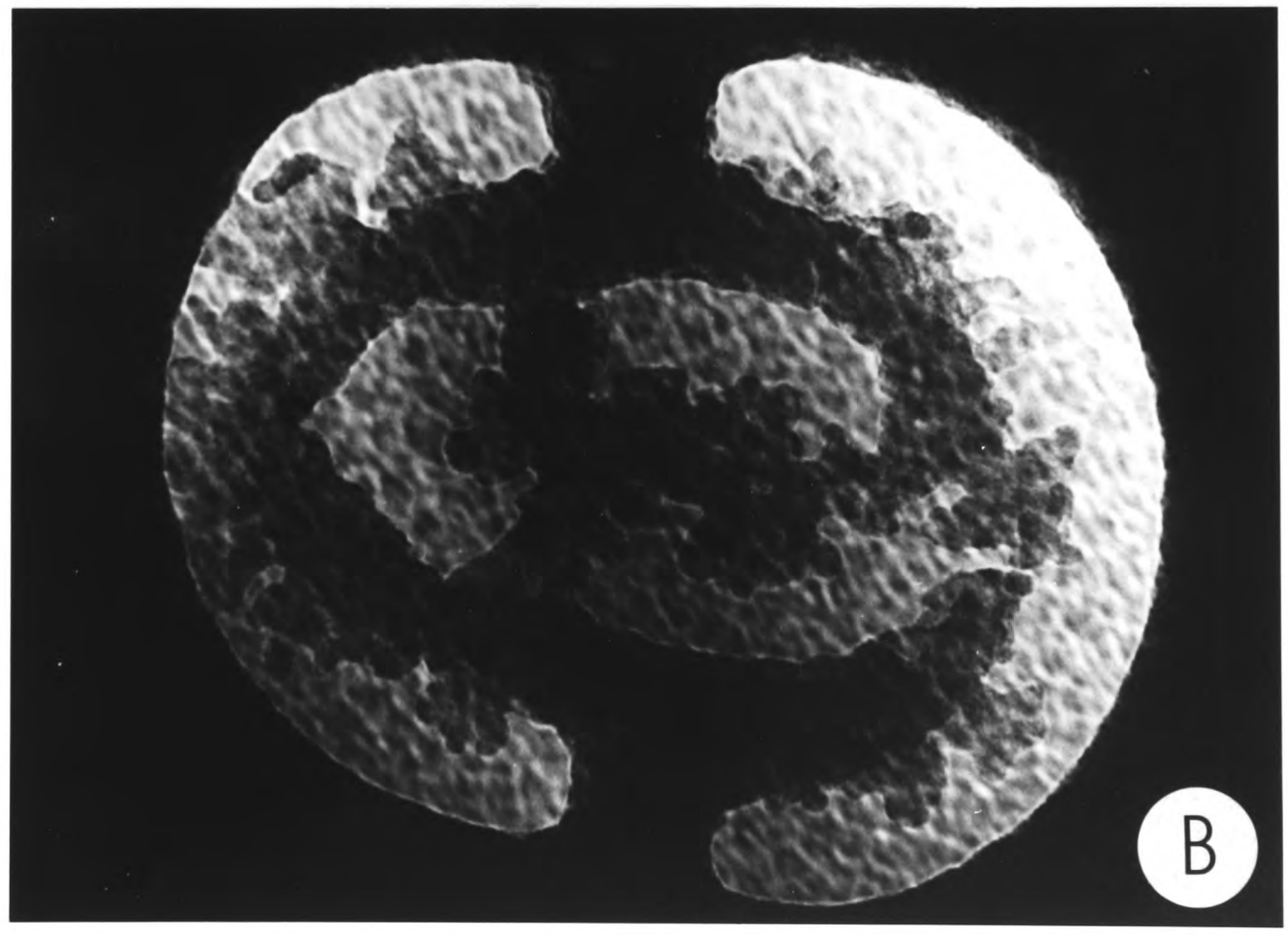

Figure 1.2 Electron micrographs of diatom pores illustrating the elaborate secondary silica structures within these objects and the design mechanisms inherent in biomineralisation processes;
a, Cocconeis x300,000;b,Achnanlties x365,000.

direction-devices in certain organisms. The first biological precipitates of magnetite (Fe_3O_4) were found in the teeth of chitons (11) and it was suggested that these permanant magnets could explain the chitons well-established homing behaviour. Recently, single domain crystals of magnetite have been located in mud bacteria (12), honey bees (13), and pigeons (14). Similar magnetic material has also been recently isolated in the head of dolphins (15). In the case of the magnetotactic bacteria it has been suggested that these creatures steer themselves north in the earth's magnetic field (the field is directed downward in the Northern hemisphere) in order to reach the sediment where they live and feed. Their orientation appears to be entirely passive; dead bacteria align themselves with the earth's field just as accurately as live ones (16). Similar bacteria have been discovered in the southern hemisphere where they swim southward in order to reach the sediment (17).

In bees, magnetite has been located in the front of the abdomen (13) and has been suggested as an explanation for the honey-bee dance effects associated with changes in the surrounding magnetic field (18). In pigeons single domain crystals of magnetite have been located between the brain and the skull and it has been postulated that this material is responsible for a homing mechanism of the birds on cloudy days when navigation by the position of the sun is not possible (14). The magnetic material found in dolphins appears to be magnetically weak and not expected to behave as a permenant magnetized 'compass' but could still be used as a basis for field direction since such material would still be susceptible to changes in position in the earth's field.

The evidence that these biomineralised magnetite

crystals act as magnetic field detectors is not conclusive except for the case of magnetotactic bacteria. However, the biodeposition of magnetite is interesting from a chemical/ biochemical point of view since magnetite is a mixed valence oxide containing Fe(II) and Fe(III) ions in an inverse spinel structure (chapter 5) and precipitation of this material will require specific biological conditions. An aim of this thesis has been to investigate the formation of Fe-oxides within the microenvironment of lipid vesicles in order to ascertain whether such solids can be prepared in crystalline and magnetic states.

In general, then, the work reported in this thesis follows two lines of approach; (a) the chemistry of intravesicular precipitation in model systems and (b) the characterisation and properties of a biologically deposited material, SiO_2, formed in intracellular vesicles of a silico-flagellate. The techniques used to further these aims are described in chapter 2. The general method of approach of this work, including systems (model and biological) which could be incorporated at later stages is illustrated schematically in figure 1.3.

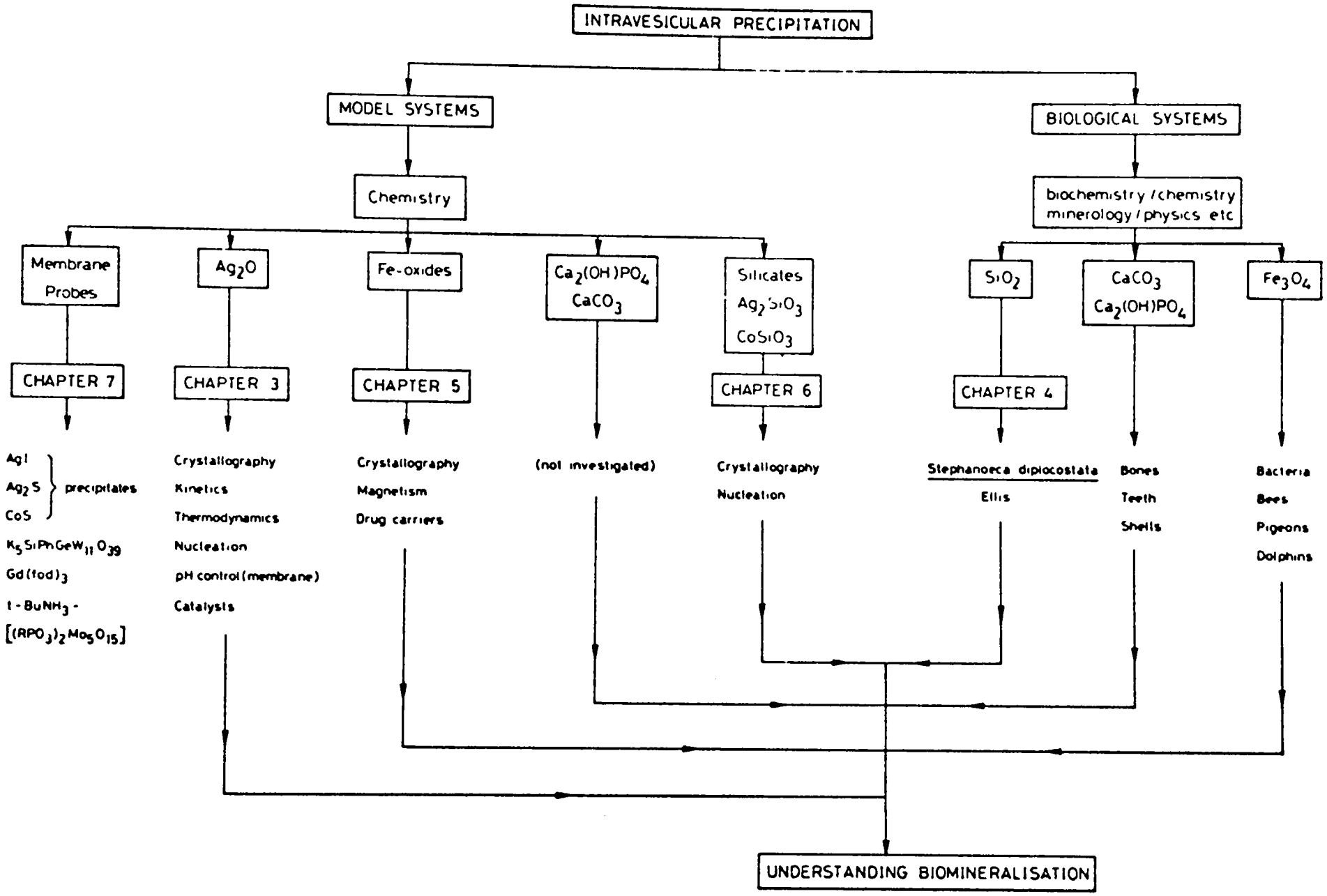

Figure 1.3 Schematic representation of the approach undertaken in this thesis relating the chemical investigations of intravesicular precipitation in model systems to that studied in biological systems.

1.1 References

(1) Orten J.M. Neuhaus O.W., In Human Biochemistry pp 674-676, 9th Edition (Mosby) 1975.

(2) Serck-Hanssen G., Helle K.B. B.B.A. 273, 199-207, 1972.

(3) Becker G.L., Chen C.H., Greenawalt J.W., Lehninger A.L., J.Cell.Biol. 61, 316-326, 1974.

(4) George S.G., Pirie B.J.S., B.B.A. 580, 234-244, 1979.

(5) Degens E.T., Top.Curr.Chem. 64, 1-112, 1976.

(6) Inoué S., Okazaki K., Scientific American 236, 82-92, 1977.

(7) Alexander G.B., Heston W.M., Iler H.K., J.Phys.Chem. 58, 452-455, 1954.

(8) Bendz G. and Lindqvist I. eds. Biochemistry of Silicon and Related Problems (Plenum. New York) 1978.

(9) Bhattacharyya P., Volcani B.E., P.N.A.S., 77, 6386-6390, 1980.

(10) Hecky R.E., Mopper K, Kilham P., Degens E.T., Marine Biol. 19, 323-331, 1973.

(11) Lowenstam H.A., Geol.Soc.Am.Bull 73, 435-438, 1962.

(12) Blackemore R.P., Science 190, 377-379, 1975.

(13) Gould J.L., Kirschvink J.C., Deffeyes K.S., Science 201, 1026-1028, 1978.

(14) Walcott C., Gould J.L., Kirschvink J.L., Science 205, 1027-1029, 1979.

(15) Zoeger J., Dunn J.R. Fuller M., Science 213, 892-894, 1981.

(16) Kalmijm A., Blakemore R.P., Magnetic behaviour of mud bacteria. In Schmidt-Koenig and Kleeton pp 354-55. 1978.

(17) C & EN, Jan. 5, p52, 1981.

(18) Lindauer M., Martin H., Z.Vgl.Physiol 60, 219-243, 1968.

CHAPTER 2

OPERATIONAL AND EXPERIMENTAL METHODS

The work presented in this thesis concerns the application of electron microscopy and ^{1}H n.m.r. spectroscopy in the identification and structural analysis of intravesicular precipitates. In this chapter operational procedures for electron microscopy and n.m.r. spectroscopy and general experimental methods are described. Since a greater proportion of the work has been concerned with the use of high and ultra-high resolution electron microscopy a summary of the general principles of electron optics, image formation, electron diffraction and X-ray microprobe analysis is included in Appendix I.

Electron microscopy is an excellent method for investigating the nature of precipitates formed within vesicles. In order to utilise this technique to its full potential several modes of operation, particularly TEM, STEM, and electron diffraction were used. EM analytical facilities were available to characterise the images observed. Ultra-high resolution electron microscopy was occasionally used to image lattice structures of crystallites and to investigate the possibility of short-range order within amorphous compounds.

2.1 Operational methods

2.1.1 Electron microscopy

For routine investigations the JEOL 100CX TEMSCAN analytical electron microscope was used operating at a accelerating voltage of 100keV. This EM consisted of three

operating modes; the JEOL 100CX and an ASID-4D attachment which allowed SEM and STEM modes to be used. In the TEM mode images could be observed at magnifications from x330 to x250,-000 in the normal magnification mode and from x3,300 to x66,-000 in the selected area mode. In the selected area diffraction mode camera lengths from 20 to 260cm could be specified. Images in SEM could be recorded at magnifications from x10 to x200,000 whilst in STEM magnifications from x300 to x300,000 were available.

The system incorporated a Kevex Si(Li) X-ray detector with an energy resolution of 150eV and a LINK SYSTEMS Nova 290 computer for X-ray microanalysis in the SEM and STEM modes. X-ray spectra were visualised on a 625 line video monitor and could be plotted on a 30000 X-Y recorder (Bryans Southern Instruments Ltd). Integrated peaks were obtained from a 390 printer terminal (Data Dynamics).

Before commencing any investigation the electron microscope was aligned, loaded with film (if necessary) and the cold trap filled with liquid nitrogen to minimise contamination. The routine alignment consisted of (a) checking the filament characteristics, (b) centralising the beam in TEM and ASID modes, (c) condenser lens aperture alignment, (d) condenser lens astigmatism correction. For operation at 100keV the stable current from a saturated filament was 90-100μA and was achieved by optimising the filament emission and gun bias controls. The beam was then centralised with the alignment translates at the smallest beam spot size and with the gun translates at the largest spot size. A similar alignment procedure was performed for the ASID unit centralising the beam as a caustic spot with the ASID alignment tilt controls and as a normal beam with the

ASID translate controls. The condenser aperture used was number 2 (300μm) and this was centred correctly by noting that the illumination diverged and converged concentrically when the second condenser lens current was varied. Condenser lens astigmatism was corrected by checking that the illumination remained circular when going through cross-over. The gun tilts were aligned by unsaturating the filament and checking that the filament image was symmetrical. If the condenser lens astigmatism was correct at this stage the unsaturated filament would be sharply in focus.

Specimens were introduced into the electron microscope by air-drying them onto formvar coated copper EM grids previously sputtered with a thin carbon film and then mounting the grids in a specimen tilt holder. Entry into the electron microscope was achieved using a eucentric side-entry goniometer attachment with a maximum tilt angle of $\pm 60^{o}$ and varying tilt speeds. For low magnification work (<x100,000) the current centre was aligned by adjusting the beam alignment tilts over a large range of objective lens focal lengths so that the image area under consideration remained centred over a large change in focus conditions. For high magnification work (>x100,000) the voltage centre was aligned by switching on the HV wobbler and adjusting the beam tilts until the image pulsated symmetrically about the centre of the screen. This alignment minimises chromat aberration for axial image points.

For all investigations a condenser spot size of 1 was used. An object aperture of 120μm or 60μm was inserted and centred around the central beam in the selected area diffraction mode. Objective lens astigmatism was corrected by observing the grains of carbon on the grid film at x250,000 and ensuring

that there was no preferential direction in the image under optimum focus conditions. Astigmatism was always checked before taking photographs.

Diffraction patterns were obtained by switching to the selected area magnification mode, adjusting the focus and magnification, introducing a selected area aperture (diameters available were 1000, 250, 80 and 20μm), then switching to the selected area diffraction mode and adjusting the condenser and focus controls to achieve the desired image. The objective aperture was removed during this procedure. For large single crystals the specimen requires alignment to obtain a symmetrical diffraction pattern. This can be achieved by tilting and rotating the sample as indicated by the Laue zones in the unaligned pattern. The changes in specimen orientation and position on tilting can be followed directly by defocusing the diffraction pattern so that a poor quality image of the specimen can be observed within the centre diffraction spot.

However, the majority of electron diffraction investigations were concerned with very small intravesicular crystallites and therefore powder diffraction patterns were obtained since single crystallites could not be analysed. Many crystallites were included within the selected area aperture resulting in crystallites of different orientations having planes in the correct positions for diffraction. Selected area diffraction was used throughout and enabled a correlation between micrographs, X-ray microprobe analysis and diffraction features to be made on a fine scale. However, because the aperture size was limited to ca 20μm any local deviations from the gross structure had to be investigated by ultra-high resolution EM. This is particularly important for amorphous materials as

discussed in chapter 4.

D spacings (d) were calculated from the formula

$$d = \frac{\lambda L}{R}$$

where L is the camera length (cm)

λ is the relativistic wavelength of the electron (0.037Å at 100 keV)

R is the reciprocal lattice spacing (cm)

The derivation of this formula can be shown from figure I.7 (Appendix I). In general, electron diffraction is not a high accuracy technique due to fluctuations in the voltage supply, changes in specimen height and errors of measurement. The percentage error in d spacings for routine procedures will be in the range 10-20 per cent.

A great advantage of the TEMSCAN electron microscope is that it is possible to switch rapidly between the various modes of the instrument. Images in the STEM or SEM mode were obtained at condenser spot size 4 and viewed on a c.r.t. screen by a balance of contrast and brightness controls. Astigmatism and focus were continually adjusted to obtain an image which could be viewed at four different scan speeds, the lower speeds resulting in a better signal-to-noise ratio.

X-ray microprobe analyses on vesicle samples were performed by scanning selected areas of the sample as viewed in the STEM mode, the collected X-rays then being electronically manipulated as described in Appendix I (section I.5). Samples for analysis were tilted 40° towards the detector and were required to be in a certain area of the grid (with respect to the detector) for sufficient count rates to be accumulated. Single vesicles and single intravesicular particulates could not be analysed due to the limit on the electron beam diameter. Background analyses

across areas adjacent to the sample were recorded in all cases. X-ray microanalysis was particularly necessary in relating the images observed in the EM to their chemical composition. Intravesicular particulates were very small in diameter and had to be characterised by this method since there were many contaminants on the grid of similar size. Hence electron micrographs by themselves provided only circumstancial evidence for the formation of such intravesicular deposits.

X-ray microanalysis was not applied quantitatively to the results obtained from intravesicular precipitates but used only as a rapid method for locating and characterising the reaction products for a particular vesicle system. Generally, quantitative X-ray microanalysis for thin specimens is very accurate since most of the corrections used for bulk specimens (the so called ZAF corrections) do not apply. A ratio method can then be used to determine the relative detector efficiency for the elements investigated. However, this method was not satisfactory for intravesicular precipitates. In general, ratios of elements for a given vesicle reaction system did not appear constant to any satisfactory degree. The reasons for this were not clear. In all analyses count rates were low due to the low concentration of sample analysed (detection limit is ca 1% weight to volume). The effects of contamination and specimen damage will then have important consequences in the analysis of these ultra-thin samples. Contamination will drastically change the specimen mass thickness during the period of analysis resulting in greater white radiation (less signal to noise) particularly for low atomic number K lines such as phosphorous (from the phospholipid). Similarly specimen mass loss in the electron beam during analysis will give spurious

results particularly if one element is more susceptible to beam damage (e.g. phosphorous in phospholipids). The use of cold stages would assist in preventing large scale mass loss. No such stages were used in the analysis presented in this thesis.

Micrographs were taken in the 100CX and 200CX (see below) TEM mode using the camera situated at the base of the column loaded with Kodak electron image film 4463. The micrographs were developed for 8 minutes in Kodak D19 developer using a 'nitrogen-burst' system, washed briefly for 30 seconds in water, fixed for a further 5 minutes in 'Amfix' fixer, washed for 15 minutes in water and left to dry in a drying chamber. Images were photographed in SEM or STEM modes using a Mamiya 6 x 7 roll film camera loaded with Ilford FP4 film. Exposed films were developed for 5 minutes using Ilford Microphen developer, washed briefly, and fixed, washed and dried as for TEM micrographs. Routine A6 prints were obtained from Mr. K. Waters (Inorganic Chemistry Laboratory, Photographic Services). Enlarged prints and high contrast photographs presented in this thesis were developed by the author using Kodax Veribrom papers F3, F4 and F5. Final plates were re-photographed and kindly printed by Mr. J. Broad on Kentmere photographic document paper (grade 3).

For ultra-high resolution imaging the JEOL 200CX THG2 electron microscope was used operating at 200keV. The electron microscope had a high brightness LaB_6 electron source and a point-to-point resolution of 2.46Å for a spherical aberration constant of 1.2mm and a chromatic aberration constant of 1.4mm. The point-to-point resolution describes the limit to resolving two features in the object by direct lattice imaging. The

images observed are then two-dimensional and directly related to the object given the correct defocus conditions. This is very different from line-to-line resolution which is the limit to resolving discrete point sources as one-dimensional images, i.e. as a simple interference pattern. Operational procedures for the JEOL 200CX were as described for the JEOL 100CX except that the specimen entry system consisted of a specimen holder magazine and specimen exchange knob. The specimen stage was so designed for high resolution work that it was extremely expensive and samples were only allowed to be entered by authorised users.

For lattice imaging the following conditions and procedure were undertaken. The condenser aperture diameter was 200μm and the objective aperture diameter 40μm. The optimum defocus was -650Å for the lens aberration constants quoted. The ultra-fine focus control was calibrated to be equivalent to 31Å per click and the fine focus control 500Å per click. The voltage centre and astigmatism were corrected as before. It was often found that specimen drift was a problem up to two hours after sample entry into the electron microscope. The cold trap was continually kept at liquid nitrogen temperature throughout the investigation.

For large single crystals the procedure for recording lattice images was to align the crystal in the selected area diffraction mode as previously described and then return to the normal magnification mode and obtain a reference focus. The reference focus was taken as the Gaussian focus and located by observing the carbon film or a hole in the grid for the position of minimum focus. The optimum focus was then obtained by counting focus steps as calibrated for the microscope.

Several images were usually recorded close to the optimum focus.

For crystalline intravesicular precipitates investigated in this way it was not possible to align the crystals in the diffraction mode because of their small size. Many crystallites were investigated and photographs taken of those which showed lattice fringes although it was appreciated that measured lattice spacings may be suspect to errors due to mis-alignment.

Photography at this level of resolution was undertaken with great care. The film advance mechanism was operated before final focus adjustments were made because vibration from this mechanism can alter the specimen height. Final adjustments to focus and stigmator controls were then made and the shutter opened carefully without otherwise touching the microscope. During exposure it was necessary to remain still and silent to prevent image distortions.

2.1.1 (a) Image artefacts in the EM

Any investigation using the EM is susceptible to image artefacts. These can arise from the method of sample preparation, be it from long and elaborate embedding and sectioning techniques for biological specimens, or from simple air drying of the material onto the EM grid. Once the specimen is placed in the EM it is then subject to conditions which may markedly effect its structure and composition. For instance, specimen damage from beam irradiation resulting from inelastic interactions of the electrons with the sample may disrupt the crystalline structure or cause polymerisation of molecules. Similarly, electron beam heating due to poor thermal conductivity of the specimen can cause gross disruption of the material under investigation.

These disadvantages are more severe for biological specimens than for inorganic material. In the case of biological specimens there may be no relationship between the structure investigated in the EM and the living system. However, the presence of beam damage in inorganic materials must also be considered. As an example, figure 2.1 shows the same AgCl crystal photographed after 200, 400, 500, and 800 seconds in the SEM mode. The presence of secondary crystallites on the surface of the AgCl crystal is seen to increase with time. The corresponding X-ray microanalysis of this crystal at different times is shown in table 2.1. The ratio of AgLα to Cl K counts increases markedly with time indicating that Cl is lost from the sample due to interactions of the sample with the electron beam, the resulting crystallites presumably being Ag(O). Hence the in situ chemical reduction of AgCl to Ag can be observed in the EM.

Specimen damage of crystalline materials can often be observed directly by recording the diffraction pattern at different intervals of time. Materials susceptible to damage will often show polycrystalline rings superimposed on the single crystal pattern within a short space of time. High resolution photography of such materials is difficult and often a minimum exposure technique is used in which the EM is correctly focused away from the sample, the sample is quickly brought into view and the image recorded immediately without any further focusing procedures.

The micrographs included in this thesis are thought not to be severely affected by artefacts as discussed above, although aggregation on air drying appeared to be a problem for very small objects such as vesicles and intravesicular

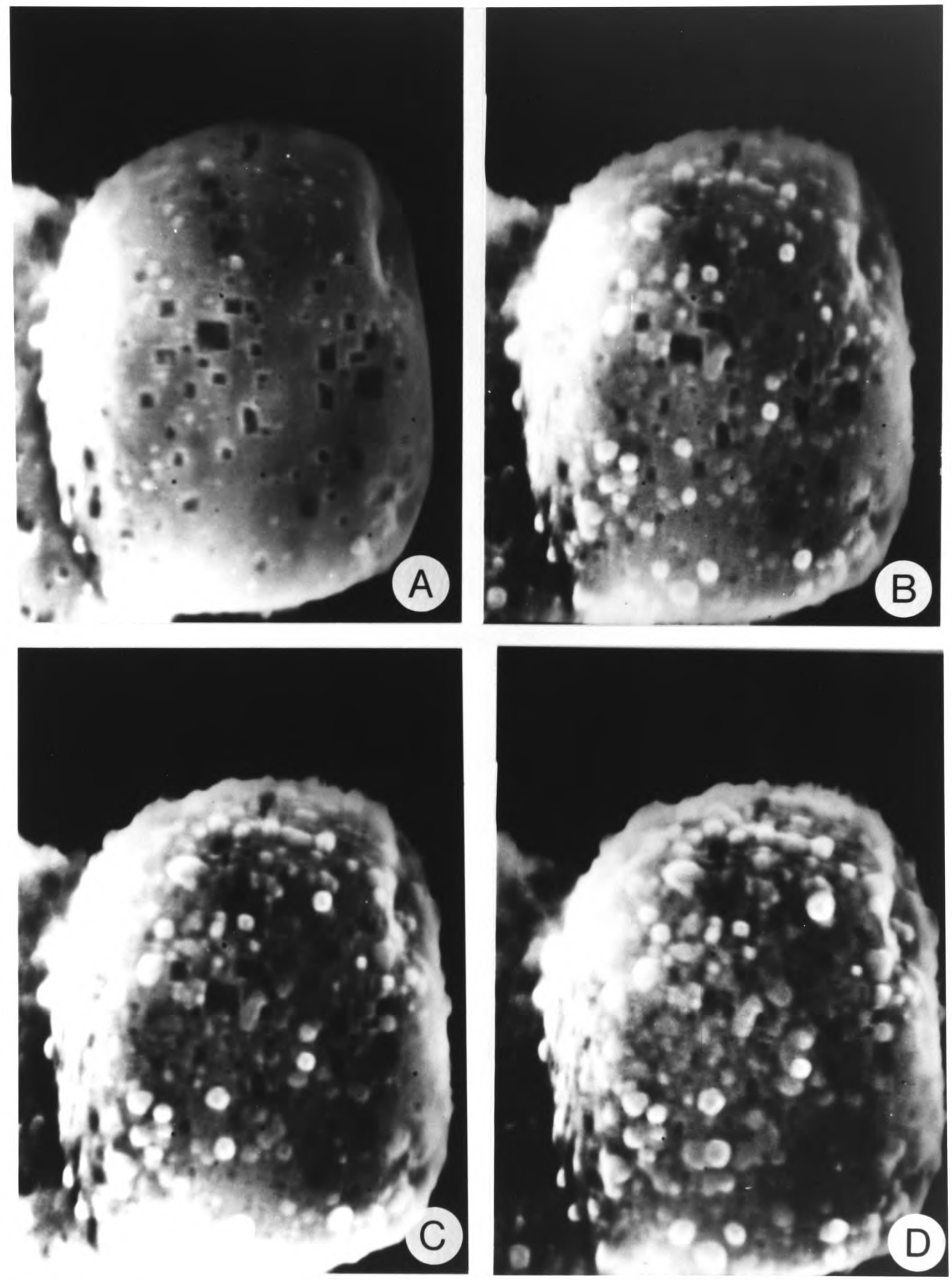

Figure 2.1 SEM electron micrographs of a AgCl crystal showing secondary crystallites growing in the presence of the electron beam;
a,200 s;b,400 s;c,500 s;d,800 s.
All micrographs,x63,500.

Table 2.1 X-ray microprobe analysis data for the same AgCl crystal recorded at different times in the electron beam

Time (min.)	Counts above background/50s		
	Cl (K)	Ag(Lα)	Ag/Cl
2	15017	23215	1.55
4	12143	21588	1.77
6	10426	21065	2.01
8	10790	24942	2.30
10	10023	24429	2.39
12	8500	23396	2.75
14	10095	28303	2.81
16	8569	25105	2.93
18	8181	25719	3.14
20	7323	24341	3.32

precipitates.

2.1.2 N.m.r. spectroscopy

Fourier transform n.m.r. spectroscopy was used to complement the investigation undertaken by EM. In this method a strong radio-frequency pulse is applied to the sample for a short time which excite the nuclei to a non-equilibrium state. After the pulse the nuclei relax towards their equilibrium state and a free induction decay is recorded in the time domain. In practice many free induction decays are recorded and summated to average out the noise. The data is then transfered to the frequency domain by a Fourier transform operation performed by a computer. The resulting resonance positions in the spectrum are measured with respect to a reference in parts per million (ppm) of the applied field. These chemical shift values are determined by the chemical environment of the different nuclei in the sample under investigation

2.1.2 (a) Collection of n.m.r. data

^{1}H n.m.r. spectra were recorded at 270MHz, using a Bruker GFX 270 spectrometer, fitted with an Oxford Instrument Co. superconducting magnet, and at 300 MHz, using a Bruker WH-300 spectrometer fitted with a similar magnet. Both spectrometers were equipped with computers for collecting and manipulating the data, disc storage systems, (used in conjunction with Nashua 4415 or DD15-8 cartridges) and deuterium field frequency locks.

Vesicle spectra were recorded at a sweep width of 4000Hz for 100 scans. Solvent (HOD) suppression was performed by

irradiating at this resonance position for a long period (0.5s) before the observation pulse was applied to all the protons in the system. By adjusting the power of the pulse on the solvent the solvent resonance was suppressed without causing substantial perturbation to the rest of the spectrum. The ^{1}H n.m.r. spectrum of sonicated dispersions of phosphatidyl-choline in D_2O is shown in figure 2.2. The spectrum has been assigned on the basis of chemical shift and intensity data, pH titration, titration with $LaCl_3$ and through the use of homonuclear and heteronuclear decoupling (1). This typical high resolution spectrum is not observed with unsonicated liposomes. Previous workers have suggested that the resolution in the vesicle spectrum is due to the tumbling motion of the vesicles averaging out the dipolar line broadening effect (2), and that the lipid in the vesicle bilayer has greater conformational freedom (3). All chemical shift values are quoted downfield of DSS.

^{31}P n.m.r. spectra were recorded on a Bruker WH 300 spectrometer operating at 121.49 MHz as described in chapter 3.

2.2 Experimental methods

2.2.1 Vesicle preparation

Vesicle preparations containing specific metal ions are described in the relevant chapters of this thesis. In this section a general outline of the preparation of phosphatidyl-choline (PC) vesicles is described. PC (average MW = 720) is the main constituent of egg yolk lecithin and has the formula

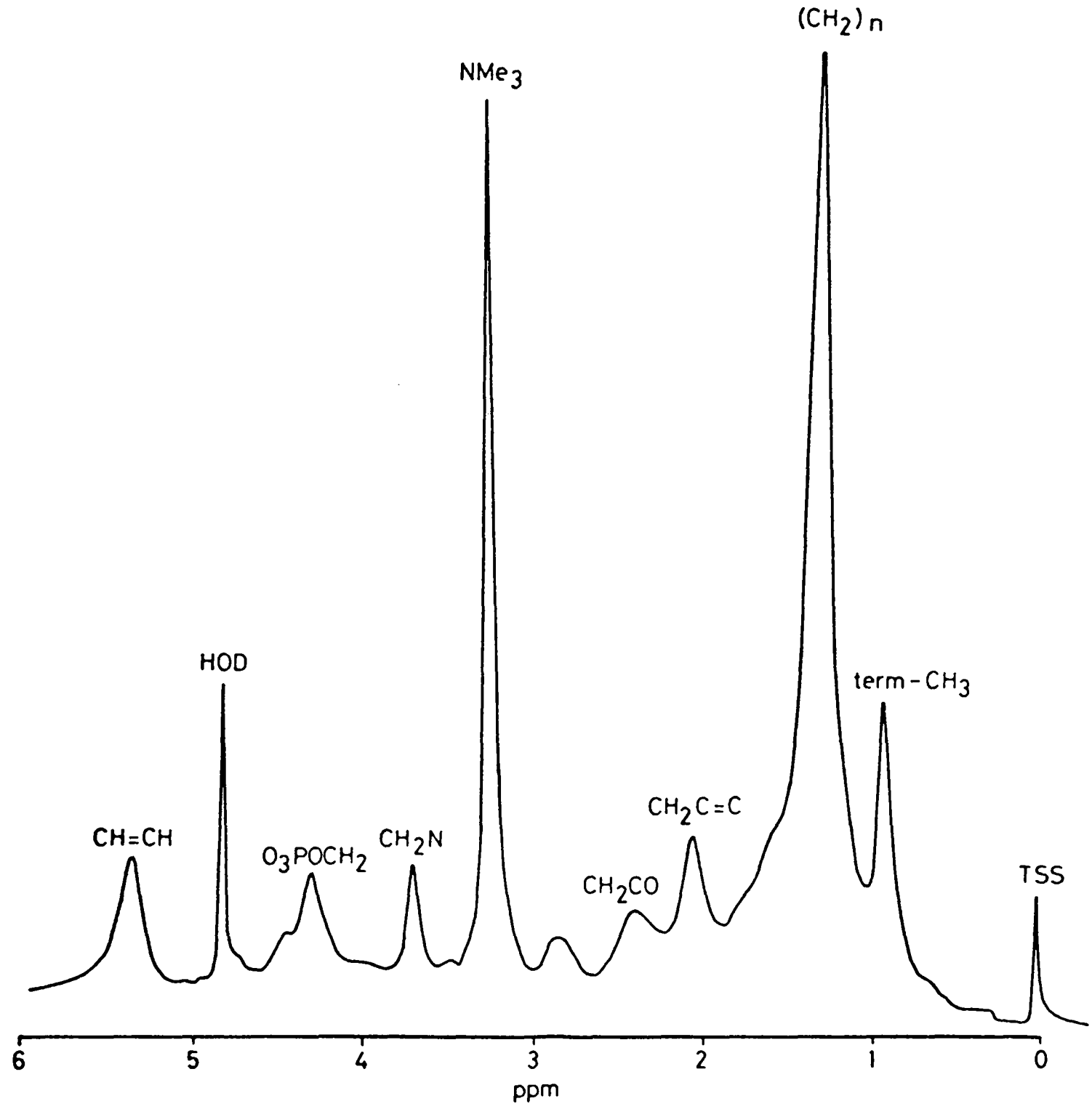

Figure 2.2 ^{1}H n.m.r. spectrum of PC vesicles in D_2O.

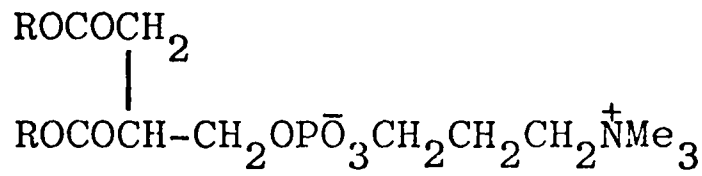

where

R is $(CH_2)_7CH = CH(CH_2)_7Me$

PC (from a glass ampoule) was transferred to a glass standard flask and the solution made up with a 4:1 mixture of chloroform/methanol to give a stock solution of 25mg/cm^3. Stock solutions were kept at 4^oC. In order to prepare vesicles, 34mM in lipid, $2cm^3$ of the stock solution was transferred to a $250cm^3$ round-bottomed flask and evaporated to dryness under vacuum using a rotary evaporator with a liquid nitrogen trap. Evaporation was aided by a water bath at hand temperature and usually complete within 20 minutes. If a combination of lipids was required or materials were to be incorporated into the lipid phase then these solutions were added at this stage. The resulting lipid film dried to the glass surface was shaken with $2cm^3$ distilled water (D_2O for n.m.r. experiments) and four glass beads in order to produce a multi-lamellar dispersion of the lipid. The milky dispersion was transferred to a sonicating vessel and centred around the 3mm diameter titanium probe of a MSE sonicator with the probe about 5-10mm into the dispersion. The vessel was surrounded by an ice water bath to remove excess energy and the dispersion sonicated at an amplitude of 9 microns peak to peak until clear (5-10 minutes) The sonicator probe was inefficient if it was placed too deeply into the dispersion but if placed too close to the surface air bubbles formed which prevented normal sonication. After much use the probe became pitted and needed to be polished smooth in order to retain efficiency.

Sonication causes lipids to reaggregate into bilayer vesicles of average diameter 30nm (4) with an internal volume of ca. $10^{-17}cm^3$.

In preparations where ions were to be removed from the extern phase of the vesicles, sonicated solutions were passed down Sephradex G-25 or ion-exchange columns and the vesicle elutant collected. Both methods were efficient in removing small cations and anions from the external phase. All pH values were measured using a Radiometer pH26 meter with a GK2321C glass electrode. The pH meter was standardised with buffers at pH 4.0 and pH 9.2.

2.3 Materials

PC was obtained as egg yolk lecithin, Grade 1, in glass ampoules containing 500mg PC dissolved in chloroform/methanol (4:1) solution under nitrogen, from Lipid Products.

Chloroform, methanol and general inorganic salts were obtained as Analar Grade reagents from BDH Chemicals Ltd. $Gd(fod)_3$ was obtained from Fluorochem Ltd. $K_5PhGeSiW_{11}O_{39}$ and $t\text{-}BuNH_3[(n\text{-}C_{22}H_{45}PO_3)_2Mo_5O_{15}]$ were gifts from Dr. M.T. Pope. Cultures of Stephanoeca diplocostata Ellis were gifts from Dr. B.S.C. Leadbeater.

D_2O (99.8%) was obtained from Merck, Sharp and Dohme. NaOD (isotopic purity 99%) and DC1 (99.6%) were obtained from CIBA. Sephredex G-25-150 beads (particle size 50-150μm) were obtained from Sigma. Cation ion-exchange resin, Zeo-Karb 225 sodium form, and anion ion-exchange resin, Zeo Karb 225 chloride form, were purchased from Permutit.

3mm and 2.3mm copper EM grids were supplied by Agar Aids.

2.4 References

(1) Hauser H, Phillips M.L., Levine B.A., Williams R.J.P. Eur.J.Biochem. 58, 133-144, 1975.

(2) Finer E.G., Flook A.G., Hauser H, B.B.A. 260, 59-69, 1972.

(3) Sheetz M.P., Chan S.I. Biochem, 11, 4573-4581, 1972.

(4) Finer E.G. Flook A.G., Hauser H., B.B.A. 260, 49-58, 1972.

CHAPTER 3

SILVER (I) OXIDE FORMATION WITHIN UNILAMELLAR PHOSPHATIDYLCHOLINE VESICLES

3.1 Introduction

In this chapter the formation of silver (I) oxide (Ag_2O) particulates within unilamellar phosphatidylcholine (PC) vesicles is studied in detail. The chemistry in such small volumes (ca. $10^{-17}cm^3$) has not been previously studied. Both electron microscopy (EM) and ^1H nuclear magnetic resonance (n.m.r.) spectroscopy are used to locate and follow the formation of Ag_2O within the vesicle compartment. The kinetics and thermodynamic equilibria of this precipitation reaction are studied by means of light scattering experiments. Of particular interest is the thermodynamics of particles in extremely small confined volumes. The surface free energy conditions of very small particle formation (less than 10nm diameter) may well lead to different solubility equilibria being maintained within the vesicle volume. The effects on nucleation would also be very interesting to study. The control of intravesicular pH by the lipid membrane and the role this plays in precipitation is studied by ^{31}P n.m.r. spectroscopy.

A study of chemistry in micro-volumes is necessary as it is related to the biomineralisation processes mentioned in chapter 1. The formation of inorganic solids within synthetic vesicles allows one to model these biological systems. Silver (I) oxide formation was taken as a suitable model system for the following reasons.

(a) The chemistry of formation of an oxide of a single

metal valency state should be relatively simple. More complicated oxides such as mixed oxidation state compounds like Fe_3O_4 (magnetite) which are related more closely to biologically formed solids (Fe_3O_4 in bacteria, bees etc, (chapter 1)) can then be studied in the light of these more simple systems.

(b) High concentrations of Ag (I) ions can be incorporated within the vesicle volume without precipitation of the lipid. Thus the vesicle system is stable over large ranges of Ag(I) concentrations encapsulated. Particles of different size can then be studied. (Compare the much lower concentrations possible with PC vesicles for Fe (II) and Fe (III) encapsulation (chapter 5)).

(c) Ag_2O is used as a catalyst in many chemical reactions. The formation of very small, high surface area particulates within vesicles could have very important implications in catalysis.

3.2 Preparation of Ag (I) oxide within PC vesicles

PC(17mM) was sonicated in the dark at 4^oC in the presence of $AgNO_3$ solution (usually 250mM in distilled water) until the solution was no longer turbid (ca. 5-10 minutes). Very high concentrations of $AgNO_3$ solution, eg. 1M, caused precipitation of the lipid preventing vesicle formation on sonication. After sonication the opalescent solution was passed down a cation ion-exchange column (sodium form) to remove the Ag (I) ions from the external phase of the vesicles. The pH of the solution containing only Ag (I) ions within the vesicle compartment was then raised to 12.0 - 12.6 by addition of NaOH solution. The vesicle solution turned progressively darker and after ca. ten minutes was light-

brown in colour. No precipitation of this solution was observed on centrifugation in a bench centrifuge.

Samples were investigated by EM, ^1H n.m.r. and light scattering within three hours of Ag_2O formation. ^1H n.m.r. studies were performed using D_2O solutions.

Leaving the vesicle samples in the air at room temperature for 24 hours at a pH of 12.3 resulted in the formation of a brown gel indicating the instability of the vesicle/Ag_2O system over this time range.

3.3 EM studies of intravesicular Ag_2O formation

One drop of the brown vesicle solution, prepared as described in section 3.2 was placed on carbon-sputtered, formvar-coated copper EM grids and left to dry on filter paper. Grids were prepared for the JEOL 100CX EM and the JEOL 200CX ultra-high resolution electron microscope. The program of investigation was as follows.

(a) Utilising the 100CX electron microscope;

  (i) Location and imaging of intravesicular Ag_2O particulates at different Ag (I) concentrations and at different reaction times.

  (ii) X-ray electron microprobe analysis on particulates observed.

  (iii) Electron diffraction measurements on particulates to reveal crystallographic structure.

(b) Utilising the 200CX electron microscope;

  (i) Ultra-high resolution imaging of Ag_2O particulates to reveal crystallographic structure.

3.3.1 Characterisation of intravesicular Ag_2O particulates by high resolution electron microscopy

For a vesicle system prepared in the presence of 250mM Ag (I) ions, removal of external Ag (I) ions followed by a pH rise to ca. 12.3 resulted in the imaging of discrete electron-dense spheres in the 100CX electron microscope (figure 3.1). The range of particle size is extremely small as shown by the frequency distribution curve in figure 3.2. One hundred particles were measured. The arithmetic mean diameter is 10.55nm with a standard deviation of population of 1.25nm. This degree of homogeneity may be expected since the sonication method of vesicle preparation forms vesicles of uniform size, 30±2nm in diameter (1). Some larger particulates could sometimes be observed of diameter ca. 50nm, which may indicate the presence of larger vesicles (liposomes) or of some vesicle fusion occuring within the sonicated sample. Only the area enclosed by the Ag_2O particulates could be observed; the lipid membrane is not imaged due to the low contrast (small degree of electron scattering) of its constituent atoms.

X-ray electron microprobe analysis was performed over areas of particulates in order to identify the elements present in these regions of space. The smallest area analysed was 30nm x 30nm and thus it was not possible to analyse a single particulate. Analysis was generally performed for 100 seconds at a tilt angle of 40^{o}. 'Dense' regions of particulates such as in figure 3.1 gave well resolved X-ray peaks above background (figure 3.3) revealing the presence of phosphorous (P) (from the phospholipid) and silver (Ag) only in these regions. (Copper peaks are seen and originate from the EM grid) X-ray microprobe analysis in regions away from the particulates did not detect P or Ag. Table 3.1

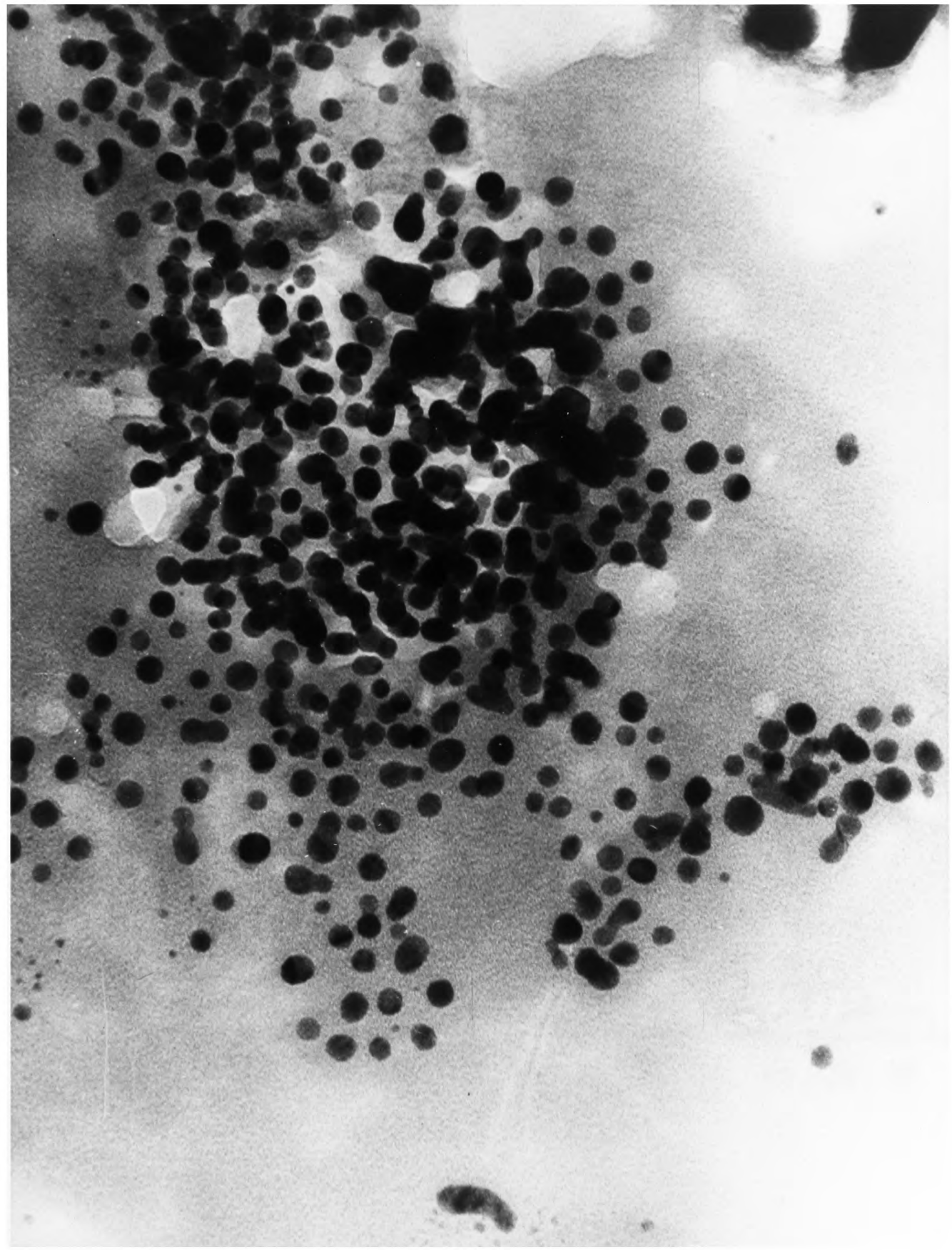

Figure 3.1 Electron micrograph of intravesicular Ag_2O particulates x286,000.

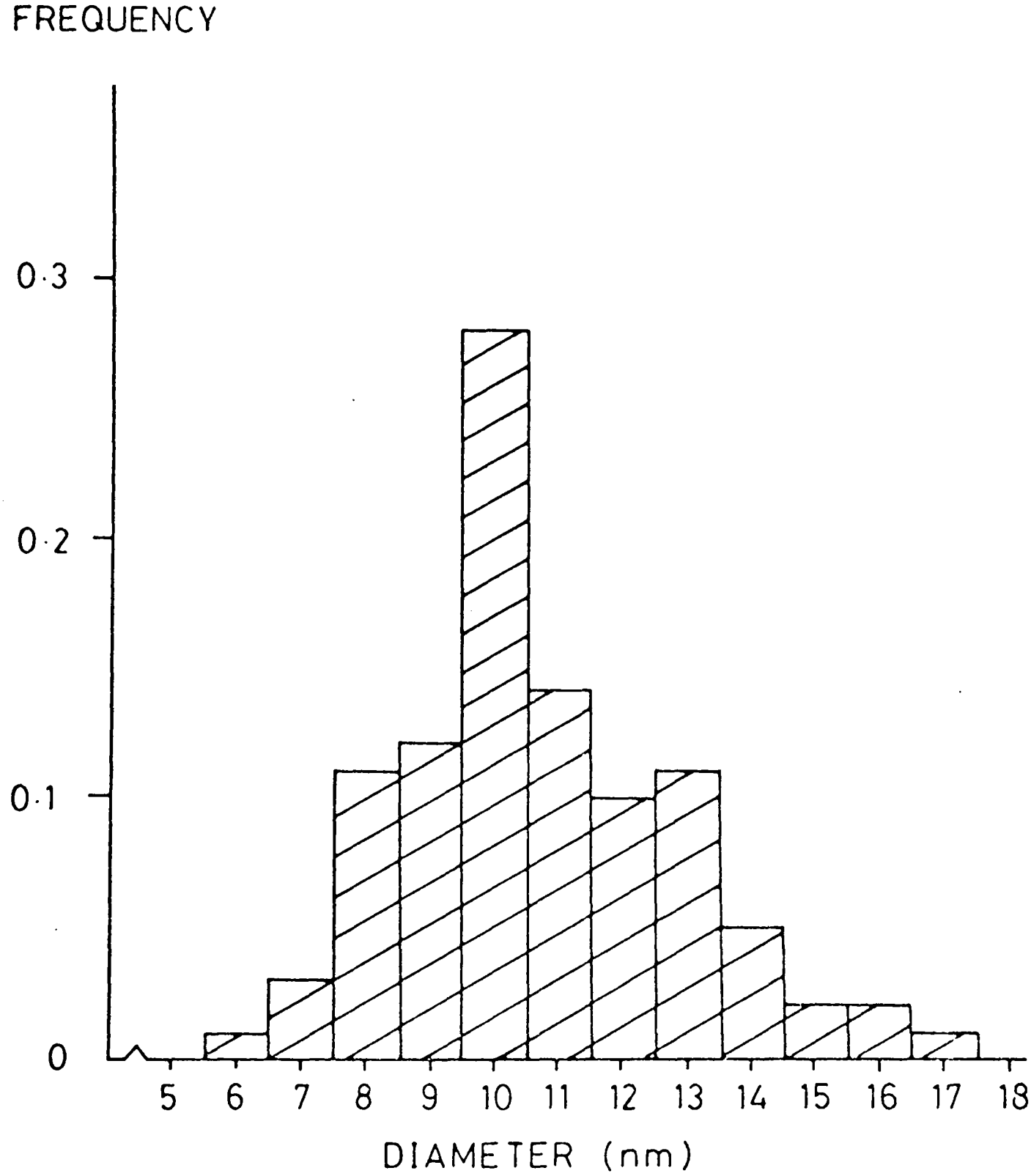

Figure 3.2 Frequency distribution diagram for intravesicular Ag_2O particulates formed from a sonicated solution of 250mM Ag(I) ions.

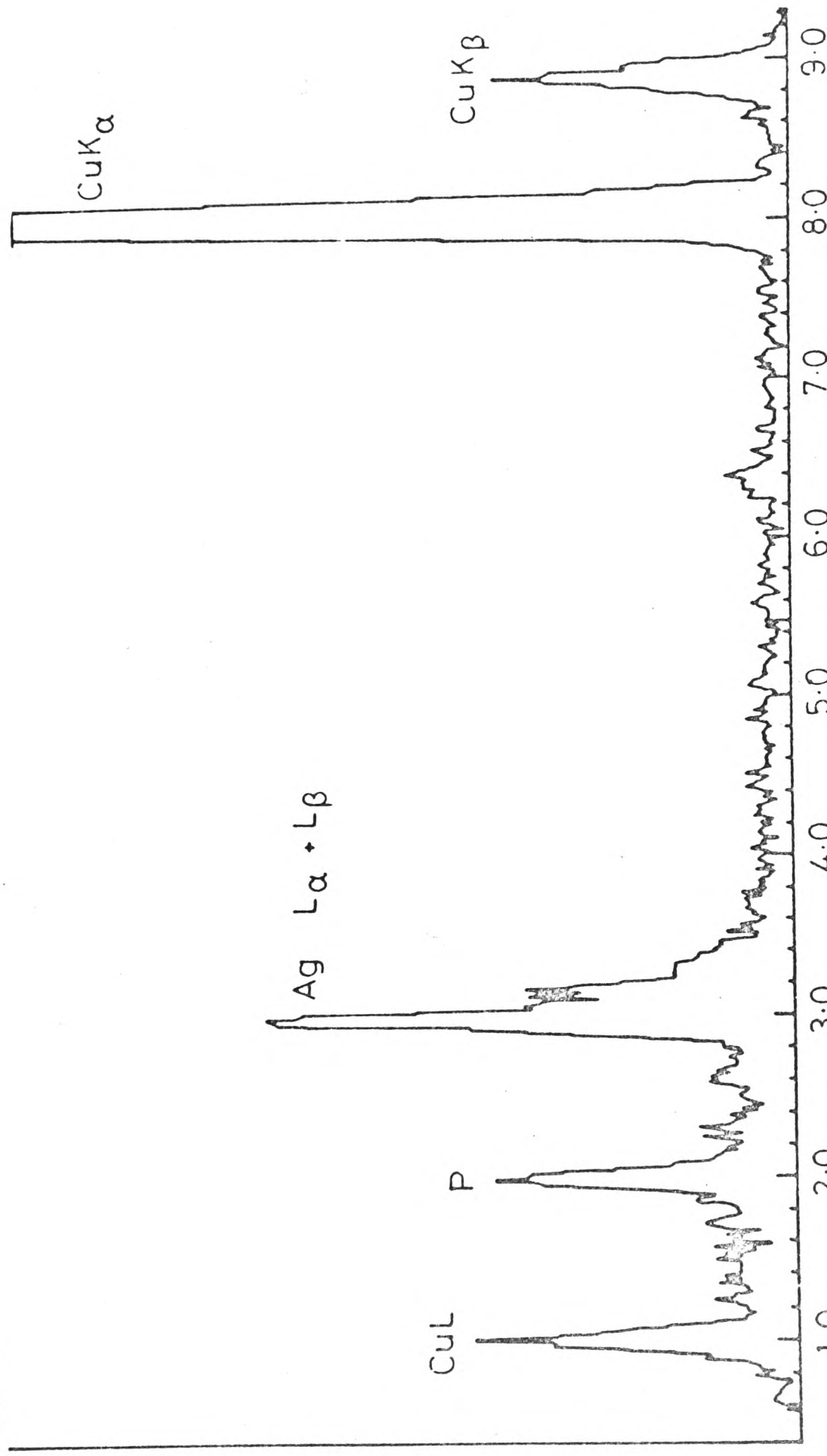

Figure 3.3 X-ray microprobe analysis of intravesicular Ag_2O particulates.

lists the integrated counts above background for 100 seconds for P(K) and Ag(Lα + Lβ) peaks for five separate micro-analyses.

The Ag/P ratio does not appear to be constant over the different areas analysed, although in each case the Ag intensity is much greater than for P. This is probably due to the low peak-to-background ratio for phosphorous resulting in a large percentage error in P measurements indicating a relatively large difference in Ag/P ratios. Also, the phospholipid is possibly more susceptible to beam damage than the Ag_2O particulates.

Electron diffraction was performed over areas of the Ag_2O particulates and powder diffraction images could be observed (figure 3.4a). Thus the intravesicular Ag_2O formed is crystalline D spacings were calculated in Å and then compared with similar measurements made for a Ag_2O sample prepared similarly in distilled water without the presence of lipid (figure 3.4b). Table 3.2 shows d spacings for Ag_2O (distilled water), Ag_2O (intravesicular), and reference standards for cubic Ag_2O(2) and hexagonal Ag_2O(3).

Reference to table 3.2 shows that the intravesicular Ag_2O has the same crystal morphology as the Ag_2O prepared in distilled water without the presence of lipid. Comparing the d spacings of the lines for Ag_2O (intravesicular) with the reference standards it is clear that the intravesicular crystallites are cubic in structure. The strong line at a d spacing of 2.68Å in Ag_2O (intravesicular) corresponds to the 2.72Å line in cubic Ag_2O and not the 2.64Å line in hexagonal Ag_2O since this line is only weak in intensity. Also, the hexagonal lines at d spacings of 1.53Å and 1.30Å(str) are not present in the spacings of intravesicular Ag_2O.

In conclusion, high resolution EM and X-ray microprobe

Table 3.1

X-ray microprobe analyses for Ag_2O particulates

Analysis	Counts above background/100s		
	$P(K_\alpha)$	$Ag(L_\alpha + L_\beta)$	Ag/P ratio
1	239	2160	9.05
2	348	2260	6.5
3	340	2600	7.65
4	248	1730	6.98
5	1240	7290	5.88

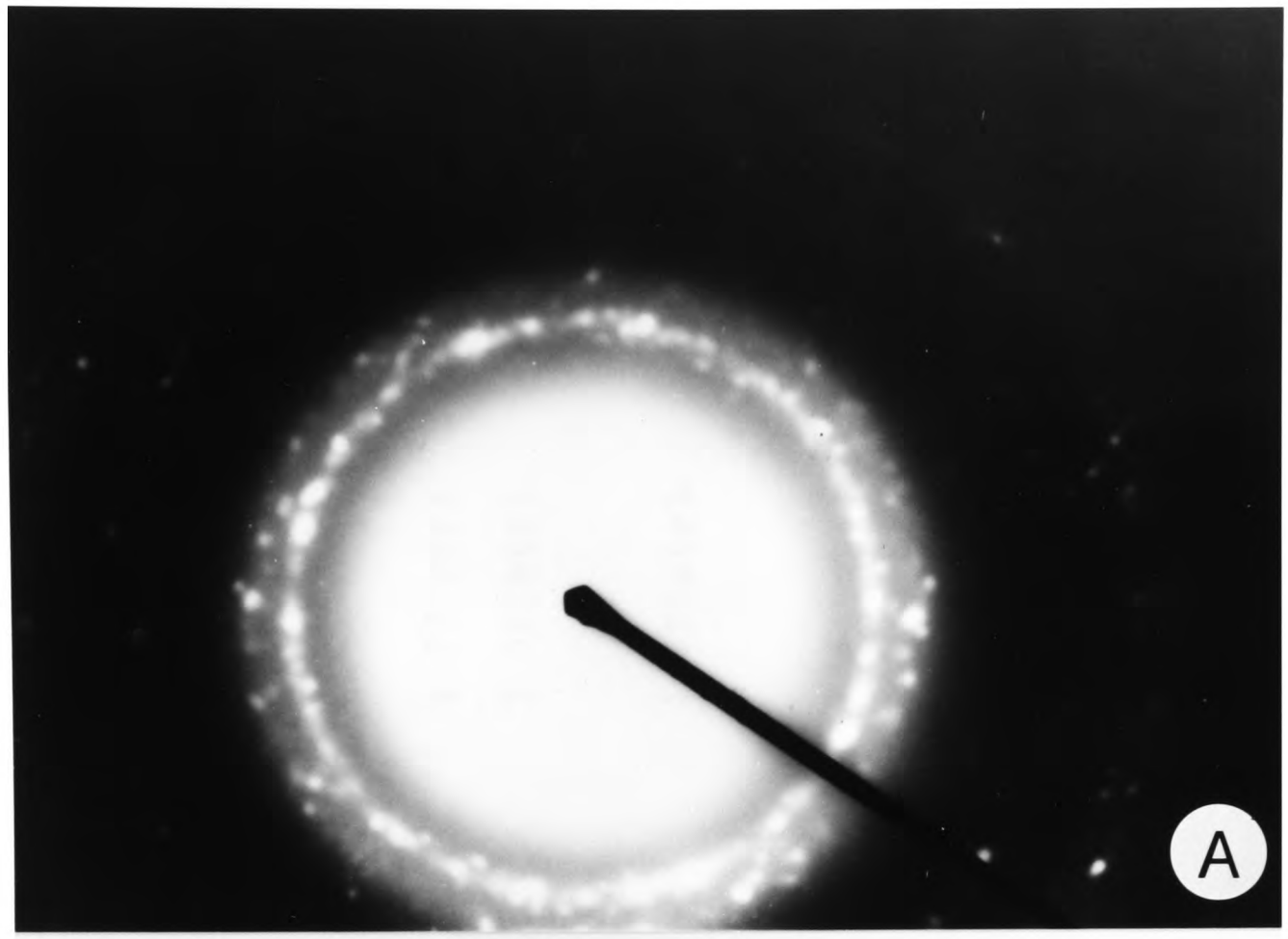

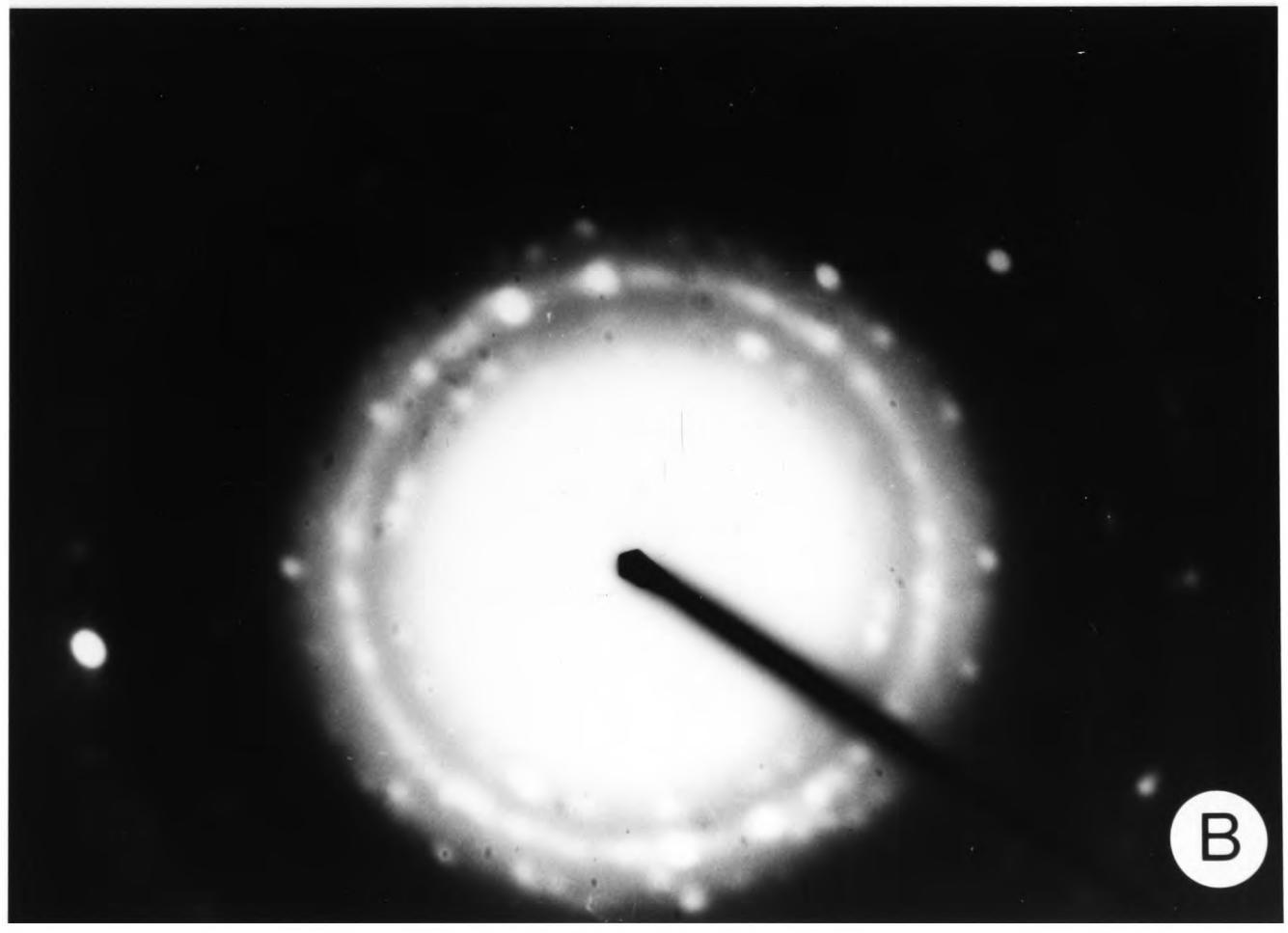

Figure 3.4 Powder diffraction images for Ag_2O particulates; a, prepared within PC vesicles; b, prepared in normal aqueous solution. Camera length 215 cm in both cases.

Table 3.2 Powder diffraction d spacings in Å for various Ag_2O samples

(str) = lines of strong intensity

* = reference standards (see text)

Ag_2O (distilled water)	Ag_2O (intravesicular)	*Ag_2O(cubic)	*Ag_2O (hexagonal)
3.06		3.35	
2.65(str)	2.68(str)	2.73(str)	2.64
2.22(str)	2.28(str)	2.37(str)	2.33(str)
			1.81(str)
1.64	1.64(str)	1.67(str)	1.64
			1.53
1.41	1.41(str)	1.43(str)	1.40(str)
			1.30(str)
1.11	1.04	1.06	

analysis have shown that the formation of very small crystallites of cubic Ag_2O is possible within PC vesicles. In the next section the investigation of these crystallites under conditions of ultra-high resolution EM is discussed.

3.3.2 Ultra-high resolution EM investigation of intravesicular Ag_2O crystallites

A drop of a solution of Ag_2O crystallites prepared as in section 3.3.1 was placed on 2.3mm carbon-coated EM grids and examined in the ultra-high resolution 200CX electron microscope. The resolution of this instrument allows atomic lattice planes to be imaged on suitably prepared samples. In the case of intravesicular Ag_2O crystallites the sample was thin enough for atomic spacings to be imaged successfully. In the majority of micrographs taken the Ag_2O crystallites were observed to be single domain with a lattice spacing calculated to be 2.65Å corresponding to the 111 lattice plane (2). Figure 3.5 shows lattice fringes of the 111 plane running across a Ag_2O crystallite with the edge of the particle towards the top of the figure. The 111 lattice plane is also the strongest d spacing observed in the electron diffraction pattern of intravesicular Ag_2O as discussed in section 3.3.1. Lattice spacings could be resolved on particulates down to 6nm in diameter; for particulates below this size no spacings could be imaged.

The formation of single domain crystallites suggests that nucleation occurs at one site in the vesicle and that subsequent growth of the crystallites is slow along preferential faces of the crystal. This important factor is discussed in greater detail in section 3.7. Occasionally multi-domain crystallites are observed which suggests that in these cases nucleation has

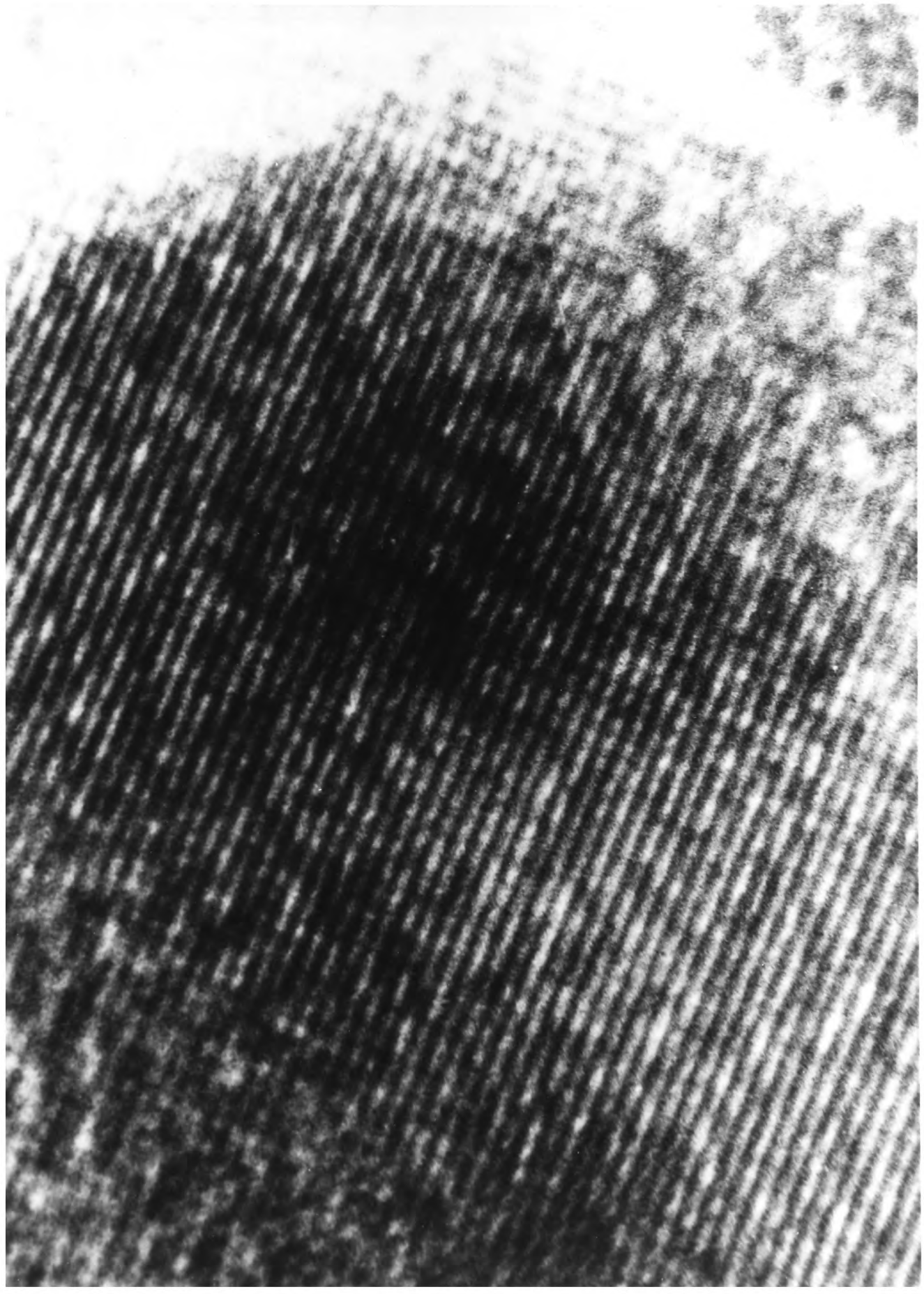

Figure 3.5 Ultra-high resolution electron micrograph showing lattice fringes across an intra-vesicular Ag_2C crystallite x9,800,000.

occurred at several different sites within the vesicle.

3.3.3 Formation of intravesicular Ag_2O crystallites from low Ag (I) concentrations

Initial Ag (I) concentrations lower than 250mM were used to prepare Ag_2O crystallites within PC vesicles. Figure 3.6a shows the images observed in the 100CX electron microscope at a sonicated Ag (I) concentration of 31.25mM. As expected the particle diameter is much smaller ranging from 2-7nm with very few crystallites greater than 10nm. Weak powder electron diffraction patterns were obtained from these images showing that the particulates were crystalline, cubic Ag_2O.

In principle this method of controlling the Ag (I) concentration incorporated within the vesicle compartment could result in the formation of very small (< 2nm) discrete crystallites of Ag_2O. The possible implication of this on catalyst preparation is discussed in section 3.7.

3.3.4 Imaging of Ag_2O crystallites at initial stages of particle growth

In section 3.3.1 and 3.3.2 the characterisation of the final reaction product of Ag_2O precipitation within vesicles was discussed. To a similar system, consisting of vesicles sonicated in the presence of 250mM Ag (I) ions, NaOH solution was added and a drop of the solution placed onto an EM grid within ten seconds. The images observed in the 100CX electron microscope are shown in figure 3.6b. Particles of diameter 2-4 nm are imaged but unfortunately X-ray microprobe analysis was not possible on these areas due to the impossibility of locating such small images in the STEM mode. 'Dense' areas of these small

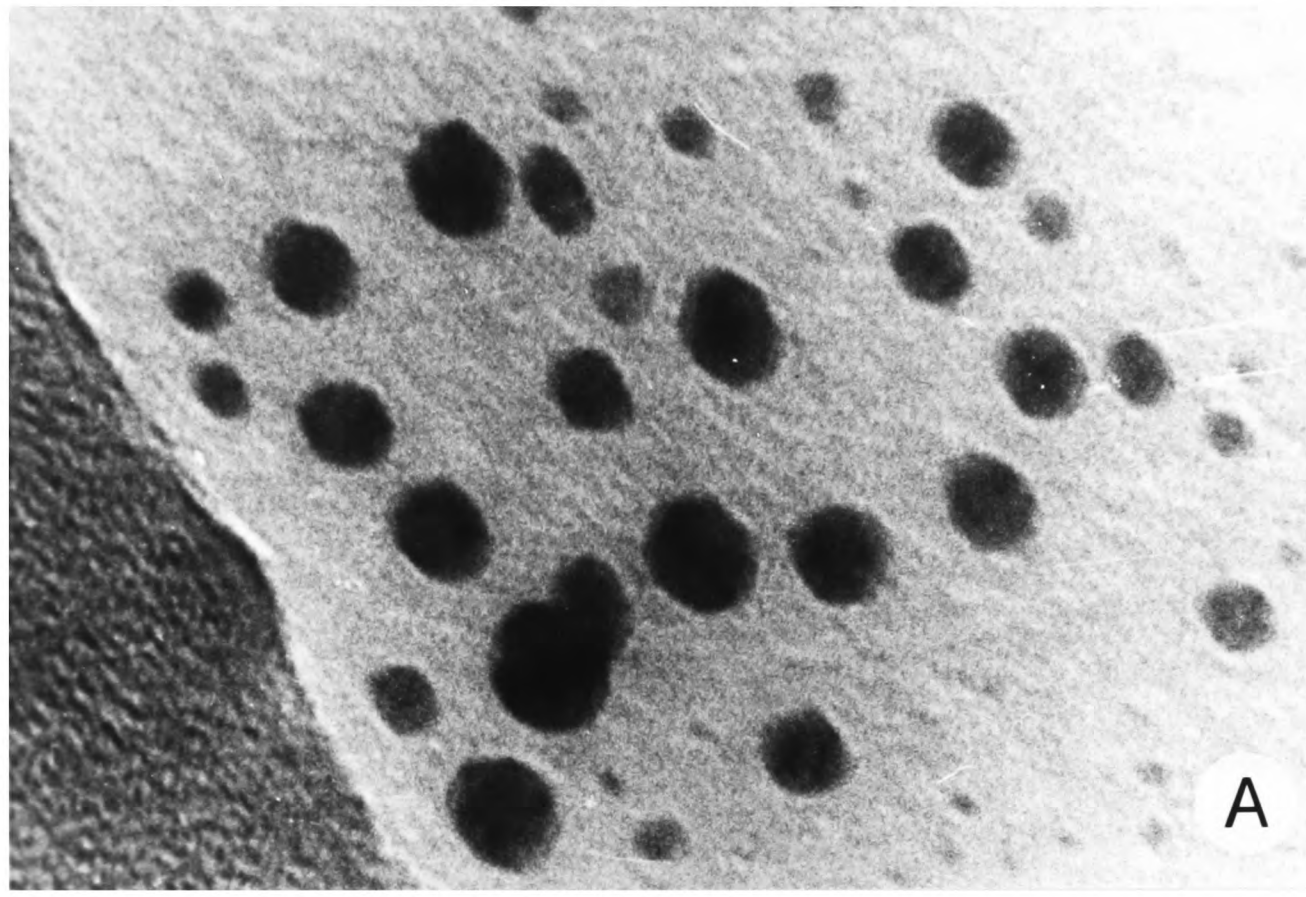

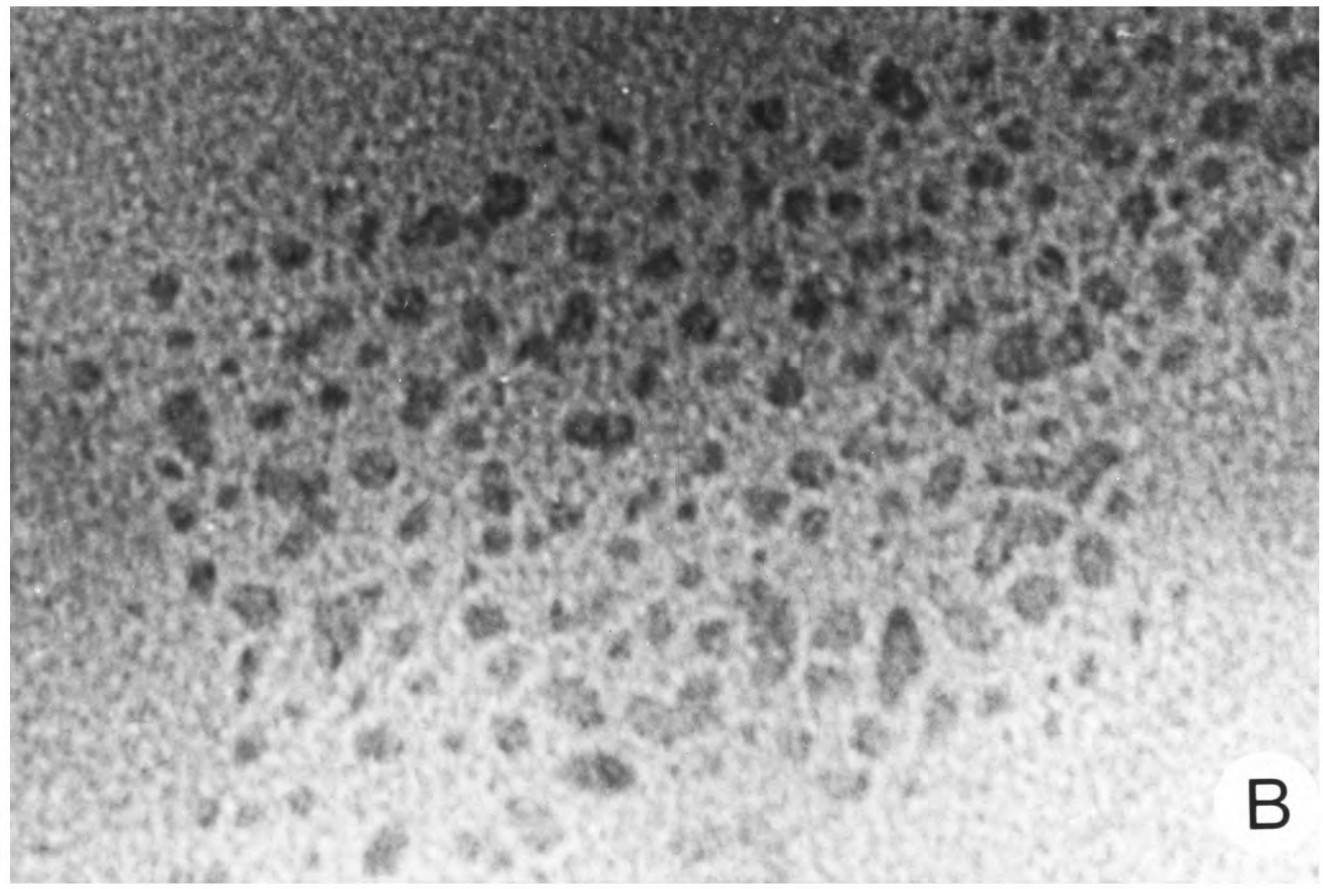

Figure 3.6 Intravesicular Ag_2O particulates under different reaction conditions; a, final reaction product from a sonicated Ag(I) concentration of 31.25mM x164,000; b, reaction product after ten seconds for a sonicated Ag(I) concentration of 250mM x208,000.

particulates could not be observed. Similarly, electron diffraction on these particles showed no d spacings. This is probably due to the low mass concentration of Ag_2O present in the regions investigated. Hence it is only circumstancial evidence that these images are very small Ag_2O crystallites.

If these particulates are the initial stages of formation of vesicular Ag_2O then it is important to note that they are continuous and not 'hollow' in appearence. Nucleation at myriad sites along the lipid membrane may well result in an initial annulus of material which could then be filled in as crystal growth proceeded (assuming that further diffusion of hydroxide ions was possible into the interior of the vesicle volume). Since the images at this stage of growth are continuous and often angular in appearence this would suggest that the nucleation proceeds at one centre along the vesicle membrane (see section 3.7).

The reaction product of this vesicle system was also examined in the electron microscope after one minute of reaction and showed larger particulates of diameter 4-8 nm. X-ray microprobe analysis detected P and Ag over these spheres. Particulates imaged after three minutes of reaction showed spheres of diameter 8-10nm, which gave cubic Ag_2O electron diffraction spacings and P and Ag peaks in the X-ray energy spectrum.

In this section the use of electron microscopy in locating and identifying Ag_2O crystallites formed within ca. 30nm diameter PC vesicles has been discussed. One of the disadvantages of EM is that it observes only static systems under abnormal conditions (high vacuum for instance). ^1H n.m.r. spectroscopy provides a means to study the dynamic formation of Ag_2O

crystallites within vesicles under normal conditions. Also, although we detect phosphorous in the X-ray micro-analysis of such crystallites, this is not sufficient evidence that the vesicles are still intact at the final stage of reaction; we may have Ag_2O crystallites attached to phospholipid fragments for instance. ^1H n.m.r. spectroscopy provides a method of investigating the stability of the vesicle system under the necessary reaction conditions. This method is discussed in detail in the next section.

3.4 ^1H n.m.r. spectroscopy studies of intravesicular Ag_2O crystallites

3.4.1 Stability at high pH

It is important to investigate the stability of a vesicle system containing Ag_2O crystallites since, at the high pH required for precipitation, phospholipids will be subject to hydrolysis (4).

The stability of PC vesicles containing Ag(I) ions was studied by recording ^1H n.m.r. spectra of D_2O solutions before and after (30 minutes) the addition of NaOD solution. If extensive hydrolysis occurs within this time then the vesicle spectrum should show a significant decrease in the intensity of lipid resonances.

Figure 3.7a shows the ^1H n.m.r. spectrum of PC vesicles with Ag (I) ions encapsulated in the internal compartment recorded before the addition of NaOD. Figure 3.7b shows the same vesicle sample 30 minutes after the addition of NaOD. No change in intensity or in the chemical shift of lipid resonances was observed (table 3.3) which indicates that the vesicles are still intact after Ag_2O precipitation.

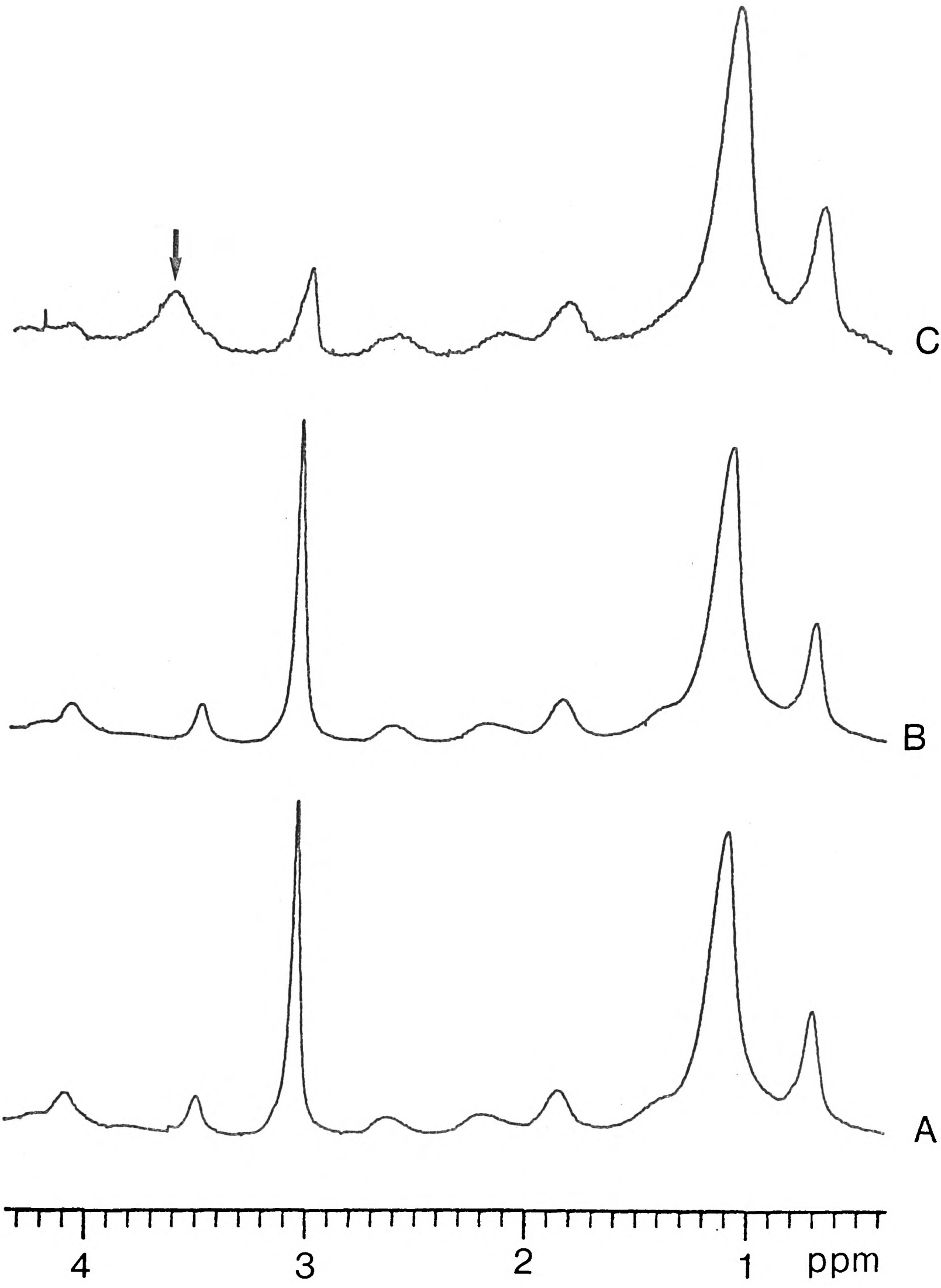

Figure 3.7 ^{1}H n.m.r. spectra of vesicles containing Ag(I) at different pH values; a, ca. 8.0; b, 12.3 c, ca. 2.0 . Spectrum c was taken after addition of 5mM Pr(III). The arrow indicates the external NMe_3^+ resonance.

Table 3.3 Chemical shift values for several lipid resonances in vesicle spectra containing Ag(I)ions at different pH

Spectrum	pH	Chemical shifts (δ)					
		t-Me	$(CH_2)_n$	$\overset{+}{N}Me_{3IN}$	$\overset{+}{N}Me_{3OUT}$	($\overset{+}{N}Me_{\overline{3OUT}}$ t-Me)	($\overset{+}{N}Me_{\overline{3IN}}$ t-Me)
$Ag(I)_{IN}$	ca.8.0	0.65	1.04	3.00	3.00	2.35	2.35
Ag_2O_{IN}	12.3	0.65	1.035	3.00	3.00	2.35	2.35
Ag_2O_{IN} + Pr(III)	ca.2.0	0.57	0.96	2.91	3.53	2.96	2.34

The presence of an intact bilayer at high pH can further be deduced by addition of a shift/broadening reagent to one phase of the vesicle system. An intact bilayer will then show two lipid headgroup resonances corresponding to the internal and external facing $\overset{+}{N}Me_3$ groups.

Pr(III) ions (final concentration 5mM) was added to an acidified solution of the vesicle sample corresponding to the spectrum in figure 3.7b. Figure 3.7c shows the spectrum obtained after 100 scans. Pr(III) ions could not be added directly at pH 12.3 as $Pr(OH)_3$ would be precipitated. The outer $\overset{+}{N}Me_3$ resonance in figure 3.7c is shifted and broadened to a chemical shift value of 3.53 ppm from an original position of 3.00 ppm. The internal $\overset{+}{N}Me_3$ resonance has shifted slightly upfield from 3.00 ppm to 2.91 ppm. This is the same shift observed for the entire vesicle spectrum on changing from alkaline to acid conditions (table 3.3). Thus the shift of only the external $\overset{+}{N}Me_3$ headgroup resonance on addition of external Pr(III) ions shows that the vesicle bilayer is intact and hence Ag_2O formation occurs within an intact vesicle compartment.

3.4.2 Use of paramagnetic probes to follow precipitation reactions within vesicles

The passage of hydroxide ions across the vesicle membrane and subsequent reaction with the internally trapped Ag (I) ions cannot be followed directly by ^1H n.m.r. However, substitution of the encapsulated Ag (I) ions for paramagnetic Co(II) ions allows a related chemical process, namely the formation of $Co(OH)_2$ particulates within the vesicle, to be studied by ^1H n.m.r.

A 250mM $CoCl_2$ solution in D_2O was sonicated in the presence of 17mM PC. The Co(II) ions in the external phase of

the vesicle solution were removed by cation ion-exchange chromotography. ^{1}H n.m.r. spectra were recorded on the vesicle solution now containing only internally trapped Co(II) ions (figure 3.8a). The spectrum shows two resonances from the $\overset{+}{N}Me_3$ headgroups with the internal resonance at a chemical shift value of 2.82 (arrow) and the external resonance at a value of 3.11 ppm. Addition of NaOD to this solution (final pH 12.4) resulted in the disappearance of the internal $\overset{+}{N}Me_3$ resonance after ten minutes (time taken for spectrum to be recorded) leaving one $\overset{+}{N}Me_3$ resonance (at 3.11 ppm) corresponding to internal and external headgroups (figure 3.8b).

Co(II) ions are initially bound close to the inner surface of the vesicle membrane resulting in the splitting of the chemical shift of the $\overset{+}{N}Me_3$ lipid headgroups due to magnetic perturbations in this region of space. Addition of hydroxide ion (OD^-) removes the Co(II) ions from the binding sites and incorporates the ions within the solid phase of $Co(OH)_2$. Hence the internal $\overset{+}{N}Me_3$ resonance position disappears, being shifted back under the external $\overset{+}{N}Me_3$ resonance.

The formation of $Co(OH)_2$ particulates within the vesicle volume results in a broader $\overset{+}{N}Me_3$ resonance than before precipitation. The presence of a paramagnetic solid will cause large bulk magnetic susceptibility effects at the membrane surface giving rise to broader resonances. No extensive broadening was seen on the formation of diamagnetic intravesicular Ag_2O particulates (figure 3.7b).

^{1}H n.m.r. is then one method of following precipitation reactions within the internal compartment of PC vesicles. The method provides evidence for the stability of vesicle systems at high pH and is a means to study the passage of hydroxide ions

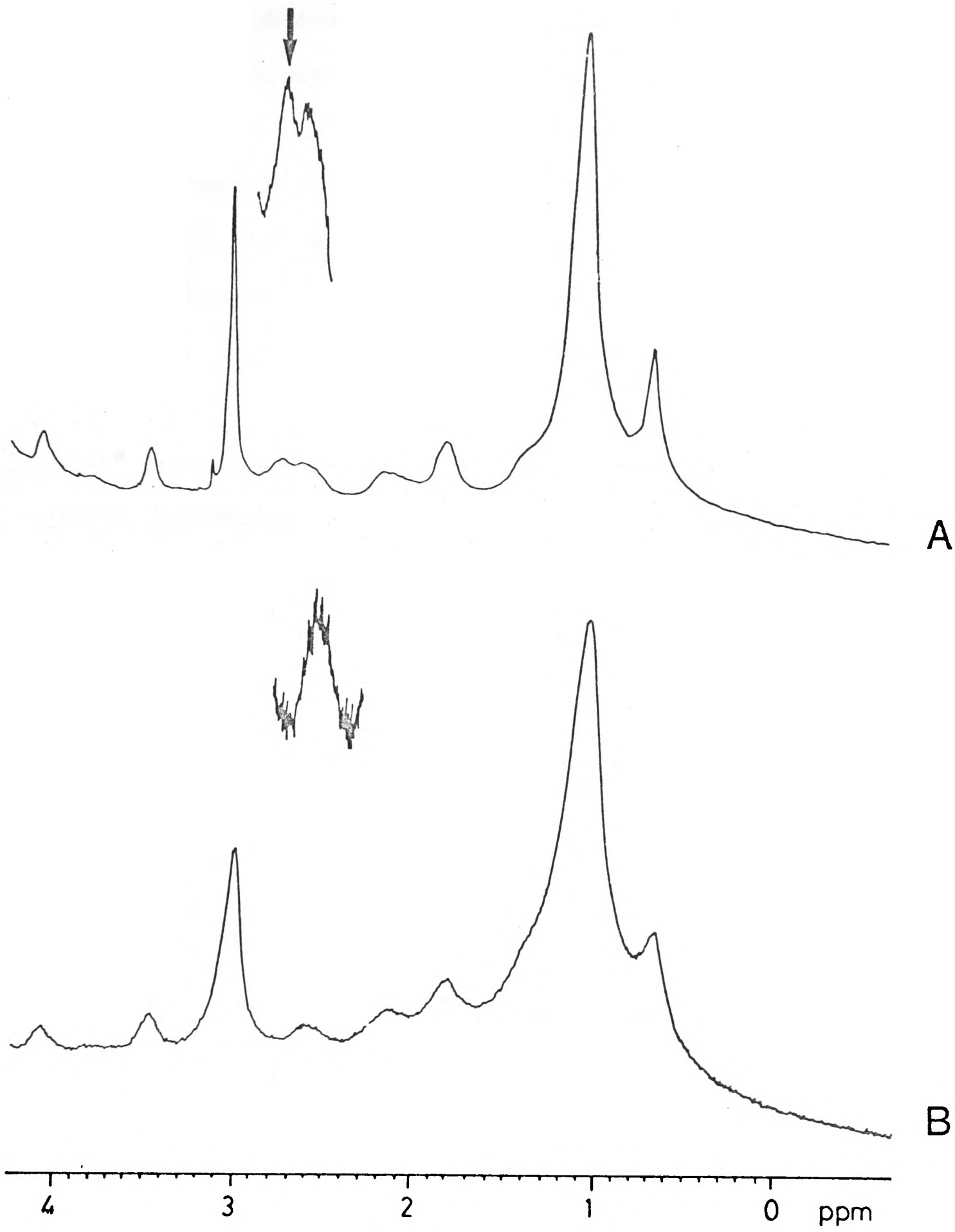

Figure 3.8 ^{1}H n.m.r. spectra of Co(II)-containing vesicles at different pH values; a, ca. 8.0, b; 12.4. The arrow in a locates the shifted internal $\overset{+}{N}Me_3$ resonance. This peak disappears in b.

through the lipid membrane. Unfortunately in the latter case the method is dependent on the presence of a paramagnetic ion within the vesicle. A direct method of studying the formation of a diamagnetic solid such as Ag_2O is through light scattering measurements of the system at different time intervals. In the next section several light scattering experiments on intravesicular Ag_2O formation are described.

3.5 Light scattering studies of intravesicular silver (I) oxide formation

Light scattering is a method often used in colloidal chemistry as a criterion for studying the extent of reaction in an aggregating system. The formation of Ag_2O particulates within vesicle compartments will be accompanied by a corresponding increase in light scattering. The reaction can then be followed by measuring solution turbidity with time.

One of the largest errors of the light scattering method arises from the need to have a high degree of uniform particle size (5). This criterion holds for intravesicular Ag_2O crystallites since they are formed within a narrow range of particle diameter (section 3.3.1). Further refinement of the vesicle size distribution could be obtained by fractional separation using Sephradex gels. This was not undertaken in the work reported in this chapter.

Two main areas of intravesicular Ag_2O formation are discussed.

(a) The kinetics of formation of crystallites of different size and at different pH.

(b) The thermodynamic equilibria of Ag_2O formation at different pH values.

3.5.1 Theory of light scattering

During its propagation in a material medium, the electromagnetic wave of light polarises atoms and molecules composing the medium. This polarisation follows the frequency of the illuminating light beam, thus causing the polarised structural elements of the substance to become themselves sources of luminescence. In a completely homogeneous medium, such as in an ideal crystal, the diffuse light thus obtained produces interference so that the lateral light is completely extinguished and the beam propagates without any weakening (scattering). When the polarisability of the micro-regions of the medium is not the same everywhere, then the scattered light does not undergo complete extinction and opalescence appears.

The polarisability of a substance is governed by its dielectric constant ε or, because

$$\varepsilon = n^2$$

by its refractive index n. Consequently any inhomogeneity with respect to ε or n is a source of opalescence. Such inhomogeneity occurs in heterogeneous disperse systems of a substance whose refractive index differs from that of the dispersion medium. Hence colloidal sols will show a pronounced ability to scatter light.

The theory of light scattering has been extensively studied (6), (7). For large particle sizes the theory is complex but for particles of radius $< \lambda/10$ where λ is the wavelength of the light scattered, the theory is relatively simple and obeys the Rayleigh condition;

$$\tau = \frac{\kappa r^6}{\lambda^4} \qquad 3.(1)$$

Where τ = turbidity, measured by optical density (absorbance)

κ = constant dependent on the refractive indices of solute and solvent.

r = particle radius

λ = wavelength of scattered light.

Since the volume of a spherical particle ν is related to the particle radius by

$$\nu \alpha r^3$$

then

$$\tau = \frac{\kappa^1 \nu^2}{\lambda^4} \qquad 3.(2)$$

Thus for a very small Ag_2O crystallite, growing within a vesicle and obeying the Rayleigh condition, the value of turbidity at any given time will be proportional to the square of the particle volume at that time, which in turn is a measure of the extent of particulate formation.

3.5.2 Methods

Vesicles containing $AgNO_3$ solution encapsulated within the internal volume but with Ag (I) ions removed from the external phase were prepared as before. Samples were used within three hours of preparation for light scattering experiments. The spectrophotometer used was a Carey Model 17, operating at a fixed wavelength of 600nm, slit width 0.2-0.35mm. Glass cells of 1cm path length were used to contain the vesicle solutions. All experiments were completed at room temperature (298K ± 3K).

Light scattering and pH measurements were taken before and after addition of small aliquots ($0.05cm^3$) of sodium hydroxide solutions (0.1-1.0M) to the vesicle solutions. The change in turbidity at 600nm was then followed directly with time.

Intravesicular Ag(I) concentrations were calculated from flame atomic absorption spectroscopy performed by Mr. J. Kench (Inorganic Chemistry Laboratory, Analytical Service). Concentrations are quoted as moles of internal Ag(I) per litre of vesicle solution. A series of vesicle solutions (17mM lipid) with known Ag(I) concentration were analysed by atomic absorption spectroscopy in order to derive a calibration curve for unknown vesicle samples. The presence of lipid was observed to suppress the Ag(I) concentration measurements (figure 3.9).

3.5.3 Determination of Rayleigh condition for vesicle samples

A test of the Rayleigh condition of light scattering can be performed on vesicle samples by measuring the light scattered over different wavelengths of incident light. From equation 3.(1), a plot of log τ against log λ should be a straight line of gradient - 4.0 provided that that particle/vesicle radius is constant.

The light scattered from (a) vesicles (17mM lipid) containing Ag(I) ions, (250mM) and (b) vesicles (17mM lipid) containing Ag_2O particulates was measured over a wavelength range of 400-650nm. No absorbance bands were seen over this wavelength range. Figure 3.10 shows the plots of log τ against log λ for these two vesicle systems. The gradients were calculated as -3.4 for a and -3.5 for b. The deviation of these values from the theoretical value of -4.0 is due to the various simplifications made in the Rayleigh theory. These include; (a) No light absorption. Ag_2O is black/brown and will therefore absorb to some extent a fraction of the illuminating light. (b) The light scattered by each particle is the same. This may not be strictly true for the experimental concentrations used, hence multiple

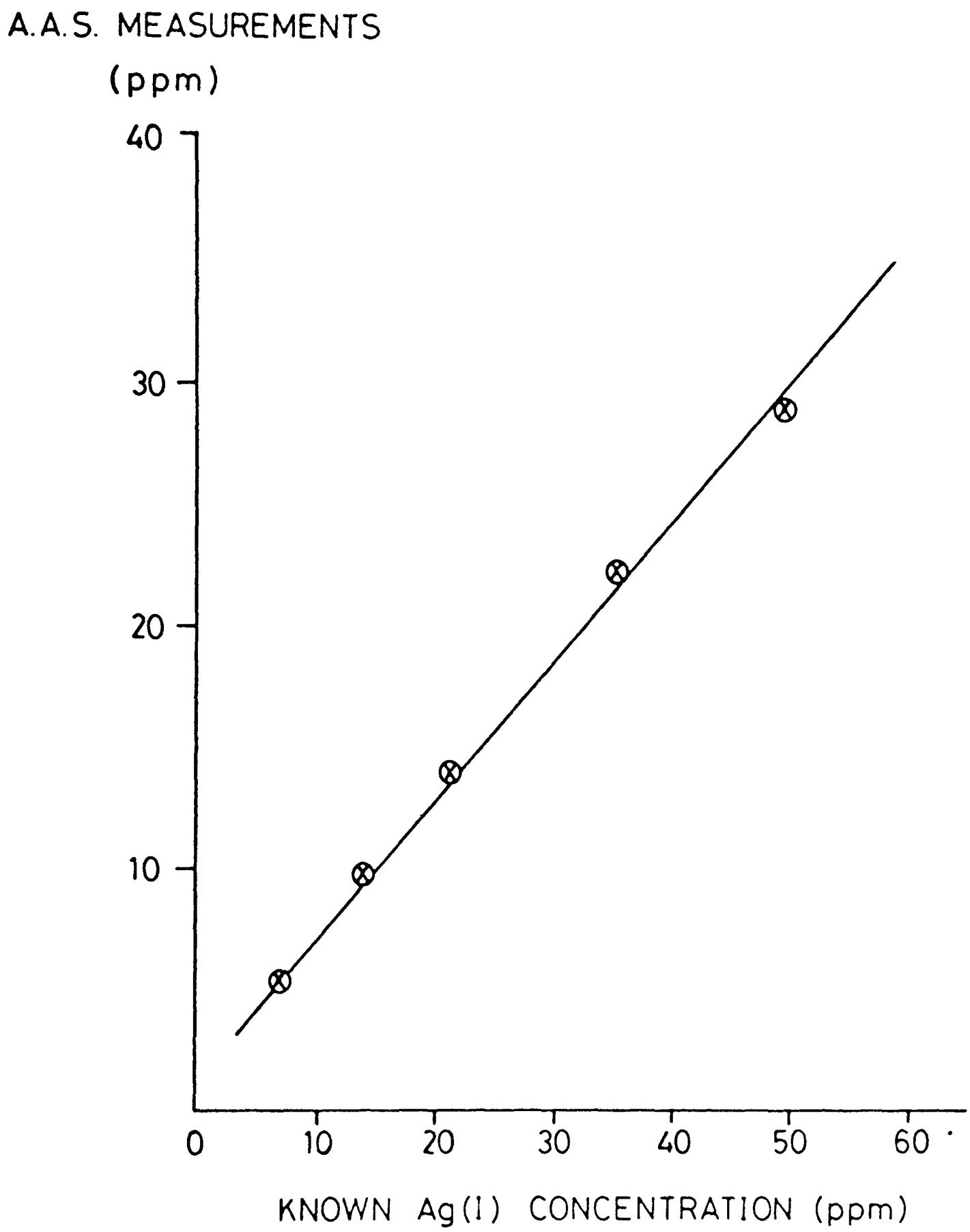

Figure 3.9 Atomic absorption spectroscopy (A.A.S.); calibration curve for Ag(I) vesicle solutions.

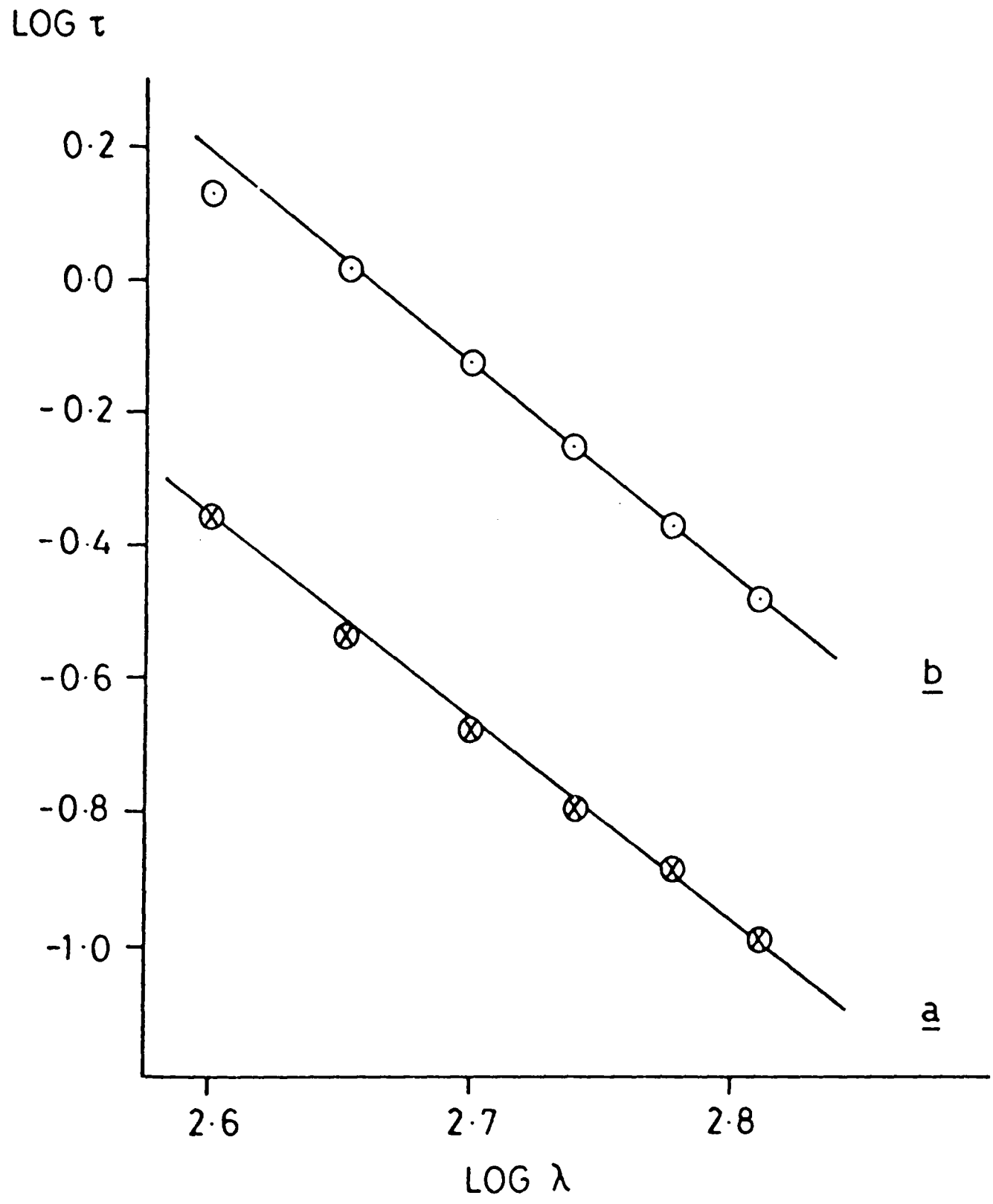

Figure 3.10 Calculation of Rayleigh exponetial for; a, vesicles containing Ag(I) ions; b, vesicles containing Ag_2O crystallites.

scattering may occur due to the particles being illuminated not only by the external source but also by the diffuse light from other particles. (c) Uniform particle size. There will be some inhomogeneity within the Ag_2O size range.

In the light of these factors the deviation of the calculated gradients is ca. 15% which is not very great. Hence the proportionality between turbidity and the square of the particle volume is taken to hold and will be used in the forthcoming sections.

3.5.4 Kinetic studies of intravesicular silver (I) oxide formation

(a) Light scattering measurements for different intravesicular Ag(I) concentrations

The increase in turbidity on forming Ag_2O crystallites within PC vesicles can be related to the square of the particulate volume at a given time (section 3.5.1, equation 3(2)). For two vesicle solutions of equal concentration in lipid containing different encapsulated Ag(I) concentrations raised to the same final pH value so that the reaction goes to completion (steady state equilibrium) in each case, then the particulate volume formed will be directly proportional to the initial mass of Ag(I) present and hence is proportional to the initial Ag(I) concentration encapsulated within the vesicle. Hence if the Rayleigh condition holds for such a system, the total increase in turbidity ($\Delta\tau$) will be proportional to the square of the initial Ag(I) concentration.

Eight vesicle samples (17mM in lipid) were prepared incorporating different Ag(I) concentrations within the internal vesicle volume. The initial pH of vesicle solutions after ion-

exchange chromotography was in the range 8.0-9.0. For each vesicle sample the pH was raised to 12.3 by sodium hydroxide solution and the increase in turbidity at 600nm (τ_{600}) measured with time.

Figure 3.11 shows the results for four different initial internal Ag(I) concentrations. The initial light scattered due to the vesicles alone is in the range 0.20-0.24, which shows a small difference in vesicle concentration due to dilution effects on the chromotography column. The curve for vesicles prepared in the absence of Ag(I) ions (curve a, 'blank' vesicles) shows a characteristic small (0.01) initial rise in turbidity after sodium hydroxide addition followed by a decrease in light scattered back to its original value. No further change in turbidity at pH 12.3 was observed over 3.5 hours which indicates that the vesicles are stable at high pH over this time range since degradation and fusion of vesicles would result in larger lipid aggregates with a corresponding increase in light scattered. The reason for the initial rise in turbidity for 'blank' vesicles is not clear. One possibility is that vesicle swelling may occur on addition of sodium hydroxide due to increased ionic gradients across the lipid membrane. Curves b, c, d show the changes in turbidity at 600nm for different internal Ag(I) concentrations. The formation of intravesicular Ag_2O is slow as shown from the slope of the curves. For Ag_2O precipitation in normal aqueous solution (no vesicles) the resulting turbidity change is instantaneous.

Figure 3.12 shows a plot of the square root of the total increase in turbidity ($\Delta\tau_{600}^{\frac{1}{2}}$) calculated from graphs as in figure 3.11, against the concentration of intravesicular Ag(I) ions expressed in mole per litre of vesicle solution.

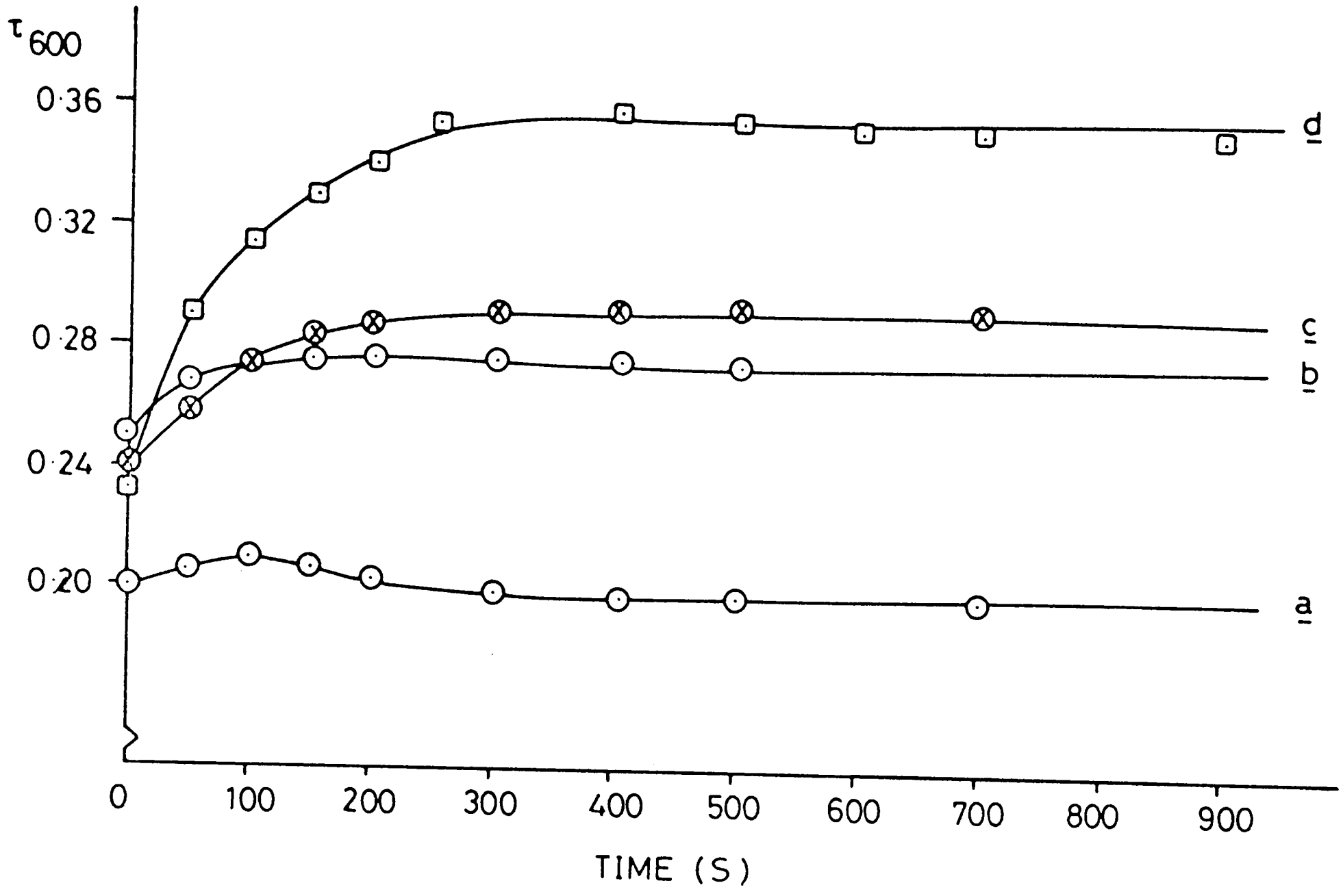

Figure 3.11 Change in turbidity at 600nm (τ_{600}) with time after the addition of $NaOH_{(aq)}$ to a final pH value of 12.3 for vesicle solutions containing different internal Ag(I) concentrations; a, 'blank' vesicles; b, 5.1×10^{-5} mol l^{-1}; c, 17.2×10^{-5} mol l^{-1}; d, 33.8×10^{-5} mol l^{-1}.

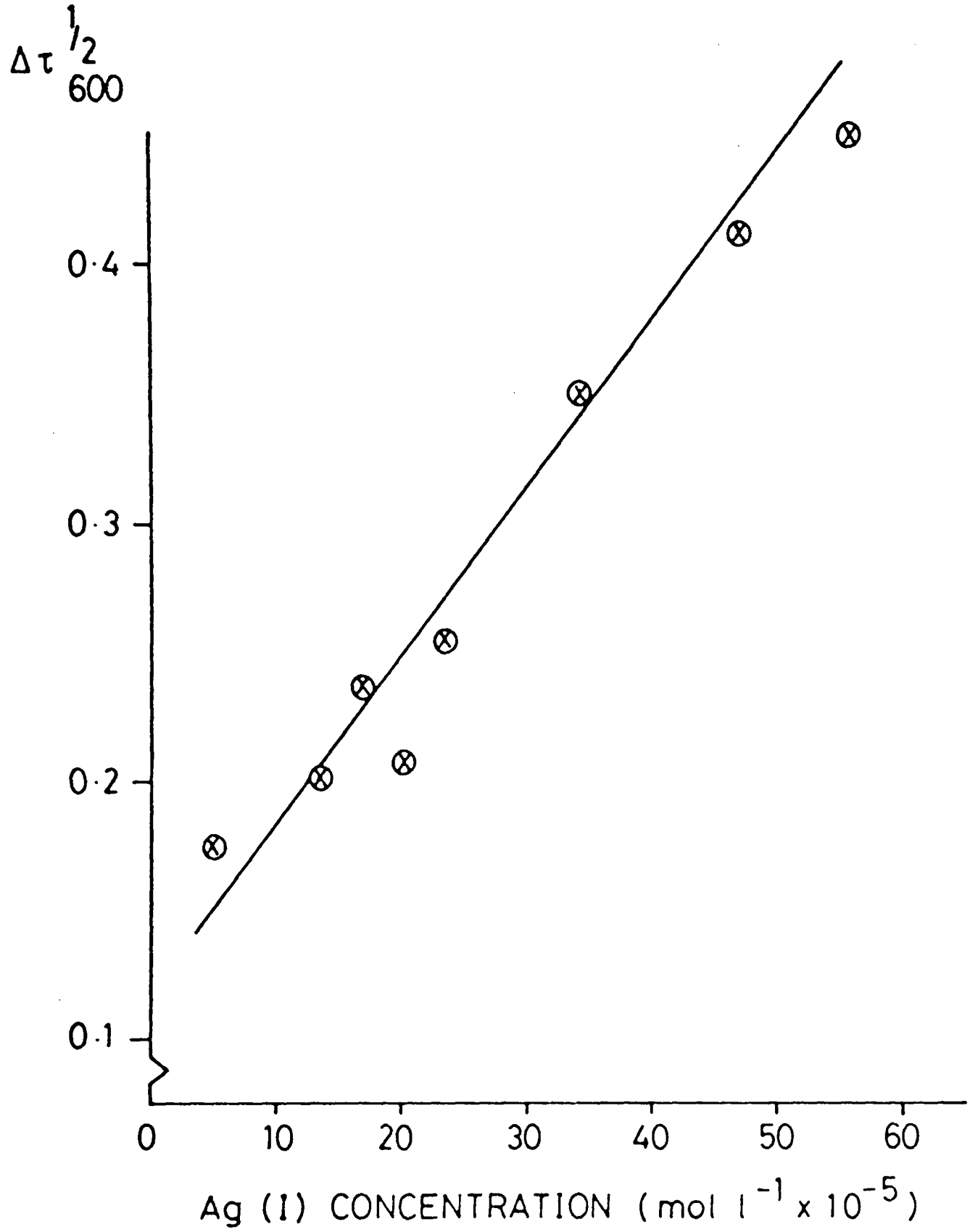

Figure 3.12 Relationship between the square root of total turbidity change of 600nm ($\Delta\tau_{600}^{\frac{1}{2}}$) and intravesicular Ag(I) concentration (final pH = 12.3).

The graph presents a linear relationship between $\Delta\tau_{600}^{\frac{1}{2}}$ and Ag(I) concentration indicating that Rayleigh scattering is observed under these experimental conditions.

(b) Precipitation rates for different intravesicular Ag(I) concentrations

There are at least two possible steps in the reaction mechanism of Ag_2O formation within PC vesicles.

(i) $OH^-_{OUT(aq)} \xrightarrow{K_{diff}} OH^-_{IN(aq)}$

(ii) $2OH^-_{IN(aq)} + 2Ag^+_{IN(aq)} \xrightarrow{K_1} Ag_2O_{IN(s)} + H_2O$

The first step is diffusion controlled and depends on the rate of passage of hydroxide ions through the lipid membrane. The diffusion rate of anions is known to be ca. 10^5 times faster than for cations which have very low permeabilities across lipid membranes (8). Thus the possibility of increasing intravesicular pH by efflux of H^+ ions seems to be low.

Step (i) appears to be more likely to be rate determining when compared with step (ii) since Ag_2O formation is rapid at the pH where precipitation is possible in normal aqueous solution. However, step (ii) occurs within the vesicle and therefore may involve complex kinetics depending on the step growth processes, whether at the membrane surface or in the inner aqueous phase, occurring at the developing crystal surface.

Figures 3.11 and 3.12 showed the light scattering results for vesicles with different intravesicular Ag(I) concentrations.

In each case the rate of OH^- diffusion at any given time in the reaction will be the same since the intra- and extra-vesicular hydroxide concentrations at that time do not vary from one system to another. Thus the dependency of the reaction rate for step (ii) on intravesicular Ag(I) concentration can be determined, since under these conditions,

$$\text{reaction rate} = \frac{-d[Ag(I)]_{IN}}{dt} = k[Ag(I)]^{M}_{IN} \qquad 3.(3)$$

We can relate the initial change in Ag(I) concentration with time to the initial change in turbidity with time by

$$\frac{d[Ag(I)]}{dt}_{IN_o} = \frac{d[Ag(I)]}{d\tau^{\frac{1}{2}}}_{IN_o} \times \frac{d\tau^{\frac{1}{2}}}{dt} \qquad 3.(4)$$

Such a relationship will be linear since the term $d[Ag(I)]/d\tau^{\frac{1}{2}}_{IN_o}$ is a constant and is given by the inverse of the gradient of figure 3.12 and calculated to be 1.30×10^{-3} mol l^{-1}

The initial rate of change of turbidity for different Ag(I) concentrations was calculated by measuring the initial slope of curves such as those of figure 3.11. The corresponding plot of these gradients against initial vesicular Ag(I) concentration is shown in figure 3.13. The graph reveals a linear relationship between the initial rate of precipitation and trapped Ag(I) concentration at constant hydroxide ion values. Thus over the concentration range investigated the initial kinetics appear to be pseudo-first order.

The rate constant for such a reaction can be calculated by combining equations 3.(3) and 3.(4), m being equal to 1.0.

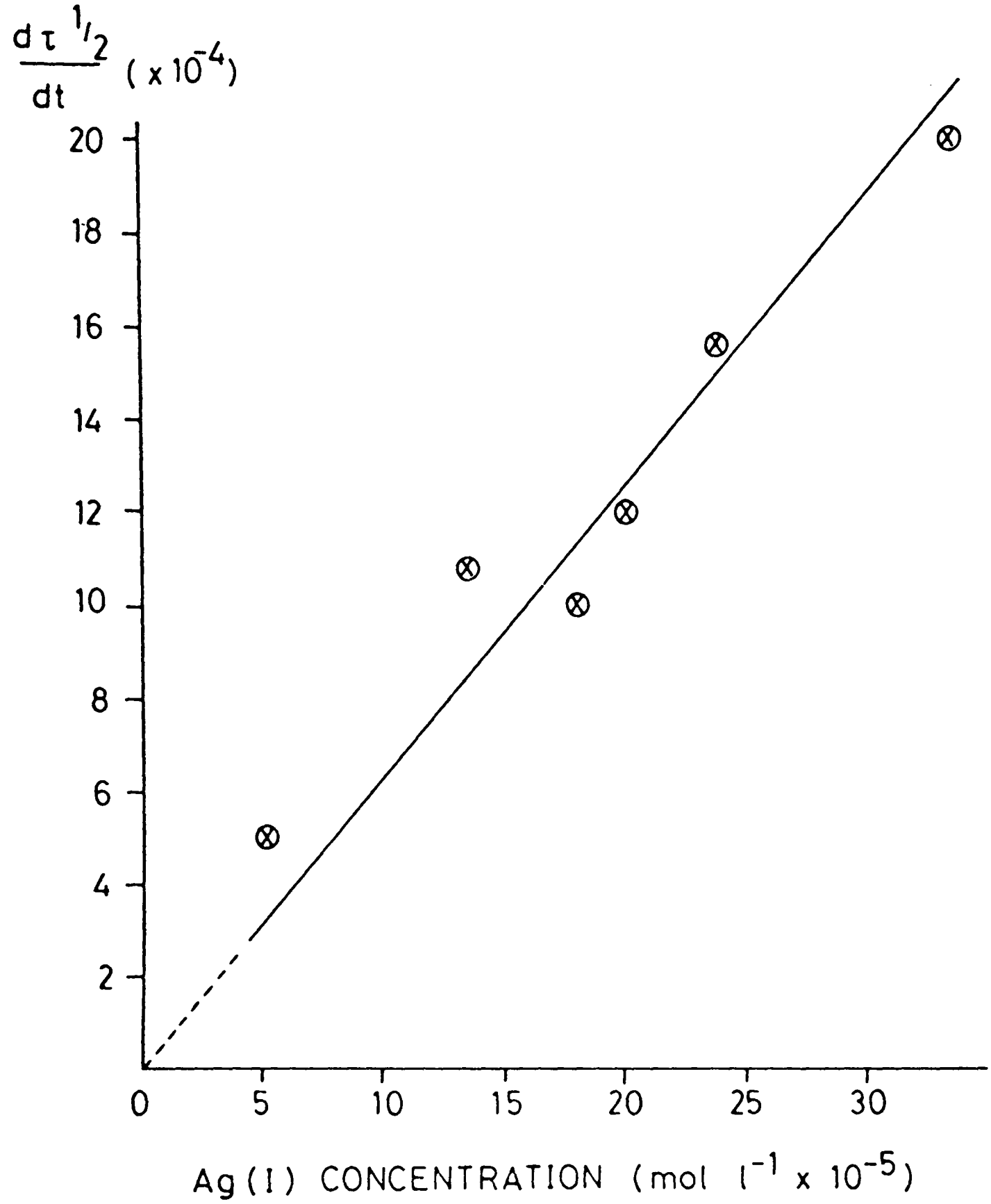

Figure 3.13 Plot of initial rate of precipitation ($d\tau^{\frac{1}{2}}/dt$) against initial intravesicular Ag(I) concentration (final pH = 12.3).

Thus,

$$-\frac{d[Ag(I)]_{IN_o}}{d\tau^{\frac{1}{2}}} \times \frac{d\tau^{\frac{1}{2}}}{dt} = k[Ag(I)]_{IN_o}$$

A plot of $\frac{d\tau^{\frac{1}{2}}}{dt}$ against $[Ag(I)]_{IN_o}$ will have a gradient of $\frac{k}{d[Ag(I)]_{IN_o}/d\tau^{\frac{1}{2}}}$

The gradient of figure 3.13 was calculated to be 5.77 $mol^{-1}l\ s^{-1}$ $d[Ag(I)]_{IN_o}/d\tau^{\frac{1}{2}}$ is 1.30×10^{-3} mol l^{-1}(figure 3.12) resulting in a value for the psuedo-first order rate constant of 7.50×10^{-3} s^{-1}.

Rate constants for each different value of encapsulated Ag(I) concentration can also be found from normal first order kinetic equations. The integrated form of the rate equation for a first order reaction at any time t, is

$$\ln \frac{[Ag(I)]}{[Ag(I)]_t^o} = kt$$

Also,

$$[Ag(I)]_o = [Ag_2O]_\infty = K(\tau_\infty - \tau_o)^{\frac{1}{2}}$$
$$[Ag(I)]_t = ([Ag_2O]_\infty - [Ag_2O]_t) = K(\tau_\infty - \tau_t)^{\frac{1}{2}}$$

Where K is a constant of proportionality.

Thus,

$$\ln\left[\frac{(\tau_\infty - \tau_o)}{(\tau_\infty - \tau_t)}\right]^{\frac{1}{2}} = , kt$$

A plot of log $[(\tau_\infty - \tau_o)/(\tau_\infty - \tau_t)]$ against time should be linear with a gradient equal to 2k/2.303.

Calculations based on the data presented in figure 3.11 were performed in order to plot the above relationship. Figure 3.14 shows a typical plot for an internal Ag(I) concentration of

18.0×10^{-5} mol l^{-1}. In all cases linear graphs were observed. The values of the rate constant for different Ag(I) concentrations were calculated from the gradient of each graph and are listed in table 3.4. The mean rate constant is $7.03 \times 10^{-3} s^{-1}$ with a maximum deviation from the mean of 23.2%. This degree of deviation may be expected since light scattering methods based on Rayleigh theory are subject to several errors (section 3.5.3).

(c) Precipitation rates at different final hydroxide ion concentrations

In this section the effect of changing the concentration of hydroxide ion on the rate of Ag_2O precipitation in a vesicle system of constant internally entrapped Ag(I) concentration is discussed.

$10cm^3$ of Ag(I) encapsulated PC vesicles (17mM) was prepared as described before. $1.2cm^3$ aliquots of this sample were placed in the spectrophotometer and different known amounts of hydroxide ion (OH^-) were added and the turbidity change at 600nm due to the resulting Ag_2O precipitate measured with time. The final pH was also measured. The initial concentration of Ag(I) ions was 22.3×10^{-5} mol l^{-1} from atomic absorption spectroscopy measurements.

Figure 3.15 shows the change in turbidity with time for five different final pH values. Addition of OH^- to a final pH value less than 10.8 resulted in no observable increase in turbidity. Only a slight fall in turbidity is noted due to dilution effects. Thus no Ag_2O formation was observed below this pH value. At intermediate pH values (11.5-12.0) an increase in turbidity is observed after an induction period of ca. 20 seconds implying that the reaction proceeds but is slow in this

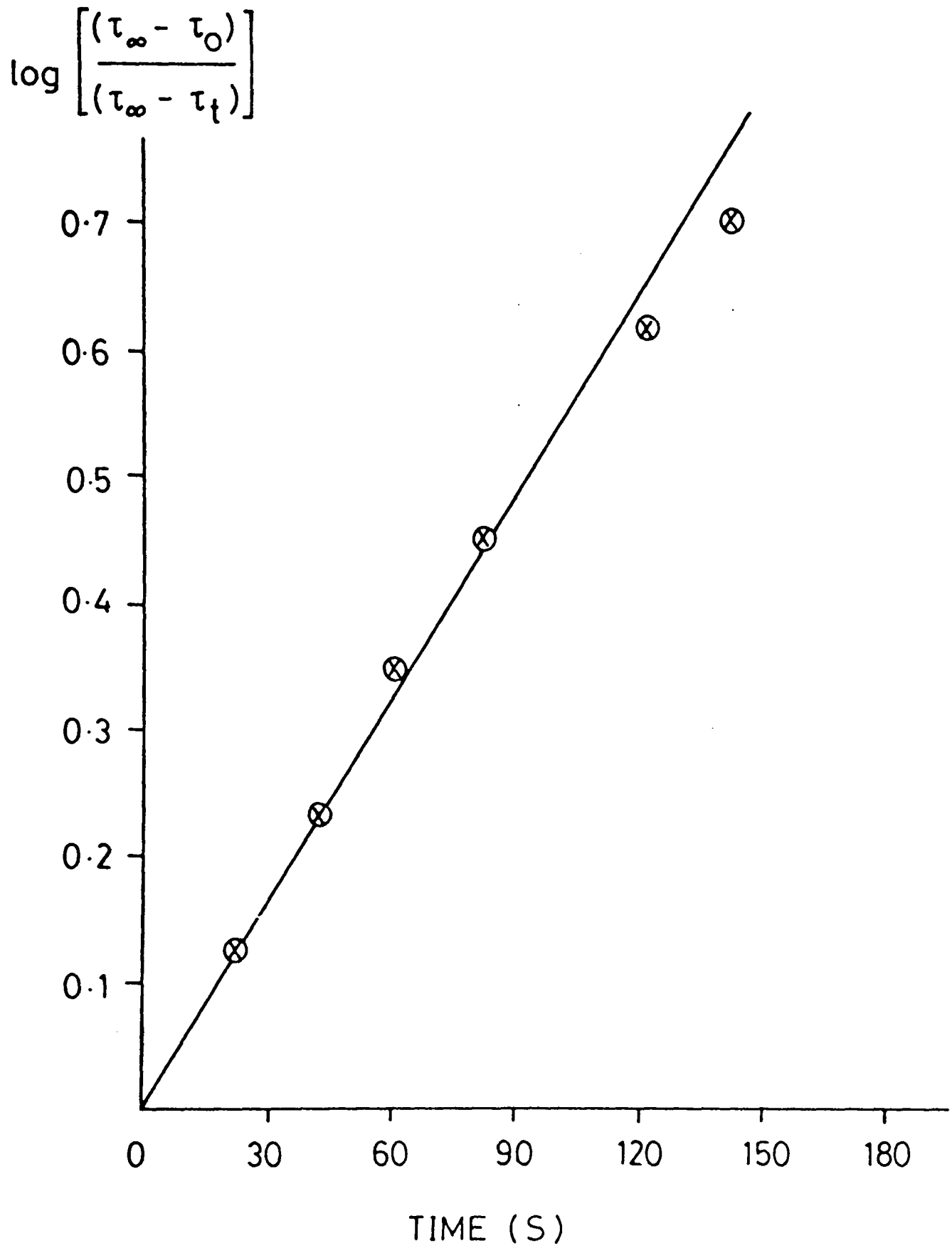

Figure 3.14 First order rate plot for initial intravesicular Ag(I) concentration of 18.0×10^{-5} mol l^{-1}.

Table 3.4 First order rate constants for different vesicular Ag(I) concentrations

$[Ag(I)]_{IN}$ ($moll^{-1}$) $x10^{-5}$	rate constant (s^{-1}) $x\ 10^{-3}$
5.1	8.28
17.1	5.4
18.0	6.32
19.9	8.6
23.6	7.8
33.8	5.86

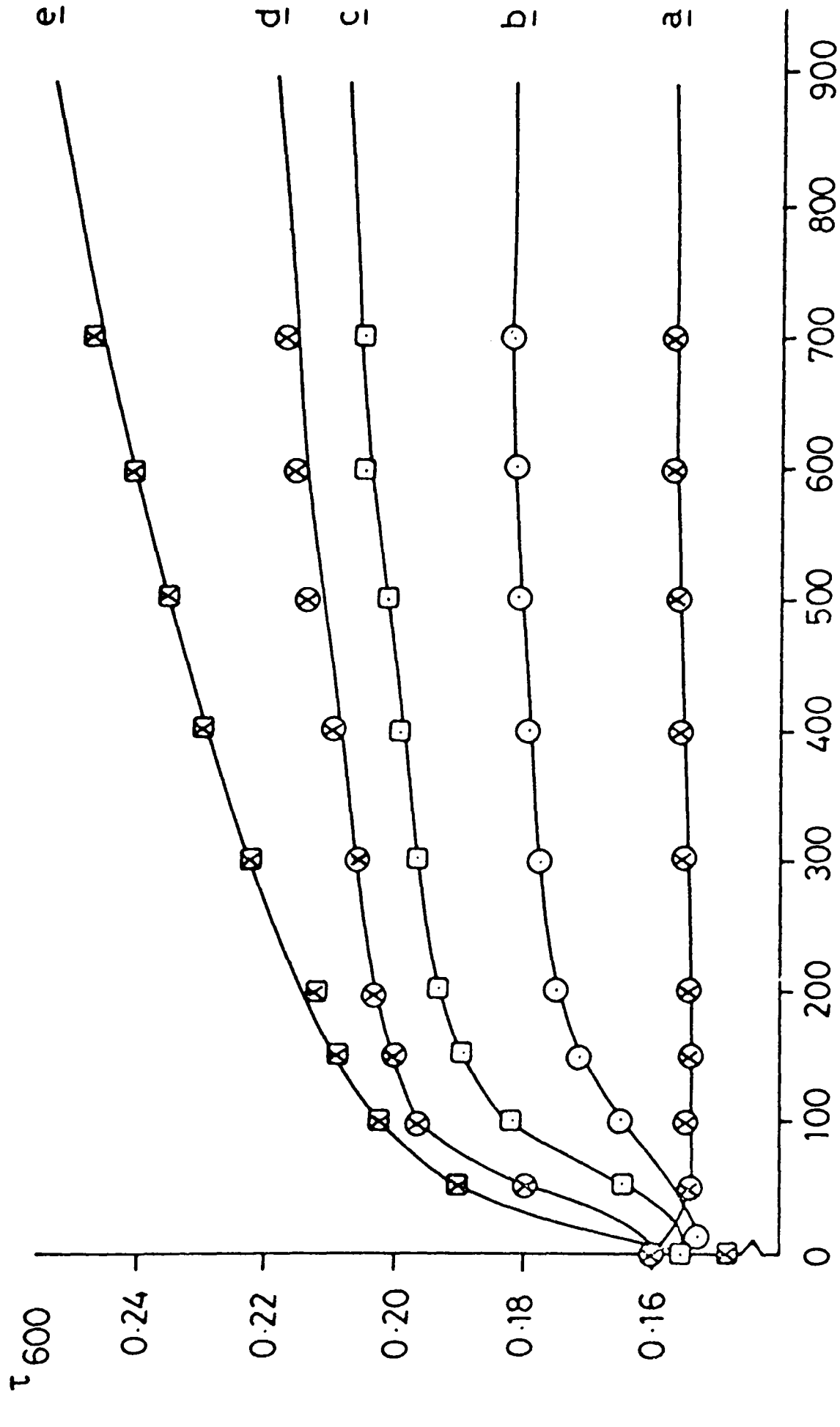

Figure 3.15 Turbidity curves for Ag (I)-containing vesicles (20.3×10^{-5} mol l^{-1}) raised to different final pH values; a, 10.8; b, 11.5; c, 11.95; d, 12.3; e, 12.6.

pH range. At high pH (12.0-12.6) the increase in turbidity follows a similar pattern as observed in section 3.5.4(b).

The initial rate of precipitation, $d\tau^{\frac{1}{2}}/dt$ was calculated by measuring the initial slopes of the graphs in figure 3.15. A plot of initial rate against initial hydroxide ion concentration $[OH^-]$ is shown in figure 3.16. In all cases the $[Ag(I)]_{IN}$ was the same. At pH values below 12.0 the initial rate of precipitation is strongly dependent on $[OH^-]$ Above this pH the initial rate becomes much less dependent on change of $[OH^-]$. At low values of pH rate of crystal growth is dependent on $[OH^-]$ which will be related to the rate of diffusion of the anion through the lipid membrane; that this dependency falls at high external pH seems to suggest that there is a limiting maximum rate of diffusion through the membrane such that the rate of increase of pH inside the vesicle is no longer determined by changes in the external hydroxide concentration.

(d) Turbidity curves for other anions

The kinetics of formation of different Ag(I) precipitates within PC vesicles will markedly change according to the anion to be incorporated into the solid lattice. The greatest effect will be caused by the relative permeabilities of such anions across the lipid membrane.

Figure 3.17 shows the change in turbidity for the same concentration of intravesicular Ag(I) after addition of different anions. Graph a is for AgCl formation. Graph b is for Ag_2O precipitation as described above and c is for Ag_2S precipitation.

In the case of intravesicular AgCl formation the increase in turbidity with time due to the addition of Cl^- is much slower than for Ag_2O formation indicating that Cl^- ion diffusion across

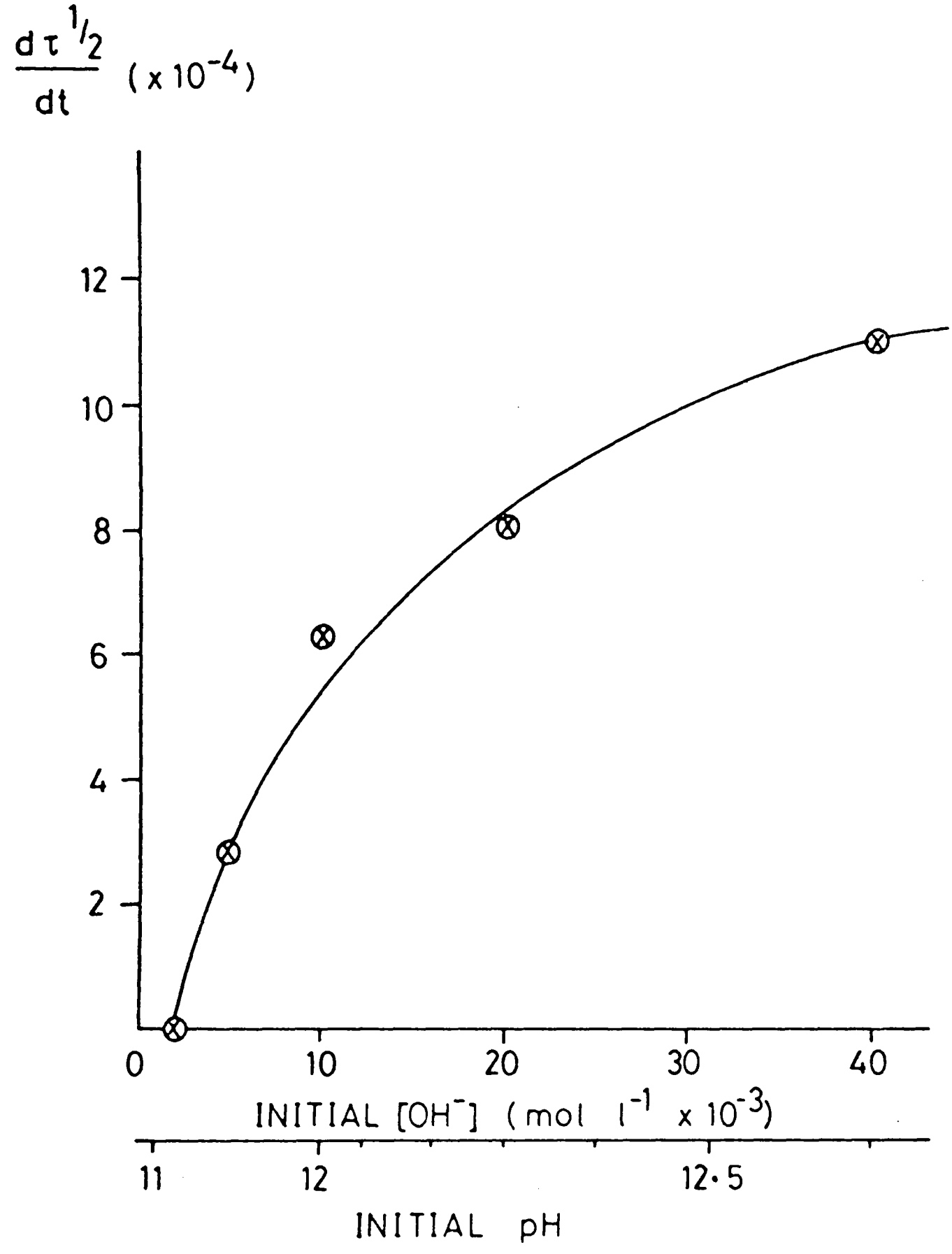

Figure 3.16 Plot of initial rate of precipitation ($d\tau^{\frac{1}{2}}/dt$) against OH^- concentration (pH) for Ag(I)-containing vesicles (20.3×10^{-5} mol l^{-1}).

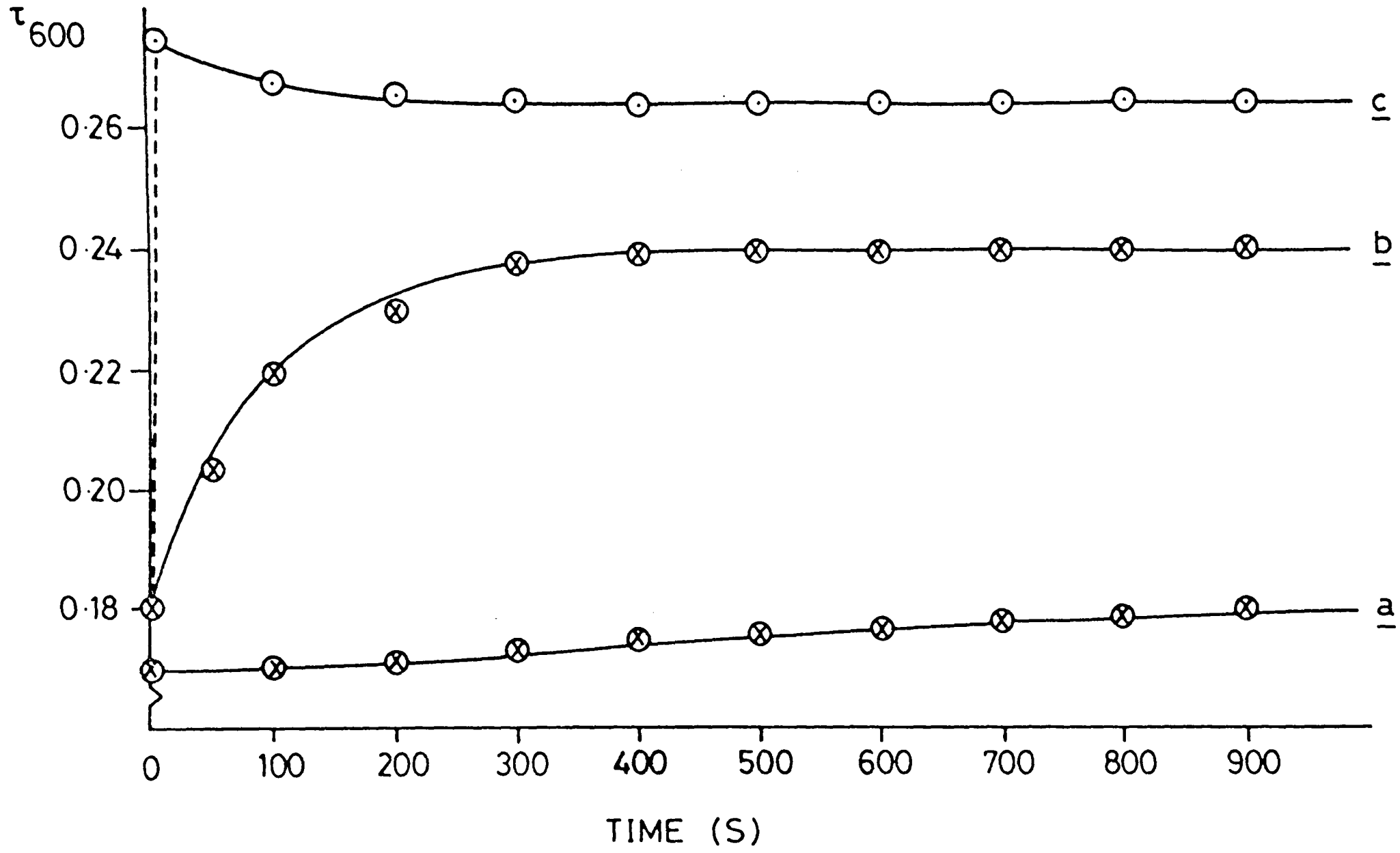

Figure 3.17 Turbidity curves for; a, AgCl; b, Ag_2O; c, Ag_2S formation within vesicles containing the same concentration of Ag(I) ions.

the lipid membrane is much slower than OH^-.

In c the formation of intravesicular Ag_2S occurs instantaneously after the addition of $(NH_4)_2S$. The turbidity of this sample rises immediately from 0.178 to 0.275. This is due to the rapid diffusion across the vesicle membrane of free molecular H_2S in the $(NH_4)_2S$ solution. There is a slight decrease in turbidity with time before reaching a steady turbidity value which seems to indicate that the particulates formed initially are in non-equilibrium conditions and come to equilibrium within 150 seconds of formation.

The final turbidity values for intravesicular Ag_2S, Ag_2O and AgCl formation will be different depending on the refractive indices of the different particulates formed (section 3.5.1).

3.5.5 Thermodynamic aspects of intravesicular Ag_2O formation

In section 3.5.4(c) it was shown that the kinetics of intravesicular Ag_2O formation is dependent on the final extravesicular pH. In this section some aspects of the thermodynamic characteristics of intravesicular Ag_2O formation are discussed. With reference to figure 3.15, the square-root of total increase in turbidity ($\Delta\tau_{600}^{\frac{1}{2}}$) is a measure of the extent of particulate formation. A plot of $\Delta\tau_{600}^{\frac{1}{2}}$ against final hydroxide ion concentration at constant Ag(I) concentration will then be a measure of the extent of reaction at different final pH values. Figure 3.18 shows such a plot derived from the data of figure 3.15. At high pH (12.3-12.6) $\Delta\tau_{600}^{\frac{1}{2}}$ is almost constant indicating that in this range of hydroxide ion concentration the reaction virtually goes to completion. At lower pH values the formation of Ag_2O crystallites is incomplete, with the following equilibrium being maintained.

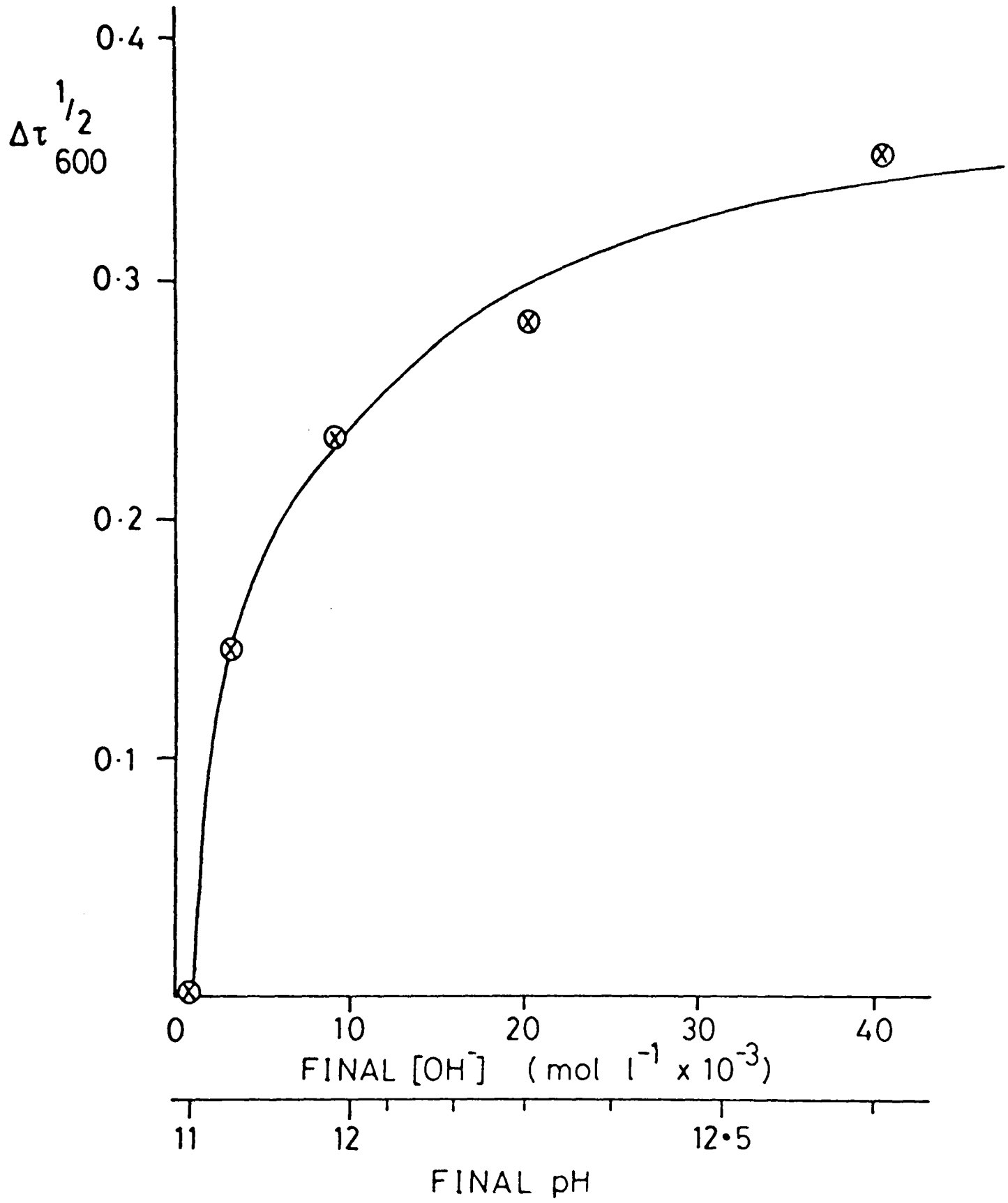

Figure 3.18 Relationship between the square root of total turbidity change at 600nm ($\Delta\tau^{\frac{1}{2}}_{600}$) and hydroxide ion concentration for Ag(I)-containing vesicles (20.3×10^{-5} mol l^{-1}).

$$Ag^{+}_{IN(aq)} + OH^{-}_{IN(aq)} \rightleftharpoons \tfrac{1}{2}Ag_2O_{IN(s)} + \tfrac{1}{2}H_2O_{(aq)}$$

In this section the above equilibrium is investigated within vesicular space and normal space (free aqueous solution). It is important to study such equilibria because crystal formation within vesicles may be thermodynamically different to that in bulk solution. One possibility is that the surface free energy of small confined crystallites will be much greater than for crystals grown in free solution due to the greater surface area to volume ratio of small particulates. The corresponding increase in more positive free energy of crystallisation would result in different solubility equilibria being established. One immediate problem to resolve is the observation that intravesicular Ag_2O precipitation does not occur below an external pH value of 11.0; is this a solubility characteristic, or a diffusion effect of hydroxide ion permeability?

(a) Stability and change of equilibrium with pH

Initial experiments were performed in order to investigate the equilibrium maintained over periods of time and different pH ranges. Figure 3.19 shows the turbidity changes of Ag(I)-containing vesicles at different pH values. Curve a shows a normal Ag_2O turbidity curve for vesicles raised from pH 8.9 to 12.6 by one aliquot of NaOH. No increase of turbidity above 0.45 was observed after 1 hour of reaction. Curve b shows the same solution first raised to a pH of 11.8 and then after 25 minutes further addition of NaOH raised the pH to 12.7. After the equilibrium has been established at pH 11.8 raising the pH further has no effect on turbidity until after ca. 20 minutes. After this time turbidity increases slowly to a plateau value of 0.47. These results show that the extent of crystallisation

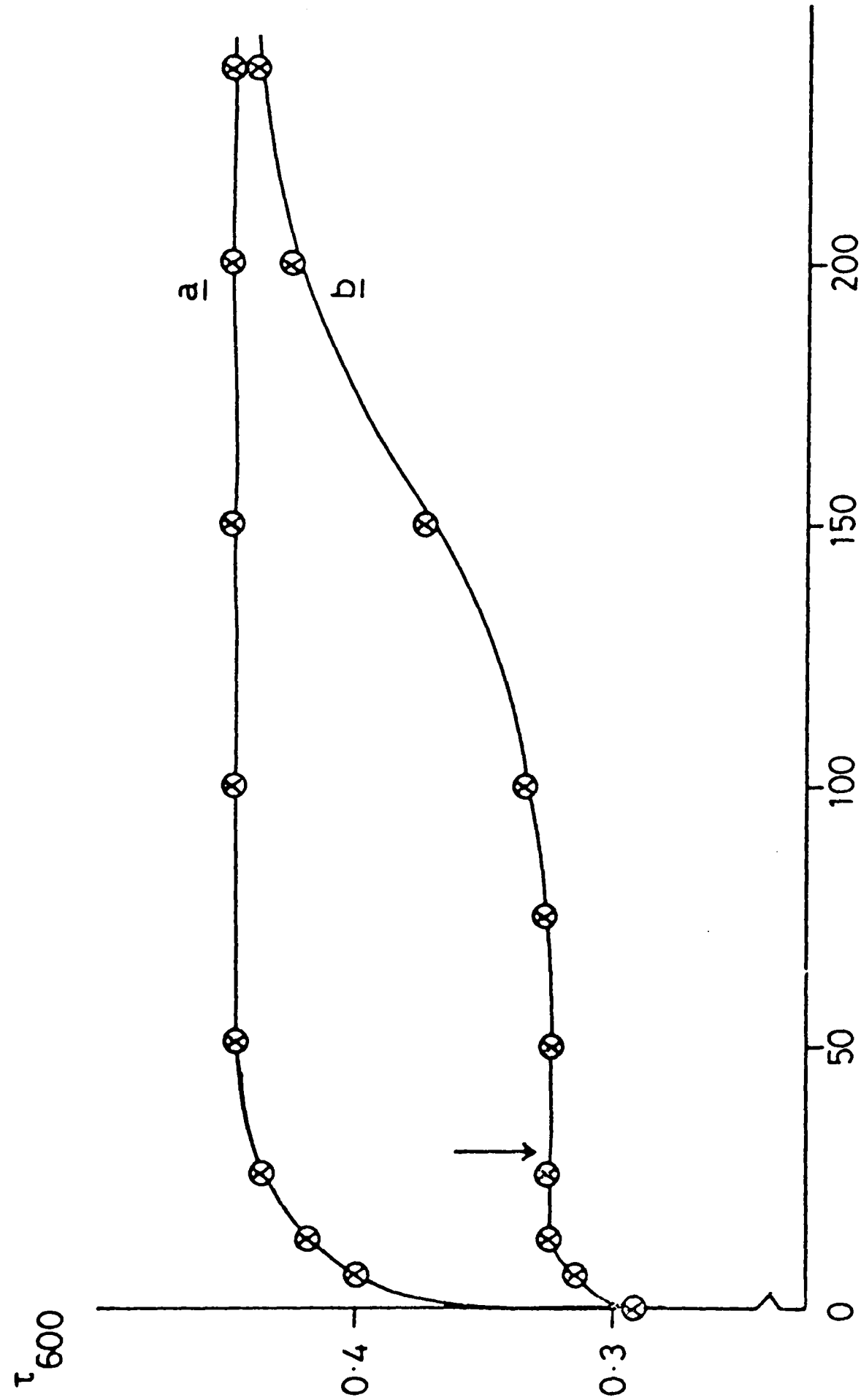

Figure 3.19 Stability and equilibrium conditions for Ag(I)-containing vesicles (pH = 8.9) after addition of $NaOH_{(aq)}$; a, final pH = 12.6; b, pH = 11.8 then after 25 minutes (arrow) raised further to pH 12.7.

of Ag_2O within vesicles is dependent on hydroxide ion concentration and at intermediate pH the crystal is in dynamic equilibrium with aqeuous Ag(I) and OH^- ions. The shift of equilibrium appears to be slow. Thus it takes ca. 250 minutes to grow crystallites of the same size by a series of pH changes (curve b) but only ca. 60 minutes if the pH is raised in one step (curve a). A possible explanation for this observation may be that there is a greater activation energy barrier to further crystallisation onto the existing crystal surface once a stable equilibrium condition has been established. This could be due to the difficulty in creating new nucleation centres on a Ag_2O surface which may be relatively free from defects.

(b) pH titration curves for Ag_2O precipitation in free solution and in vesicular space

The precipitation of Ag_2O in distilled water was studied by the use of a pH glass electrode to monitor hydroxide ion concentration when added to $0.5cm^3$ of 50mM $AgNO_3$ solution. A plot of pH against percentage Ag(I) incorporated into the Ag_2O solid phase is shown in figure 3.20a. The percentage Ag(I) incorporated at a given pH corresponds to the extent of precipitation and was calculated, assuming one Ag(I) ion combines with one hydroxide ion, by the equation,

$$\%\text{Ag(I) incorporated at pH X} = \frac{\text{Volume of NaOH added at pH X}}{\text{Volume of NaOH added at end point}} \times 100$$

In distilled water precipitation begins at a pH of ca. 7.5 for 50mM Ag(I) and follows a normal precipitation titration curve with the end point at a pH value of 10.0. The solubility product of Ag_2O in distilled water can be calculated from this

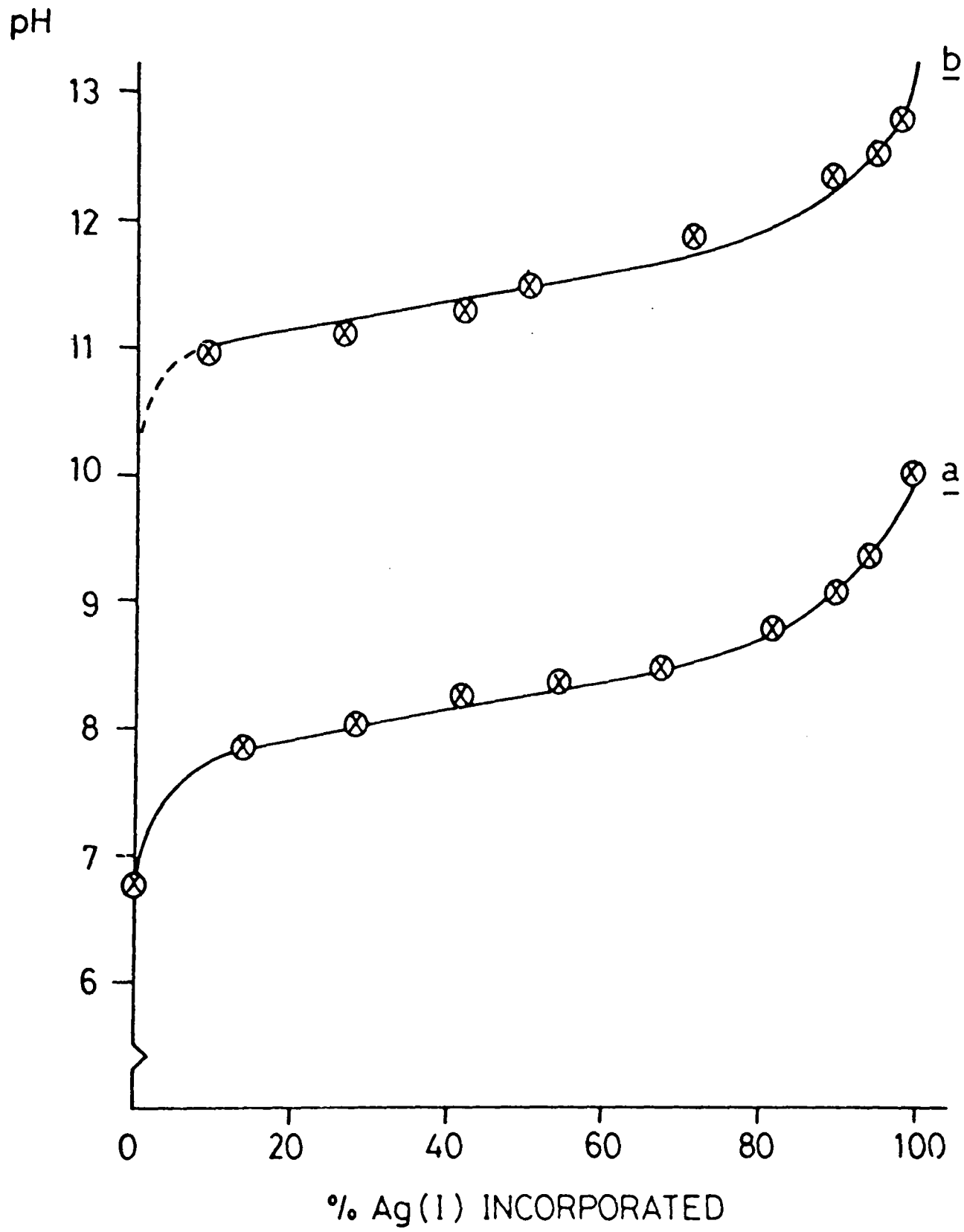

Figure 3. 20 % Ag(I) incorporated in $Ag_2O_{(s)}$ at different pH values; a, Ag_2O formation in normal aqueous solution; b, intravesicular Ag_2O formation.

value, assuming ionic activities coeffcients to be equal to 1.0. Thus,

$$Ksp = [Ag(I)]\ [OH^-]$$

and at the end point

$$[OH^-] = [Ag(I)]$$

The end point pH of 10.0 is equivalent to 10^{-4} moles 1^{-1} hydroxide ion and thus

$$Ksp = [OH^-]^2$$

$$= (10^{-4})^2\ mol^2\ l^{-2}$$

$$Ksp = 10^{-8}\ mol^2\ l^{-2}$$

which is very close to the value of $1.95 \times 10^{-8} mol^2 l^{-2}$ by more detailed methods (9).

A similar curve, (figure 3.20b)was estimated for intravesicular Ag_2O precipitation in the following manner. From the plot of $\Delta\tau_{600}^{\frac{1}{2}}$ against $[OH^-]$ (figure 3.18) it was assumed that a value of $\Delta\tau_{600}^{\frac{1}{2}}$ of 0.35 corresponded to complete reaction, ie 99.8% Ag(I) ions were incorporated in the Ag_2O crystal. Values of % Ag(I) incorporated at other pH values were calculated from the ratio

$$\frac{Y}{0.35} \times 99.8\%$$

where Y was the $\Delta\tau_{600}^{\frac{1}{2}}$ measurement at lower pH.

Theoretical values for the change in pH from 10% to 50% and 50% to 90% Ag(I) incorporation into the Ag_2O crystal lattice are 0.26 and 0.70 pH units respectively. Similar theoretical calculations for a complexation reaction,

$$Ag(I)_{aq} + OH^-_{aq} \rightleftharpoons AgOH(aq)$$

give a change in pH of 0.95 units for both 10% to 50% and 50% to 90% Ag(I) incorporation into the AgOH complex. Table 3.5 shows the observed pH differences for 10%, 50%, 90% Ag(I) incorporation

into the Ag_2O solid phase under different circumstances. The experimental results agree very closely with the theoretical values obtained for a precipitation reaction except at the initial stages of precipitation where some complex formation appears to take place. In both normal and intravesicular precipitation the equilibrium conditions maintained over the total extent of reaction are the same. There appear to be no thermodynamic differences once precipitation has begun in terms of solubility equilibria, such as complex formation rather than precipitation, in Ag_2O formation within a confined vesicular space as compared to the similar process in normal solution. However, there is an obvious difference between these two reaction environments in that precipitation in normal solution begins at ca. 7.5 whereas in vesicular space it does not initiate below a pH ca. 11.0. Similarly, the reaction within the vesicle shows an apparent end point of ca. pH 12.8 which results in a calculated solubility product of 3.98×10^{-3} mol^2 l^{-2}, a factor of ca. 10^{-5} larger than in normal aqueous solution.

This discrepancy in solubility product may indicate different initial solubility equilibria of very small crystallites. However, the pH measured in these experiments corresponds to an extravesicular pH and therefore may not be indicative of the actual intravesicular pH. In order to resolve this question experiments were designed in order to measure intravesicular pH as external pH is changed. ^{31}P n.m.r. spectroscopy was used to further this aim.

Table 3.5 Calculated and experimental values of the change in pH for % Ag(I) incorporation for the equilibria

(a) $Ag(I)_{aq} + OH^-_{aq} \rightleftharpoons AgOH_{(complex)}$

(b) $Ag(I)_{aq} + OH^-_{aq} \rightleftharpoons Ag_2O_{(crystal)} + \frac{1}{2} H_2O$

$\frac{\Delta pH}{\text{for \% Ag(I)}}$ incorporation	Theoretical		Experimental	
	(a) complex	(b) precipitation	Ag_2O (normal solution)	Ag_2O (vesicular)
50% - 10%	0.95	0.26	0.55	0.56
90% - 50%	0.95	0.70	0.75	0.76

3.6. ^{31}P n.m.r. measurements of pH gradients across PC vesicles

It is important to know whether the extravesicular pH measured by a glass electrode represent the same intravesicular pH or if a pH gradient exists across the membrane and if so, what is the magnitude of this pH difference and for how long can it be maintained? In section 3.5.5 it was shown that the equilibrium conditions for intravesicular Ag_2O formation were the same as in free solution except that a much higher initial pH was required for onset of crystallisation within the vesicles. Also, ^1H n.m.r. has shown that diffusion of the hydroxide ion across the vesicle membrane takes place (section 3.4) indicating an expected rise in intravesicular pH on increasing external pH.

^{31}P n.m.r. is an excellent non-perturbing method for measuring the pH of inorganic phosphate solutions localised in small compartments (10),(11). However, no studies have been reported on pH gradients across unilamellar PC vesicles at high values such as 12.0.

The ^{31}P chemical shift of an inorganic phosphate ion is dependent upon the degree of ionisation and thus upon the pH of the phosphate solution. For ortho-phosphate, the following acid-base equilibria are established.

$$H_3PO_4 \underset{H^+}{\overset{OH^-}{\rightleftharpoons}} H_2PO_4^- \underset{H^+}{\overset{OH^-}{\rightleftharpoons}} HPO_4^{2-} \underset{H^+}{\overset{OH^-}{\rightleftharpoons}} PO_4^{3-}$$

$$pK_1=2.15 \qquad pK_2=7.1 \qquad pK_3 \approx 12.4$$

Increasing the alkalinity decreases the shielding of the P nucleus due to the distribution of the same number of electrons over a larger volume (12). A shift of ^{31}P resonances downfield is thus observed at high pH and hence a calibration curve of pH

against chemical shift can be drawn.

3.6.1 Experimental

^{31}P n.m.r. spectroscopy was performed on vesicle samples as follows. PC vesicles (34mM lipid) were prepared in phosphate or phosphate/nitrate solutions at pH of ca. 6.0 in a similar way as described previously. The following samples were prepared.

(i) 1M NaH_2PO_4 solution, internal and external to vesicle compartments.

(ii) 1M NaH_2PO_4 solution internal only. Extravesicular phosphate was removed by passing the vesicle solution down a sephradex G-25 column saturated in 200mM NaCl solution.

(iii) 800mM NaH_2PO_4/200mM $NaNO_3$ solution, internal only. Extravesicular phosphate ions were removed by a sephredex G-25 column saturated in 200mM $NaNO_3$ solution.

Solutions were placed in 8mm diameter n.m.r. tubes arranged concentrically with a 10mm tube containing D_2O for the field frequency lock and a 1mM methylene diphosphoric (MDP) acid/5mM tris, pH 8.9, for the chemical shift reference of 0.00ppm. ^{31}P spectra were kindly recorded by Mr. M.J. Kime and Dr. R.G. Ratcliffe using a Bruker WH300 spectrometer run at 121.49MHz. Spectra were accumulated at 298K ±2K with the tubes spinning. Accumulation conditions were usually 2000 scans with broadband proton decoupling and a 45^{o} pulse angle giving a total accumulation time of 8.5 minutes.

Spectra were recorded on the above vesicle solutions at different pH values. PH changes were performed by addition of aliquots of NaOH solution and the external pH (pH_{OUT}) measured

using a glass electrode. Some precipitation of NaH_2PO_4 occurred at high pH for internal/external samples due to a 'salting' out effect on addition of high concentrations of Na(I) ions. No precipitation was observed at similar pH values with the intravesicular samples indicating that the vesicles were not precipitating under these conditions.

3.6.2 Spectra

(a) NaH_2PO_4 vesicles

Figure 3.21 shows the ^{31}P n.m.r. spectra recorded for a vesicle solution containing 1M NaH_2PO_4 in the internal and external compartments of the vesicle, sonicated at a pH of 6.67. Spectra a, b, c and d represent spectra of this sample recorded at pH values of 6.67, 7.4, 10.95 and 12.5 respectively. Chemical shift values are quoted upfield from the MDP acid standard of 0.00ppm (table 3.6)

The resonance at -17.15ppm (P_{LIPID}) was assigned as the vesicle phosphoester headgroup from a ^{31}P n.m.r. spectrum recorded of a vesicle solution in distilled water (no inorganic phosphate). P_{LIPID} does not change with increasing pH.

The large sharp resonance in each spectra is the external inorganic phosphate peak (P_{OUT}) and shifts downfield, as expected, with increasing pH. The secondary peak, seen as a shoulder in spectrum b, but clearly resolved in spectra c and d (see arrow) corresponds to the internal phosphate resonance (P_{IN}). Increasing the pH has no significant effect on the chemical shift of this resonance. (A significant difference in chemical shift data is one with a difference greater than 0.064ppm). Spectrum d was re-run after 1 hour and no change in chemical shifts was observed.

A similar result was observed when the ^{31}P n.m.r. spectra

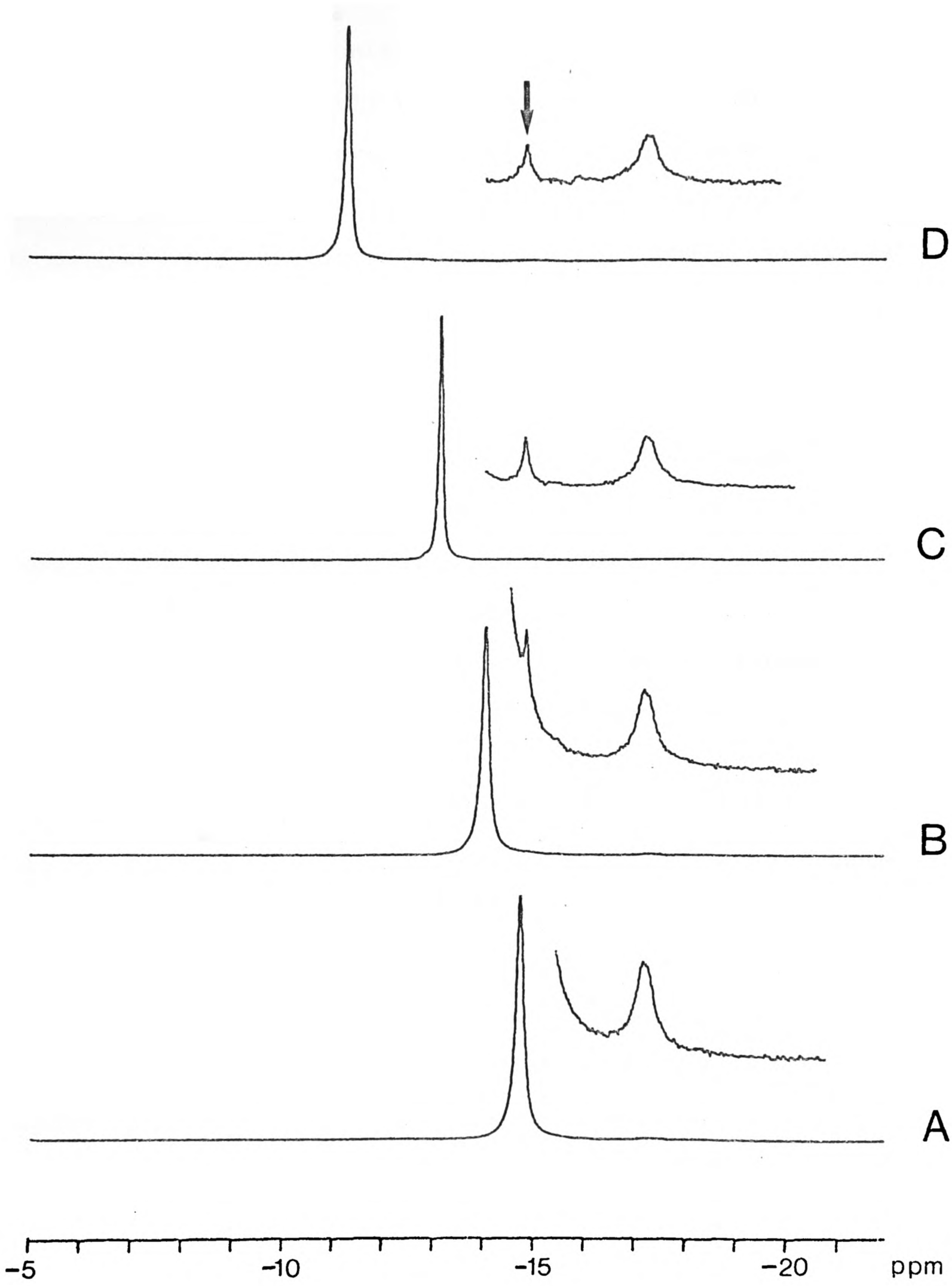

Figure 3.21 ^{31}P n.m.r. spectra of 1M NaH_2PO_4 vesicle solutions at different pH values; a, 6.67; b, 7.4; c,10.95; d,12.5. The arrow indicates the intravesicular phosphate peak.

of the vesicle sample containing only 1M NaH_2PO_4 in the inner compartment of the vesicle was recorded at different pH values. Figure 3.22 shows the spectra recorded at pH values of 7.4 (spectrum e), 10.25 (spectrum f) and 12.07 (spectrum g). Again, the phospholipid resonance is at -17.15ppm. Only one significant inorganic phosphate peak was observed, much lower in intensity, and corresponding to P_{IN}. There is a small shift of this peak (0.13ppm) on raising the pH from 7.4 to 10.25. A further increase of pH to 12.05 resulted in no further change in this resonance position even after one hour. The initial shift is probably due to errors in standard measurement.

A resonance of very low intensity (see arrow) can be observed in spectra f and g at -13.68ppm and -12.78ppm respectively which indicates that there is a small amount of inorganic phosphate (less than 1mM) external to the vesicles. This could be due to the leaking of some vesicles or it may well be residue from column chromotography. Table 3.6 summaries these results.

It can be seen from these experimental results that the intravesicular pH does not change on increasing the external pH since no change in the chemical shift position of the P_{IN} resonance is observed. Thus, at an external pH of 12.5, a pH gradient of ca. 6 pH units can be maintained for at least 1 hour at room temperature. This is rather surprising and also shows the stability of this vesicle system at high pH over this time range.

It is very likely that the reason for this apparent impermeability of the lipid membrane towards hydroxide ions is due to the difficulty of the complementary process of phosphate diffusion out of the vesicle to take place. Over the pH range

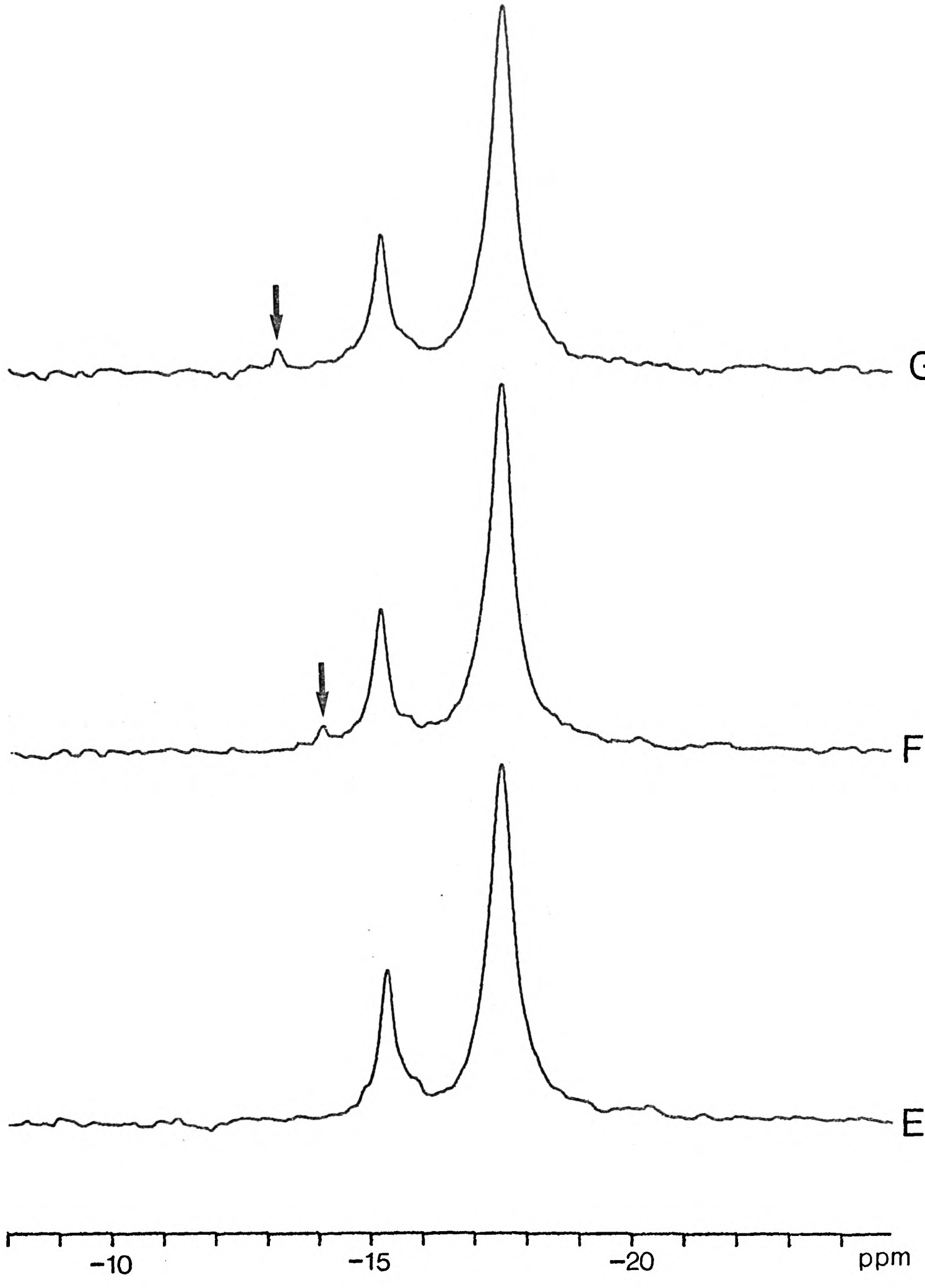

Figure 3.22 ^{31}P n.m.r. spectra of vesicles containing 1M NaH_2PO_4 only in the internal phase at different pH values; e, 7.4; f, 10.25; g, 12.07. Arrows show trace P_{OUT} resonance.

Table 3.6 ^{31}P n.m.r. chemical shift data for HPO_4^{2-} vesicles (see figures 3.21 and 3.22). Measurements in brackets refer to trace peaks.

Spectrum	pH_{OUT}	P_{LIPID}	P_{IN}	P_{OUT}
a	6.67	-17.15	-14.80	-14.80
b	7.40	-17.20	-14.78	-14.00
c	10.95	-17.15	-14.74	-13.09
d	12.50	-17.15	-14.76	-11.19
e	7.40	-17.15	-14.95	-
f	10.25	-17.20	-14.82	(-13.68)
g	12.07	-17.15	-14.82	(-12.78)

considered (6-12.6) the main phosphate species present will be HPO_4^{2-} and PO_4^{3-} (above 12.4). The high charges on these anions will prevent diffusion through the highly hydrophobic regions of the lipid membrane. Thus a high charge potential is maintained between the two sides of the membrane preventing hydroxide ion influx.

To test this hypothesis, vesicles were prepared in a solution of 800mM NaH_2PO_4 and 200mM $NaNO_3$; the presence of the diffusable NO_3^- ion (smaller charge) should allow the influx of hydroxide as observed in intravesicluar Ag_2O formation from encapsulated $AgNO_3$ solution.

(b) $NaH_2PO_4/NaNO_3$ vesicles

Vesicles containing 800mM NaH_2PO_4 and 200mM $NaNO_3$ in the internal phase were raised to various pH values (pH_{OUT}) and ^{31}P spectra were run as before until steady-state conditions were observed, i.e. there was no change in phosphate resonances when the spectra were re-run at a later time. For most samples a steady state had been established within 1 hour.

Figure 3.23 shows spectra recorded at steady state conditions at external pH values of a, 8.4; b, 10.4; c, 11.5; d, 12.46. The peak at -17.2ppm does not shift with pH_{OUT} change and corresponds to the phosphoester of the lipid. The intravesicular resonance, initially at -14.98 ppm does not shift significantly until above pH ca. 11.0 after which it shifts steadily downfield.

Figure 3.24 shows spectra recorded at an extravesicular pH of 13.05 at different time intervals. e, 45 minutes; f 80 minutes; g, 100 minutes. The internal phosphate resonance shifts from a position at -14.21ppm (45 minutes) through a broad peak -14.16ppm with a shoulder peak at -13.64, (80 minutes) and reaches a

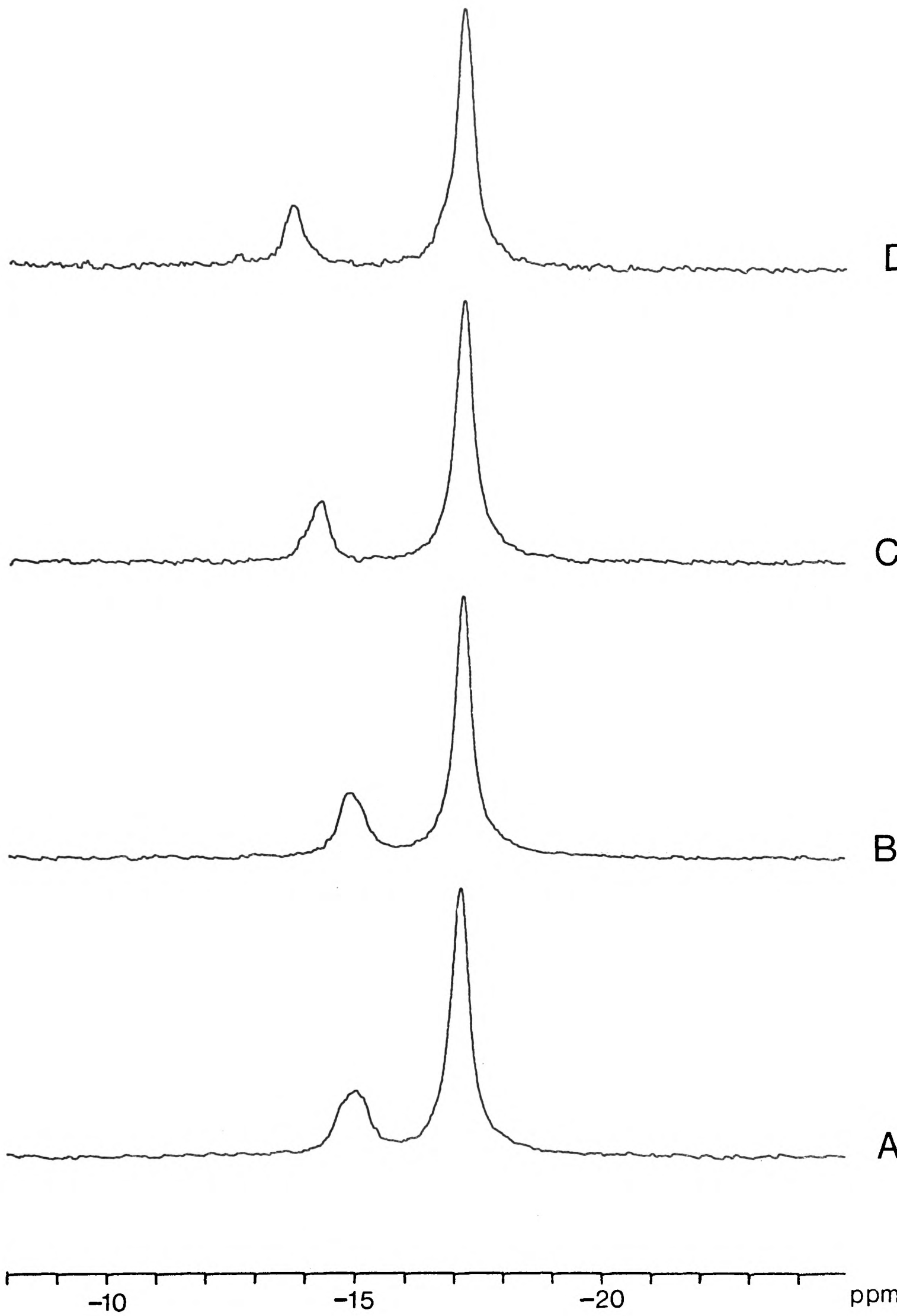

Figure 3.23 ^{31}P n.m.r. spectra of vesicles with intravesicular concentrations of 800mM NaH_2PO_4 and 200mM $NaNO_3$ at various pH values; a, 8.4; b, 10.4; c, 11.5; d, 12.46. All spectra were recorded under steady state conditions.

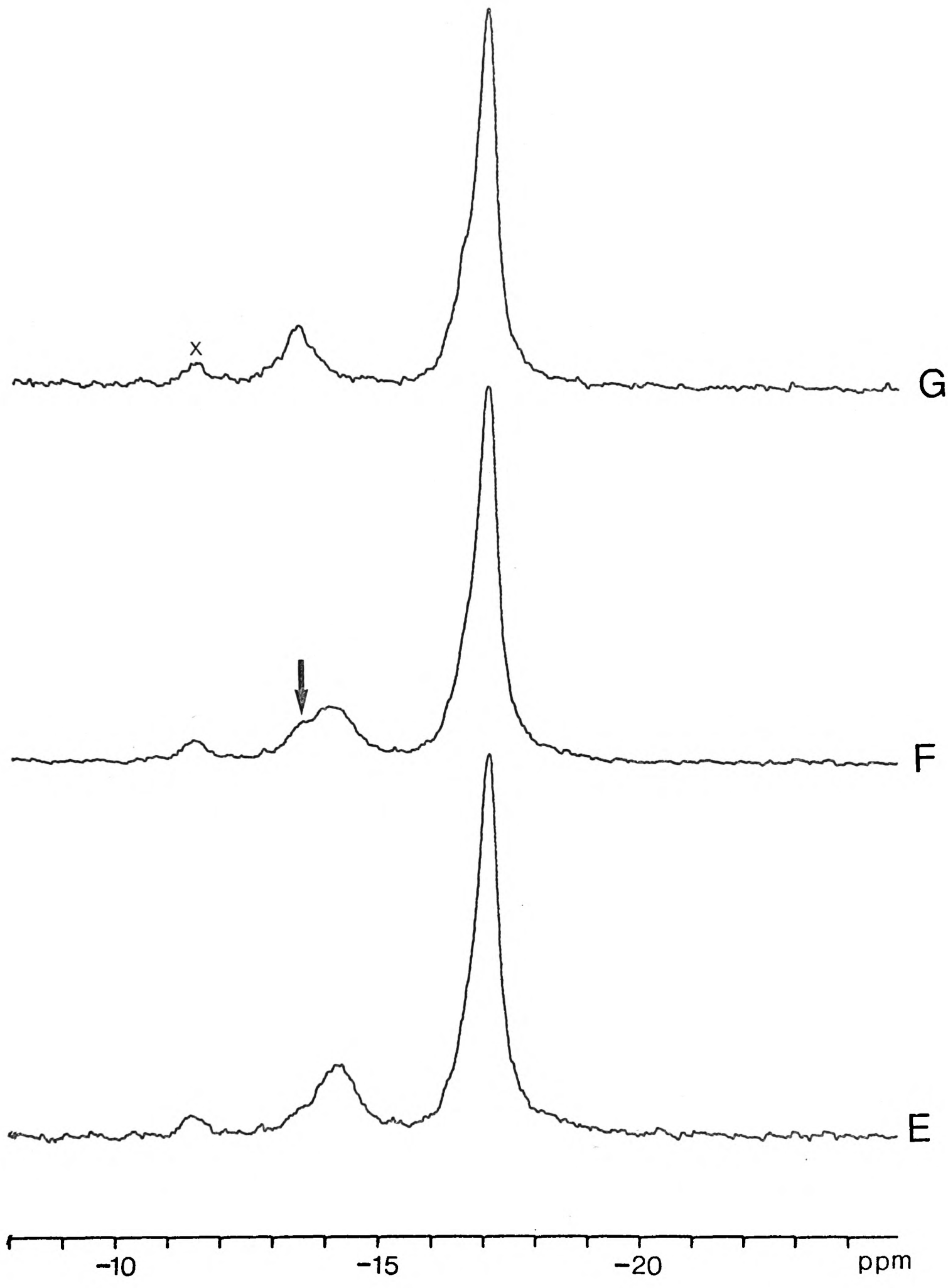

Figure 3.24 ^{31}P n.m.r. spectra of vesicles with intravesicular concentrations of 800mM NaH_2PO_4 and 200mM $NaNO_3$ at pH 13.05; e, after 45 minutes; f, after 80 minutes; g, after 100 minutes. Arrow shows shoulder peak indicating a changing pH_{IN} environment; x indicates a trace P_{OUT} peak.

steady state position at -13.52ppm (100 minutes). A small external phosphate peak can also be seen at -11.54ppm implying that some vesicle degradation has occurred at this very high pH. Before a steady state value of intravesicular pH is attained the internal phosphate resonance is broad indicating that there is a changing pH environment (slow exchange) within the vesicles.

These results show that the incorporation of NO_3^- ions into the internal compartment of vesicles allows influx of OH^- ions to occur, subsequently raising the intravesicular pH. The same results were also observed with phosphate (800mM) and nitrate (200mM) in both vesicle compartments. The choice of a diffusable anion is thus very important when considering a chemical reaction within vesicular space. Alternatively, inhibition of reaction and maintainance of high pH gradients, such as may be required in vesicles used as drug carrier systems (see chapter 5) can be accomplished by choosing an impermeable anion to be encapsulated within the vesicles.

3.6.3 Discussion

Control of intravesicular pH by lipid membranes

Figure 3.25 summarises the data obtained for phosphate and phosphate/nitrate - containing vesicles at different external pH values (pH_{OUT}) under steady state conditions. The ^{31}P chemical shift of extravesicular inorganic phosphate with pH serves as a calibration curve from which intravesicular pH can be calculated (table 3.7). The corresponding plot of pH_{OUT} against pH_{IN} under steady state conditions is shown in figure 3.26.

Intravesicular pH does not appreciably rise until a pH of *ca*. 11.0 is attained. Above this value pH_{IN} rises linearly with pH_{OUT}; a rise of 1pH unit in the external compartment resulting

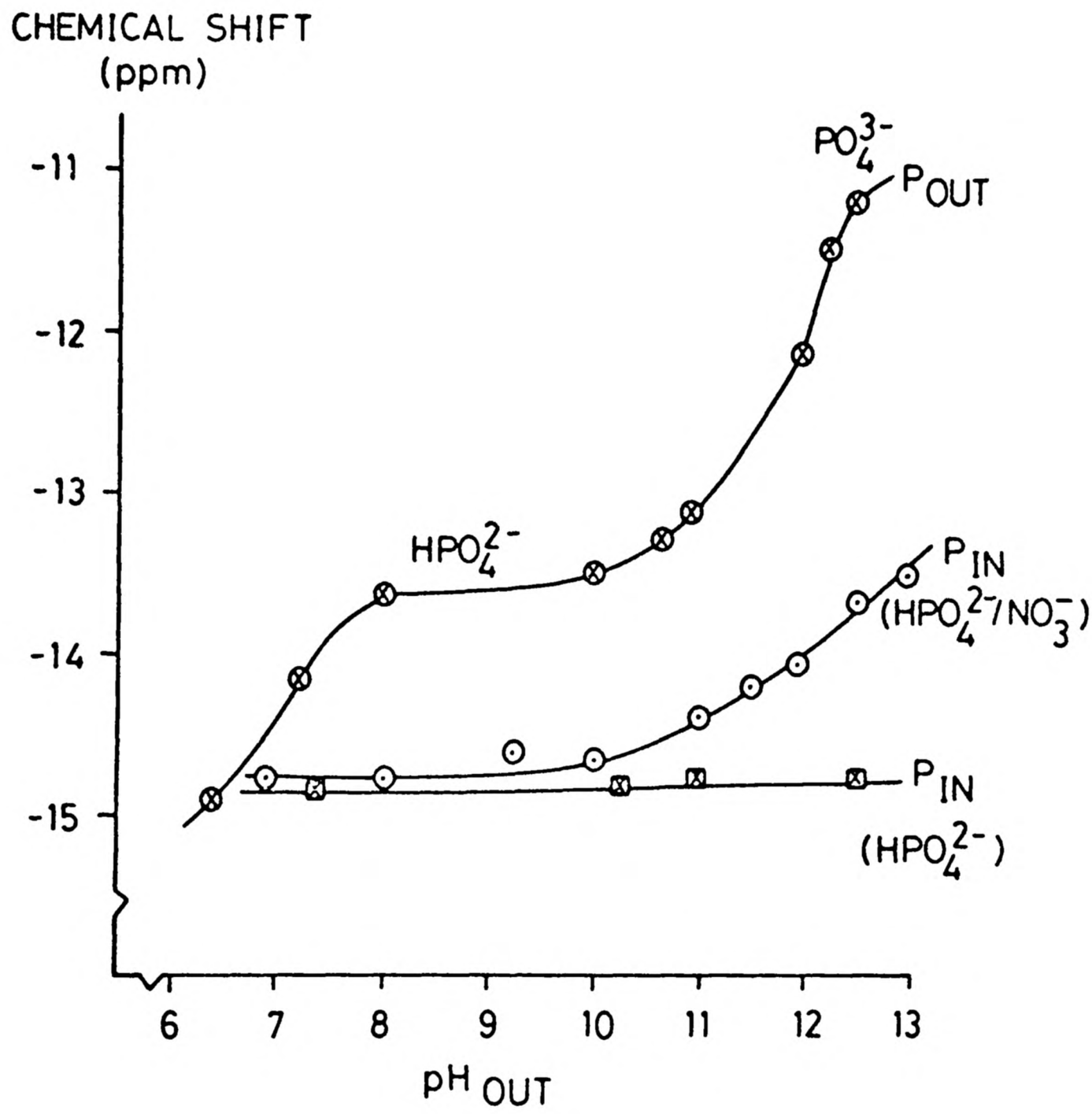

Figure 3.25 Summary of chemical shift data for ^{31}P n.m.r. experiments under steady state conditions.

Table 3.7 Chemical shift and pH data for HPO_4^{2-}/NO_3^- vesicles at steady state conditions

P_{LIPID}	P_{IN}	pH_{OUT}	pH_{IN}
-17.15	-14.8	6.9	6.6
-17.12	-14.79	8.03	6.65
-17.18	-14.55	9.31	6.80
-17.22	-14.59	10.08	6.70
-17.15	-14.39	11.05	7.0
-17.15	-14.23	11.5	7.2
-17.13	-14.07	11.96	7.4
-17.17	-13.65	12.46	7.95
-17.15	-13.52	13.05	8.75

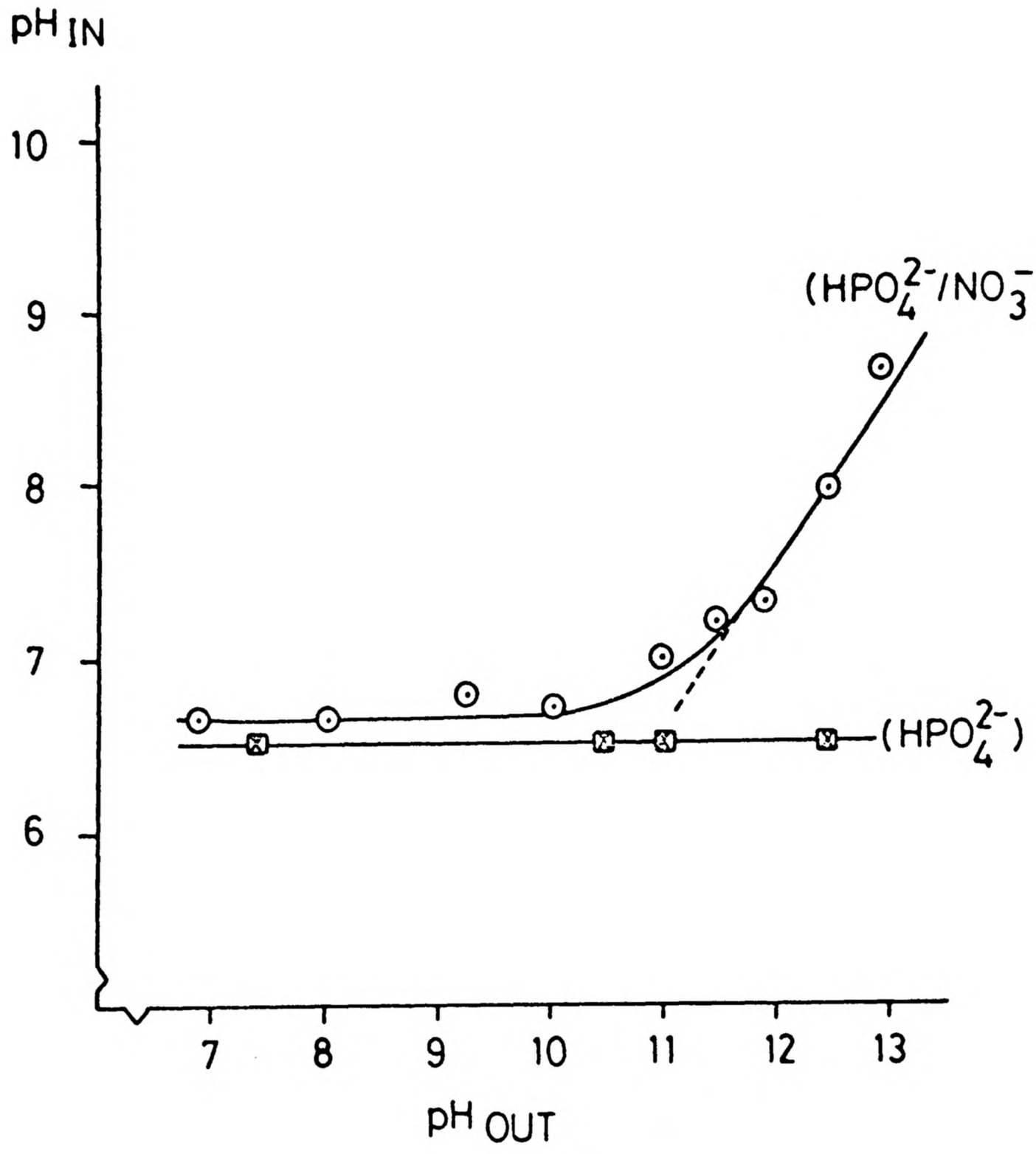

Figure 3.26 Plot of extravesicular pH against intravesicular pH for HPO_4^{2-} and HPO_4^{2-}/NO_3^- vesicles.

in a similar increase in the internal phase of the vesicle. The control of pH_{IN} by the lipid membrane is extremely important in the deposition of solids within the vesicular space and hence plays a crucial role in biomineralisation within biological compartments. In order to understand the role the membrane plays in intravesicular pH control the rate of migration of ions and the subsequent electrical potential gradient ($\Delta\psi$) established across the membrane must be discussed.

The net rate of migration of ions through a lipid membrane will be affected by two forces; (a) thermal agitation giving rise to a net diffusive movement due to differences in chemical potential between the two phases (entropy effect), and (b) net movement due to electrical potential gradients established across the membrane due to diffusion of the penetrating ion creating a charge separation between the different compartments. Thus work must be done increasingly in moving the permeant ion through the membrane due to the repulsive force of the charge build up in the compartment of the more dilute solution. By convention, work must be done in moving a positive charge up the potential gradient or in moving a negative charge down the potential gradient.

When the membrane is permeable to all ions on both sides of the membrane then at equilibrium the electrical potential gradient, $\Delta\psi = 0$. In the case where the membrane is non-permeable to one or more ions a $\Delta\psi \neq 0$ will exist at equilibrium. This can be seen as follows:

The flux J (current) for any permeant ion i is made up of two velocity components due to (a) differences in chemical potential, and (b) differences in electrical potential. The flux for ion i can be written,

$$J_i = - D_i \frac{dc_i}{dx} + U_i C_i \frac{d\psi}{dx} \qquad 3.(5)$$

Where

$$D_i = \frac{U_i kT}{ze}$$

and U_i = mobility of ion i in an electric field of 1 V/cm

k = Boltzmann's constant

T = temperature

ze = charge in coulombs on the ion.

$\frac{dc_i}{dx}$ = concentration gradient across the membrane

$\frac{d\psi}{dx}$ = electrical potential gradient across the membrane and will be positive or negative according to whether it acts with or against the field.

In the case where ion species i is the only permeant species in the system, and there is no external source of current, J_i must = O for otherwise i would accumulate on one side of the membrane and set up repelling electrostatic forces. Hence equation 3.(5) rearranges (substituting for D_i),

$$\frac{d\psi}{dx} = \frac{kT}{zec_i} \frac{dc_i}{dx}$$

which when integrated gives the Nernst equation

$$\Delta\psi = (\psi_{IN} - \psi_{OUT}) = \frac{RT}{ZF} \ln \frac{[i]}{[i]_{IN}^{OUT}} \qquad 3.(6)$$

(in mole units)

The Nernst equation describes an equilibrium state in which the tendency for an ion to move down its chemical potential gradient in one direction is balanced by its tendency to move down its electrical potential gradient in the opposite direction.

This equilibrium state is established when the total electrochemical potential ($\bar{\mu}$) is the same at both sides of the membrane; the electrochemical potential for ion i being related to the chemical potential (μ_i) and electrical potential (ψ) by the equation

$$\bar{\mu}_i = \mu_i + zF\psi$$

(where $\mu_i = \mu_i^o + RT \ln a_i$)'

In the case of vesicles containing HPO_4^{2-} ions the results from ^{31}P n.m.r. spectroscopy show that there is no change in intravesicular pH as pH_{OUT} is increased to a value of 12.5. Raising pH_{OUT} creates an electrical potential gradient across the lipid membrane preventing extensive OH^- influx. The pH_{IN} will not rise significantly since the opposing potential gradient will increase rapidly with, from a chemical point of view, only a small number of entering OH^- ions (A rise of pH_{IN} from 7.0 to 8.0 requires ca. 6×10^{17} ions/l to be transported. The corresponding Nernst potential for $\Delta pH = 1$ is ca. 60mV, and given a membrane capacitance C of say $10^{-6}F$, the total charge transferred Q($Q = CV$) will be 6×10^{-8} coulombs, equivalent to only 4×10^{11} ions/l)

Since HPO_4^{2-} ions cannot penetrate the membrane a very large chemical gradient in OH^- would be required for pH_{IN} to rise significantly. Thus the presence of impermeable ions within vesicles will prevent pH_{IN} rising unless a mechanism of active transport (i.e. work done by chemical carriers) is present to permit passage of ions against the potential gradient. Such systems are present within biological membranes and must play an important part in biomineralisation processes.

In the presence of intravesicular NO_3^- pH_{IN} does not rise as

pH_{OUT} is increased to a value of ca. 11.0. Over this pH_{OUT} range the potential existing across the membrane is that calculated from the Nernst equation (3.(6)). Hence no NO_3^- efflux and consequently no OH^- influx occurs. These ion currents are both dependent on the electrical potential gradient existing across the membrane and can be expressed in terms of the Boltzmann distribution for ions with sufficient energy to travel up/down the potential gradient.

For OH^- ions travelling against $\Delta\psi$,

$$OH^- \text{ influx } \alpha\ [OH^-]_{OUT}\ \exp(-\frac{ZF\Delta\psi}{RT})$$

For NO_3^- ions travelling with $\Delta\psi$,

$$NO_3^- \text{ efflux } \alpha\ [NO_3^-]_{IN}\ \exp(\frac{ZF\Delta\psi}{RT})$$

Hence NO_3^- efflux will be more prominent at high $\Delta\psi$ and there must be a critical $\Delta\psi$, ($\Delta\psi_o$) at which NO_3^- efflux overcomes the small OH^- influx. The fact that pH_{IN} begins to rise after a pH_{OUT} of 11.0 is reached indicates that this $\Delta\psi_o$ is ca. equivalent to ΔpH of 4.5 units (pH_{IN} initially = 6.5); ie 270mV. Figure 3.26 shows that once $\Delta\psi_o$ is reached then pH_{IN} rises linearly with further rise in pH_{OUT}. Hence we can write,

$$pH_{OUT} = \Delta\psi_o + pH_{IN} \quad \text{(in appropriate units)}$$

or

$$\Delta pH = \Delta\psi_o$$

As pH_{OUT} is raised above 11.0 the potential gradient across the membrane will rise above $\Delta\psi_o$ and NO_3^- efflux, increasing exponentially, will be greater than OH^- influx and thus will lower the $\Delta\psi$ back to a level of $\Delta\psi_o$ at which NO_3^- efflux will become very small. The efflux of NO_3^- ions will permit OH^- influx to rise and therefore pH_{IN} will increase. The final

ΔpH will always be the same;i.e. equivalent to $\Delta\psi_o$. Figure 3.27 illustrates these observations.

The amount of NO_3^- ions required to lower the potential to $\Delta\psi_o$ is very small. For instance, at pH_{OUT} of 12.5 if no NO_3^- diffusion takes place $\Delta\psi$ = 360mV (Nernst). With NO_3^- efflux $\Delta\psi$ is lowered to $\Delta\psi_o$ of 270mV. The contribution from NO_3^- efflux is therefore 90mV or 1.5pH units. Raising pH_{IN} from 6.5 to 8.5 requires an increase of ca. 10^{-6}M OH^- ions, which will be of the same order of magnitude as NO_3^- efflux. Since $[NO_3^-]_{IN}$ is 200mM the effect of NO_3^- efflux on total $[NO_3^-]_{IN}$ is insignificant.

A steady state condition exists across the membrane when the electrical potential gradient has been lowered to $\Delta\psi_o$ and there is no net flow of ions between the two phases. This explains why the solubility equilibria for intravesicular Ag_2O precipitation calculated from light scattering measurements (figure 3.20) show the same characteristics as for Ag_2O precipitation in normal aqueous solution. Once $\Delta\psi_o$ is reached pH_{IN} rises linearly with pH_{OUT}, K_{sp} (Ag_2O) is overcome and precipitation begins in the normal way.

In reality, $\Delta\psi_o$ may fluctuate to some extent due to the effects of vesicle swelling (osmosis) and binding to the lipid membrane of ions at different concentrations.

3.7 Overview

3.7.1 Kinetic experiments

The fact that kinetic measurements can be made from light scattering studies implies that the rate of precipitation of intravesicular Ag_2O is limited in some way. The results obtained in this work are summarised as follows;

(1) Ultra-high resolution EM has shown (section 3.3.2) that

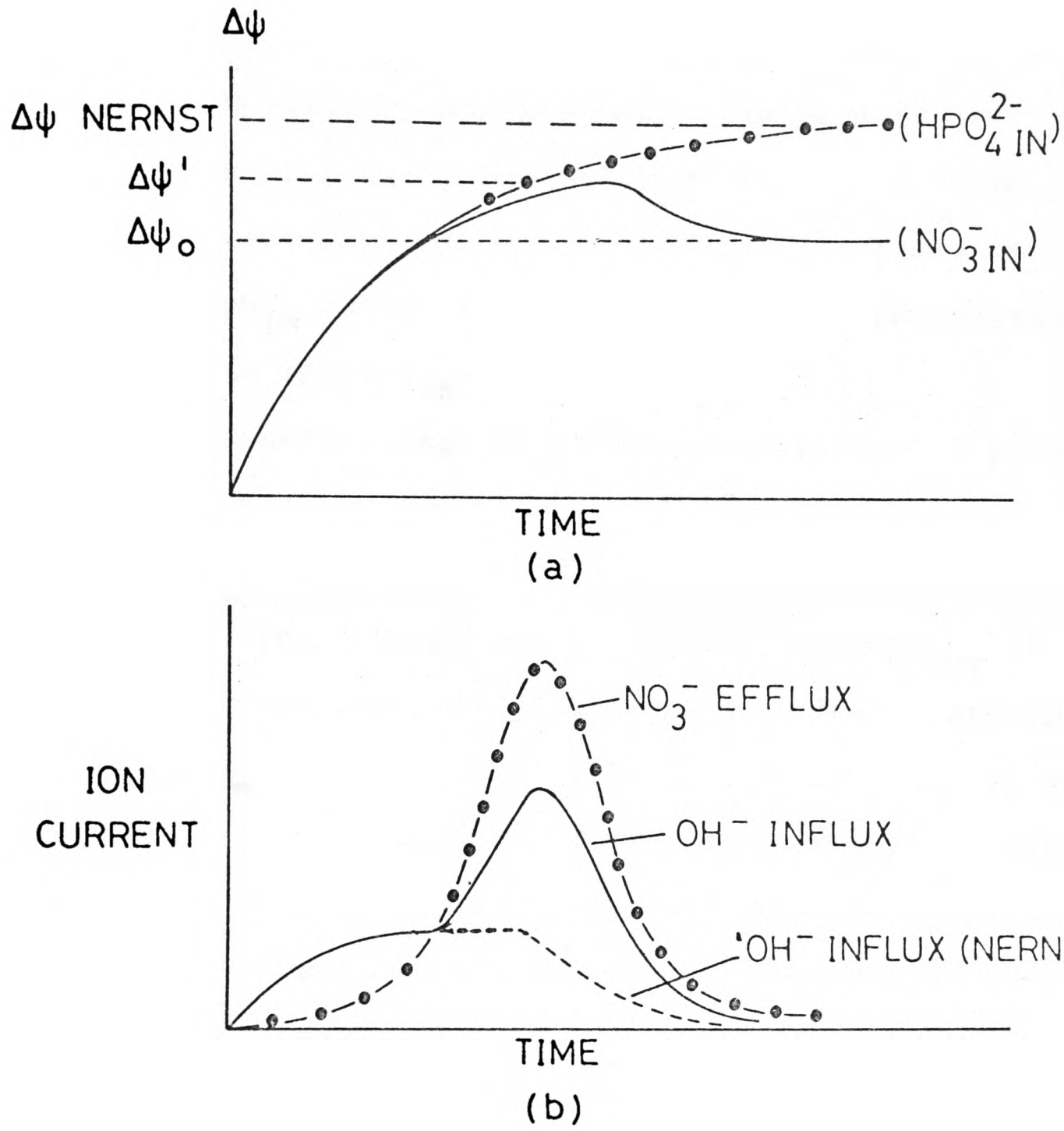

Figure 3.27 a; change in the electrical potential gradient ($\Delta\psi$) across a vesicle membrane with time for impermeable (HPO_4^{2-}) and permeable (NO_3^-) encapsulated ions,
b; change in OH^- influx and NO_3^- efflux through a vesicle membrane with time. NO_3^- efflux rises above OH^- influx once a critical potential $\Delta\psi_o$ is established across the membrane. As this efflux lowers $\Delta\psi$, further OH^- influx will then occur.

most intravesicular Ag_2O crystallites are single domain implying that the nucleation occurs at one site and that the growth processes are kinetically slow.

(ii) ^{31}P n.m.r. spectroscopy has shown that pH_{IN} only rises when a certain critical potential gradient $\Delta\psi_o$ is surpassed. OH^- influx can then occur due to a rapidly rising NO_3^- efflux lowering the potential back to $\Delta\psi_o$ (section 3.6.3).

(iii) For vesicles of variable $[Ag(I)]_{IN}$ raised to the same steady state pH_{IN} value, the initial rate of precipitation is proportional to $[Ag(I)]_{IN}$ (figure 3.13).

(iv) At constant $[Ag(I)]_{IN}$ the initial rate of precipitation is strongly dependent on $[OH^-]_{OUT}$ at pH_{OUT} values between 11.0 and 12.0 and becomes less dependent at higher pH_{OUT} values. (figure 3.16) There is no precipitation below pH_{OUT} of 11.0.

There are two possible limiting processes in precipitation; (a) nucleation, or (b) crystal growth. In general the rate of nucleation will be a function of the supersaturation since it is postulated that in nucleation theory aggregates of ions or molecules are formed by statistical fluctuations in the solution and so the probability of a cluster of molecules exceeding the critical nucleus required for continued crystal growth will be higher at larger supersaturation values. In more detail, the rate of nucleation will be a function of (i) the arrival rate per unit area of molecules at a cluster, (ii) the fraction of molecules arriving that actually are incorporated into the crystal, (iii) the surface area of the cluster and (iv) the concentration of clusters.

The rate of crystal growth will depend essentially on the supply of ions to the crystal surface i.e. the supersaturation. It will also be dependent (particularly at low supersaturation

levels) on defects in the crystal surface, particularly screw dislocations (13).

The turbidity curves presented for intravesicular Ag_2O precipitation (figures 3.11 and 3.15) show that crystallisation begins almost immediately and then continues at a slow rate. This is in agreement with the rate of precipitation being dependent on the rate of crystal growth. If the rate of nucleation had been the limiting process, turbidity would have risen sharply over a short time range after which precipitation would have been essentially complete.

In general, the kinetic behaviour of intravesicular Ag_2O precipitation can be expressed;

rate of precipitation = rate of crystal growth

$$R = K(\text{supersaturation})$$

or at time t,

$$R_t = K \{[Ag(I)]_{IN,t} [OH^-]_{IN,t} - K_{sp}\}$$

For vesicles containing the same $[Ag(I)]_{IN}$ but raised to different steady state pH_{IN} values;

$$R_t \alpha [OH^-]_{IN,t}$$

where

$$[OH^-]_{IN,t} = \left[[OH^-]_{IN,(o)} + \int_o^t J_{OH^-,t}\,dt\right] - [OH^-]_{crystal,t}$$

and

$J_{OH,t}$ = OH^- influx at time t.

Figure 3.16 shows that the initial rate of Ag_2O precipitation at constant $[Ag(I)]_{IN}$ becomes less dependent on $[OH^-]_{OUT}$ at high pH_{OUT}. The initial OH^- influx will depend on the initial NO_3^- efflux once $\Delta\psi_o$ is reached. The initial NO_3^- efflux will therefore be dependent on the magnitude of $(\Delta\psi' - \Delta\psi_o)$ where $\Delta\psi'$ is the maximum potential gradient reached

after which NO_3^- efflux lowers the gradient back to $\Delta\psi_o$ (figure 3.27a). However at high pH_{OUT} there appears to be a maximum rate for NO_3^- efflux. NO_3^- diffusion will be eventually hindered due to steric effects of NO_3^- passage through the closely packed lipid bilayer. Thus a maximum limiting OH^- influx will be observed at very high pH_{OUT} values.

For vesicles of different $[Ag(I)]_{IN}$ but raised to a constant steady state pH_{IN}, $[OH^-]_{IN}$ will be the same in each case at any time t. Hence,

$$R_t \alpha [Ag(I)]_{IN,t}$$

as is shown in figure 3.13.

The rate of precipitation is thus dependent on $[Ag(I)]_{IN}$ and $[OH^-]_{IN}$. At values below pH_{OUT} 11.0, $[OH^-]_{IN}$ does not rise significantly and supersaturation is not reached (For $[Ag(I)]_{IN}$ of 100mM a pH_{IN} of 7.0 is required for precipitation). At pH_{OUT} above 11.0 crystal growth is slow due to the slow rate of membrane diffusion of OH^- ions. However, the rate is not solely limited by this process since at constant steady state pH_{IN} the rate is dependent on $[Ag(I)]_{IN}$. The combination of Ag(I) and OH^- ions at the growing crystal surface must then be also important in controlling the rate of crystal growth. The rate of advance of steps on a crystal surface will depend on (a) the rate of ionic diffusion towards the crystal surface and (b) the rate of diffusion of adsorbed ions/molecules towards the steps and exchange with these sites. Process (a) may be particularly limiting since a single ion (eg Ag^+) migrating towards a vacant site in the crystal surface will experience a repulsive force at close proximity due to sites occupied by similarly charged species. Crystal growth by incorporation of larger ionic clusters around which there is a lower electric field intensity

has been suggested to be kinetically more favourable over crystal growth by incorporation of single ions (14).

Process (b) will depend on the activation evergy between neighbouring equilibrium positions on the surface and on the 'fusion' energy from the surface back to the liquid phase. The mean displacement of adsorbed species will also be a function of crystal face, in general being smallest for closest packed surfaces (13)

3.7.2 Nucleation

Nucleation within vesicles must be homogeneous in the sense that the vesicle volume is so small that the probability of there being a foreign particle in the vesicular space is very low, but heterogeneous in the sense that there is a lipid surface on which nucleation may initiate. Ultra-high resolution electron micrographs (figure 3.5) show only single crystals which implies that nucleation occurs at one site in the vesicle. The location of this nucleation centre will probably be close to the lipid membrane since Ag(I) ions will be essentially located within this region under the influence of the negatively charged phosphate headgroups. Since the membrane is homogeneous (unlike biological membranes) there must be an equal probability of any site on the membrane acting as a nucleation centre, but once nucleation has begun and the critical nucleus surpassed (see Appendix II) then this site must be far more favourable than any other site for single crystals to develop . If nucleation occured simultaneously at many headgroup sites it may be expected that an annulus of material would form around the vesicle membrane and further crystal growth could then be inhibited due to the difficulty of further OH^- ions reaching

the central vesicular space (figure 3.28). Only small continuous Ag_2O particulates are observed after 10 seconds of reaction (section 3.3.4) which supports the single site model of nucleation. The formation of amorphous solids from cations bound to the lipid membrane (eg Co(II) ions) results in different images being observed in the electron microscope (chapter 6).

3.7.3. Colloidal and catalyst systems

In section 3.3.3. very small Ag_2O particulates were observed by lowering $[Ag(I)]_{IN}$. One aim of colloidal chemistry is to prepare stable sols which have very small particulate sizes. Preparation of intravesicular solids may well be an excellent method to further this aim. One immediate problem is the presence and instability of the lipid membrane. Removal of the lipid would be possible by use of detergents. In systems where it would be preferable to keep the vesicle intact, lowering the pH_{OUT} to 7.0 would prevent substantial hydrolysis of the lipids. Further stability could be obtained by fixation with glutaraldehyde although the effects on the permeability of such treated membranes would have to be considered.

One use of very small intravesicular Ag_2O particulates may be as a catalyst of very high surface area. It may also be possible to study catalytic reactions within the vesicle space. Reactants (and perhaps products) would need to be permeable to the membrane. An example of such a system would be the reduction of acidified $Cr_2O_7^{2-}$ to Cr(III) using H_2 and Ag(I) catalysts. Ag(I), $Cr_2O_7^{2-}$ and H^+ ions could be encapsulated within the vesicle compartment and H_2 gas bubbled through the membrane. The reduction could then be followed spectrophoto-

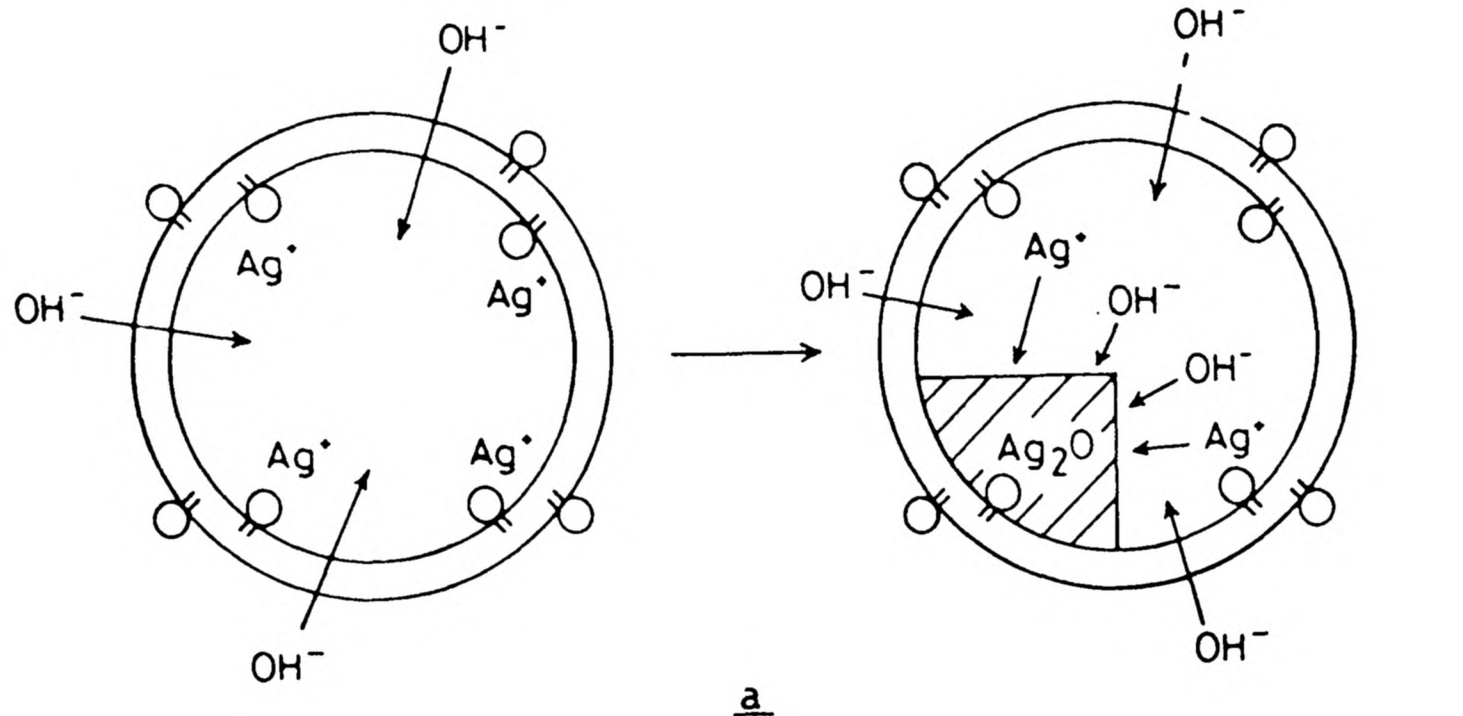

Figure 3.28 Ag_2O nucleation within vesicles; a, nucleation at a single site; b, nucleation at several sites along the vesicle membrane.

metrically, and the yield and reaction rates compared with data obtained from the same reaction under normal conditions (15).

3.7.4 Model systems for biomineralisation

An important field of study in physical chemistry is the enquiry into the process of nucleation and crystal growth in aqueous solution. Related to this field of study is the initiation and development of bioinorganic solids in living systems. The processes occurring in the formation of intravesicular Ag_2O are related closely to one possible mechanism of biomineralisation, namely the inclusion of a cation and its absorption onto an organic matrix followed by precipitation. Hence nucleation and particulate growth studies using the vesicle system provide an excellent model for mineralisation in biological compartments.

The general methodology of solid formation within vesicles allows systems which are more closely related to biomineralised solids such as SiO_2, $CaCO_3$, $Ca(OH)_x(PO_4)_y$, Fe_3O_4, to be studied. Of special interest is the role the membrane plays in intravesicular pH control and also the crystallographic nature of solids prepared within the confined vesicular space.

Silicates can be prepared within vesicles by a similar method to that studied in this chapter. (see chapter 6) This process resembles the deposition of silica occurring in cellular vesicles of the marine choanoflagellate, Stephanoeca diplocostata Ellis, described in detail in the next chapter.

3.7.5 Further experiments

There are obviously a wide range of potential precipitation reactions that can be studied within vesicles (see chapter 6 for further examples).

Photochemical reactions of Ag(I) may be possible within vesicles. One possible route to very small Ag metal particulates would be to prepare intravesicular AgCl and then photochemically reduce to Ag(O).

Further kinetic/nucleation experiments could incorporate inhibitors such as long chain malonates or phosphonates in the vesicle membrane and their effect on crystallisation studied using ultra-high resolution EM to image the reaction product. Use of such techniques would also make it possible to study the nature of defects in crystallites prepared within vesicles.

Further experiments using ^{31}P n.m.r. spectroscopy to investigate the control of intravesicular pH using different lipids and lipid protein mixtures within the membrane could be undertaken. The ability of these vesicles to control precipitation could then be studied by similar methods as employed in this chapter.

In conclusion, this chapter has considered in detail the precipitation of Ag_2O within PC vesicles as a system for studying chemical nucleation and crystal growth and as a model for biological precipitation. In the next chapter a biological system with the ability to deposit SiO_2 within cellular vesicles is investigated.

3.8 References

(1) Huang C. Biochem., 8, 344-352, 1969.

(2) ASTM Powder Diffraction File. 12-793, 1972.

(3) ASTM Powder Diffraction File. 19-1155, 1972.

(4) BBA Library Vol. 3, 28-29, 1964.

(5) LaMer V., Barnes M. J.Colloid Sci., 1, 71, 1946.

(6) Lord Rayleigh. Phil Mag. 47, 375-384, 1899 .

(7) Mie G., Ann Physik. 25, 377-445, 1908.

(8) Bangham A.D. Protoplasma 63, 183-187, 1967.

(9) Bederman G., Sillen L.G., Acta Chem. Scand 14, 717-725,1960.

(10) Patalini P., De Kruijff B. De Gier J. J. Experienta 34, 1580-1582, 1978.

(11) Casey P.R., Njus D., Radda G.K., Sehr P.A. Biochem. 16, 972-976, 1977.

(12) Jones R.A.Y., Katritzky A.R. J. Inorg. Nucl. Chem., 15, 193, 1960.

(13) Burton W.K., Caberra N., Frank F.C., Phil Trans A 243, 299-358, 1951.

(14) Gunn D.J. Murthy M.S., Chem. Eng. Sci., 27, 1293-1313, 1972.

(15) Webster A.H., Halpern J. J.Phys. Chem., 60, 281-288, 1956.

CHAPTER 4

HIGH RESOLUTION ELECTRON MICROSCOPY STUDIES OF THE SILICA LORICA OF THE CHOANOFLAGELLATE STEPHANOECA DIPLOCOSTATA ELLIS

4.1 Introduction

In the previous chapter the precipitation of an inorganic compound, Ag_2O, within phosphatidylcholine unilamellar vesicles was discussed. This system provides a model for the study of similar processes involved in biomineralisation. In this chapter an electron microscopy (E.M.) study is presented of a biological system known to deposit hydrated silica (SiO_2) within membrane-bounded vesicles.

The organism chosen for study was a marine choanoflagellate called Stephanoeca diplocostata Ellis. Choanoflagellates are common members of marine nanoplankton. An opportunity to study this organism came about due to the interest of Dr. B.S.C. Leadbeater who had previously investigated this organism and had been successful in establishing it in culture (1). The following is a brief account of the work reported previous to the results presented in this chapter.

Stephanoeca diplocostata Ellis is a loricate choanoflagellate commonly found in British marine and brackish habitats (2). It has also been found in coastal waters around Europe (3),(4) and the Mediterranean (5). The cells are usually found free-floating in the open sea whereas in stagnant sea water they are found often attached to the surface of marine algae and other suitable objects. The cells comprise a colourless protoplast with a single anteriorly directed flagellum surrounded by a ring of tentacles (the collar). The protoplast is lodged in a

basket-like casing (lorica) constructed of 150-180 silica strips (costae). The cells feed phagotrophically using the undulation of the flagellum to bring food particles and bacteria into contact with the collar which are then ingested by linguiform pseudopodia arising from the protoplast.

In Stephanoeca diplocostata new costal strips are produced in advance of mitosis within long thin vesicles in the peripheral cytoplasm and then released sideways through the plasmalemma in to the cavity of the posterior lorica chamber. Bundles of strips are transferred to the top of the collar until sufficient strips to form a new lorica have been accumulated. Cell division then proceeds, the juvenile taking the accumulation of supernumerary strips as it leaves the parent lorica and assembling its own lorica within 2-3 minutes (6).

The lorica of Stephanoeca diplocostata is attached to the protoplast by a thin investment at the waist of the lorica chamber. Each costal strip has a radius of curvature approximately equal to that of the protoplast surface but not all the costae are the same. A group of thicker strips are seen around the waist of the lorica. It is not known how the cell differentiates between strips during lorica production or how the strips are joined during the final lorica assembly.

Previous investigations of Stephanoeca diplocostata have concentrated on light microscopy and low resolution electron microscopy to reveal knowledge of the taxonomy and ultra-structure of the species (1), (2), (6). The work undertaken in this chapter utilises high and ultra-high resolution electron microscopy to investigate the following questions.

(a) What is the nature of the micro-structure of the hydrated SiO_2 within costal strips? (section 4.3)

(b) How are the costal strips linked together in the intact loricae? (section 4.4)

(c) How do the the costal strips grow within the cellular vesicles? Is there any evidence for the presence of an organic template initiating SiO_2 deposition? (sections 4.5 and 4.6)

(d) What is the nature of the surface silica in costal strips? Is there, for instance, an organic coating around the costae? (section 4.7)

4.2 Materials and Methods

Stephanoeca diplocostata Ellis was grown in culture by Dr. B.S.C. Leadbeater as described elsewhere (1). The cells were grown in batches of 1.5.1 at ca. 20°C in the dark. In most cases the cultures were stirred. All samples were freshly cultured and used within one week of collection (except for dissolution experiments). Cells used for electron microscopy were centrifuged for 5 minutes using a Gallenkamp Junior bench centrifuge and then washed in distilled water. This procedure was sufficient to destroy the protoplast by osmotic shock and leave the remaining loricae intact. The loricae were then reconcentrated by centrifugation and washed again with a further aliquot of distilled water. This procedure was repeated three times. One drop of a concentrated suspension of the loricae was placed on a formvar-coated copper grid, previously sputtered with a thin film of carbon to minimise beam damage in the electron microscope, and left to dry on filter paper in the air at room temperature.

The electron microscope used for ultra high resolution imaging was the Oxford JEOL 200CX instrument with a high

brightness LaB_6 cathode. An accelerating voltage of 200 KeV was used throughout and micrographs were obtained at magnifications up to 1,000,000 times. For normal resolution work a JEOL 100CX Temscan analytical electron microscope fitted with a Kevex Li-drifted Si detector, operating at 100 KeV was used. Micrographs were taken at magnifications up to 250,000 times. Samples for X-ray micro-analysis were analysed at 40^{o} tilt angle for a time of 250 seconds in the STEM mode.

Binding studies of costal strips with the hydrated cations Co^{2+} and Fe^{3+} were achieved by treating the intact loricae for 24 hours at room temperature with 2mM solutions of $CoCl_2$ and $FeCl_3$ respectively. Similar studies with (a) phosphatidylcholine (PC) liposomes and (b) collodial SiO_2 were performed by treating the intact loricae for 24 hours at room temperature with 17mM PC solution and a colloidal SiO_2 solution (Syton X30, Monsanto chemicals) respectively.

Staining experiments were carried out in the following manner. A drop of stain solution was placed onto an EM copper grid containing intact loricae, the excess liquid was removed after 10-15 minutes, and the grid washed with distilled water and left to dry on filter paper.

Fixed and stained sectioned material was kindly provided by Dr. B.S.C. Leadbeater. Sections were fixed with OsO_4 and stained with uranyl acetate and lead citrate.

4.3 Chemical and crystallographic nature of costal strips

Figure 4.1 shows an intact lorica with the protoplast removed by osmotic shock. The length of the lorica is ca. 18µm with costal strips of length ca. 3µm and width 50-100nm. The posterior section of the lorica is closed whereas the anterior

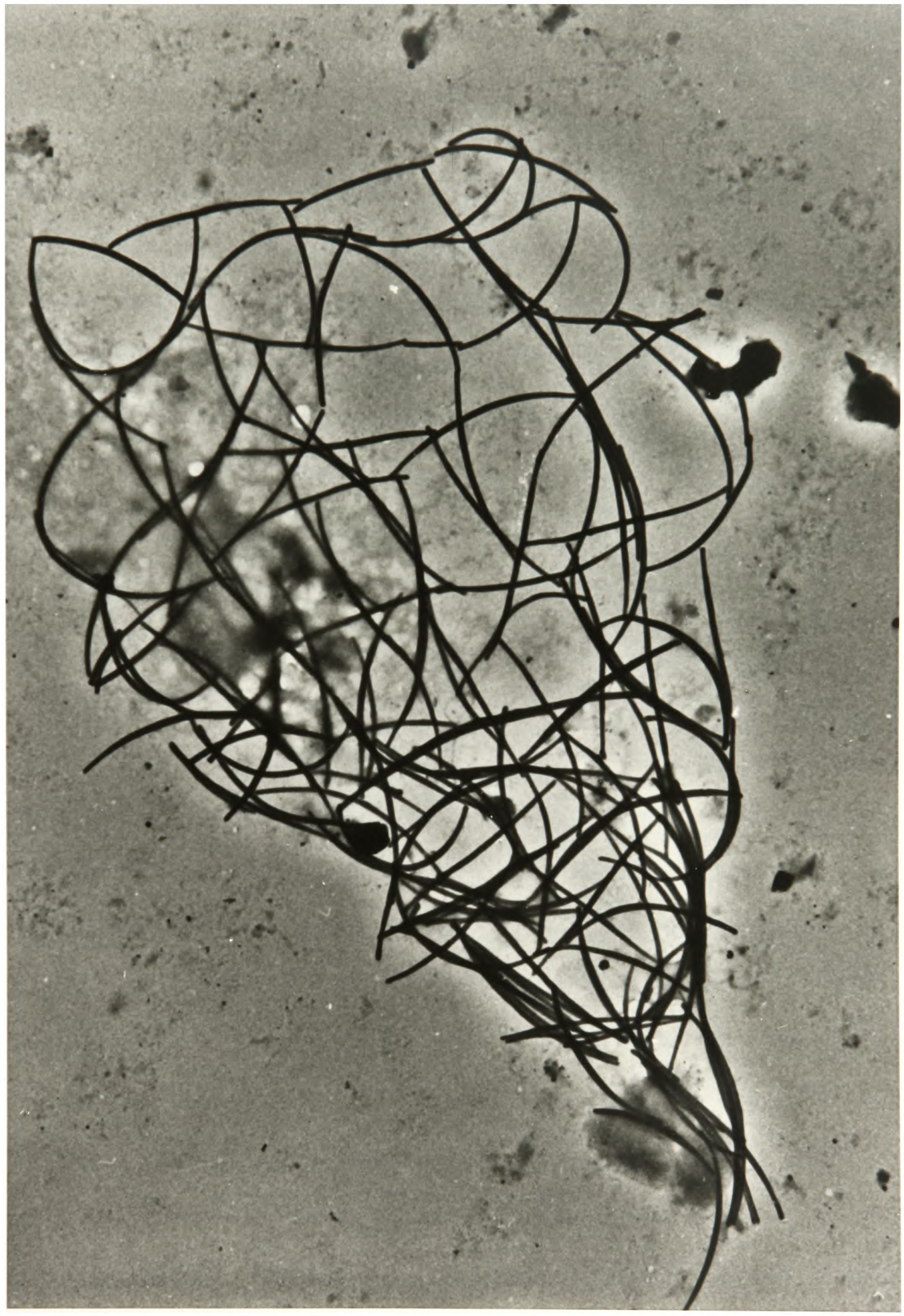

Figure 4.1 Whole mount of an empty lorica of Stephanoeca diplocostata Ellis x8,800.

end, through which the daughter cell leaves after mitosis, is open-ended. The arrangement of costal strips is disorganised to some extent due to the drying process onto the EM grid, but note that most junctions between costae are still intact. A substantial amount of debris (bacteria, fragments of protoplast etc) can also be seen around the lorica. This is because it is very difficult to remove such contaminants by centrifugation (7). Care was taken in all experiments to observe and analyse only costal strips which appeared free from such contaminants. Full ultrastructural details of whole mounts of empty lorica at low magnification can be found elsewhere (1).

X-ray microprobe analysis on single costal strips resulted in only Si being detected in the areas analysed (figure 4.2). This corresponds with previously published results (2). Analysis along costal strips showed higher count rates in the middle regions than in areas towards the ends, indicating the greater mass thickness in the middle areas of the costae (table 4.1). This can also be seen from images observed by scanning electron microscopy (figure 4.3). X-ray microanalysis over areas between joining strips (strip junctions) also detected only Si Electron diffraction was performed over many areas of costal strips but no diffraction patterns were observed. Previous workers (2) have also been unsuccessful at obtaining electron diffraction images, and have thus presumed an amorphous form of SiO_2 comprising the costal strips. However since electron diffraction yields only statistical data averaged over the area selected, the possibility of localised micro-crystalline phases within the costal strips had still to be resolved. Hence thin areas of costal strips were examined using the ultra-high resolution (200 CX) electron microscope.

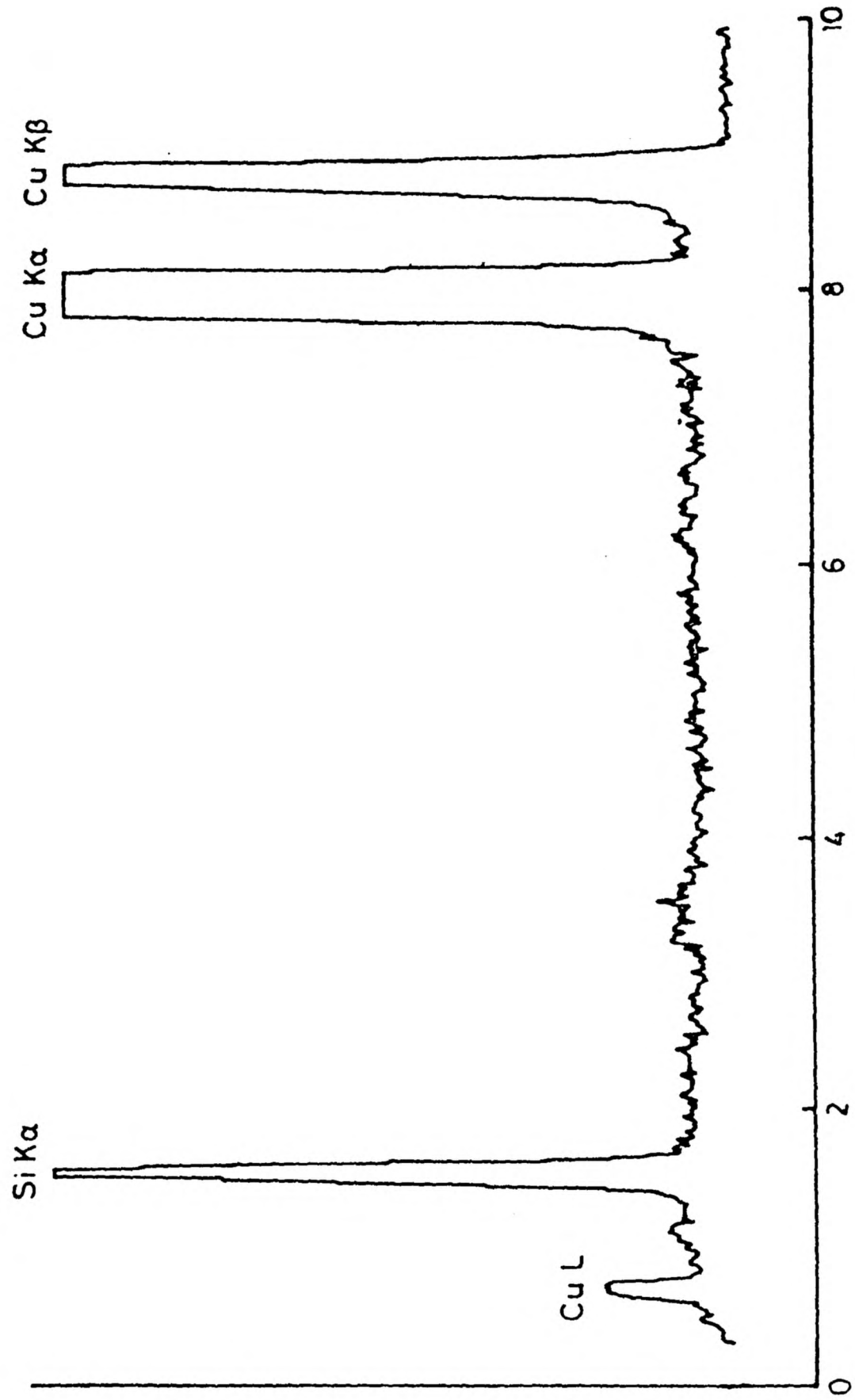

Figure 4.2 X-ray microprobe analysis of costal strips.

Table 4.1 X-ray microanalysis data along costal strips showing greater mass thickness in middle regions. The area analysed in each region was 50nm x 50nm

Analysis area	Si counts above background/100s	
Distance from middle region (μm)	Strip 1	Strip 2
$1\frac{1}{2}$	769	532
1	847	584
$\frac{1}{2}$	1422	812
$-\frac{1}{2}$	1334	1060
$-1\frac{1}{2}$	956	488

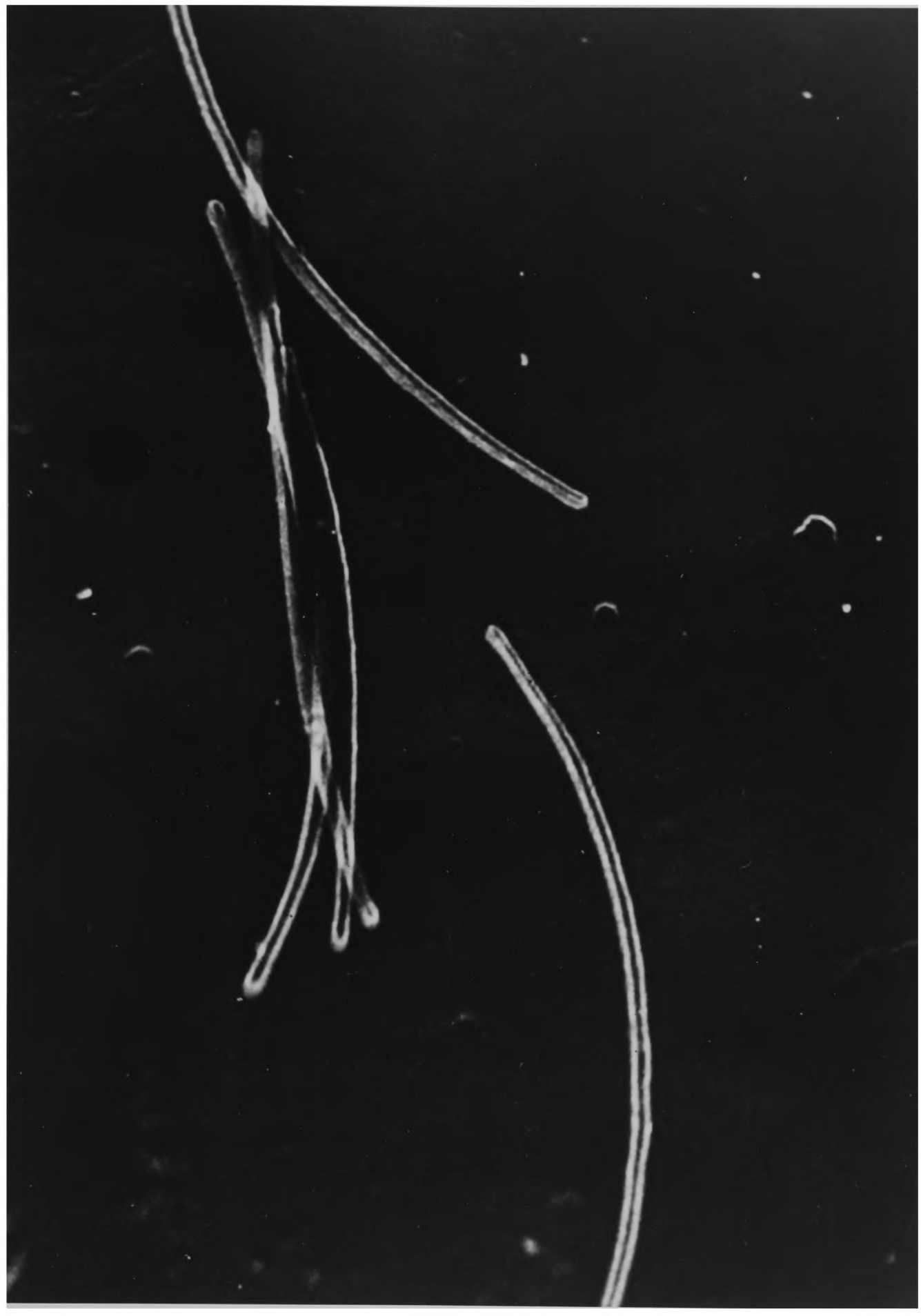

Figure 4.3 SEM micrograph of costal strips x67,000.

Figure 4.4 shows a costal strip in an intact lorica at a magnification of 3,400,000. The outer regions of the strip are more opaque due to the onset of demineralisation in the central zone (section 4.5). The strip is imaged across a hole in the formvar grid so that there is no background noise from the carbon-coated film. No crystallographic structures can be observed at this high level of resolution (compare figure 3.5 in chapter 3 for similar images of a material of crystalline nature) and therefore it is concluded that no micro-crystalline regions are present in the extremely amorphous network of SiO_2.

It is however extremely difficult to determine the presence of small ordered domains within a non-crystalline sample. Optical simulation techniques have been reported to be of potential use in furthering this aim (8).

4.4 Junctions between costal strips in intact loricae

One of the final processes in the assembly of loricae must be the joining together of costal strips in a manner which allows the intact loricae to be resistant to forces arising in its marine environment. In order to try and gain some information about the junctions between costal strips in intact loricae many joins were examined at high and ultra-high resolution in the electron microscope.

There are three types of strip linkage; end-to-end, end-to-middle and side-to-side overlap. In this work only end-to-middle junctions between costal strips were examined extensively since these are more easily observed and imaged in the electron microscope.

Figure 4.5 shows a representative junction at normal electron microscope resolution. Two continuous filaments of

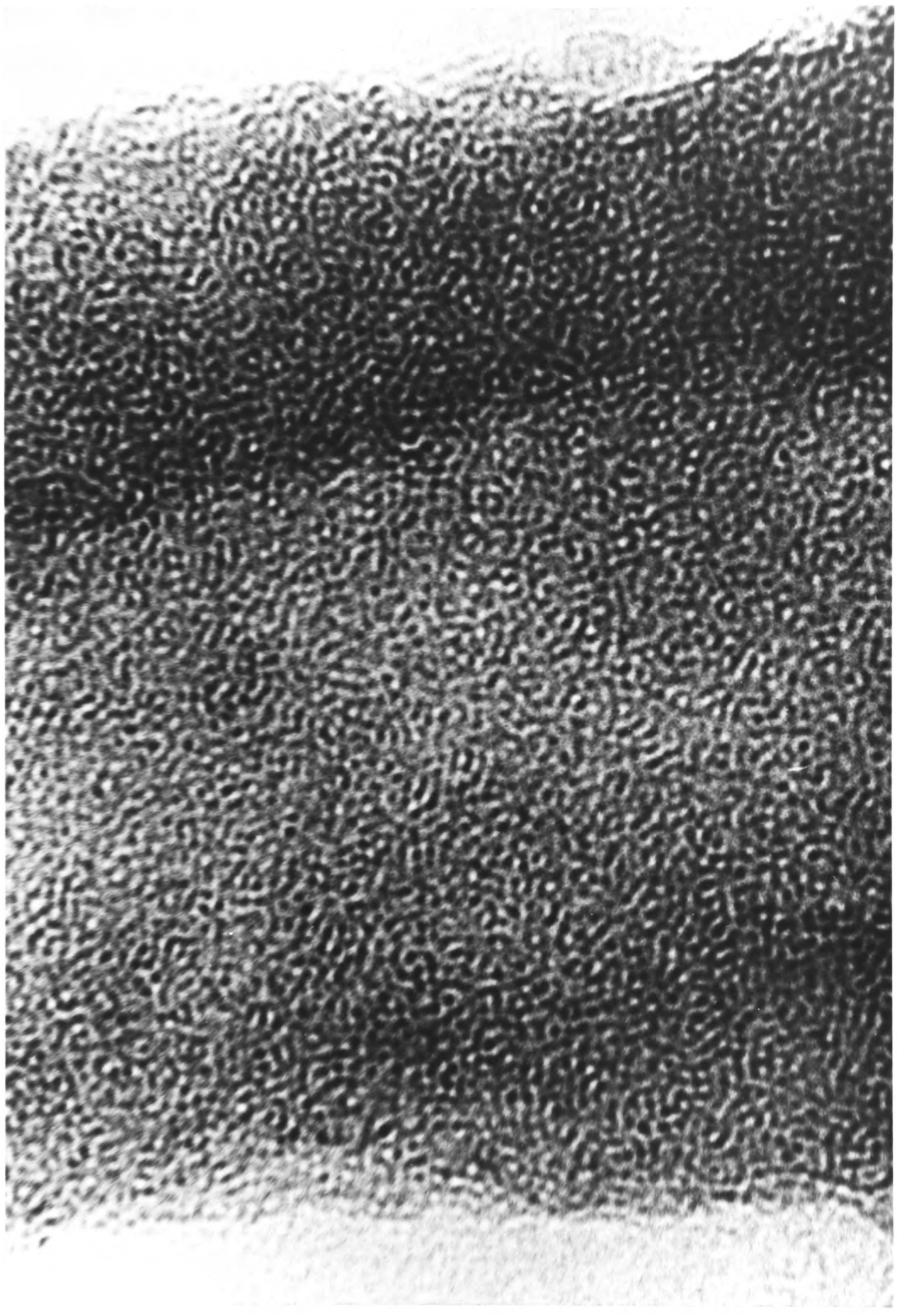

Figure 4.4 Ultra-high electron micrograph of a costal strip in an intact lorica showing the amorphous nature of the silica x3,400,000.

opaque material can be seen running between the two costal strips. The distance between the strips at the centre of the join is 13.5nm. The opaque filamentous material runs close to the edge of one strip whilst in the other strip the filaments extend further into the central zone before running out towards the edge. In other micrographs linkages were observed where the thread-like material runs close to both edges of the two joining costal strips.

Figure 4.6 shows an ultra-high resolution image of a similar costal strip junction at a magnification of 1,100,000 times. The join lays across a hole in the carbon-coated formvar grid but parts of the carbon-coated film can be seen in various areas of the micrograph and these should not be confused with the siliceous material of the costal strip (open arrow on diagram). Only one filament of opaque material of thickness ca. 5nm can be observed traversing the join which is only partially intact. (black arrow on diagram)

In figure 4.7 the join between costal-strips occurs between a strip running from top-right to the middle-left of the micrograph, with a second strip (the tip of which is just seen) running downwards out of the micrograph. The join is only half-intact with an unattached nodule of material of width 17.5nm connected to one strip and an intact join of width 17.0nm between the two strips. The distance between the two costae across the intact join is 25nm. No filamentous material is observed in this junction. The join is imaged over a hole in the formvar grid. The material traversing the join is electron dense and stable in the electron beam.

Different types of linkages between costal strips were occasionally observed. Figure 4.8 shows a join

Figure 4.5 T-join between two costal strips at normal EM resolution x610,000.Two continuous filaments of opaque material traverse the junction.

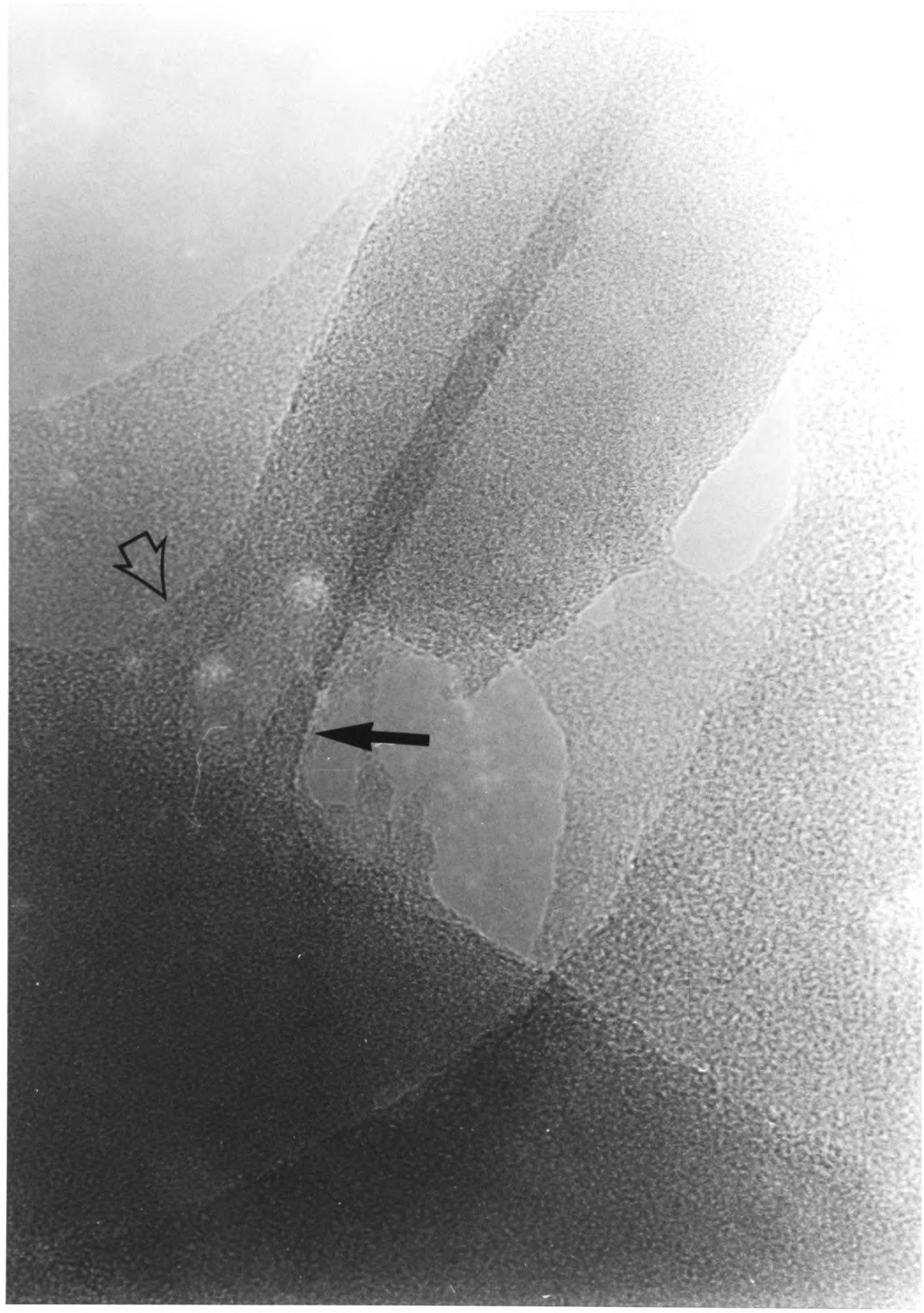

Figure 4.6 Ultra-high resolution micrograph of a costal strip join x1,100,000.A single filament traverses the join(black arrow).The open arrow indicates the siliceous material of the costal strip join above the carbon-coated support film.

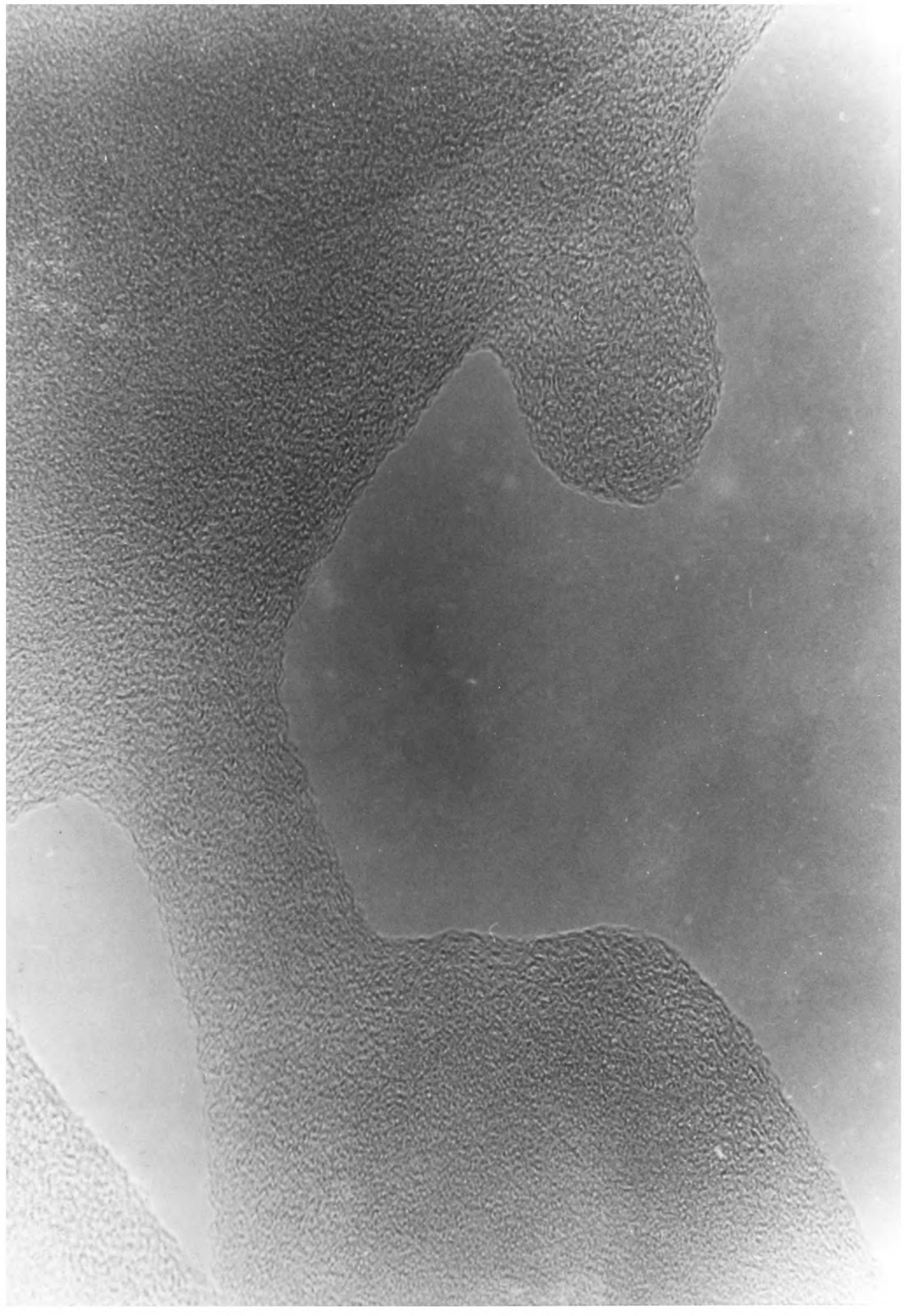

Figure 4.7 Ultra-high resolution micrograph of a partially intact join with an unattached nodule of silica connected to one costal strip x1,700,000.

between the middle edges of two costal strips imaged under conditions of ultra-high resolution. The pertinent feature of these micrographs (figures 4.6, 4.7, 4.8) is that the material within the strip join appears to be the same as that within the costal strip itself, ie a continuum of amorphous silica traverses the intact join.

In order to try and show the presence of organic material within the costal strip junctions, whole mounts of loricae were stained with the following reagents; phosphotungstic acid (pH 6.5), uranyl acetate (pH 7.0), KIO_4/ammonical $AgNO_3$, alcian blue, and ruthenium red. No selective staining of junction regions was observed in any method providing no evidence for organic material within the joins.

A full interpretation of the results presented in this section can be found in section 4.8.

4.5 Costal strip demineralisation

One very important question to try and resolve is the mechanism of costal strip growth within cellular vesicles. Two approaches have been taken in this work. Firstly, sectioned material has been examined at different stages of costal strip development in order to try and gain ultra-structural evidence of costae growth characteristics. Secondly, the process of costal strip demineralisation has been studied assuming that this reverse process of growth will provide information about how the strip is constructed within the vesicles. This method has the advantage that whole mounts of strips are observed and are thus less suceptible to artefacts unlike samples prepared from sectioned material.

In this section the second approach is discussed whereas

Figure 4.8 Ultra -high resolution micrograph of a costal join between the middle edges of two costal strips x930,000.

in section 4.6 a preliminary study of sectioned material is presented.

Detailed quantitative studies of the uptake and release of silica from Stephanoeca diplocostata Ellis are recorded elsewhere (9). The silica-containing costal strips are only meta-stable and redissolve back into the aqueous medium. The total process of demineralisation depends on the physical growth conditions; at 20°C in an agitated solution demineralisation is complete within 10 days (9).

Samples of loricae in late stages of development (6-8 days) were dried onto EM grids as before. Most loricae were observed to be still intact but showed distinct characteristics of demineralisation. The extent of silica demineralisation differed not only between different loricae but sometimes within the same loricae, presumably the initially formed costae redissolving first.

The initial stage of demineralisation takes place at localised centres along the central axis of the strip (figure 4.9a). The distance between the centres of each demineralised zone is ca. 40nm. These centres become increasingly demineralised until they extend and join together along the central axis forming tubular, brittle rods (figure 4.9b). As demineralisation increases further, the hollowing becomes more extensive and at later stages the outer edges of the costal strips also show signs of demineralisation, becoming rough and pitted (figure 4.9c).

These dissolution characteristics seem to indicate that there is a central zone within the strip which is destabilised at a faster rate than the surface silica. This suggests that the central silica has a different mode of chemical binding

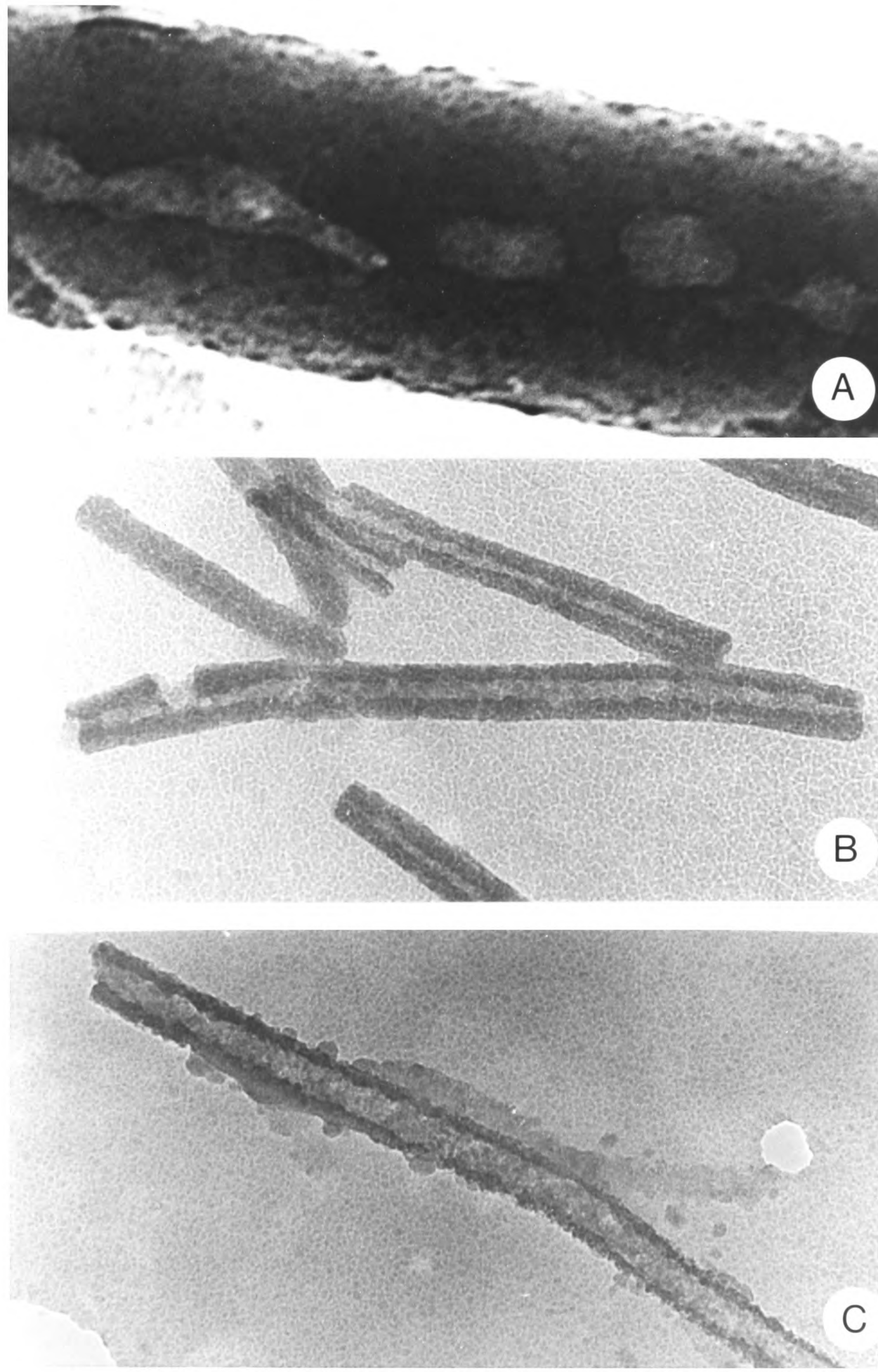

Figure 4.9 Demineralisation of costal strips; a, initial stage of demineralisation showing localised dissolution zones along the central axis of the costal strip x600,000; b, intermediate stage of demineralisation, costae becoming tubular and brittle x140,000; c, late stage of demineralisation showing thin hollow rods with pitted surfaces x145,000.

than the silica at the surface of the strip. This could be due to the presence of a central core of organic material (organic template) which degrades faster than the silica phase and/or that the surface silica is stabilised by an external coating of some kind (inorganic/organic).

However, it is not clear whether the presence of localised demineralised sites along the central axis of the costal strips indicates a specific pattern of degradation of an organic phase or whether they are merely random sites of (organic) degradation.

4.6 Preliminary EM study of sectioned material

Sectioned material is often very difficult to interpret due to staining, fixing, dehydration and cutting artefacts. Nevertheless many sections of cells of Stephanoeca diplocostata were studied in the hope that some understanding of the initiation of silica deposition within vesicles and subsequent costal strip growth could be obtained. Very few sections showed vesicles cut in a manner such that the very early stages of costal strip development was apparent. Where such images seemed possible, X-ray microprobe analysis was utilised to provide information on the silica content of such vesicles.

Figure 4.10 shows a stained section of a cell containing two parallel orientated vesicles. Vesicle A (diameter 170nm as cut) contains a mature nascent costal strip of diameter 84nm. Vesicle B is much smaller (diameter 35nm) and contains two thin filaments of electron dense material running approximately parallel at a distance of 8.7nm (see figure 4.11). These filaments disappear into a more dense single thread which may or may not be part of the same structure, eg a sectioned cylinder. X-ray microprobe analysis over areas of vesicle A showed high Si

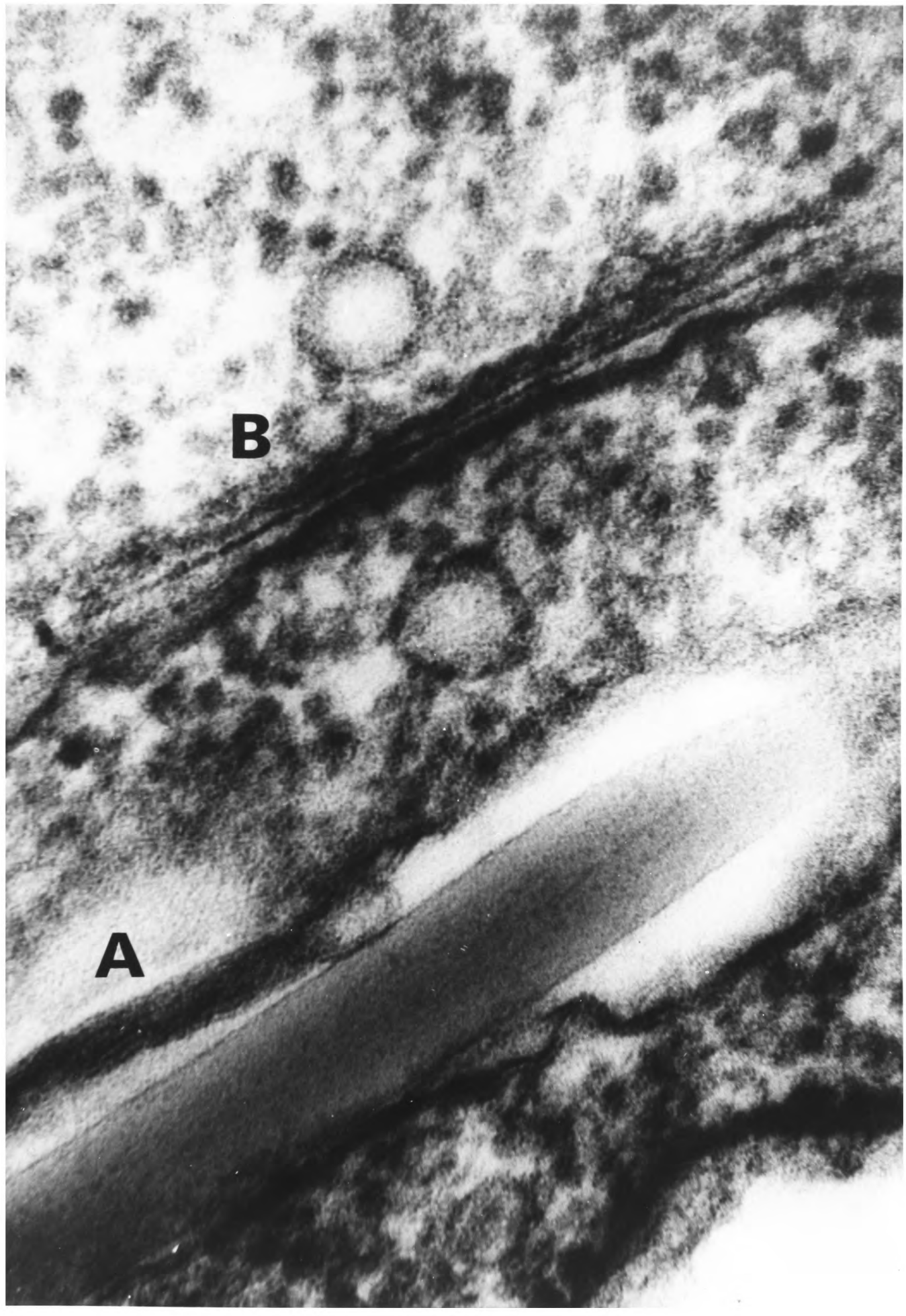

Figure 4.10 Sectioned cell of Stephanoeca diplocostata Ellis showing nascent strips at late (A) and early (B) stages of development x270,000.

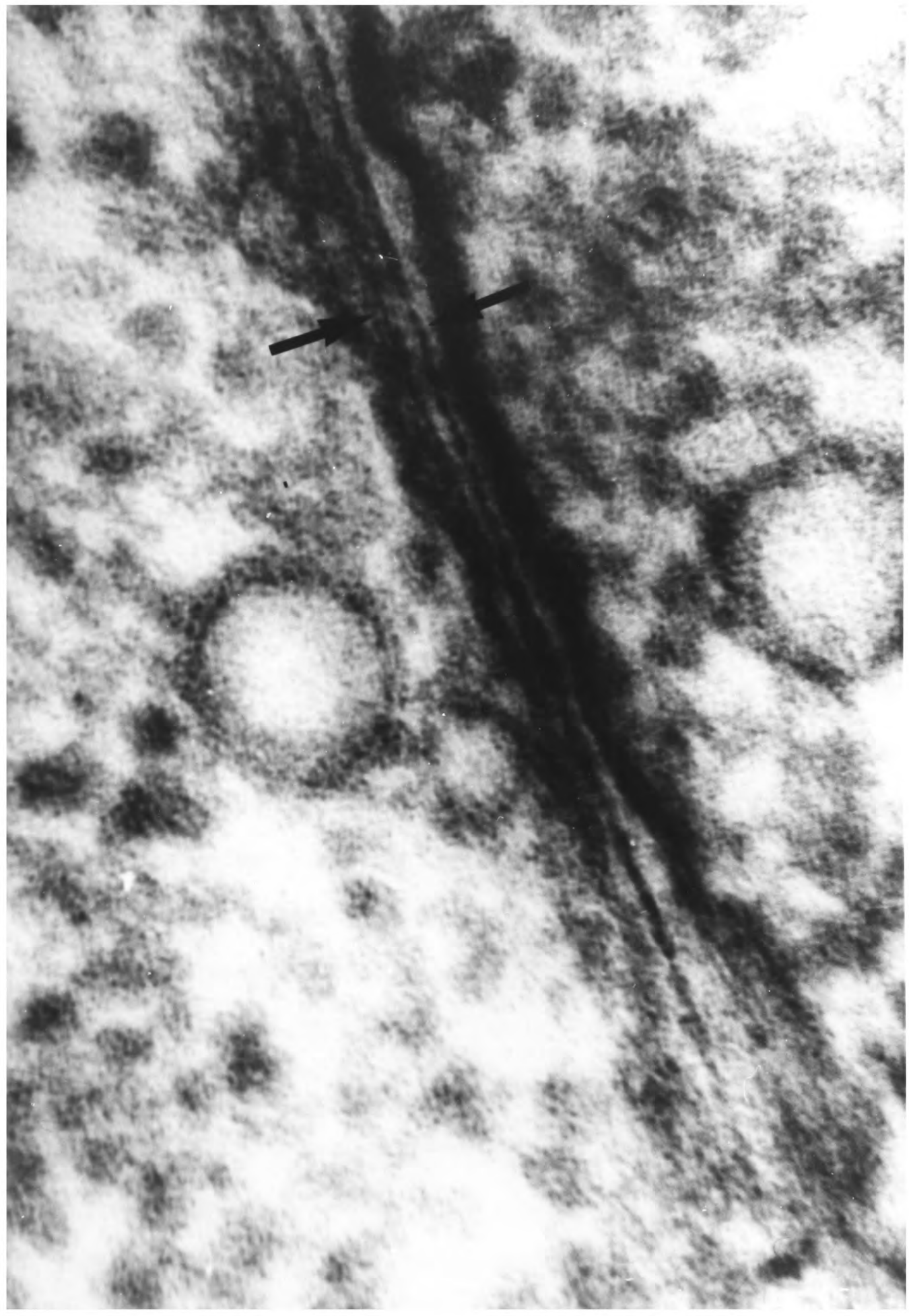

Figure 4.11 High magnification image of a cellular vesicle containing silica and showing intravesicular filaments (arrows) x430,000.

counts (figure 4.12c). Analysis on areas of vesicle B also detected Si but in much lower mass concentration (figure 4.12b). Analysis on normal cellular areas showed no Si and only stain materials (Pb, U, Os, Cl) and Cu from the EM grid (figure 4.12a).

The imaging of these electron dense filaments may represent the initial stages of silica deposition within the vesicles. If this is so, then the filaments could be a preformed template laid down in order to act as a nucleating surface on which silica deposition can take place. Once a silica phase has been established, further silica could be deposited onto the silica surface resulting in the space between the filaments being filled.

The detailed mechanism of staining by uranyl acetate/lead citrate in sections is not known. Both these stains appear to have a strong affinity for organic material although their action is not specific. An obvious problem of interpretation of micrographs such as figure 4.11 is whether the contrast of the filaments is due to stain materials or silica deposition. In either case the possibility of an organic matrix within the vesicles seems most likely.

4.7 The nature of the surface silica of costal strips

4.7.1 Binding studies of aqueous cations to costal strips

The detailed nature of the surface of costal strips is not known. Evidence from demineralisation studies (section 4.5) suggested that the surface of costal strips may be stablised in some way. The possibility of cation-binding to silica surfaces was investigated by treating costal strips with low concentrations of Co(II) and Fe(III) solutions.

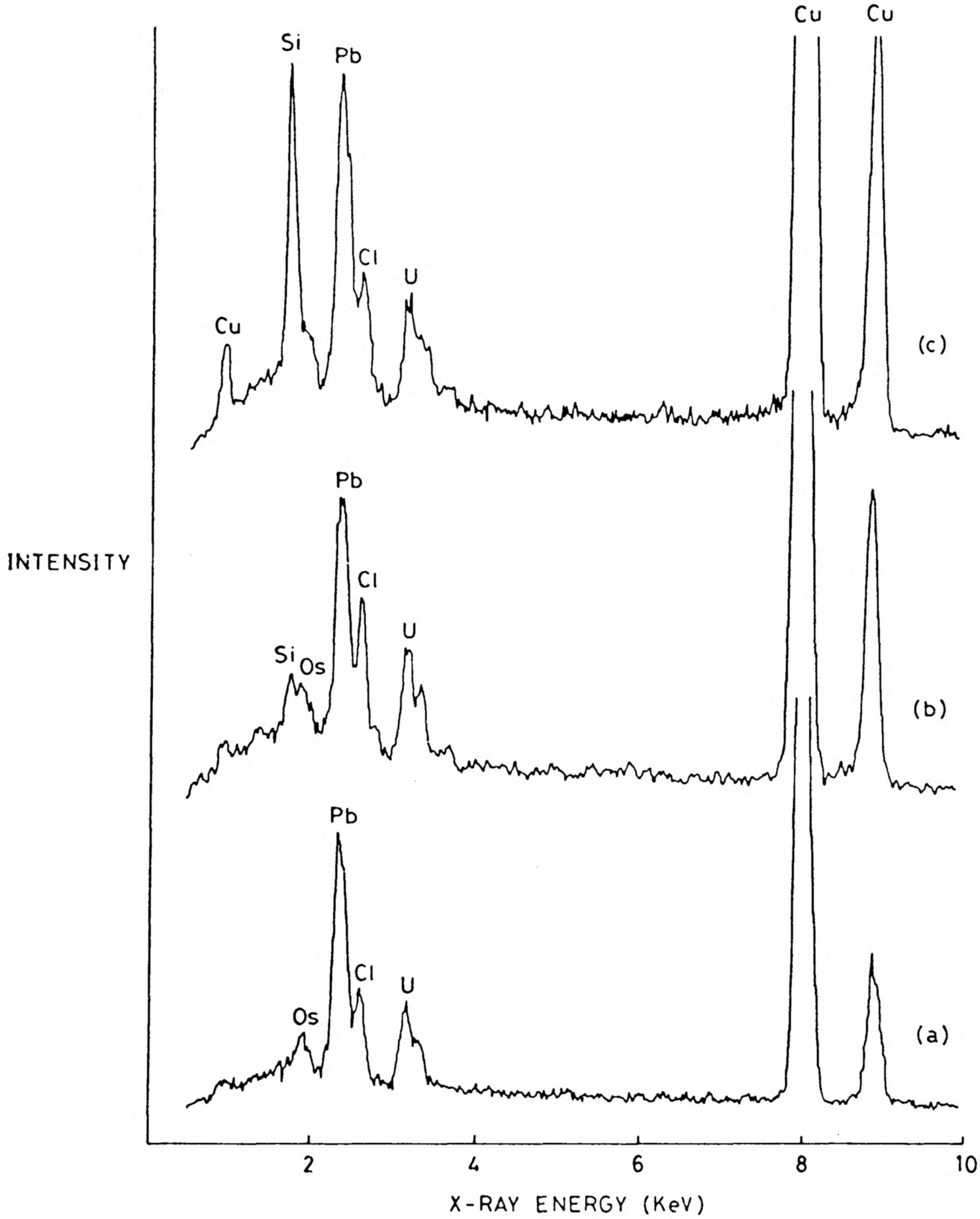

Figure 4.12 X-ray microprobe analysis of sectioned costae; a, normal cellular areas; b, analysis across immature vesicle (see figure 4.11); c, analysis across vesicle containing a mature costal strip (see figure 4.10 (A)).

The results for Co(II) binding are shown in figure 4.13 and table 4.2a. X-ray microprobe analysis was performed on many costal strips in intact loricae with the background analysis obtained at a distance of 100nm from the costal strips. There is a small Si background count rate due to a small degree of X-ray scatter from the surrounding lorica. X-ray energies corresponding to the elements Si, Co and Cu (from the grid) are observed for analysis across the strips. Background analysis reveals only Si (background) and Cu. Hence Co(II) ions are bound preferentially to the surface of the costal strips.

Similar results for Fe(III) binding are shown in figure 4.14 and table 4.2b. Fe(III) ions are found bound preferentially to costal strips.

These results show that the surface of costal strips is active towards cations in low concentrations in the external solution.

4.7.2 Binding of phosphatidycholine (PC) liposomes to costal strips

In the previous sub-section the binding of cations to costal strips was discussed. In this section the binding of lipid PC liposomes, prepared by gently sonicating PC (17mM) in distilled water, to costal strips is presented.

In order to observe liposome binding in the electron microscope, samples prepared by treating costal strips with PC liposomes for 24 hours were dried onto EM grids and stained with uranyl acetate at pH 7.0. Many costal strips were found to contain liposomes closely attached to their surface (figure 4.15). The stain does not penetrate the lipid lamellae as seen from

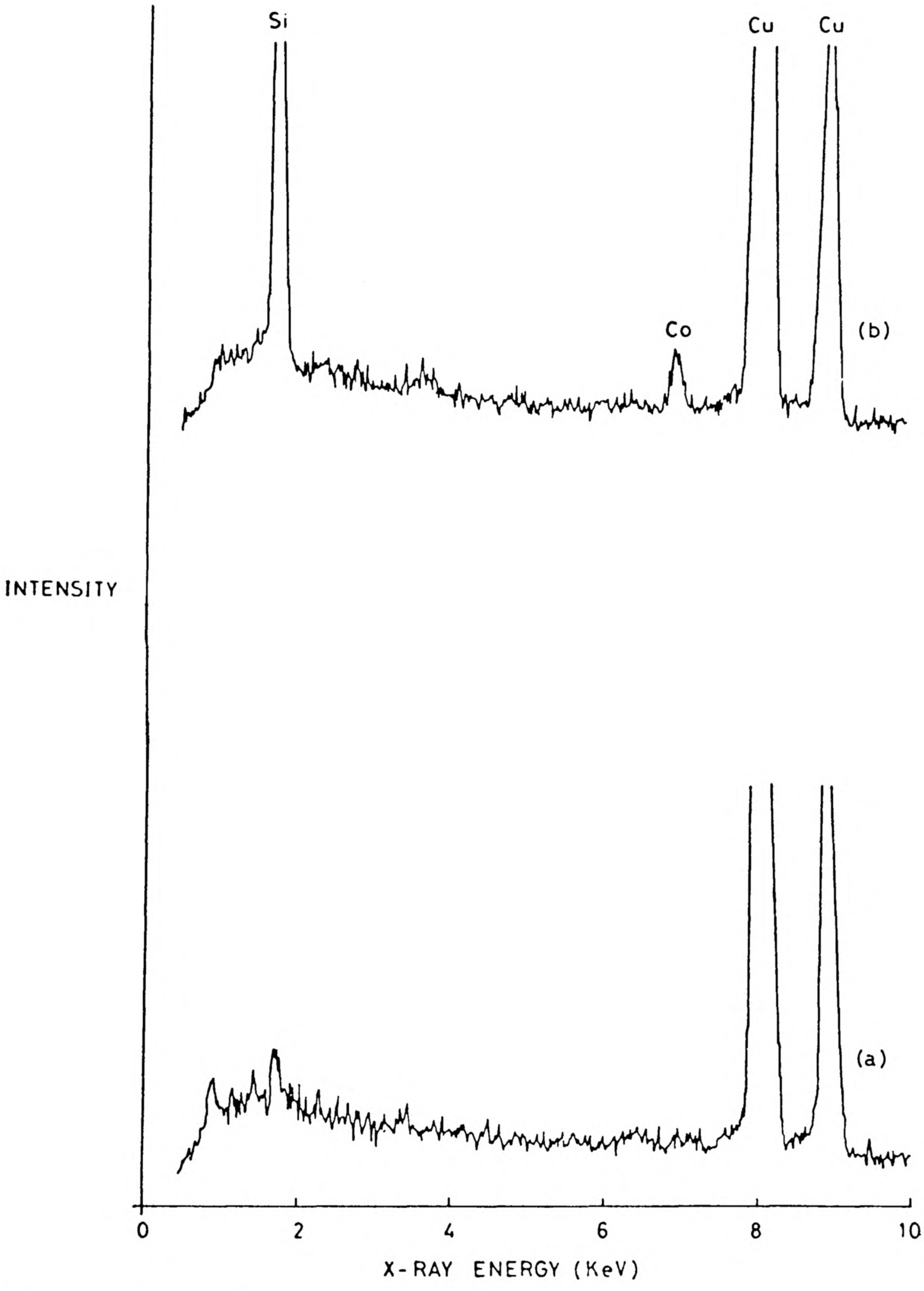

Figure 4.13 X-ray microprobe analysis of costal strips in 2mM $CoCl_2$ solution; a, background analysis (100nm from costal strip); b, analysis across single costal strip.

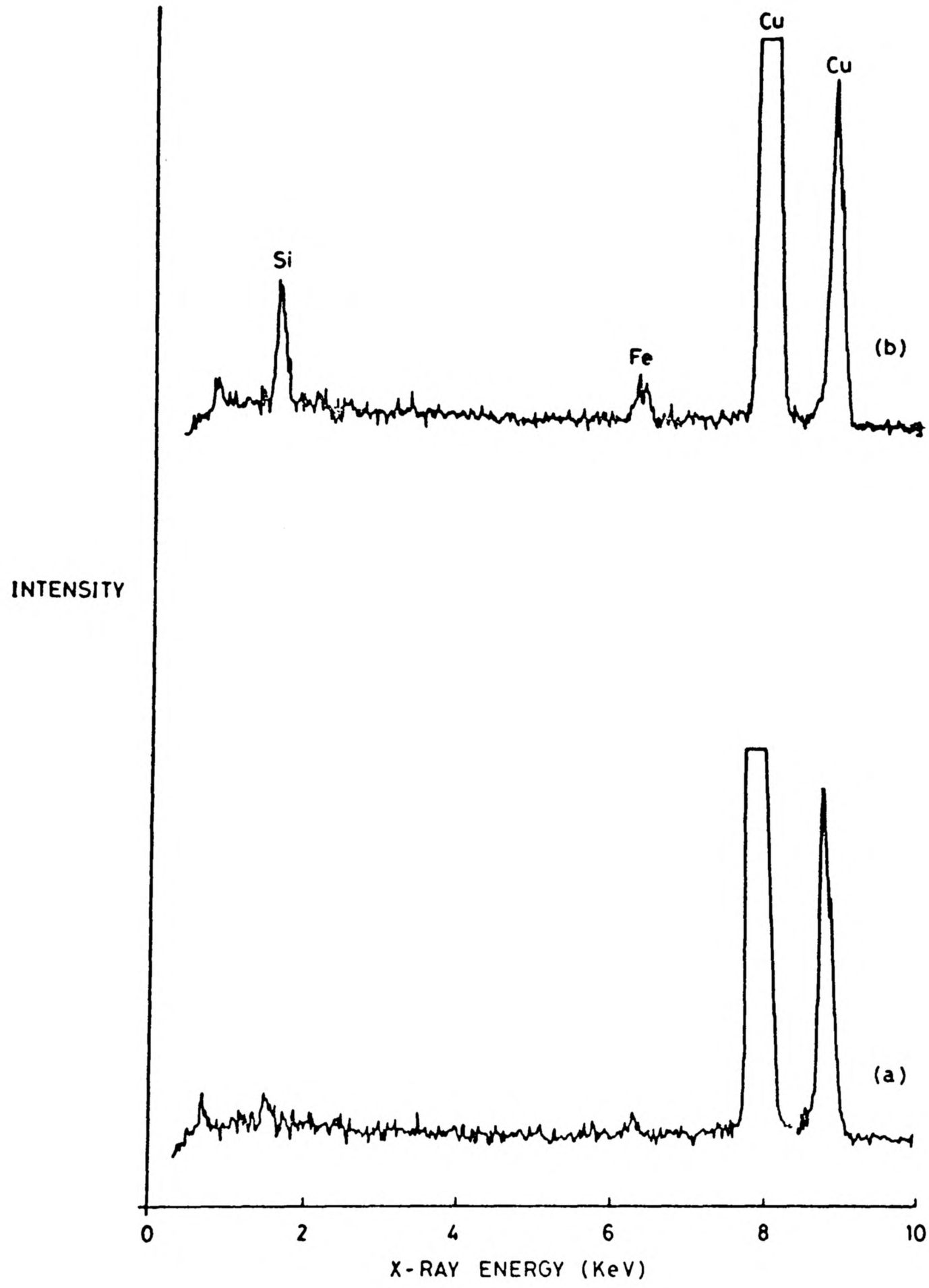

Figure 4.14 X-ray microprobe analysis of costal strips in 2mM $FeCl_3$ solution; a, background analysis; b, analysis across a costal strip.

Table 4.2 X-ray microanalysis data for cation-binding to costal strips.(a)Co(II);(b)Fe(III)

a	Samples	Counts above background/100s Si	Co
	1	4402	205
	2	3440	372
	3	4207	224
	4	2111	184

b	Sample	Counts above background/100s Si	Fe
	1	1337	73
	2	3334	580
	3	9243	633
	4	5288	538

the spheres imaged in figure 4.15.

X-ray microprobe analysis over areas of costal strips, treated with PC liposomes, but unstained, detected Si and P. No Si or P was found on areas away from the strips, (figure 4.16). On some costae the P counts were very low and hardly significant above background.

4.7.3 Binding of colloidal silica to costal strips

Colloidal silica (ca. diameter 100nm) was observed to bind to costal strips within 24 hours of mixing the two solutions (figure 4.17a and 4.17b). Figure 4.17b shows the junction between a collodial particle and a costal strip at high magnification. The strip surface appears pitted in several areas.

4.8 Discussion

The manufacture of costal strips in Stephanoeca diplocostata involves the production of membrane-bounded vesicles within the peripheral cytoplasm of the cell and subsequent deposition of silica within these regions of space. Deposition could take place in several ways. Silicification could result from a binding mode for silicic acid within the vesicles such as specific sites on an organic matrix followed by polymerisation of the silica phase. Silica binding to organic molecules can occur through hydrogen bonding, ionic interactions or condensation of OH groups. Alternatively, an energised dissolved silica ($Si(OH)_4$) concentration gradient within the vesicles would allow silicification to occur through changes in pH or concentration.

Concurrent with silica deposition must be a whole range of

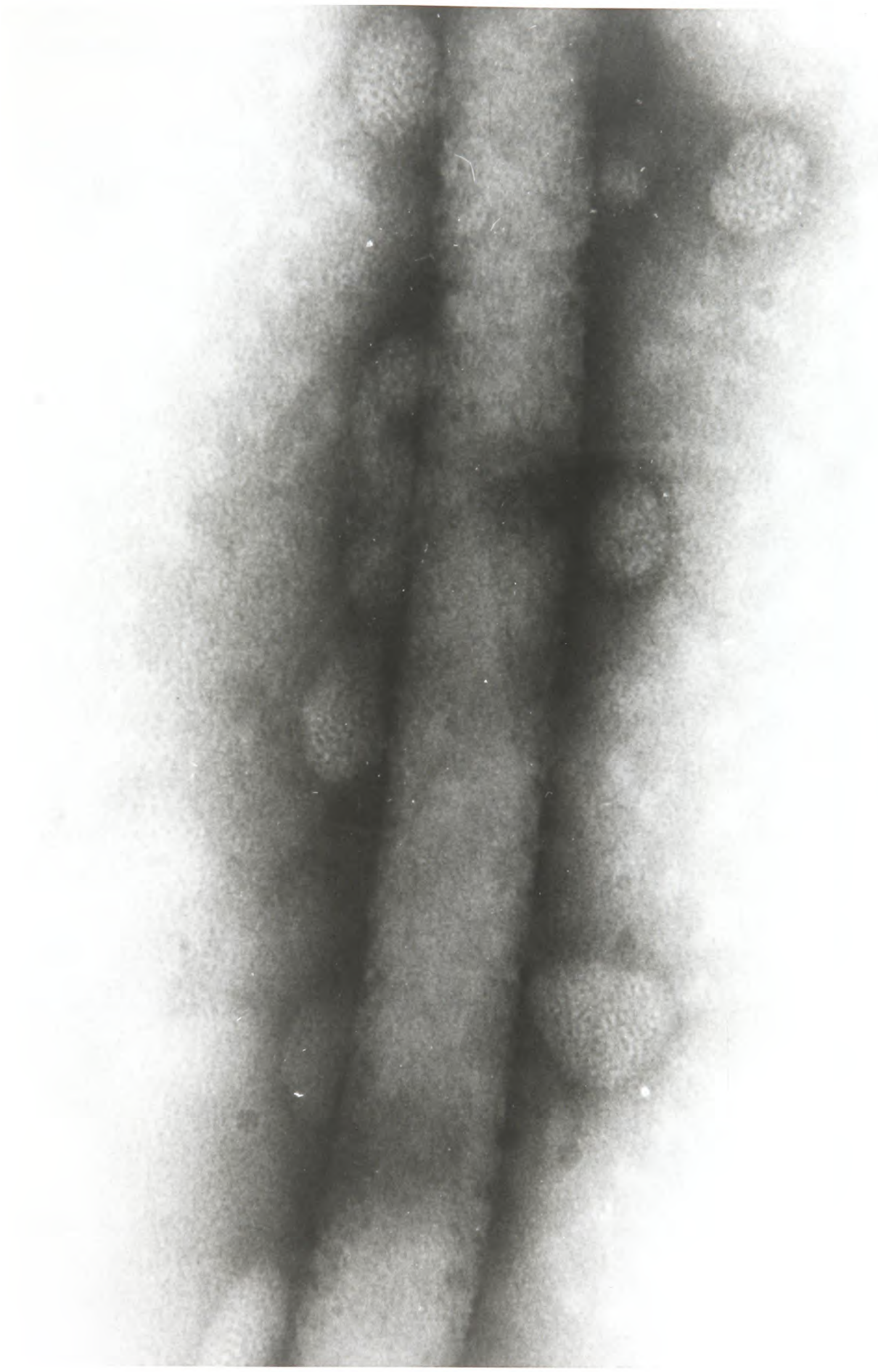

Figure 4.15 Binding of PC liposomes to a costal strip. Samples were stained with uranyl acetate at pH 7.0 x370,000.

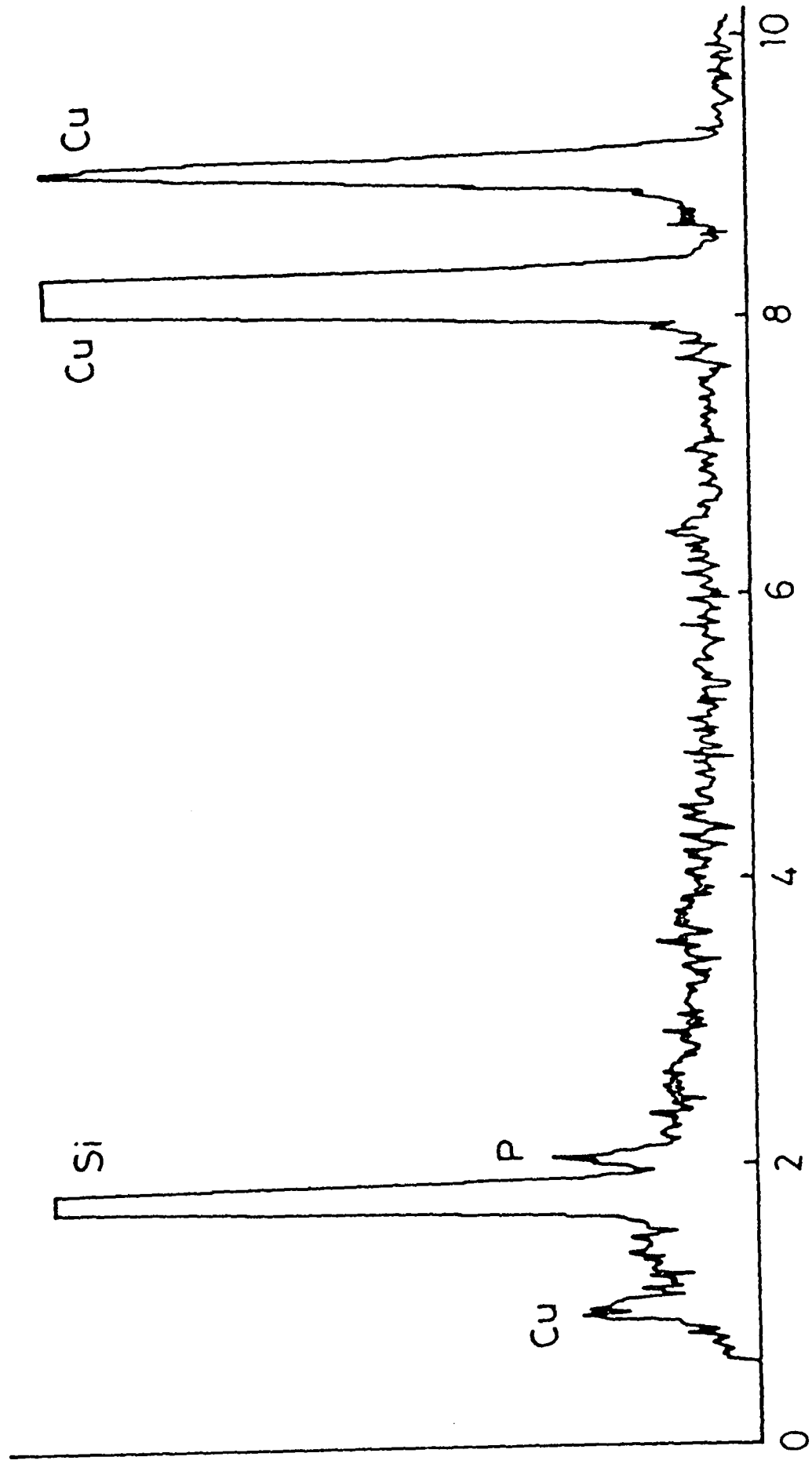

Figure 4.16 X-ray microprobe analysis across an unstained costal strip in 17mM PC aqueous solution.

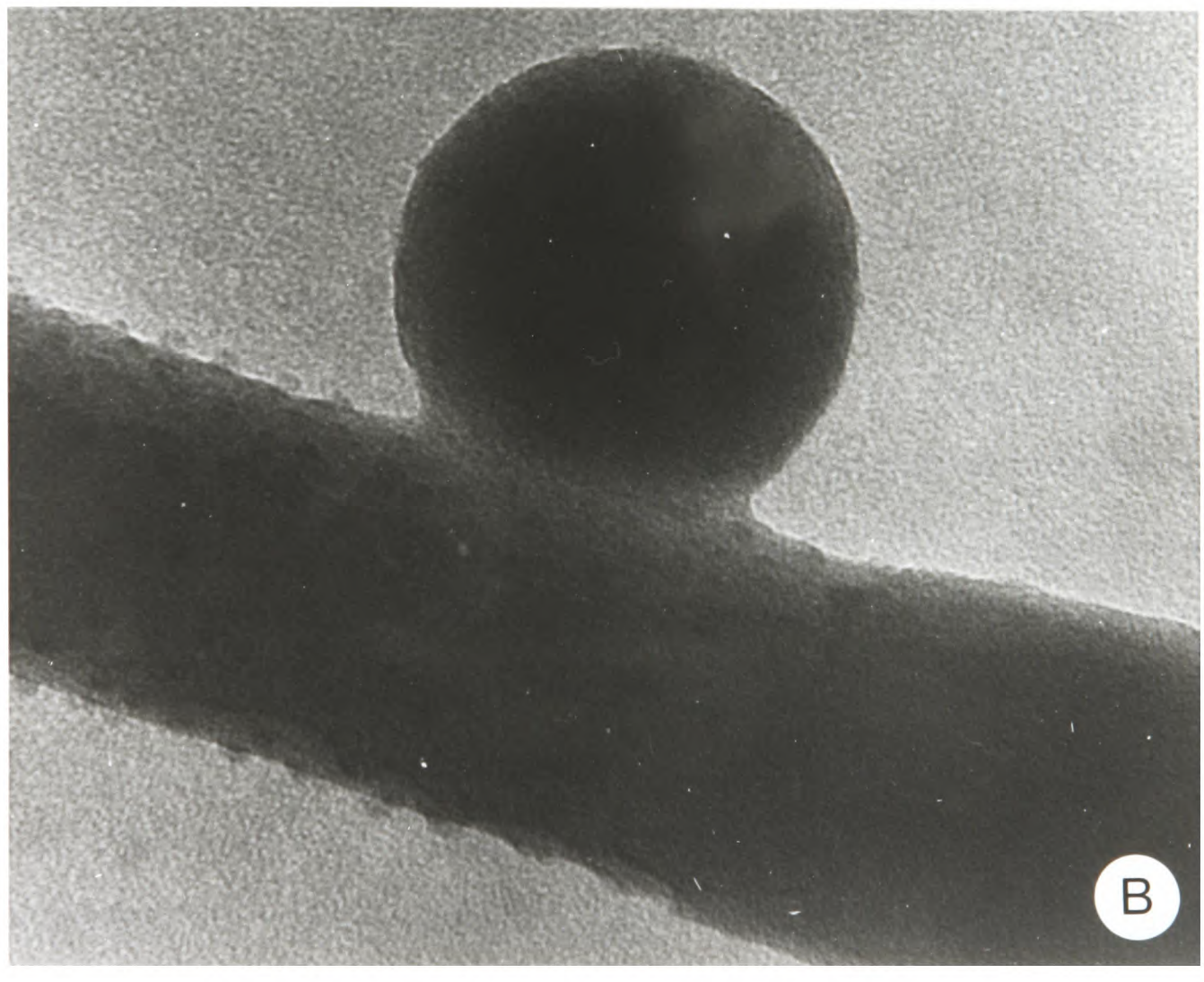

Figure 4.17 Binding of colloidal silica to costal strips; a, low magnification x39,000; b, at high magnification x57,000.

biochemical processes involving regulation of $Si(OH)_4$ metabolism and control over the organic components necessary for silicification such as vesicle and matrix growth. The silica/organic composition of developing costal strips may change as deposition continues, making it difficult to infer the initial composition of costal strips from any data derived from studies of mature costae.

That the silica is deposited in an extremely amorphous form (section 4.3) is due to the high activation energies required (of the order 200Kcal mol^{-1}) (10) for crystalline deposition. Hence the biomineralisation of silica is different from, for example, phosphate deposition (in bones and teeth). Although the two tetrahedra SiO_4 and PO_4 are isostructural, crystalline phases are observed only in the latter case in biological systems. Also, because the transition between amorphous calcium phosphate (ACP) and crystalline calcium phosphate requires much lower energy than for amorphous silica to crystalline silica (quartz), calcium phosphate occurs both in amorphous and crystalline forms in bone (11). The amount of ACP is initially high but decreases as the bone matures (12), which suggests that the initial phases of calcium phosphate deposition may be very similar to the deposition of amorphous silica but that ACP is metastable with respect to the crystalline phase and readily transforms into the more stable phase with time.

The composition of silica in costal strips is not accurately known, and may change depending on growth conditions. It would be expedient to investigate the chemical nature of costae by ^{29}Si n.m.r. and compare the data obtained with similar experiments using diatoms, silica gel, and opal.

Whether or not there is an organic component within costal strips is not conclusively known. The evidence presented in this chapter from strip demineralisation and sectioned material of very early stages of costae growth (figure 4.11) suggest that the probability of organic material being present within the costal strips is high. Similarly the electron-dense filamentous material observed between junctions of costae in intact loricae suggests a different phase running within the silica network.

Figure 4.11 could be interpreted in the following manner; There is a sectioned hollow cylinder of material within the vesicle. Such material could comprise long chains of polysaccharide residues or helices of protein chains. Along this cylinder there must be specific sites for silica binding. Once a silica phase has been established further polymerisation can then occur within the cylinder , just as in figure 4.11 the two electron dense lines within the vesicle disappear into a more dense single thread.

Strip growth could then proceed by a variety of mechanisms. One possibility is that enlargement could occur by expansion of the organic material accompanied with further silica deposition into the centre of the costal strip (figure 4.18a). This mechanism would require that the dissolved silica is directed into the central zone and that a controlled supply of organic material is available to the expanding vesicle and organic cylinder.

Another possibility is that strip growth could occur simply by further deposition on the internal and external surface of the cylinder without expansion of the organic phase. There could be several rings of organic material laid down within

the growing silica phase or alternatively, no further organic phases may be present (figure 4.18b).

The results of the several binding experiments discussed in section 4.7 imply that the surface silica of costae is active towards charged species. Costae cut in transverse section (TS) within cellular vesicles show stained surfaces. Figure 4.19 shows a vesicle cut in TS (notice vesicle bilayer) within which a costal strip is imaged with a dark halo of stain on its surface and two dark small circles of stain within the strip. Sometimes the two small circles are not imaged but often a single small line is observed instead. These internal stained areas may be artefactual. Alternatively they may represent a central hole(s) in which the stain 'sits' (see figure 4.18a) or a central region of organic material. Demineralisation occurs from this central region and hence a mechanism has to be postulated in order to explain how $Si(OH)_4$ can leave the polymerised strip if the surface is blocked. Diffusion through a central pore would then have to be possible.

What seems less susceptible to artefacts is the imaging of surface costal strip staining (figure 4.19). The growing nascent strip will be meta-stable and is protected from dissolution by a surface 'coat'. It is known that the SiOH group is labile to neutral O and N atoms of alcohols, ketones, ethers, and amides. Hence t-butyl alcohol, poly vinyl alcohols, and lipids have all been shown to adsorb onto the surface of colloidal silica(13). At pH values below 7.0, hydrogen bonding is the most likely form of interaction; at pH values above 7.0 the proportion of $Si-O^-$ surface sites becomes larger and ionic interactions become important. It has also been shown that

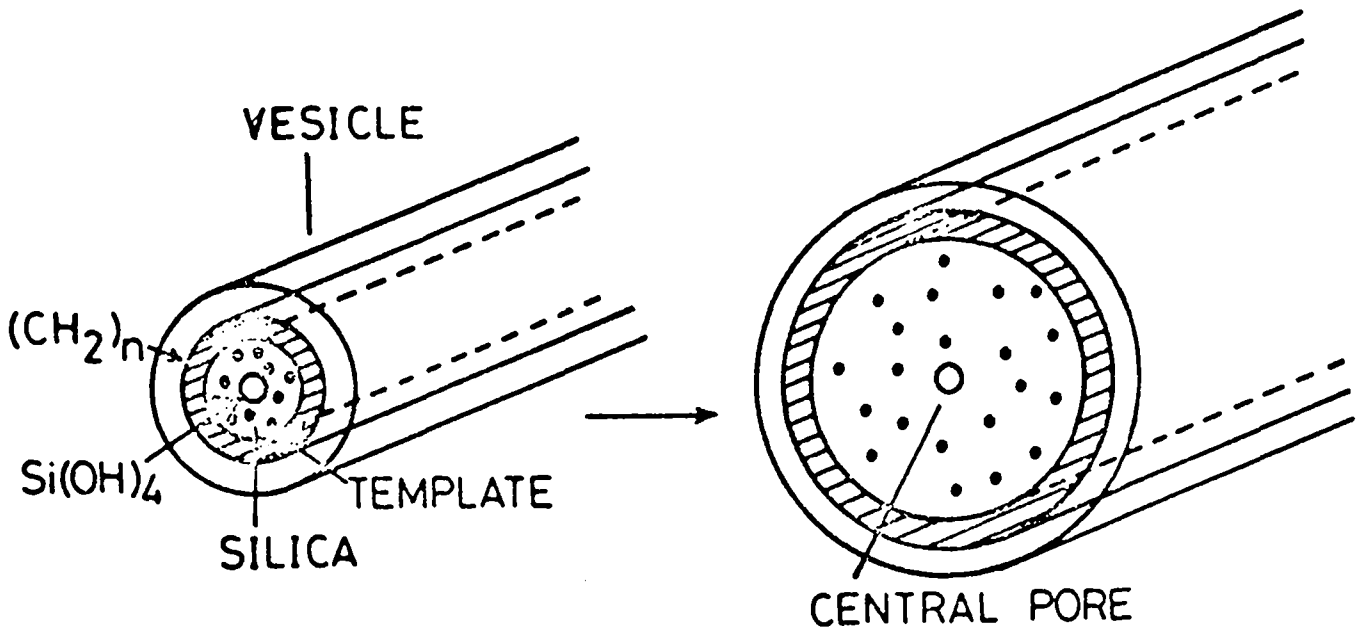

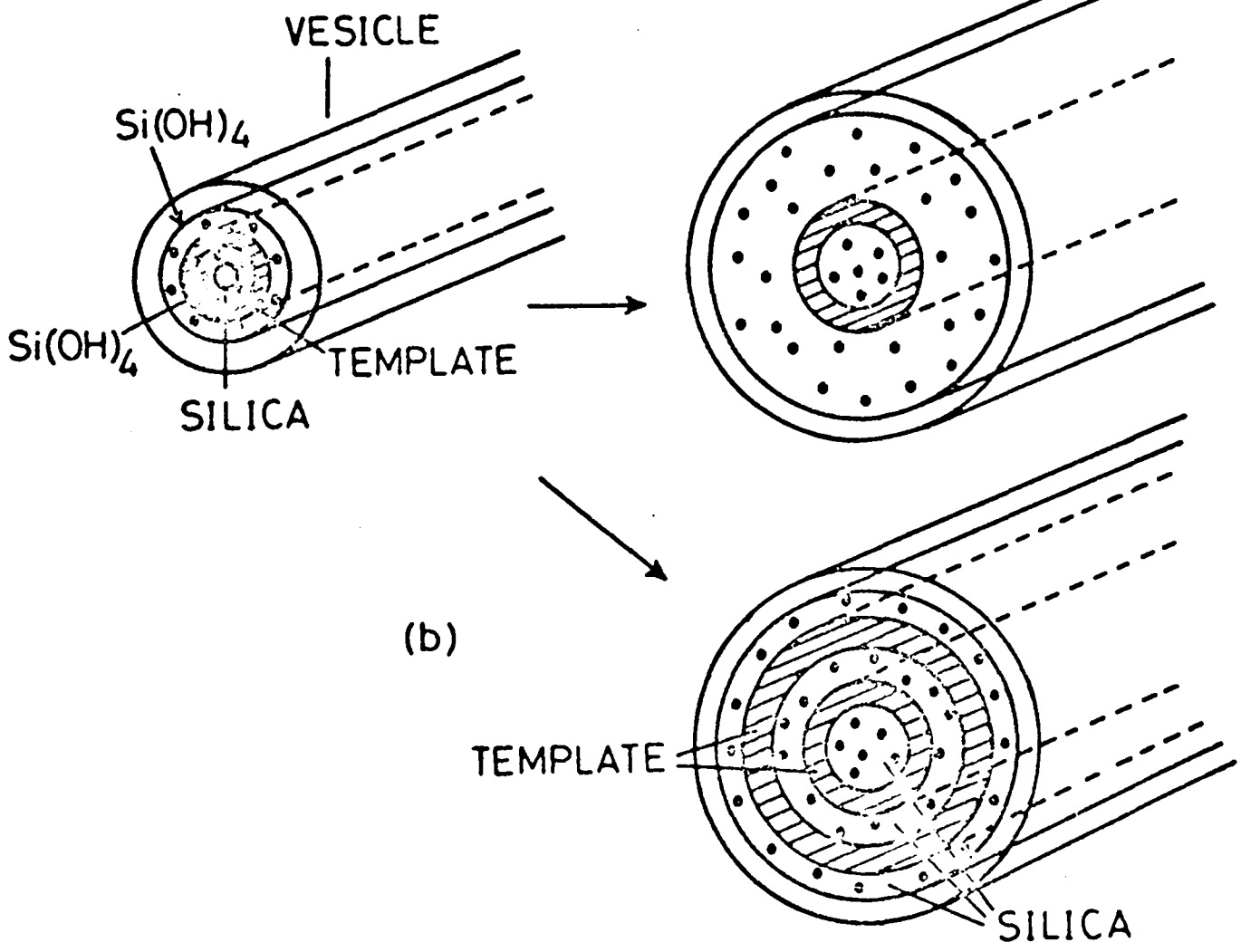

Figure 4.18 Possible mechanisms of costal strip growth within cellular vesicles; a, growth occurs from the central region of costae accompanied by an expansion of an organic cylinder initially established as a template for silicification; b, growth occurring by polymerisation of silica on the internal and external surface of the establish organic cylinder with or without the addition of further organic phases.

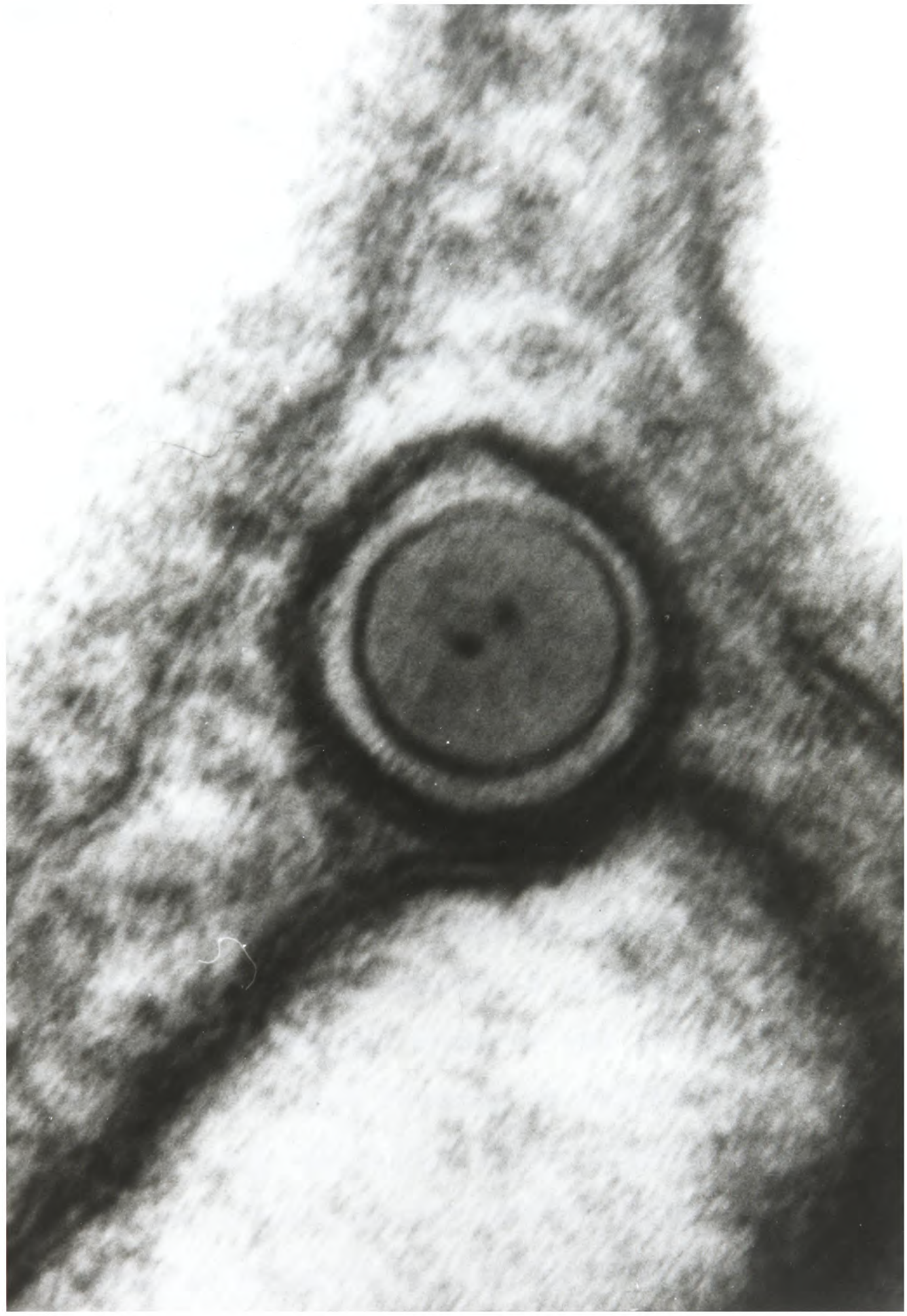

Figure 4.19 Costal strip within a cellular vesicle cut in transverse section showing surface and internal stained regions x700,000.

SiO_2 has an extremely strong affinity for organic compounds such as catechols (13). Thus the possibility of an organic 'coat' bound to the costae can be postulated through the interactions of alcohol (OH), amino acid, or catechol residues of a long chain organic molecule(s) with the surface Si-OH groups (figure 4.20). Similarly the possibility of cation binding (section 4.7(1)), PC binding (section 4.7(2)) and colloidal silica binding (section 4.7(3)), to costal strips can be considered in terms of ionic or hydrogen bonding interactions to this organic 'coat' (figure 4.20).

The assembly of loricae in Stephanoeca diplocostata after mitosis must be a controlled sequence of events in which the daughter cell mobilises and joins together the supernumerary costae produced by the parent cell. In section 4.4 it was shown that the junction between costal strips contains silica and a filamentous material which may or may not be organic in nature. Figure 4.5 could be interpreted in several ways. The structure traversing the join could be (a) an annulus of connective material centred around an annulus of filamentous material running through the strip or (b) two connecting sites each centred around a thin filament of material running independently through the costal strip (figure 4.21). The two filaments are not always located between joins which suggests that an annulus of material may not be present. When two independent connecting filaments are orientated directly in the line of the electron beam the join will appear with a single thread (figure 4.6).

Treatment of intact loricae with concentrated nitric acid disrupts the loricae leaving intact costal strips (14). From this observation it is clear that the junction can not contain

COSTAL STRIP ORGANIC COAT ENVIRONMENT

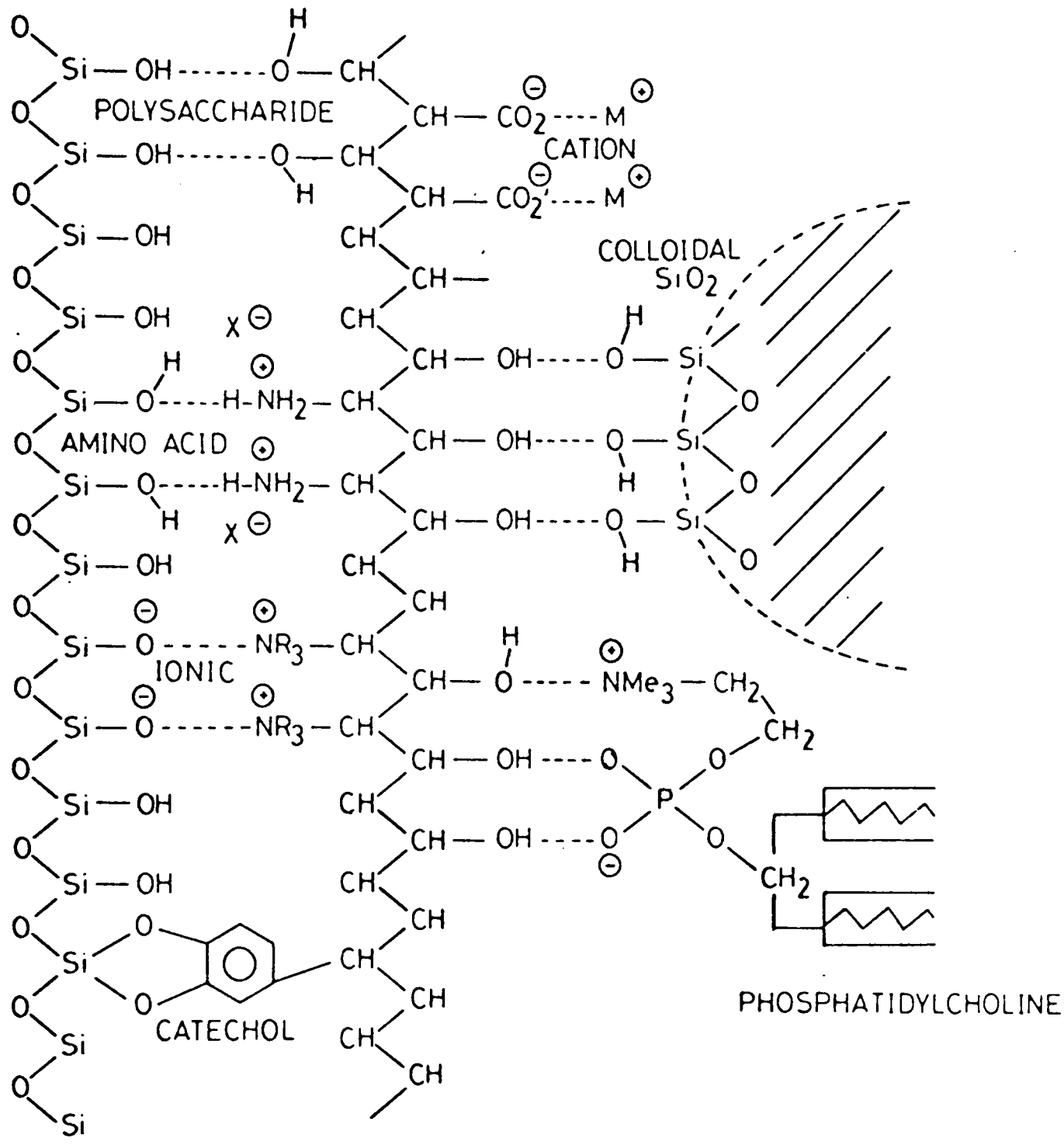

Figure 4.20 Possible modes of chemical binding between surface sites of costae, a surface organic layer, and the external aqueous environment.

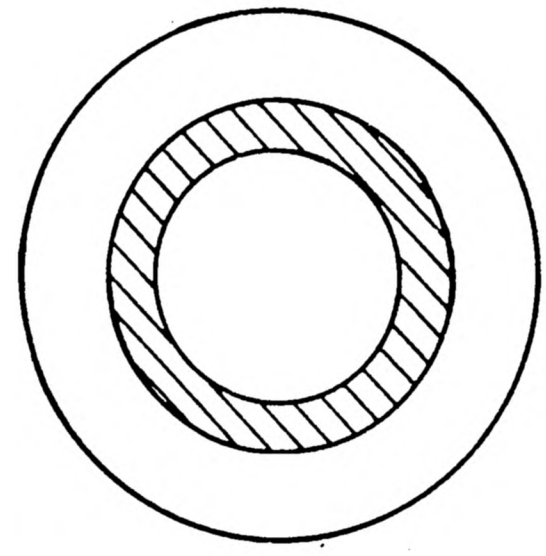

(a) ANNULUS.

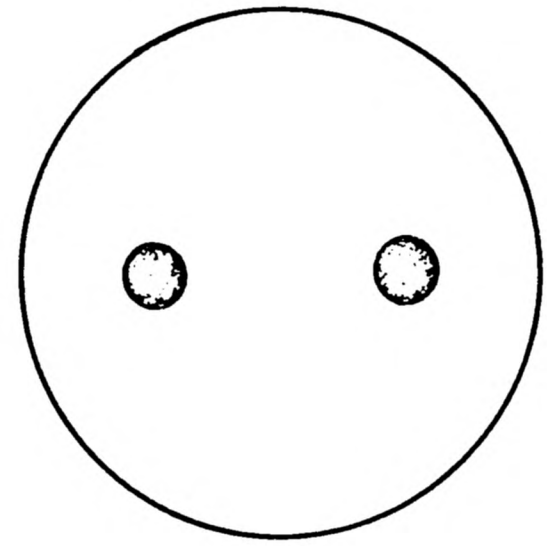

(b) INDEPENDENT FILAMENTS.

Figure 4.21 Possible structures of filamentous material within costal strips based on electron micrographs of intact costal strip joins.

SiO_2 alone and that oxidisable material must be present within the strip join indicating that a relatively high proportion of organic material is within the junction. On the other hand, figures 4.6, 4.7 and 4.8, show that SiO_2 does appear to traverse the costae joins. Also, digestion of intact loricae with trypsin and protease enzymes have not conclusively shown loricae disruption (14). Hence, the organic material present within the join must be protected from these milder reagents by the silica within the join, but this protective layer is not sufficient to prevent nitric acid penetration and subsequent disruption of the junction.

There is no evidence on how SiO_2 is mobilised into the junctions between costal strips. Circumstancial evidence from figure 4.6 suggests that the join is constructed around the two filaments running between the strips. If this is so, and the filaments are organic in nature then joins between costae could be constructed by initial attachment of the organic filaments between the strips which then serve as templates on which SiO_2 binding occurs. This will then strengthen the join between costal strips in intact loricae. The mobilisation of the silica at this stage could take place if there are exposed silica surfaces on the costae near to the joining filaments from which silica can flow and traverse the join (figure 4.22).

The distance between costae in intact junctions may be artefactual in that the strips may be 'prised' slightly apart during the drying process onto EM grids and this may allow the ultrastructural information of such joins to be so clearly observed

It is not clear how the daughter cell moves the supernumerary strips in order to assemble its lorica. There is some evidence (6) that selected tentacles are involved and provide

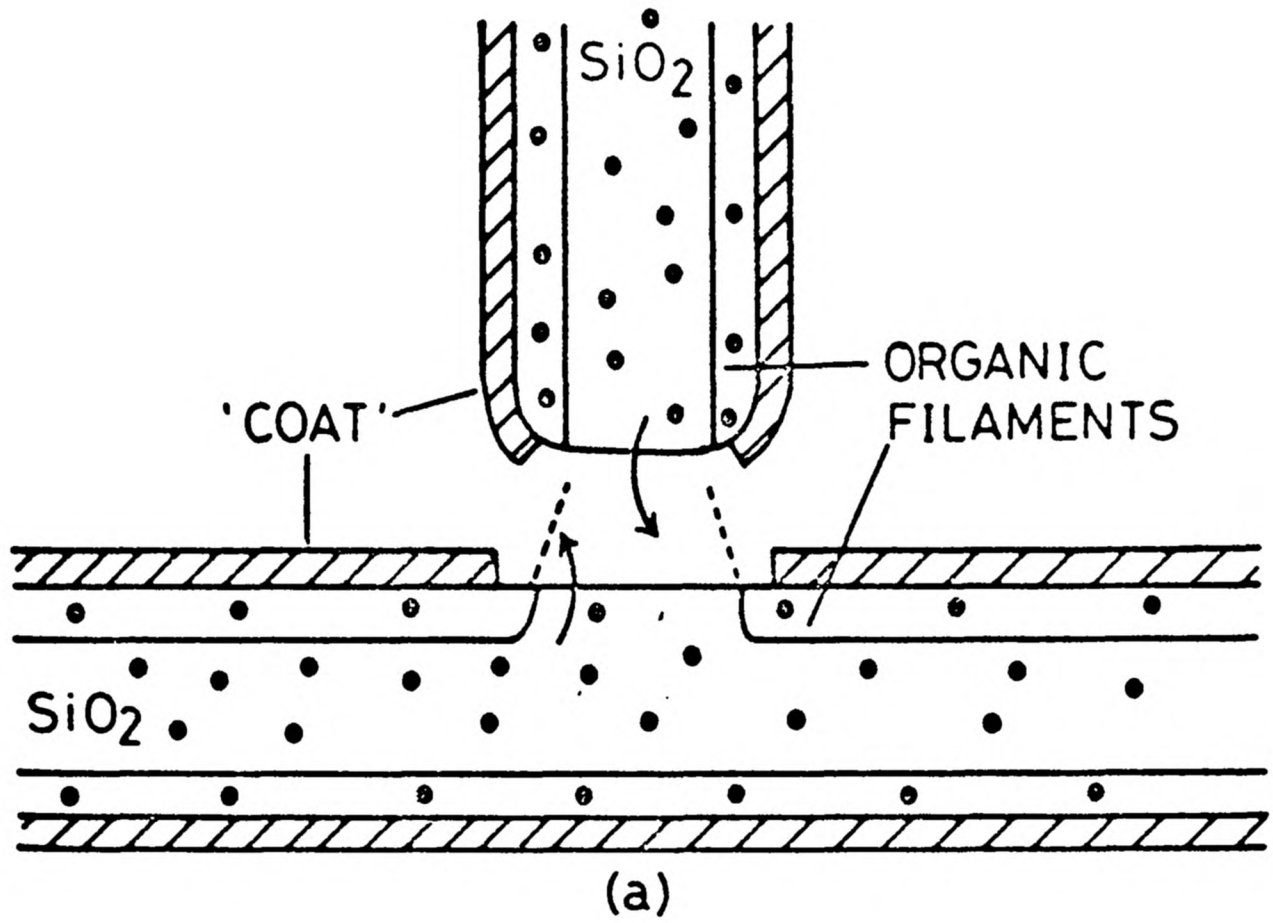

Figure 4.22 Postulated mechanism of costal strip joins in Stephanoeca diplocostata Ellis; a, costae approach into the correct position for overlap; b, join forms by attachment of organic filaments followed by fusion of mobile surface silica across the join.

the motive force for lorica assembly. It is possible that costae slide over each other until junction surface sites come into position and fuse.

4.9 Summary and further work

This chapter has been concerned with the study of silica biomineralisation in the organism Stephanoeca diplocostata Ellis. The work undertaken has concentrated on the nature of the costal strips in intact loricae, how they are joined together and the mechanism of their growth within cellular vesicles. A most crucial development in this work must be the separation (and hence verification) and characterisation of an organic component within the costae. For this to be accomplished a satisfactory method of separating loricae from cellular and bacterial debris must be developed. If this could be accomplished, and enough material collected, then an amino acid assay would be possible as has been the case with diatoms (15) and shells(16).

The existence of an organic matrix within the costae is often thought fundamental to the concept of biomineralisation. However, it is possible that silicification could occur by concentration or pH changes within the vesicle resulting in the solubility product of silica being reached. The circumstancial evidence presented in this chapter suggests that this is not the case and that an organic cylinder is first established within the cellular vesicles before silica deposition takes place.

Preliminary efforts to model this system of silica deposition within confined volumes are reported in chapter 6 where the precipation of silicates within unilamellar PC

vesicles is discussed.

4.10 References

(1) Leadbeater B.S.C., Protoplasma 98, 241-262, 1979.

(2) Leadbeater B.S.C., Manton I., J. Mar. Biol. Ass. UK 54, 269-276, 1974.

(3) Throndsen J., Nytt Mag. Bot. 16, 161-216, 1969.

(4) Leadbeater B.S.C., Brit. Phycol. J. 7, 195-211, 1972.

(5) Leadbeater B.S.C., Arch. Protistenk 115, 234-252, 1973.

(6) Leadbeater B.S.C., Protoplasma 98, 311-329, 1979.

(7) Leadbeater B.S.C., personal communication.

(8) Krivnek O.L., Gaskell P.H., Howie A. Nature 262, 454-457, 1976,

(9) Leadbeater B.S.C., 1982, in print.

(10) Degens E.T., Topics in Current Chemistry No. 64, 1976.

(11) Posner A.S., Physiol Rev., 49, 760-792, 1969.

(12) Termine J.D., Posner A.S., Science 153, 1523-1525, 1966.

(13) Iler R.H., in "Biochemistry of silicon and related problems" (Plenum) 53-76, 1977.

(14) Leadbeater B.S.C., unpublished data.

(15) Hecky R.E. et. al. Marine Biol. 19, 323-331, 1973.

(16) Degen E.T., Spencer D.W., Parker R.H., Comp. Biochem. Physiol 20, 533-579, 1967.

CHAPTER 5

PREPARATION AND CHARACTERISATION OF INTRAVESICULAR IRON OXIDES

5.1 Introduction

It is well known that iron plays an important functional role in biological systems. Iron-containing proteins participate in two main processes; (a) oxygen-transport in proteins such as haemoglobin, myoglobin and hemerythrin, and (b) electron-transfer in cytochromes and ferrodoxins. Iron metabolism requires a mechanism for storing and transporting iron. In man and many other higher animals the storage materials are ferritin and haemosiderin which are present in the liver, spleen and bone marrow. Ferritin consists of $Fe_2O_3.H_2O$ - phosphate micelles encapsulated within a spherical protein sheath ca. 120Å in diameter.

The importance of other iron stores such as in the form of magnetite (Fe_3O_4) has only recently been realised. Chapter I includes a summary of the recent investigations into the functional role of Fe_3O_4 deposits within various organisms. In this chapter the precipitation of iron oxides within synthetic phosphatidylcholine (PC) vesicles is studied. The vesicle system is chosen as it allows the chemistry of iron oxide precipitation in micro-volumes of space to be investigated and can therefore be used as a model system for the study of iron oxide mineralisation in biological systems.

This chapter is in two parts. Section 5.2 describes the inclusion of preformed magnetite crystallites into PC vesicles. These experiments are of interest for several reasons. Firstly, Fe_3O_4 is ferromagnetic and incorporation of small Fe_3O_4

crystallites within a lipid vesicle of diameter ca. 30nm may then form magnetic vesicles. The perturbation of regions of space external to the vesicle by intravesicular Fe_3O_4 could then be studied by n.m.r. For example, this system may be important as a probe in n.m.r. experiments of protein binding to lipid bilayers. Secondly, vesicles can be used as carriers of water soluble drugs. The incorporation of Fe_3O_4 crystallites may make it possible to design magnetically-directed drug carrier systems which would be more specific in action.

The second half of this chapter considers the in situ preparation of intravesicular iron oxides. In chapter 3 the preparation of crystalline intravesicular Ag_2O was shown to be possible. Is it then possible to prepare crystalline Fe_3O_4 within vesicles? The chemistry involved in such a preparation may be more complex since magnetite is an oxide of mixed Fe(II) and Fe(III) oxidation states. Several intravesicular precipitation reactions are described for vesicles containing Fe(II), Fe(III) and Fe(II)/Fe(III) ions. The reaction product in each case is characterised by normal electron microscopy techniques.

5.2 Inclusion of preformed magnetite crystallites into vesicles

5.2.1 Preparation of magnetite crystallites

Black, magnetic Fe_3O_4 was prepared in aqueous solution by the following method. Equimolar solutions (0.1M) of Fe(II) and Fe(III) salts (usually chlorides) were mixed and the pH of the resulting solution was then raised to a value of 10.0-11.5 by the addition of NaOH or NH_4OH solutions. A

black precipitate was immediately observed which is not magnetic. Shaking the sample and leaving for 1-2 hours resulted in black magnetic crystals, observed by bringing a bar magnet up to the side of the sample tube. It is not clear why magnetic behaviour is inhibited in this preparation The original precipitate appears gelatinous and crystallisation may require time for loss of water, anions or $H^+_{(aq)}$ from the initially precipitated iron hydroxides, i.e.

$$2OH^-_{(s)} \rightarrow 2O^{2-}_{(s)} + 2H^+_{(aq)}$$

Magnetic behaviour may be also inhibited by the slow rate of domain alignment in the originally-formed precipitate. Such behaviour will occur when a critical domain size is reached (section 5.2.7).

Samples were centrifuged and washed three times with distilled water. Very small crystallites were prepared by sonicating the magnetite suspension for five minutes at an amplitude of 9μ peak to peak in an ice bath. Samples examined in the EM showed particles 10-50nm in diameter.

5.2.2. Preparation of magnetite vesicles

34mM PC was sonicated in distilled water at 4^oC in the presence of a magnetite dispersion prepared as in section 5.2.1. After ca. 10 minutes the vesicle solution was almost transparent and pale-brown. Removal of Fe_3O_4 external to the vesicles was accomplished by allowing the vesicle solution to stand in a small flat-bottomed tube for 2 hours at 4^oC on top of a bar magnet. The pale-brown supernatent was decanted off from the sedimented Fe_3O_4 and left to stand on top of a magnet at

$4^{o}C$ overnight. No further sedimentation was observed. Similar preparations of (i) vesicles with only extravesicular magnetite, and (ii) sonicated magnetite dispersion (no lipid) were also left to stand on bar magnets and showed complete magnetic separation within 2 hours. No pale-brown supernatent was observed in either case.

Samples for ^{1}H n.m.r. experiments were made in D_2O and recorded on a Bruker 270 MHz spectrometer operating in the Fourier transform mode.

Vesicle solutions for EM were left to dry in the air on carbon-sputtered formvar-coated copper grids. The samples were unstained and unfixed. The EM facilities used were those as previously described.

Measurement of n.m.r. T_1 relaxation rates for magnetite vesicles was kindly performed by Mr M. Pye using a pulse n.m.r. Bruker SXP60 spectrometer.

5.2.3 EM study of preformed-magnetite vesicles

Figure 5.1 shows a representative micrograph of the images observed in the electron microscope for a sample of magnetite-containing vesicles. Dense spheres of mean diameter ca. 15nm were observed, often aggregated which is probably an artefact of the drying process. The images are similar to those observed for magnetite in the absence of vesicles since no lipid membranes can be imaged. However, the mean particle size is smaller due to the critical size of vesicle formation.

X-ray microprobe analysis was performed over areas of these particulates and P and Fe were detected (figure 5.2a). A small impurity peak of Si was also observed both on and off these areas. Since the maximum area analysed was 100 nm^2

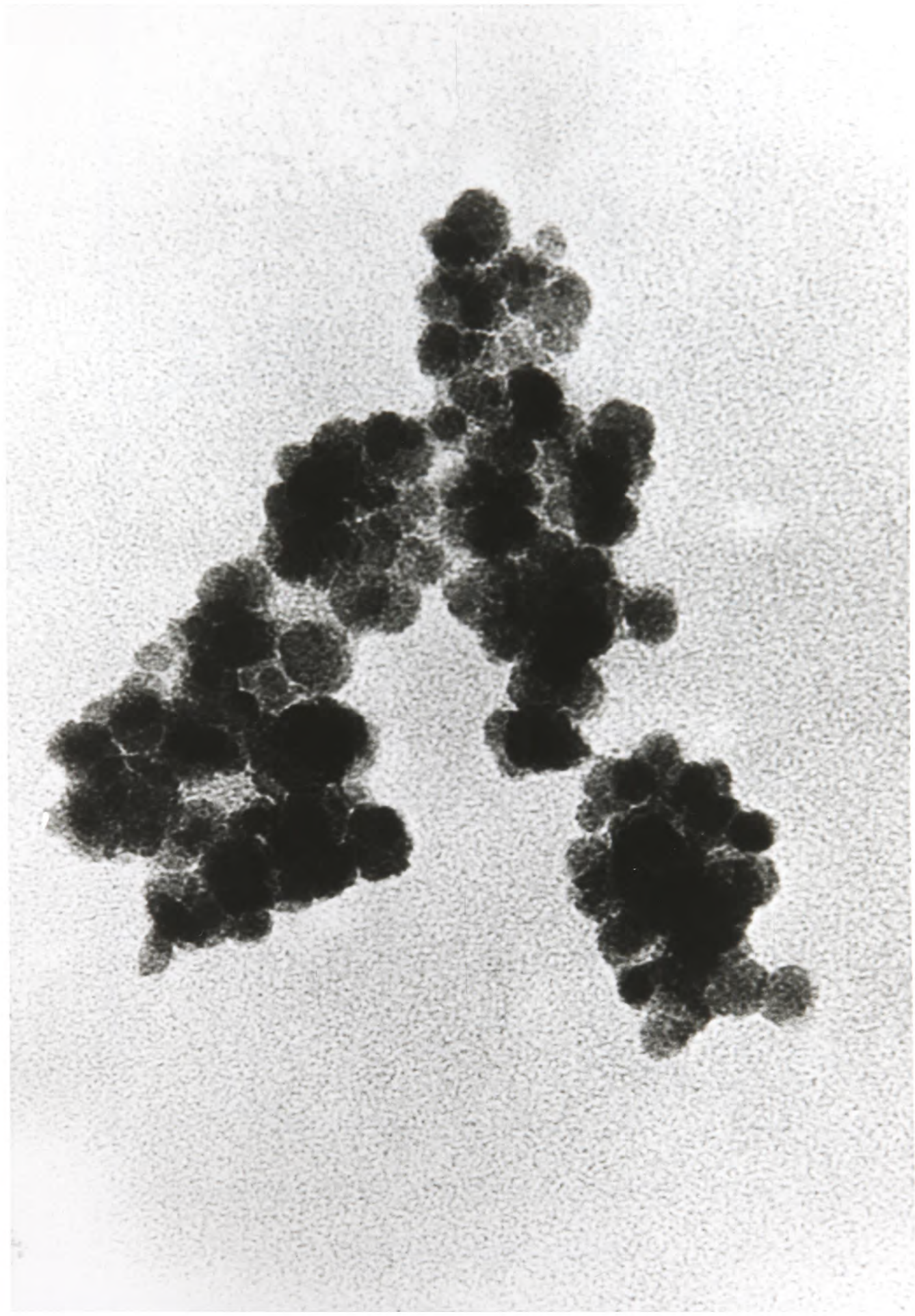

Figure 5.1 Electron micrograph of magnetite-containing vesicles x510,000.

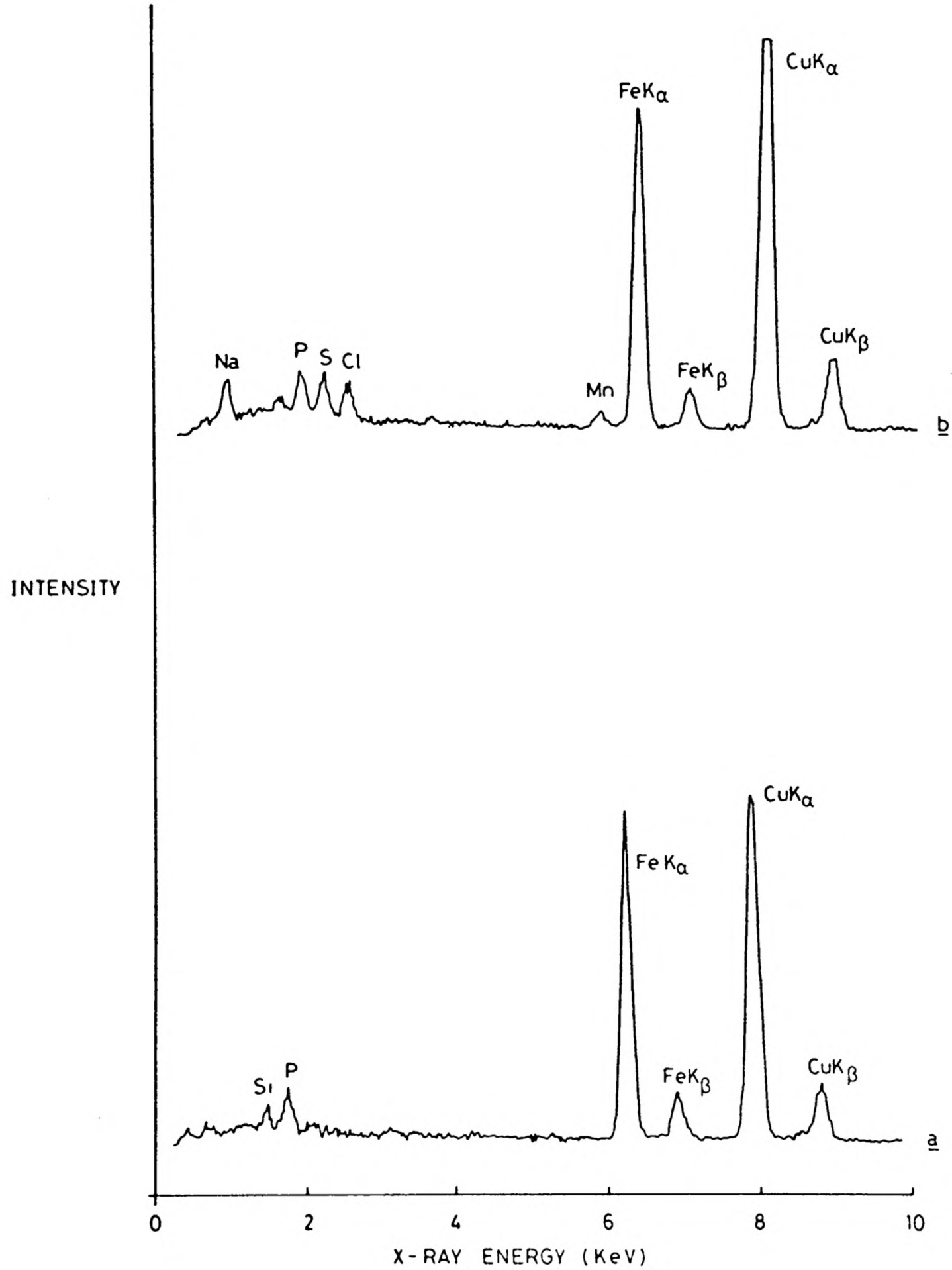

Figure 5.2 X-ray microprobe analysis for; a, magnetite vesicles; b, magnetite vesicles with intravesicular Mn(II).

single particles could not be analysed. Table 5.1 presents the data collected for three separate analyses. The contribution from background counts was determined in each case by completing a 'blank' run, i.e. analysing on an area close to the vesicles. The Fe/P count ratio was ca. 7.5.

In order to show that the imaged spheres have intact spherical phospholipid membranes similar experiments were performed but with the incorporation of a probe solution of Mn(II) (0.5M $MnCl_2.4H_2O$) within the vesicle compartment. Extravesicular Mn(II) was removed by cation ion-exchange. Images observed in the electron microscope showed similar dark spheres as in figure 5.1 but X-ray microanalysis showed the presence of Mn as well as Fe, P, Cl and Na (figure 5.2b) indicating that the vesicles containing magnetite were intact. Na could have originated from the ion-exchange column whereas S was probably a SO_4^{2-} impurity in $MnCl_2$ or in the original magnetite solution.

Electron diffraction was performed over areas of magnetite-containing vesicles and powder diffraction patterns were obtained (figure 5.3). Table 5.2 shows the calculated d spacings in $\mathring{A}$ for intravesicular Fe_3O_4 and similar spacings derived from electron diffraction performed over normal magnetite crystallites. The two patterns are identical and comparison of the spacings with those in the literature (1) confirms the material as crystalline Fe_3O_4 with an inverse spinel structure with all the Fe(II) ions in the octahedral sites and half the Fe(III) ions in tetrahedral sites and half the Fe(III) ions in octahedral sites within a cubic close packed array of O^{2-} ions.

Table 5.1 X-ray microprobe analysis data for magnetite-containing vesicles

Sample	Counts above background/100s		
	P	Fe	Fe/P
1	774	6762	8.75
2	1400	10356	7.4
3	510	3652	7.16

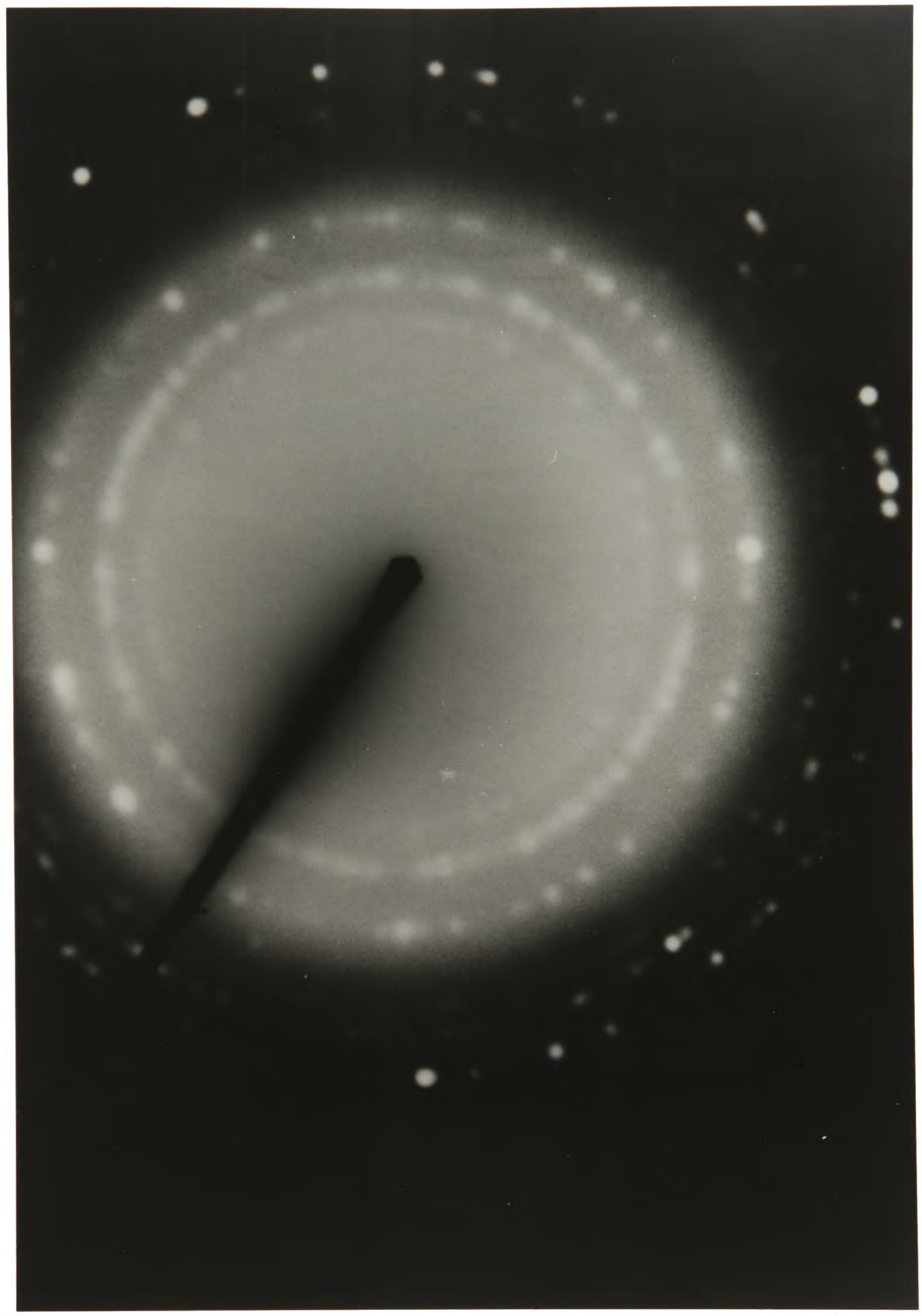

Figure 5.3 Electron powder-diffraction pattern for magnetite-containing vesicles.Camera length 310 cm.

Table 5.2 Calculated d spacings (Å) for; (i) Fe_3O_4 prepared as in section 5.2(1), and (ii) intravesicular Fe_3O_4.

Magnetite	Intravesicular Magnetite	Reference* Magnetite
3.17	3.17	2.96
2.69	2.67	2.53
2.28	2.26	2.42
1.85	1.81	2.1
1.74	1.74	1.71
1.61	1.61	1.60
1.39	1.40	1.48
1.29	1.27	1.28
1.18	1.17	1.12

*d spacings for synthetic, high temperature magnetite (1)

5.2.4 Preliminary n.m.r. studies of magnetite vesicles

Figure 5.4a shows a normal ^1H n.m.r. spectrum recorded with water suppression on a D_2O solution of PC vesicles. Figure 5.4b shows the spectrum recorded from a 1:1 mixture of 'blank' PC vesicles and magnetite-containing vesicles and figure 5.4c shows the spectrum of magnetite vesicles alone. Magnetite, being ferromagnetic, is an exceedingly powerful line broadening agent in n.m.r. experiments (see section 5.2.5). Hence figure 5.4.c shows extensive broadening of the vesicle spectrum with the $N\overset{+}{M}e_3$ and $(CH_2)_n$ chain being the only resonances identifiable. Figure 5.4b is not a superimposition of figures 5.4a and 5.4c since no sharp headgroup or t-Me- resonances are observed. Hence it must be concluded that the intravesicular magnetite can broaden lipid resonances of the 'blank' vesicles which indicates that the range of magnetic perturbation is at least 90Å (two bilayer widths).

This long range perturbation was more clearly observed in the following experiment. A n.m.r. spectrum of sodium citrate (0.1M in D_2O) was recorded (figure 5.5a) and very small aliquots of magnetite vesicles (34mM) were added to the citrate solution. The resulting spectra for $2.5 \times 10^{-3} cm^3$ and $5.0 \times 10^{-3} cm^3$ citrate addition are shown in figures 5.5b and 5.5c respectively. The initial citrate spectrum shows four peaks corresponding to the four inequivalent hydrogen atoms in the citrate ion.

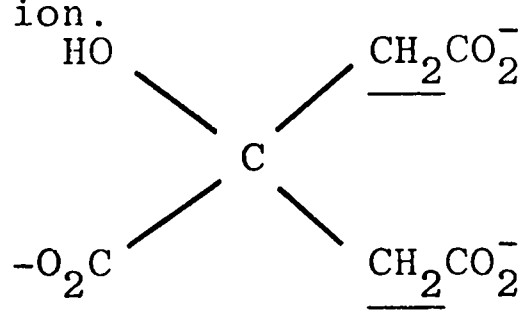

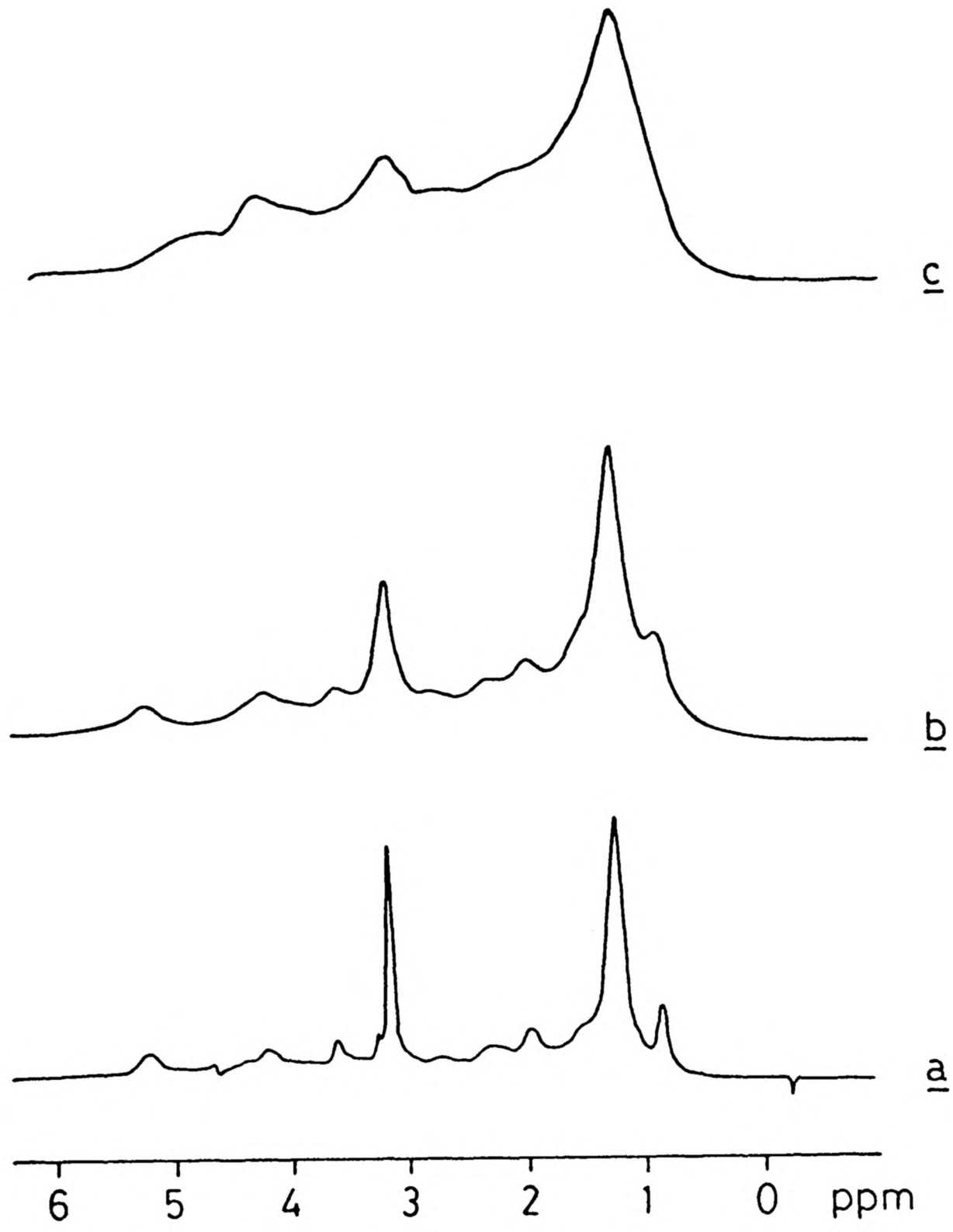

Figure 5.4 ^{1}H n.m.r. spectra; a, 34mM PC vesicles; b, 1:1 mixture of vesicles and magnetite vesicles; c, magnetite vesicles.

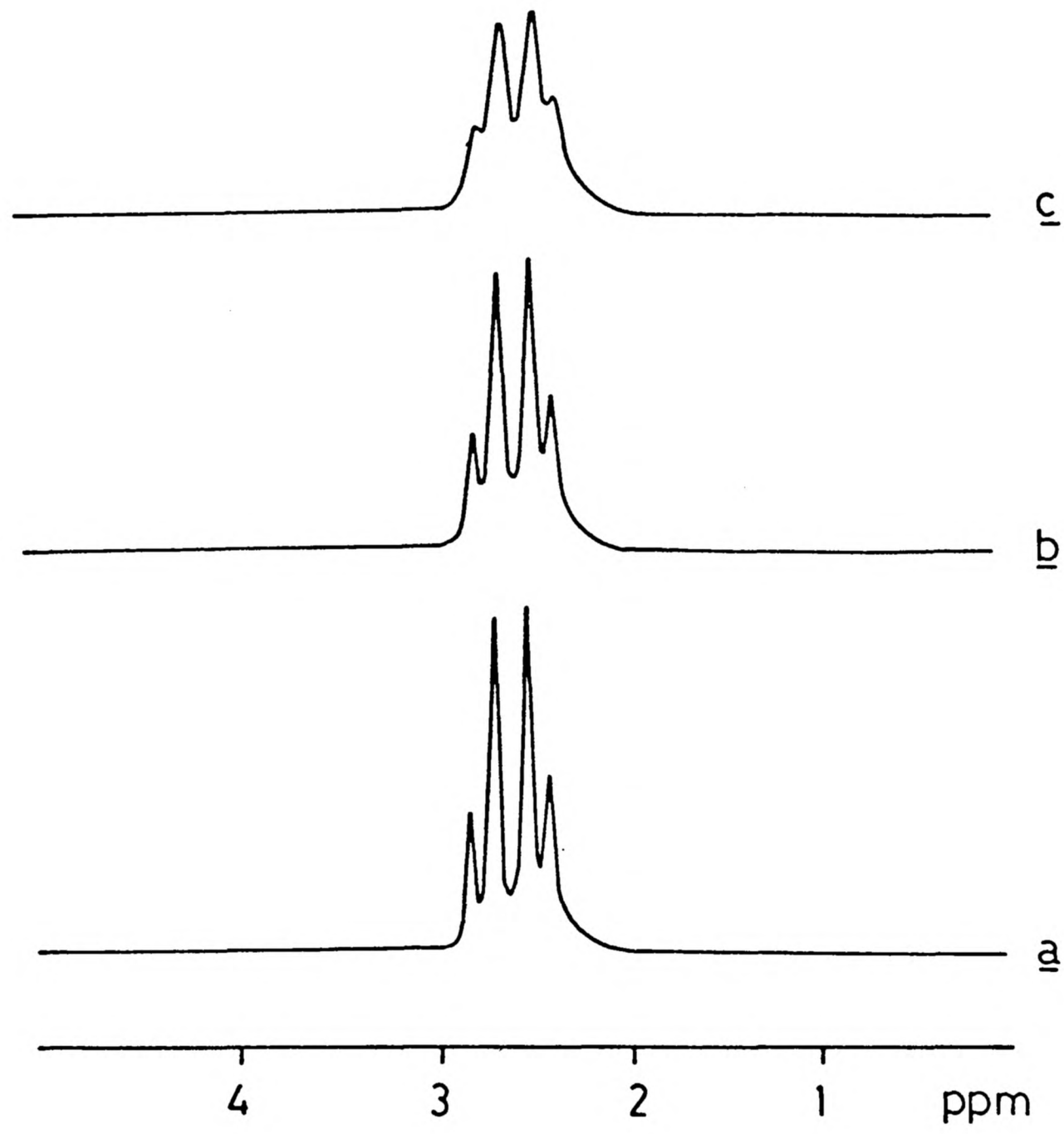

Figure 5.5 ^{1}H n.m.r. spectra of 0.1M sodium citrate solution before and after the addition of magnetite vesicles (34mM); a, 0.1M citrate; b, 0.1M citrate + 2.5 x $10^{-3}cm^{3}$ magnetite vesicles (34mM); c, 0.1M citrate + 5.0 x $10^{-3}cm^{3}$ magnetite vesicles.

Addition of magnetite vesicles increasingly broadens these four resonance positions.

Citrate ions being highly charged will be impermeable to the lipid bilayers so that the magnetic perturbation is over an extremely long distance (microscopically). Similar experiments using ordinary PC vesicles showed no broadening of the citrate resonances (figure 5.6).

This long range magnetic perturbation may have important use in the study of the interaction of proteins with membrane surfaces. The procedure would be to add to a protein, for example cytochrome c, a solution containing magnetite vesicles. The high resolution ^{1}H n.m.r. spectrum of the protein could then be examined for specific broadening of resonances in the protein area close to the binding site with the lipid membrane. Preliminary experiments using this methodology with cytochrome c and PC vesicles have been attempted but only non-specific broadening was observed. This may be due to the protein-lipid binding being very weak in this case. Further experiments need to be done using different lipids, particularly those with negative headgroups such as phosphatidyl-serine which would then increase the protein-binding to the vesicle.

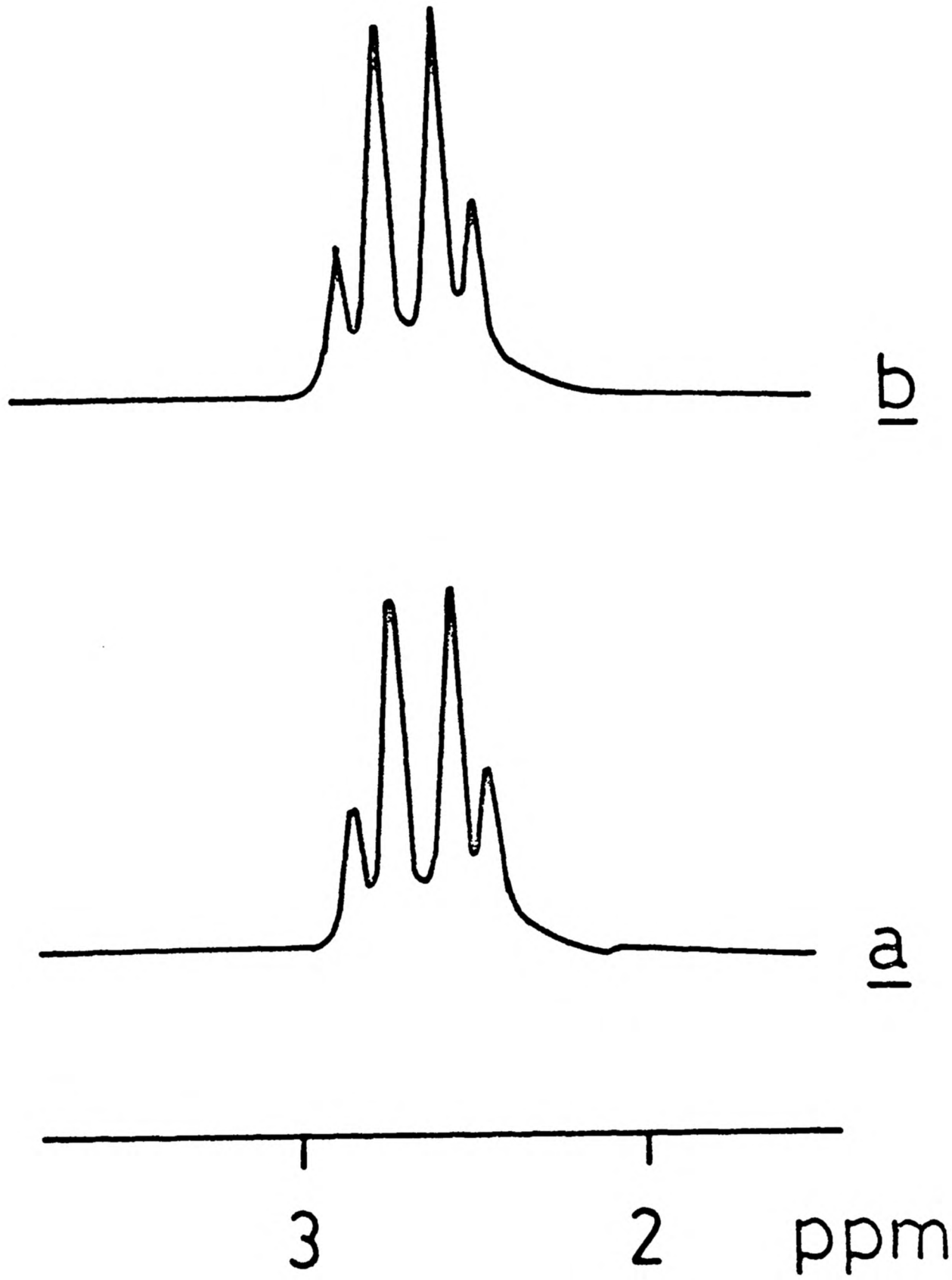

Figure 5.6 ^{1}H n.m.r. spectra of 0.1M sodium citrate solution before and after addition of PC vesicles (34mM); a, 0.1M citrate; b, 0.1M citrate + 7.5 x $10^{-3}cm^{3}$ PC vesicles.

5.2.5 N.m.r. relaxation rate measurements

In the absence of a magnetic field the magnetic moments of a system of nuclei ($I = \frac{1}{2}$) will have random orientations such that the population of the two nuclear energy levels will be equal. When the sample is placed in a magnetic field the nuclei must adopt one of two allowed orientations. At ordinary temperatures the population of the lower energy level is in excess by ca. 1 in 10^5 spins (2). The n.m.r. signal arises when energy is absorbed from the incoming radiation in promoting nuclei from the lower to the higher nuclear energy state. Without relaxation processes this signal would soon die away since the upper energy state would become saturated and the probability of further absorption become very low. Continuous absorption can take place due to the mechanism of spin-lattice relaxation where the energy gained by the nuclei in absorption is lost to the surrounding liquid molecules in thermal motion and the nuclei fall back to the lower nuclear energy state. Thus, spin-lattice relaxation allows the nuclei spin states to have a finite life time (T_1). Because of the uncertainty principle a short T_1 (i.e.a fast spin-lattice relaxation rate $^1/_{T_1}$) will result in a large uncertainty in absorption frequency producing a broad resonance line in the n.m.r. spectrum. The mechanisms that cause relaxation are due to the fluctuating magnetic field in the nuclear environment. There may be magnetic interactions between nuclei and the molecular environment (T_1) or between nuclei themselves (spin-spin relaxation, T_2). Under normal circumstances it is T_2, and not T_1 which determines the intrinsic linewidth.

The presence of unpaired electron spins in paramagnetic

or ferromagnetic ions will cause a large increase in relaxation rate due to the enormous magnetic moments of such species (ca. 10^3 times the magnetic moment of nuclei). The fluctuation of such strong local fields have the effect of decreasing T_1 and T_2 with the effect of increasing the line width of resonances in n.m.r. spectra and this effect is useful in determining the position of groups in the molecules under investigation.

The spin-lattice relaxation times (T_1) of D_2O in the presence of magnetite vesicles were measured by Mr. M. Pye on a Bruker SXP60 spectrometer. The concentration of magnetite in the initial solution of 34mM PC vesicles was measured by flame atomic absorption spectroscopy (Mr J. Kench) and found to be 0.22mM. T_1 values were measured for different concentrations of magnetite. A plot of $^1/T_1$ against the total intravesicular magnetite concentration is shown in figure 5.7a. The relaxation rate is a linear function of magnetite concentration. The gradient of the graph was found to be 1.43 x $10^4 s^{-1}$ M^{-1} at 25°C. The corresponding plot for blank vesicles is shown in figure 5.7b, and has almost zero gradient as expected. The very small effect on $^1/T_1$ on addition of blank vesicles is probably due to the change in solution viscosity on vesicle addition.

Similar results, but with spin-spin relaxation rates ($^1/T_2$) measured for D_2O in the presence of dextran-magnetite particles gave a value of 1.7 x $10^4 s^{-1} M^{-1}$(3) which is ten times that quoted for paramagnetic $MnCl_2$ (1.1 x $10^3 s^{-1} M^{-1}$)(3). Although relative magnitudes of T_1 and T_2 appear the same in this case they are not strictly comparable in any quantitative examination of the data.

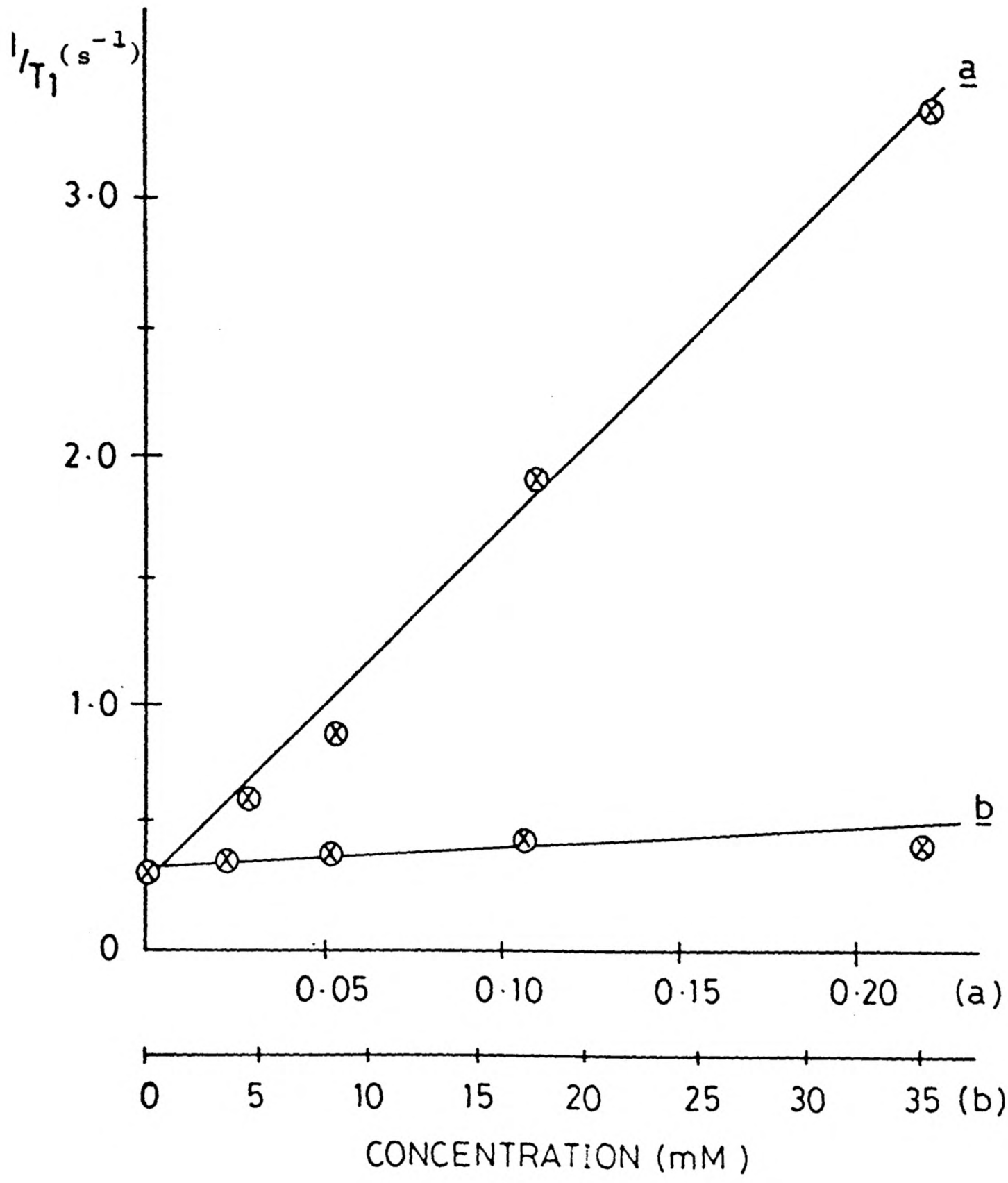

Figure 5.7 Plot of spin-lattice relaxation rates against;
a, total intravesicular magnetite concentration,
b, vesicle concentration (in the absence of magnetite

5.2.6 Magnetite vesicles as a drug carrier system

Liposomes and unilamellar vesicles have been used widely as potential drug carriers. They have been used in anti-cancer therapy (4),(5), in arthritic treatment (6), in leishmaniesis therapy (7) and for oral administration of insulin (8). However the targeting ability of such systems has been found to be low since liposomes are predominantly transported into the liver and spleen (9). Localisation of drug carriers to specific sites would reduce the systemic dose of drug whilst still achieving an effective local concentration of the agent. Efforts to impart specificity in liposome carriers by modifying surface charge (10),(11), and varying vesicle size (11),(12) have not been very successful.

One important use of magnetite vesicles could be in their ability to act as magnetic drug carriers. The increase in specificity of a drug through its localisation using external magnetic fields would be of great value in decreasing unwanted systemic distribution of drugs and also in eradicating localised disease. In order to show that such drug carriers systems can be prepared a test experiment was carried out in which magnetite vesicles were made in the presence of water-soluble K_2PtCl_4 which is related to the anti-cancer drug cis-$Pt(NH_3)_2Cl_2$.

34mM PC and a magnetite suspension were sonicated with 25mM K_2PtCl_4 and the resulting light brown solution was left on a bar magnet at 4^oC for 2 hours and then run down a sephradex G -50 (fine) chromatography column removing any extravesicular K_2PtCl_4.

Samples in the electron microscope showed dark spheres

of mean diameter 15nm (figure 5.8). X-ray microprobe analysis over these areas detected P, Fe, Pt, Cl and K (figure 5.9). Hence the vesicles are intact and contain both the drug analogue and magnetite. Other water soluble drugs could obviously be incorporated in a similar way.

One immediate difficulty with this method is that the encapsulated magnetite particles may be below the critical size for single domain formation and hence will not be fully magnetised (see section 5.2.7). If this is so then larger vesicles can be prepared (13),(14), into which larger magnetite crystallites could be incorporated.

Another problem to be considered is the toxicity of adding fine Fe_3O_4 particulates to the biological system. Other possible carriers of magnetite and drugs are serum albumin microspheres (15),(16),(17), and starch microspheres (18). The main properties of such carriers would be (a) small size (less than ca. 1.5μm) to permit capillary-level distribution and uniform perfusion of the desired target site; (b) adequate magnetic responsiveness to technically achievable local fields and gradients at flow rates found in physiological systems; (c) controllable release rates of the drugs from the carrier at the target site; (d) biodegradability with elimination or minimised toxicity of breakdown products.

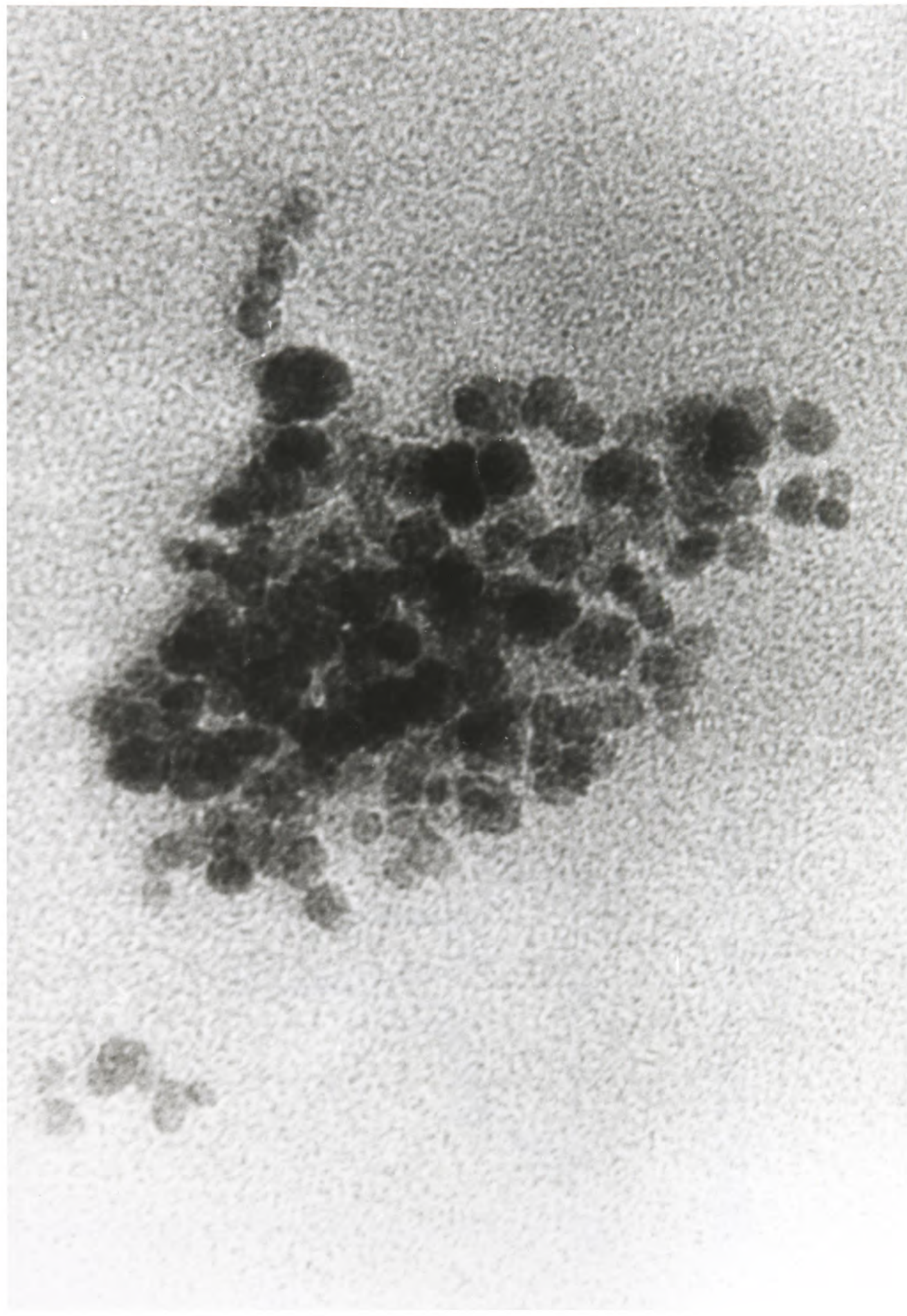

Figure 5.8 Electron micrograph of magnetite vesicles with intravesicular K_2PtCl_4 x535,000.

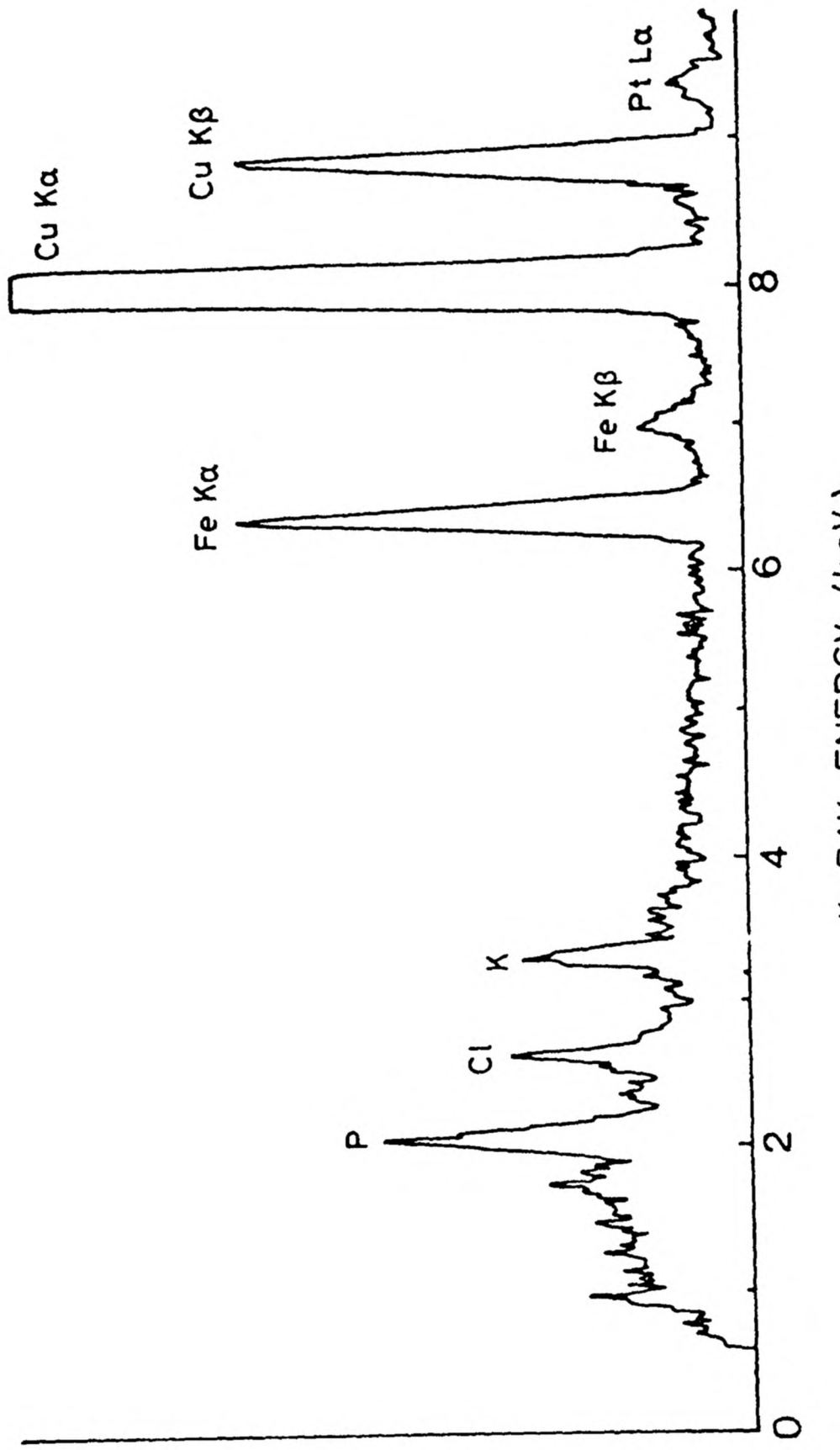

Figure 5.9 X-ray microprobe analysis for magnetite vesicles with intravesicular K_2PtCl_4.

5.2.7 Magnetic responsiveness of magnetite vesicles

It has been noted that the magnetic responsiveness of magnetite-containing vesicles is apparently much lower than for magnetite crystallites in free solution. A very concentrated dispersion of magnetite was sonicated in 34mM PC and left on a bar magnet overnight at $4^{o}C$. The brown supernatent was then placed in the poles of a very strong magnet of field gradient ca. 1.5kG/cm. No magnetic response could be observed after 30 minutes.

It is known that magnetite crystals with dimensions within the single domain size range are efficient and stable carriers of remanent magnetization (19). However, single domain grains occur within a narrow crystal size for magnetite. Previous workers have reported single domain ranges between the limits of 30nm-50nm (20) and 50-76nm (21). Below the lower threshold value, thermal agitation is sufficient to destroy the remanence-carrying capability of such particles and they become superparamagnetic. Above the higher limit, domain structure occurs and the atomic magnetic moments are no longer parallel throughout the particles.

Intravesicular magnetite particles are well below the critical size for single domain formation and therefore will behave as superparamagnetic particles. Being not fully magnetised there will be no visual magnetic response when placed in a magnetic field. Extravesicular particles will be free to aggregate and fuse until a single domain size is reached at which the particles will be fully magnetised and responsive to external magnetic fields. Hence extravesicular magnetite can be separated from intravesicular particles by standing the solution on a bar magnet.

5.3 In situ preparation of intravesicular iron oxides

In the previous section the inclusion of preformed magnetite crystallites into lipid vesicles was described in detail. In this section preliminary attempts to prepare intravesicular Fe_3O_4 and $Fe_2O_3nH_2O$ *in situ* are discussed. It was first necessary to determine whether vesicles could be prepared containing Fe(II) and/or Fe(III) ions. If this was possible then the reaction product obtained after raising the intravesicular pH could then be analysed.

5.3.1 Intravesicular Fe(III) ions in acid and alkaline solution

Vesicles were prepared in the presence of 100mM $FeCl_3$ solution as previously described. Fe(III) ions external to the vesicle compartment were removed by ion exchange or sephradex G-25 chromotography (pH of columns was *ca.* 2.0) and the resulting solution dried onto electron microscope grids. The final pH of the vesicle solution was in the range 2.0-3.0.

The electron micrographs of these unstained preparations show that the vesicles do not contain a simple salt solution but that the Fe(III) ions were adsorbed onto the internal surface of the membrane (figure 5.10). The vesicles are imaged due to the presence of the high electron scattering ability of the Fe(III) ions bound to the lipid membrane. The measured internal diameter is *ca.* 20nm indicating a total vesicle diameter of 30nm for bilayers of 5nm thickness. Fe(III) ions can then act as a very specific stain for these membranes. Combination of this precedure of staining lipid membranes with a paramagnetic ion with n.m.r. spectroscopy of such systems may provide an excellent technique for

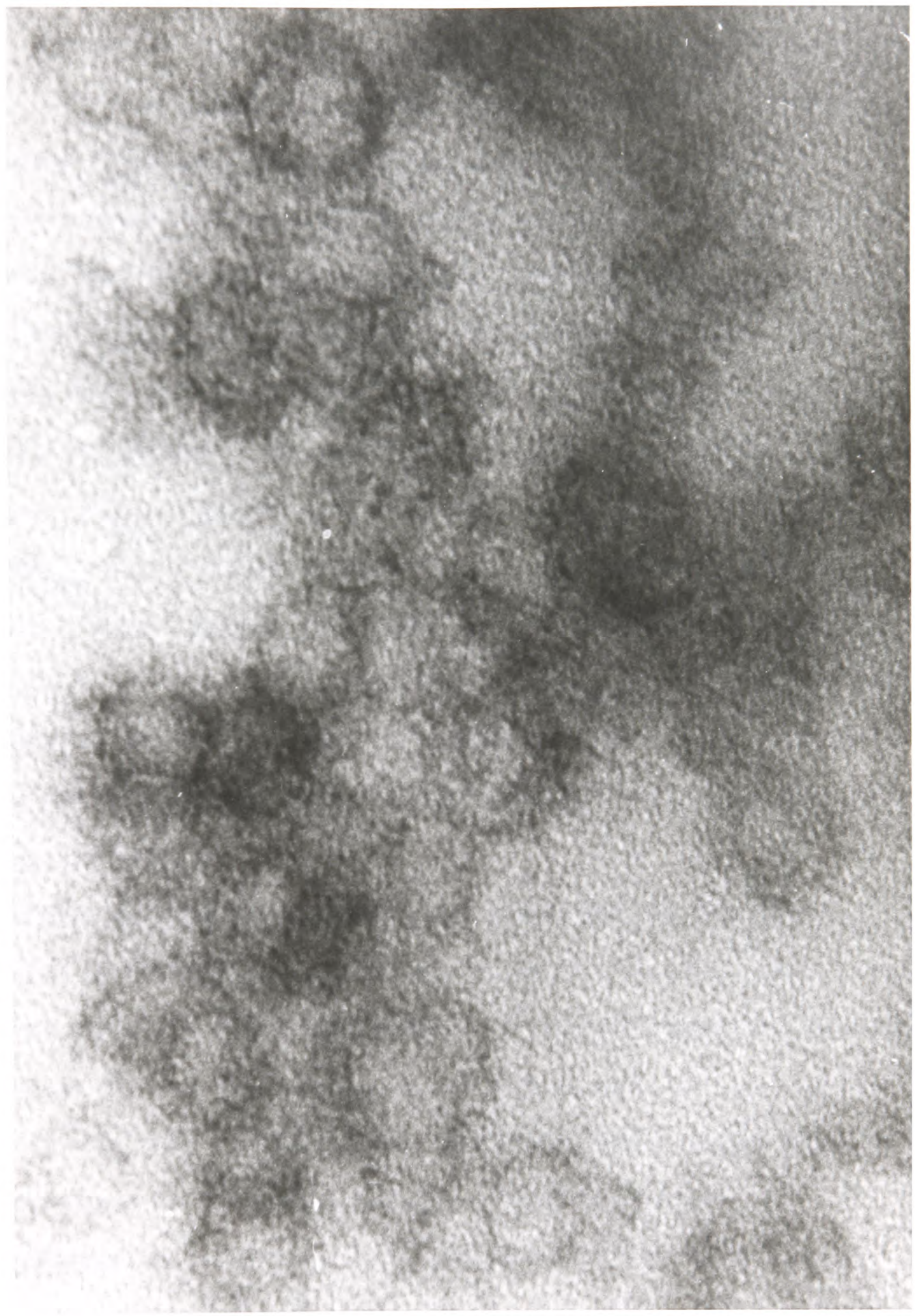

Figure 5.10 Electron micrograph of vesicles containing Fe(III) ions at acid pH x790,000.

probing biological membranes in general (see chapter 7).

X-ray microprobe analysis on these vesicles detected P, Fe, Cl, Na (from the ion-exchange column), S and K (impurities; K_2SO_4?), and Cu (from the grid) (figure 5.11.). Analysis across areas away from the particulates detected only Cu.

The extravesicular pH of these vesicle solutions was then raised by two alternative methods. Firstly pH_{OUT} was raised to ca. 12.5 by addition of strong (1M) NaOH solution. The vesicles were left for at least 30 minutes after which the solution had turned pale yellow. No precipitate was obtained on centrifugation. Secondly, pH_{OUT} was raised with NH_4OH solution increasing the final pH_{OUT} to a value of ca. 10.5. In this case the vesicle solution turns immediately pale yellow due to the rapid penetration of the lipid membrane by $NH_{3(aq)}$ molecules resulting in an almost immediate rise in intravesicular pH. In both methods the resulting pale yellow vesicle solution was dried onto EM grids as before.

Either method of preparation resulted in discrete particulates being imaged in the electron microscope, (figure 5.12), of average diameter 3.5nm. X-ray microprobe analysis over areas of the particulates detected only P, Cl and Fe (figure 5.13a and table 5.3). Analysis over areas away from the particulates detected only Cu from the grid.

Electron diffraction was performed over many areas containing particulates and only weak powder diffraction patterns could be obtained (figure 5.14a).

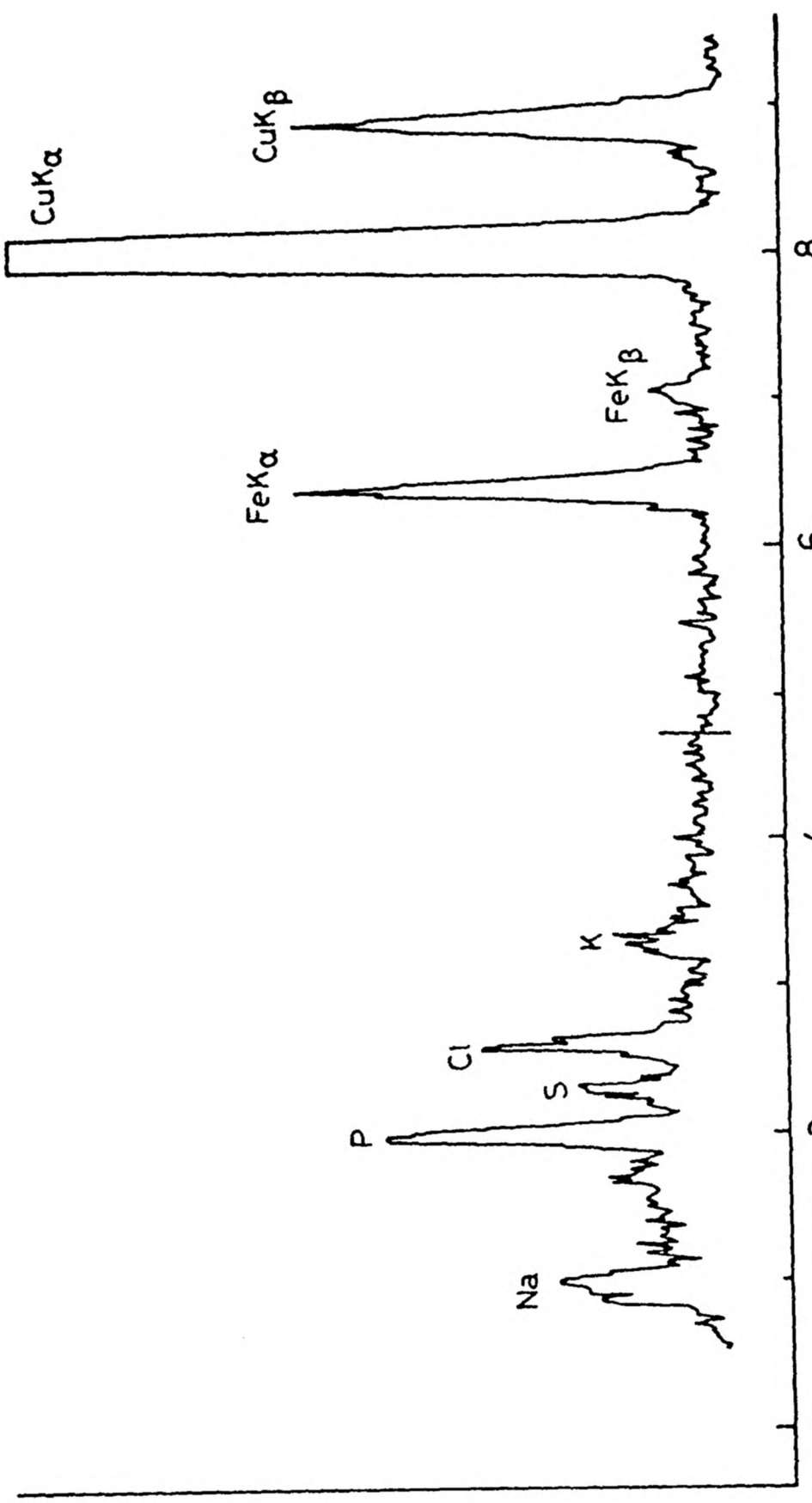

Figure 5.11 X-ray microprobe analysis for Fe(III)-containing vesicles at acid pH.

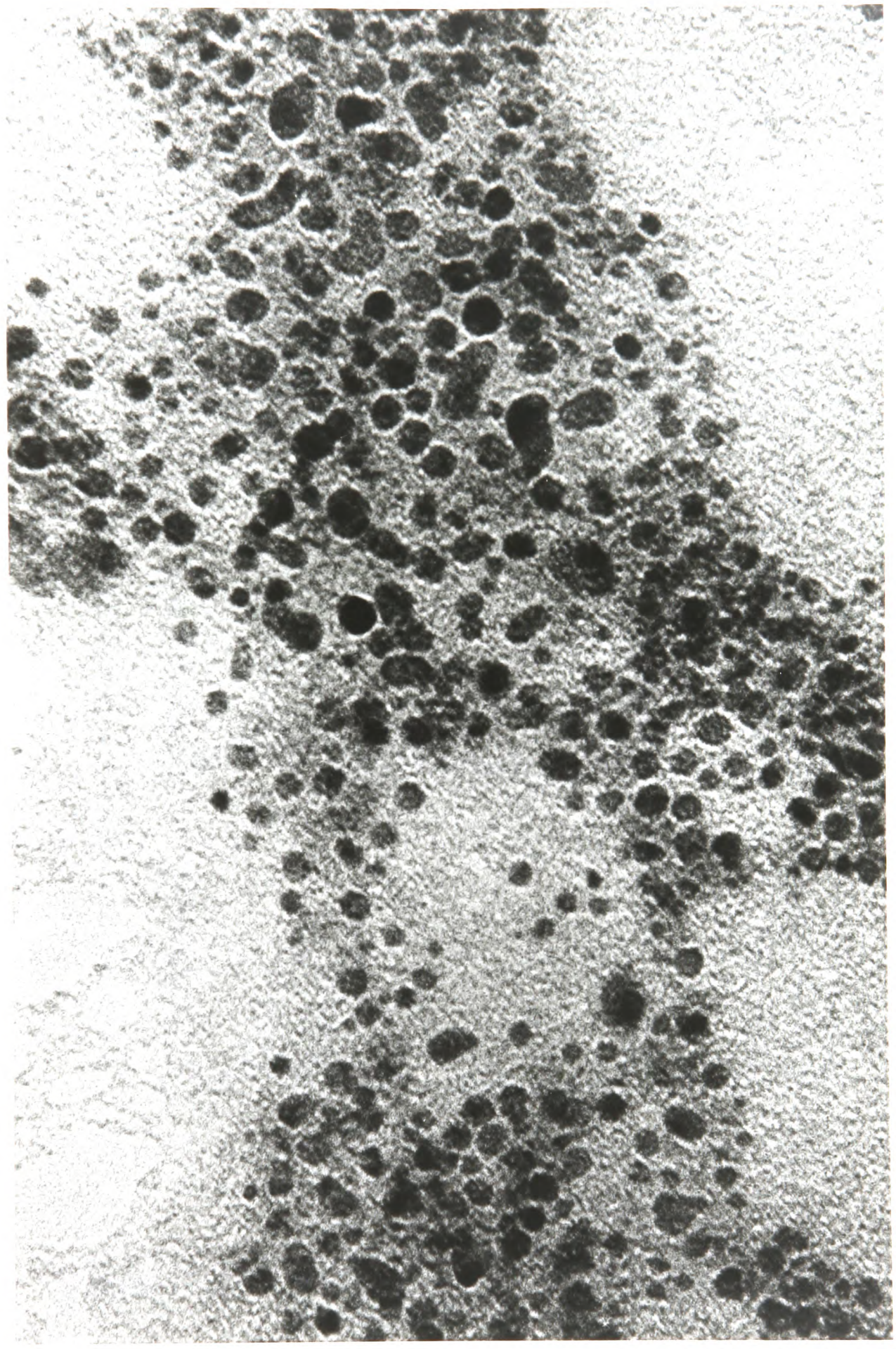

Figure 5.12 Electron micrograph of vesicles containing precipitated FeO(OH) x1,100,000.

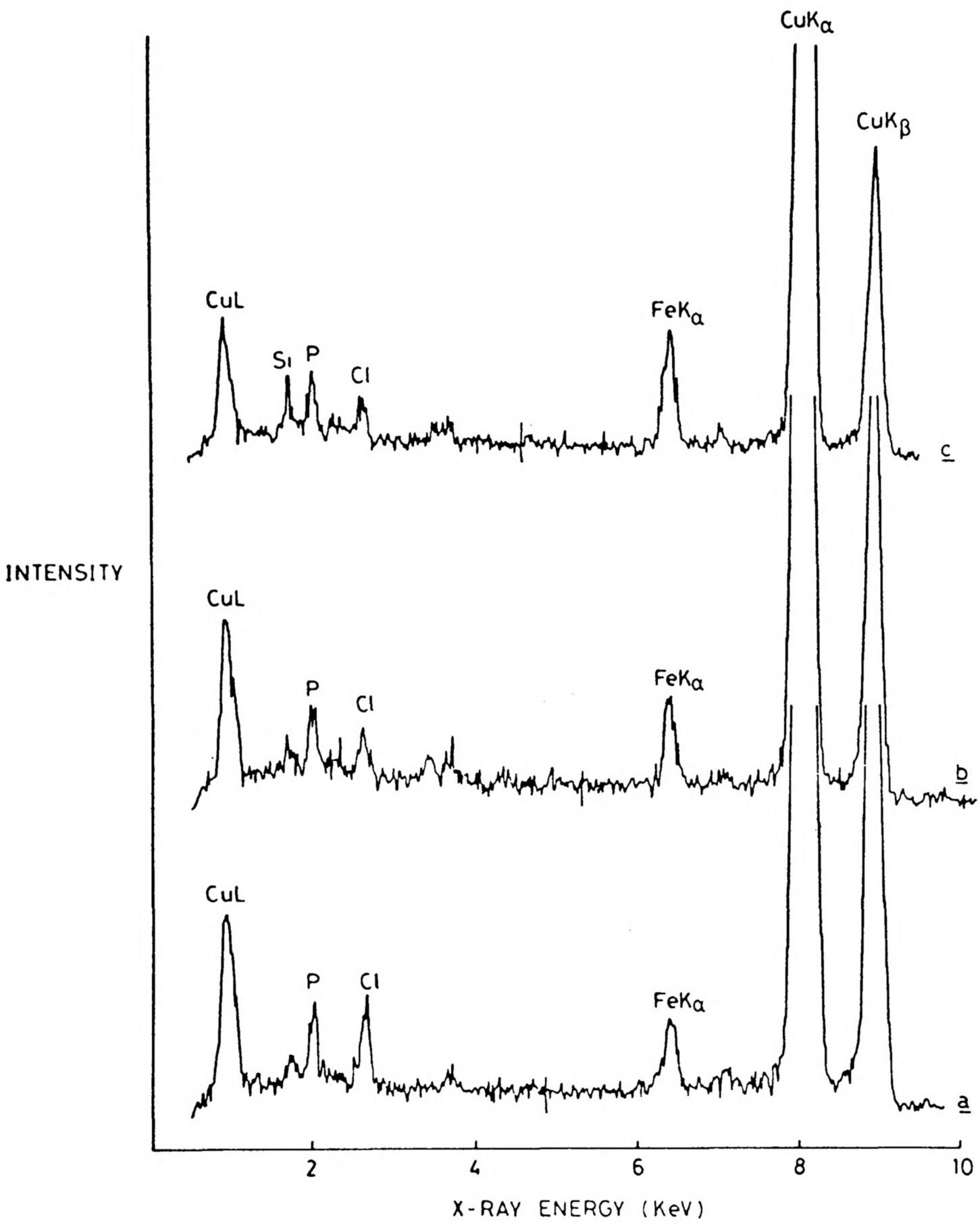

Figure 5.13 X-ray microprobe analysis results for different intravesicular Fe oxide precipitates prepared from; a intravesicular Fe(III) ions; b, intravesicular Fe(II) ions; c, intravesicular Fe(II) and Fe(III) ions.

Table 5.3 X-ray microprobe analysis data for intravesicular precipitates formed from vesicles containing Fe(III), Fe(II), Fe(II) and Fe(III) ions. In each case pH was raised by NaOH solution.

Analysis	Counts above background/100s											
	Fe(III)				Fe(II)				Fe(II)/Fe(III)			
	P	Cl	Fe	Fe/P	P	Cl	Fe	Fe/P	P	Cl	Fe	Fe/P
1	111	149	205	1.85	338	302	478	1.42	104	112	330	3.17
2	129	140	224	1.74	153	117	338	2.20	103	127	478	4.65
3	120	165	202	1.68	338	158	626	1.85	102	72	298	2.92
4	112	171	131	1.18	240	131	408	1.70	84	72	249	2.96
5	114	171	326	2.86	244	169	284	1.17	142	115	699	4.90

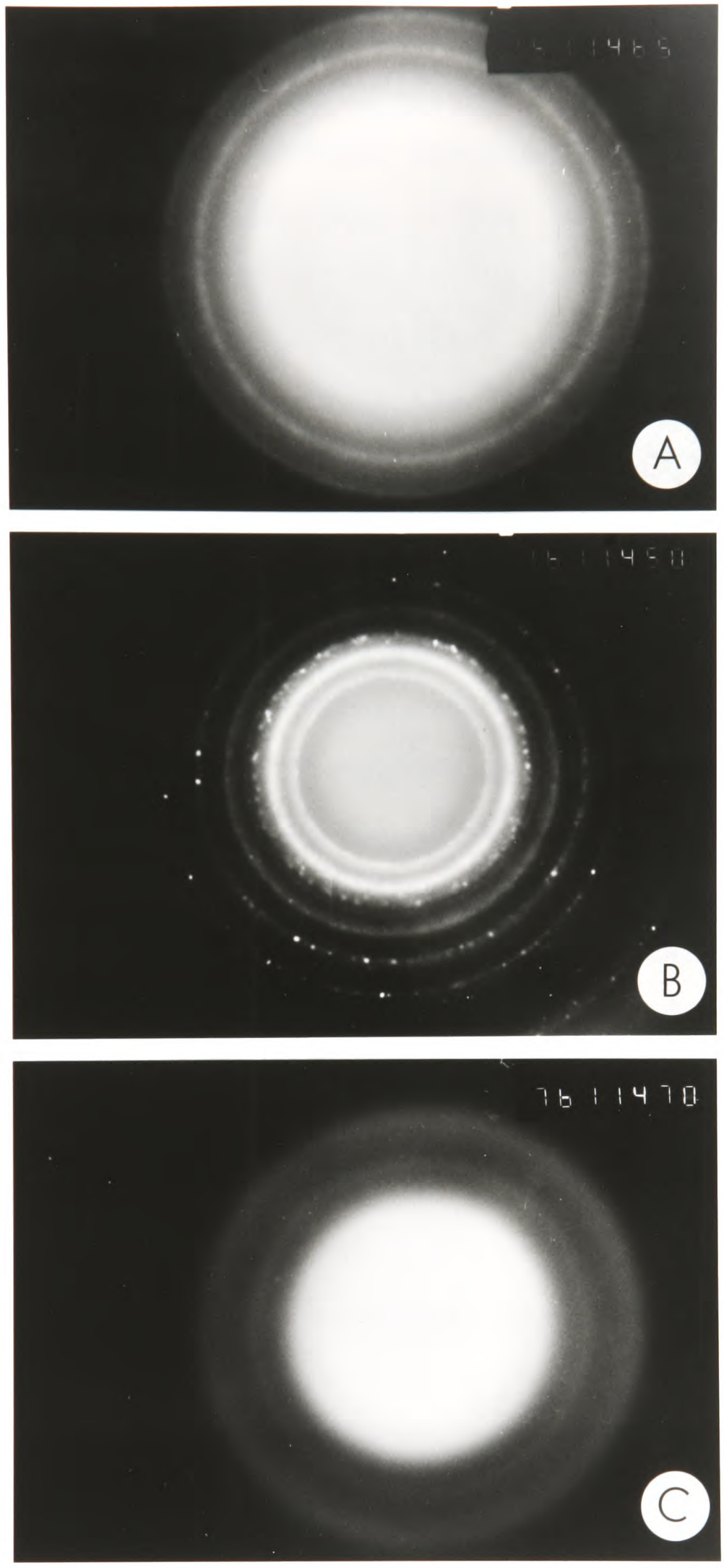

Figure 5.14 Electron diffraction patterns for intravesicular Fe-oxide precipitates; a, FeO(OH) from Fe(III) ions; b, FeO(OH) from Fe(II) followed by air oxidation; c, amorphous material from intravesicular Fe(II)/Fe(III) solution. Camera length in all cases, 98 cm.

5.3.2 Intravesicular Fe(II) ions at alkaline pH

The reaction products arising from the precipitation of intravesicular Fe(II) ions (100mM $FeCl_2$ solution) by either the addition of NaOH or NH_3 solutions were observed to be very similar to the particulates imaged from Fe(III) precipitation (figure 5.15). Mean diameter was 5.5nm. X-ray microprobe analysis over areas of these particulates detected only P, Cl and Fe, none of which were detected in background analyses (figure 5.13b and table 5.3).

Electron diffraction was performed over several areas of particulates and strong powder diffraction patterns were obtained for both methods of precipitation (figure 5.14b). The crystallites were identified as hexagonal FeO(OH) rather than hexagonal $Fe_2O_3nH_2O$ from reference data (22) (table 5.4). Hence intravesicular Fe(II) is oxidised rapidly to Fe(III) as expected in alkaline solution (E^{θ} = -0.56) forming crystalline FeO(OH).

5.3.3 In situ preparation of intravesicular magnetite

In section 5.3.1 and 5.3.2 it was shown that Fe(III) oxides could be prepared within lipid vesicles. A more interesting preparation is *in situ* Fe_3O_4 deposition since this process is closely related to magnetite biomineralisation.

A solution containing 50mM $FeCl_2$ and 50mM $Fe(NO_3)_3$ was sonicated in 34mM lipid and vesicles containing Fe(II) and Fe(III) ions were prepared using the same method as previously described. The intravesicular pH was raised by NaOH or NH_3 solution as before and the resulting solution dried onto EM grids.

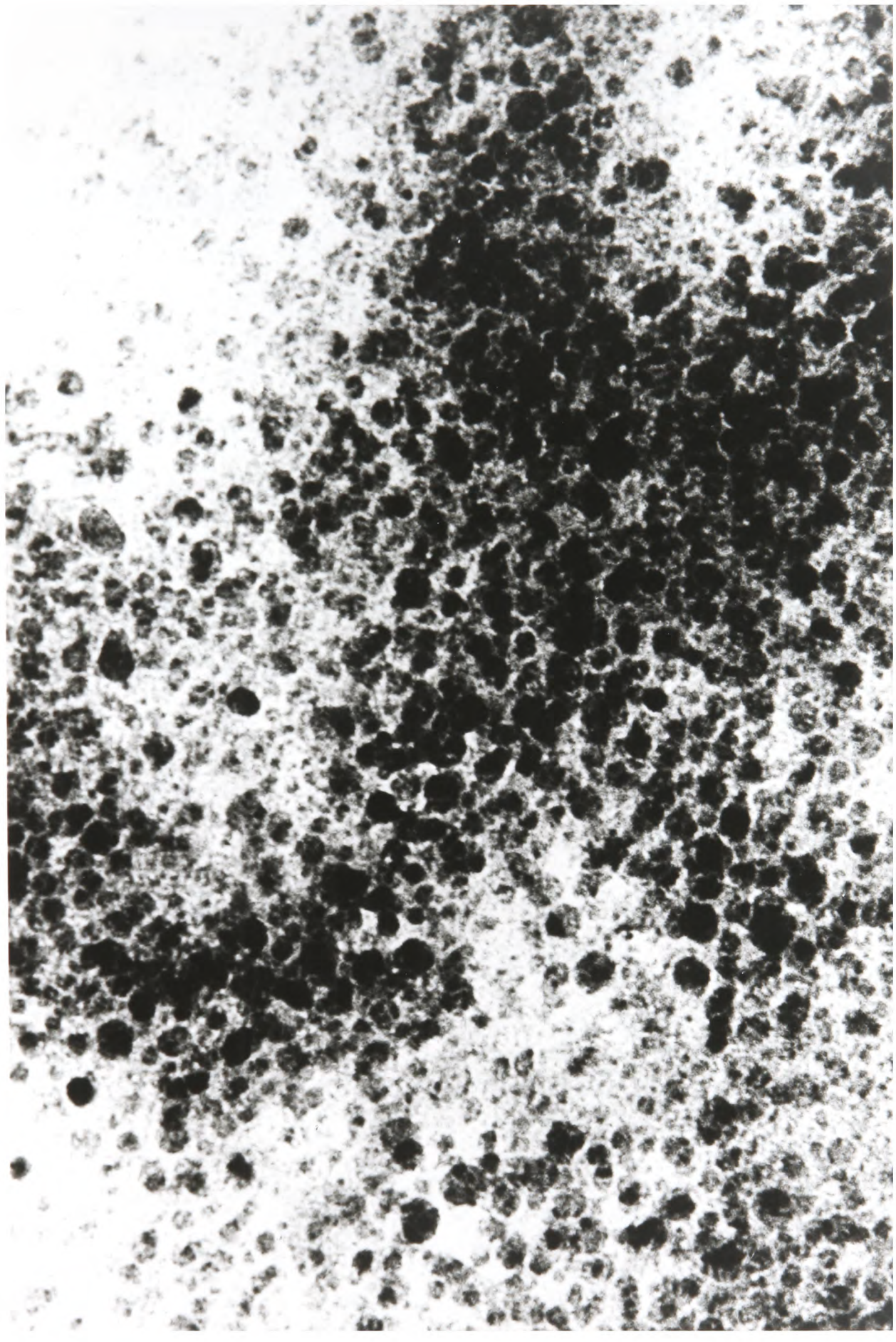

Figure 5.15 Electron micrograph of the reaction product from vesicles containing Fe(II) ions after the addition of NaOH solution x635,000.

Table 5.4 Calculated d spacings in Å for particulates formed from intravesicular Fe(II) precipitation and comparison with known reference solids

Lines of strongest intensity = (str)

Intravesicular solid	$FeO(OH)$ [22]	$Fe_2O_3nH_2O$ [23]
		10.9 (str)
	4.61	5.49 (str)
		3.65 (str)
2.58 (str)	2.55 (str)	2.74
2.29 (str)	2.25 (str)	2.66
1.87		2.46
1.61 (str)	1.68 (str)	1.71
1.34 (str)	1.47 (str)	1.56
	1.27	
1.15	1.22	
	1.104	
0.875		

Images observed in the electron microscope from both methods of preparation were similar to those discussed previously. Small particulates (4-6nm in diameter) were observed, generally low in contrast against the carbon background of the support film (figure 5.16). Figure 5.13c and table 5.3 show X-ray microprobe analysis data recorded over the areas described above. The Si peak is an impurity on the grid since background analysis also detected this peak. The mean Fe/P ratio (3.53) is much greater than for particulates formed from Fe(III)-containing (1.66) and Fe(II)-containing vesicles (1.57). It is not clear why this should be. The ratio Fe/P is not strictly comparable between different samples because the thickness of sample areas may differ and is unknown. The results seem to imply that there is a greater encapsulating efficiency in the presence of Fe(II) and Fe(III) ions than in a solution of either species alone. However this is not supported by the particulate sizes which do not differ significantly.

Electron diffraction was performed over many areas of these images and no powder diffraction patterns could be obtained (figure 5.14c). The material precipitated is then amorphous.

5.4 Discussion

The inclusion of preformed magnetite crystallites within lipid vesicles has been shown to be possible and the potential use of this system as a n.m.r. probe and drug carrier has been discussed. Alternatively intravesicular Fe oxides can be prepared and in each case the particulates formed are of small uniform size (figure 5.17). Particle diameters in the

Figure 5.16 Electron micrograph of the reaction product from vesicles containing Fe(II) and Fe(III) ions after the addition of NaOH solution x670,000.

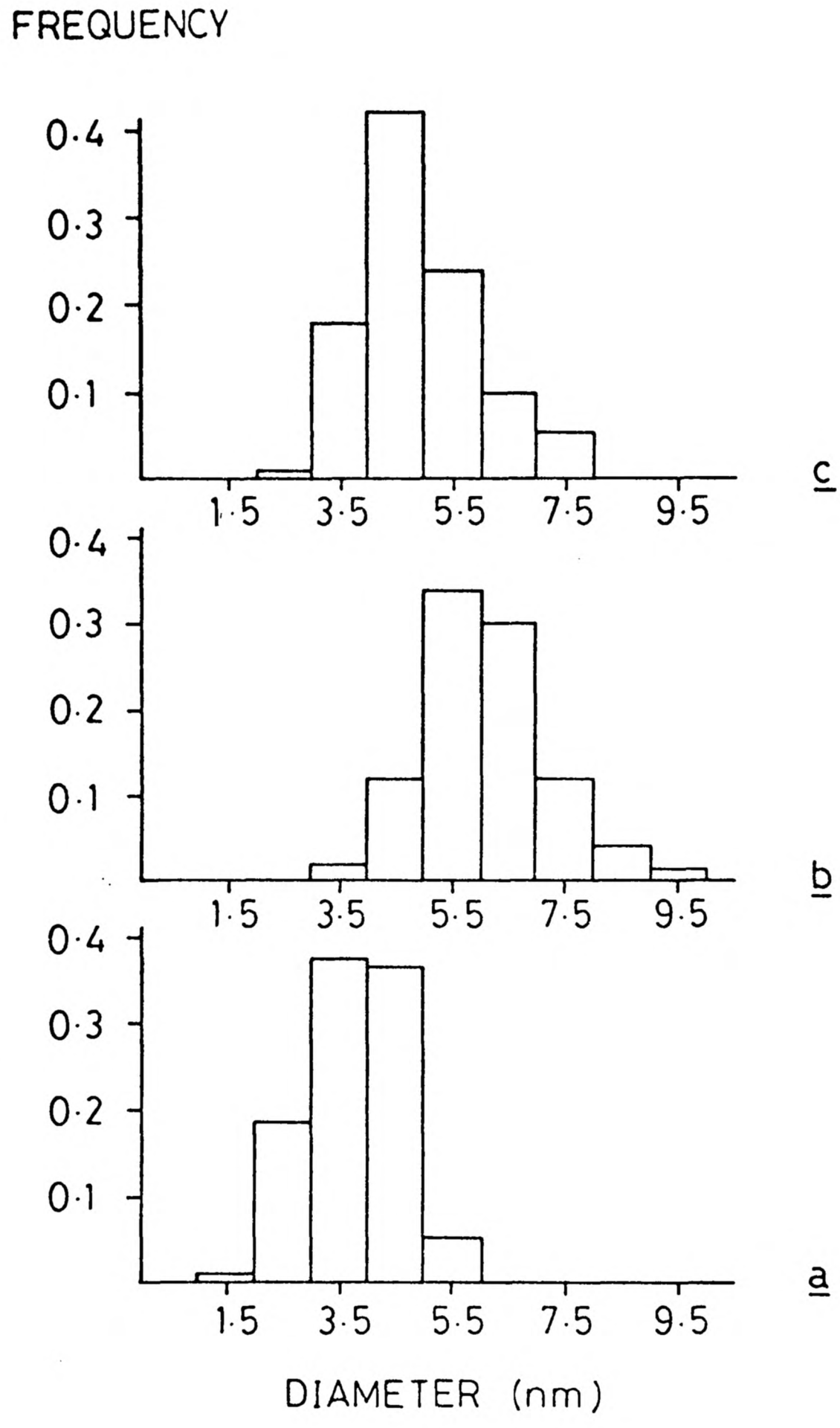

Figure 5.17 Particle size distribution; histograms for intravesicular Fe oxides prepared from vesicles containing; a, Fe(III) ions (100mM); b, Fe(II) ions (100mM); c, Fe(II) (50mM) and Fe(III) (50mM) ions.

range 4-6nm are frequently observed for initial solutions 100mM in concentration. Hence very small discrete particulates can be prepared by intravesicular precipitation.

Vesicles containing Fe(II) or Fe(III) ions can be used to prepare intravesicular FeO(OH). This process is similar to that found in biological systems eg. ferritin formation. In the former case the final reaction product occurs via rapid air oxidation of the initially formed Fe(II) hydroxide resulting in well defined crystallites of FeO(OH). With intravesicular Fe(III) ions the precipitate formed is mainly amorphous although weak powder diffraction patterns have been obtained. The discrepancy in these observations may possibly be explained by the fact that phosphate is known to inhibit the crystallisation of amorphous ferric hydroxide to hematite ($Fe_2O_3nH_2O$) (24) presumably by the linking of ferric hydroxide particles in an immobile network and by the inhibition of crystal growth by phosphate groups adsorbed onto nucleating sites on the crystal surface (25). A similar effect may well occur in the case of Fe(III) ions bound near to a lipid surface of phosphate headgroups.

For a vesicle system containing both Fe(II) and Fe(III) ions the final precipitate is amorphous whereas under the same conditions in the absense of lipid, crystalline magnetic Fe_3O_4 is obtained. It is thus not a simple chemical procedure to prepare intravesicular Fe_3O_4, unlike the case for intravesicular Ag_2O (chapter 3). This is important when considering a biological system in which crystalline Fe_3O_4 is to be deposited. A simple concentration gradient of Fe(II) and Fe(III) ions across a lipid compartment would not suffice as a mechanism for magnetite deposition since there will be

preferential adsorption of Fe(III) onto the membrane surface (assuming the presence of negative sites). This may explain why intravesicular Fe_3O_4 is not formed. Raising pH_{IN} will remove Fe(II) and Fe(III) ions from the lipid surface and incorporate them within a solid matrix. The binding constants for Fe(II) and Fe(III) with phosphate headgroups will be different, Fe(III) being preferentially adsorbed so that Fe(II) ions will be removed first on OH^- addition. Thus there is the possibility that Fe(II) ions removed from the headgroup will be oxidised before a sufficiently large enough concentration of Fe(III) ions reaches the solid state for the formation of an inverse spinel structure to occur.

Another explanation is that magnetite formation is favoured at higher pH values than ferric hydroxide precipitation. In aqueous solution $Fe_2O_3nH_2O$ precipitation occurs at pH values between 3.0 and 5.0 whereas magnetite formation requires a minimum pH of ca. 8.0. Intravesicular pH will not be equal to pH_{OUT} since (from chapter 3) there will be a pH gradient of ca. 4.5 units on OH^- addition to the external phase of the vesicles. Hence at a pH_{OUT} of 13.0 pH_{IN} will be ca. 9.5. Alternatively, addition of NH_4OH to a pH_{OUT} of ca. 10.5 implies an approximate pH_{IN} of the same value. However the rate of increase of intravesicular pH may be slow enough to favour substantial Fe(III) hydroxide formation before crystalline magnetite can be precipitated. That the final reaction product is amorphous indicates that the growth of such precipitates in a mixed Fe(II)/Fe(III) system takes place without the possibility of long range ordering being established.

Further experiments are required in order to characterise these intravesicular precipitates more accurately. One immediate possibility is to use Mössbauer spectroscopy in order to identify the Fe oxidation and spin states in different vesicle systems. Possible problems are that the content of ^{57}Fe (2% natural abundance) will be very small in the samples analysed. Also the effect of very low temperature on the vesicle system would have to be considered.

This chapter is an introduction to the preparative chemistry of intravesicular Fe oxides. It seems most likely that biology must use more sophisticated systems than the one used in this chapter in order to deposit a material such as magnetite. The mode of deposition most likely contains a template for selective Fe(II) and Fe(III) binding. However no such components of biological magnetite have yet been observed.

5.5 References

(1) ASTM Powder Diffraction File 19-629, 1972.

(2) Dwek R. N.M.R. in Biochemistry, Clarendon, Oxford 1973.

(3) Ohigushi M, Nagayama K, Wada A. J. Mag.Res. 29, 599-601 1978.

(4) Gregoriadis G, Neerunjun E.D., Biochem Biophys. Res. Commun. 65, 537- 544, 1975.

(5) Rahman Y, Cerny E.A., Tollaksen S.L., Wright B., Nance S.L., Thomson J.R., Proc.Soc.Exp.Biol.Med., 146, 1173-1176, 1974.

(6) de Silva M. et al., Lancet i, 1320-1322, 1979.

(7) Alving C.R., Steck E.A., et al. Proc.Natl.Acad.Sci., 75, 2959-2963, 1978.

(8) Patel H.M., Ryman B.E., FEBS Lett. 62, 27-32, 1976.

(9) Gregoriadis G., Nature 265, 407-411, 1977.

(10) Gregoriadis G., Neerunjun E.D., Biochem. Biophys.Res. Commun. 47, 179-185, 1974.

(11) Juliano R.L., Stamp D., Biochem. Biophys. Res. Commun. 63, 651-658, 1975.

(12) Gregoriadis G., Ryman B.E., Eur.J.Biochem. 24, 485-491, 1972.

(13) Weder H., et al. Biochem. Biophys. Acta. 512, 147-155, 1978.

(14) Enoch H.G., Strittmatter P.Proc.Nat. Acad. Sci. 76, 145-149, 1979.

(15) Widder K.J., Senyei A.E., Scarpelli D.G., Proc.Soc.Exp. Biol.Med. 58, 141-146, 1978.

(16) Widder K., Flouret G., Senyei A., J. Pharm.Sci. 68, 79-82, 1979.

(17) Senyai A., Widder K., Czerlinski G., J.Appl.Phys. 49(6), 3578-3583, 1978.

(18) Mosbach K., Schröder U., FEBS Letts 102, 112-116, 1979.

(19) Néel L., Ann.Geophys. 5, 99-136, 1949.

(20) Dunlop D.J., J.Geophys.Res. 78, 1780-1793, 1973.

(21) Butler R.F., Banerjee S.K., J.Geophys. Res. 80, 4049-4058, 1975.

(22) ASTM Powder Diffraction File 13-87, 1972.

(23) ASTM Powder Diffraction File 13-92, 1972.

(24) Schwertmann U., Geoderma 3, 207-213, 1970.

(25) Cornell R.M., Schwertmann U., Clays and Clay Minerals 27, 402-410, 1979.

CHAPTER 6

INTRAVESICULAR PRECIPITATION OF Co(II) AND Ag(I) SALTS

6.1 Introduction

In this chapter a brief account is given of several further intravesicular precipitation reactions which have been successfully carried out. The precipitation products illustrate that the method of preparing intravesicular deposits can be utilised for many different reaction schemes provided that one of the reactants is permeable in some form to the membrane. In each case electron microscopy was used to image and characterise the reaction products. A range of amorphous and crystalline intravesicular particulates of very small size can be prepared.

6.2 Intravesicular silicates

6.2.1 Intravesicular Co(II) silicate

In chapter 4 a biological system was described in which amorphous silica was deposited in intracellular vesicles. In order to model this precipitation system initial attempts were made to prepare intravesicular particulates by the general reaction scheme;

$$SiO^{2-}_{3OUT(aq)} \longrightarrow SiO^{2-}_{3IN(aq)}$$

$$M^{n+}_{IN(aq)} + SiO^{2-}_{3IN(aq)} \longrightarrow M_2(SiO_3)_{n,IN(s)}$$

It was expected that silicate ions of the type SiO^{2-}_3 at pH ca. 12.0 would be impermeable to the membrane because of

their high charge. At lower pH (for $Si(OH)_4$, pK_1= 7.8, pK_2 = 11.8) the species $HSiO_3^-$ and $Si(OH)_4$ should be able to penetrate into the internal compartment of the vesicles.

In order to test this hypothesis 34mM PC was sonicated in a D_2O solution of 100mM $CoCl_2$ and the external Co(II) ions removed by cation ion-exchange chromotography. The ^1H n.m.r. spectrum of these vesicles showed two resonance positions for the NMe_3^+ headgroup corresponding to the internal and external environments (figure 6.1a). The internal NMe_3^+ peak was shifted upfield to a position of 3.15 ppm by the internal paramagnetic Co(II) ions bound to the membrane surface. The external NMe_3^+ peak was at 3.32 ppm. Addition of 30 x 10^{-3} cm^3 of 100mM Na_2SiO_3 solution (pH 11.5) turned the vesicle solution light-blue. This resulted in the coalescence of the NMe_3^+ peaks with the external NMe_3^+ resonance remaining unchanged (figure 6.1b). (There was a slight downfield shift of the whole vesicle spectrum due to pH change but the relative positions of all groups except $NMe_{3_{IN}}^+$ remained unchanged). The slight shoulder of the NMe_3^+ peak disappeared when the spectrum was recorded 20 minutes later (figure 6.1c).

These results show that Co(II) ions bind to the inner surface of the membrane and are subsequently removed from this environment and incorporated into a solid phase within the vesicles by addition of silicate. However, these experiments are not conclusive in that they give little information about the nature of the intravesicular solid except that it contains Co(II). At a pH_{OUT} of 11.5 there must be competition between OH^- and $HSiO_3^-/SiO_3^{2-}$ ions for the intravesicular Co(II). The relative rates of anion

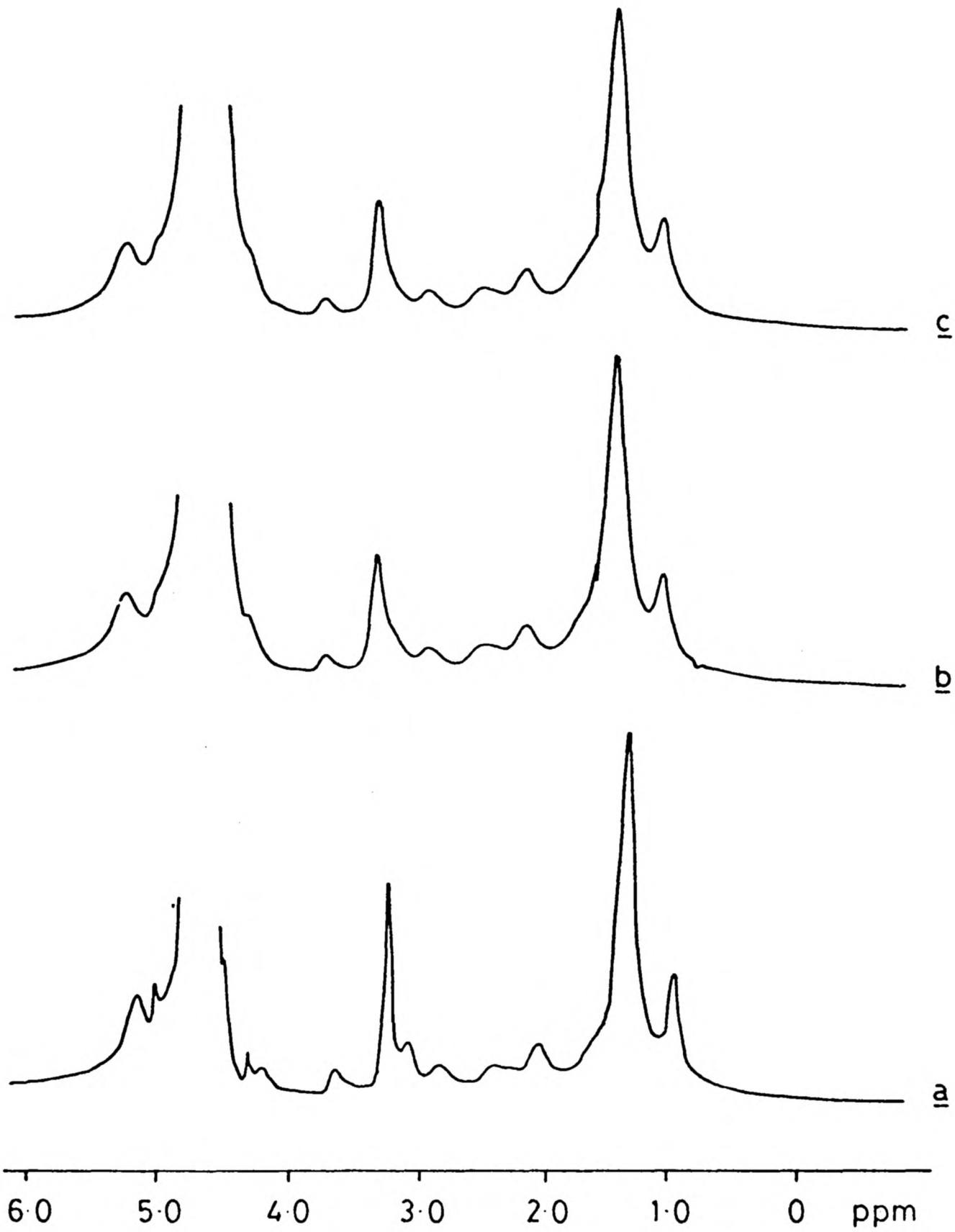

Figure 6.1 ^{1}H n.m.r. spectra of vesicles containing Co(II) ions (100mM); a, spectrum before addition of Na_2SiO_3(aq); b, spectrum recorded immediately after addtion of 30 x $10^{-3}cm^3$ of 100mM Na_2SiO_3; c, spectrum b recorded after 20 minutes.

permeability and solubility products of $Co(OH)_2$ and $CoSiO_3$ will determine which solid is precipitated.

Electron microscopy and X-ray microprobe analysis were used to determine the chemical species present in these intravesicular particulates. Precipitates prepared from an initially sonicated Co(II) solution of 200mM showed very diffuse aggregated regions in the electron microscope (figure 6.2a). Careful examination of these regions showed circles of low contrast material (see arrows on figure 6.2a) which were similar in appearance to those images observed for intravesicular Fe(III) ions in acid pH (chapter 5, figure 5.10). The diameter of these rings is ca. 25nm. There is a large degree of error in this measurement since the images were very diffuse and low in contrast.

X-ray microprobe analysis performed over areas such as in figure 6.2a detected Si, P, Cl, Co and Cu in these regions (figure 6.3a and table 6.1). None of these elements was detected in the background analysis except Cu from the grid. The intravesicular solid is then Co(II) silicate and not $Co(OH)_2$. Hence there is an accumulation of SiO_3^{2-} ions by some mechanism in the inner compartment of the vesicles.

Similar preparations were made using a 400mM $CoCl_2$ solution for sonication. In this case it was possible to observe dense spheres, diameter ca. 25nm in the electron microscope which were mostly aggregated (figure 6.2b). X-ray microprobe analysis detected Si, P, Cl and Co from these areas.

Electron diffraction was attempted over many vesicle regions and only very diffuse rings could be observed. Hence the intravesicular material is amorphous.

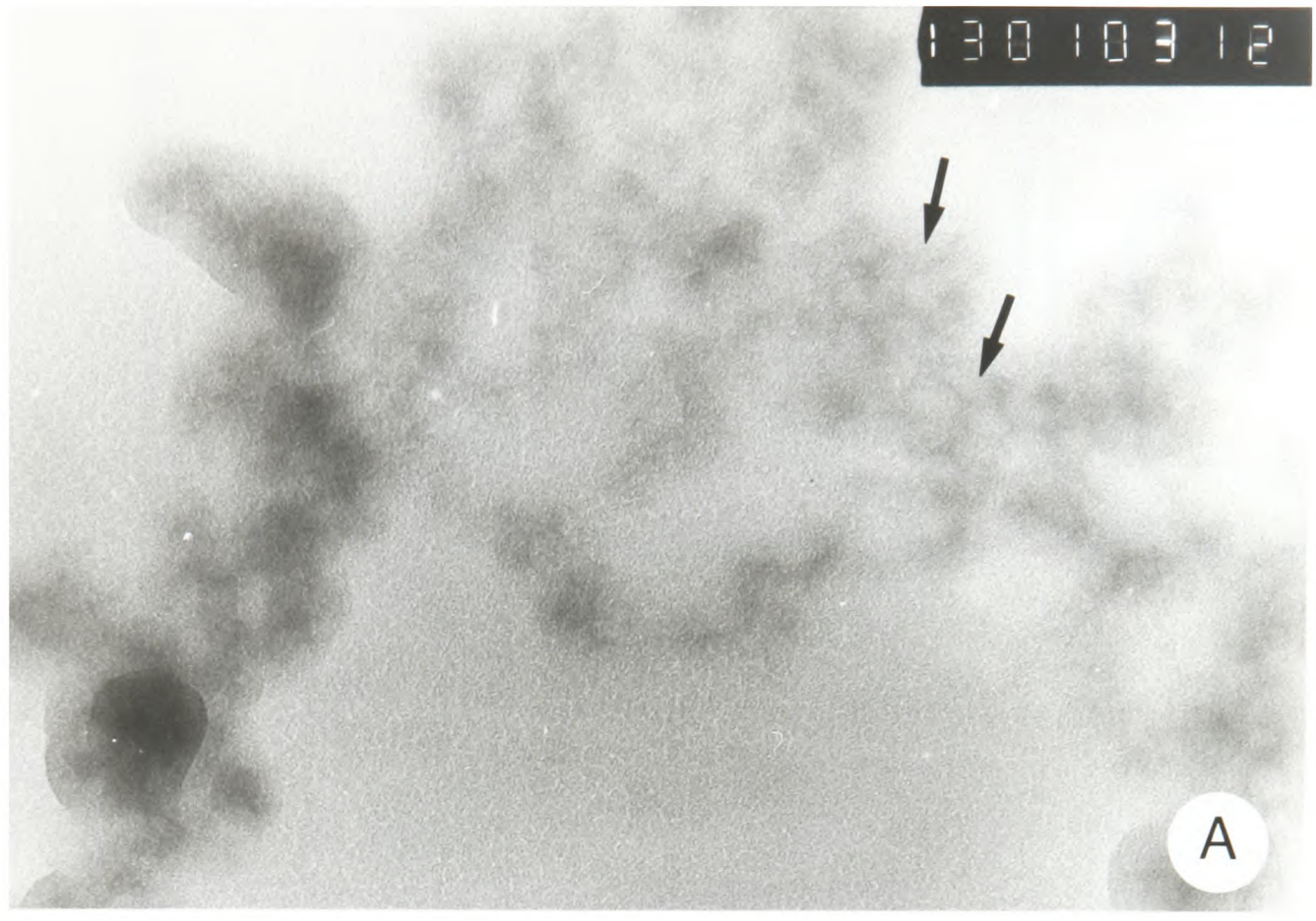

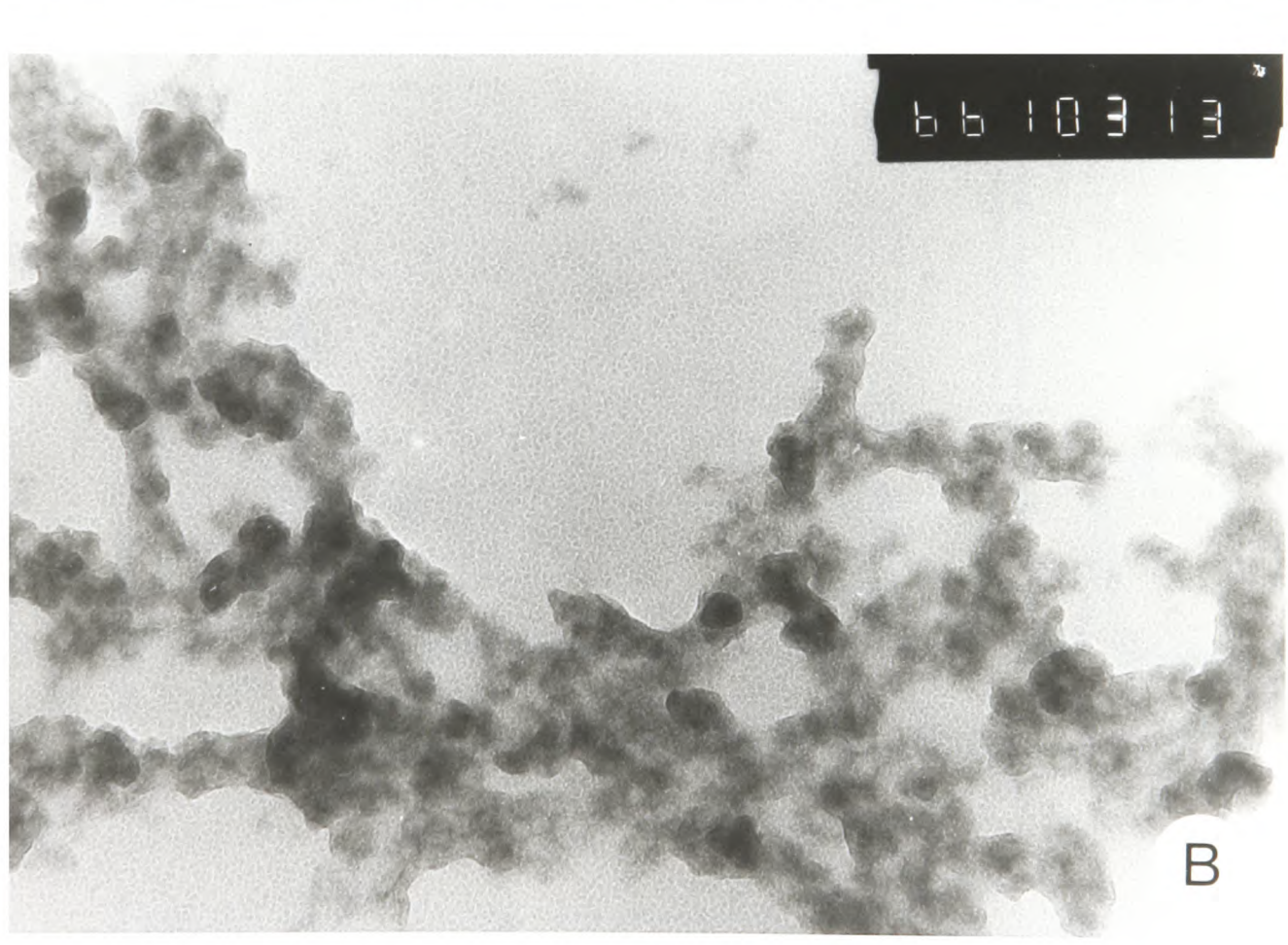

Figure 6.2 Electron micrographs for Co(II) silicate vesicles;a,particulates prepared from 200mM Co(II) solution;b,particulates prepared from 400mM solution.Arrows indicate rings of electron-dense material.
a,x242,000; b,x120,000.

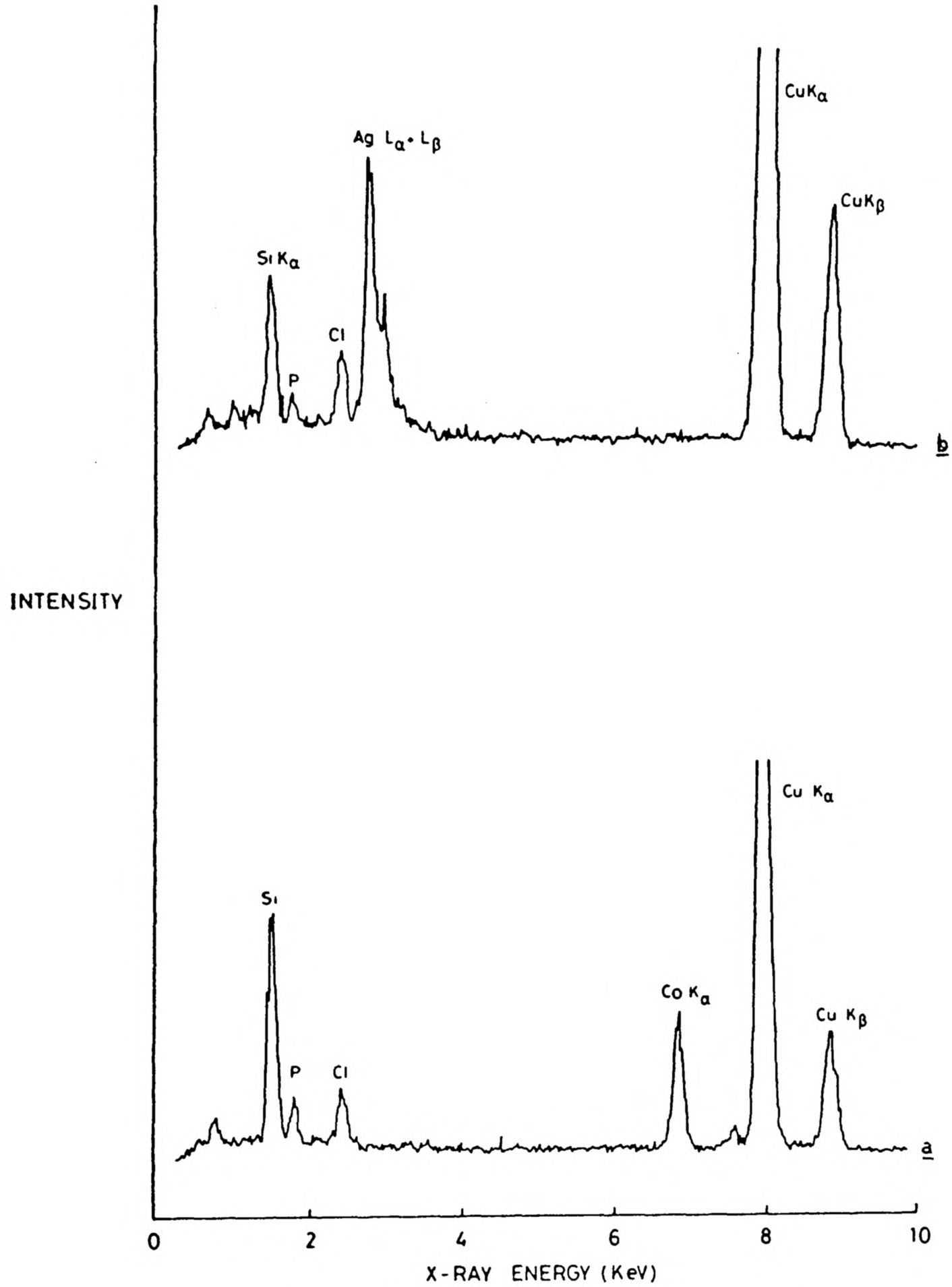

Figure 6.3 X-ray microprobe analysis for silicate-containing vesicles; a intravesicular $CoSiO_3$; b, intravesicular Ag_2SiO_3

Table 6.1 X-ray microprobe analysis data for intravesicular silicates;

a, $CoSiO_3$; b, Ag_2SiO_3

a	Sample	Counts above background/100s			
		Si	P	$Co(K_\alpha)$	Co/Si
	1	351	289	182	0.52
	2	683	192	553	0.78
	3	3414	592	2424	0.71
	4	2596	300	1820	0.70

b	Sample	Si	P	$Ag(L_\alpha + L_\beta)$	Ag/Si
	1	387	95	480	1.24
	2	870	356	1118	1.36
	3	445	201	681	1.53
	4	372	244	542	1.45

Similar experiments with Co(II) silicate prepared in the absence of lipid showed similar amorphous structures in electron diffraction experiments.

6.2.2 Intravesicular Ag(I) silicate

250mM $AgNO_3$ solution was sonicated in the presence of 34mM PC and the resulting vesicle solution passed down a cation ion-exchange column to remove extravesicular Ag(I) ions. Addition of 1 drop of 250 mM Na_2SiO_3 solution (pH 11.5) resulted in the vesicle solution turning pale yellow in colour. No precipitate was observed on centrifugation.

Corresponding images in the electron microscope were very different from those observed for intravesicular $CoSiO_3$. Electron dense discrete particulates could be imaged over many areas of the grid. Figure 6.4 shows a group of particulates 20-24nm in diameter. Thickness fringes can be observed running across one particulate. Notice also that around two other particulates membrane structures appear to be resolved of thickness ca. 3nm. These may be artefactual but an alternative explanation would be that the lipid membrane is 'stained' by SiO_3^{2-} ions.

X-ray microprobe analysis over areas of these spheres detected Si, P, Cl, Ag and Cu (from the grid) (figure 6.3b and table 6.1). The Cl peak is an impurity from solid Na_2SiO_3 since particles formed from $AgNO_3$ and Na_2SiO_3 solutions in the absence of lipid were also found to contain this element as well as Si and Ag when analysed in the electron microscope.

Electron diffraction was performed over areas of intravesicular particulates and weak powder diffraction

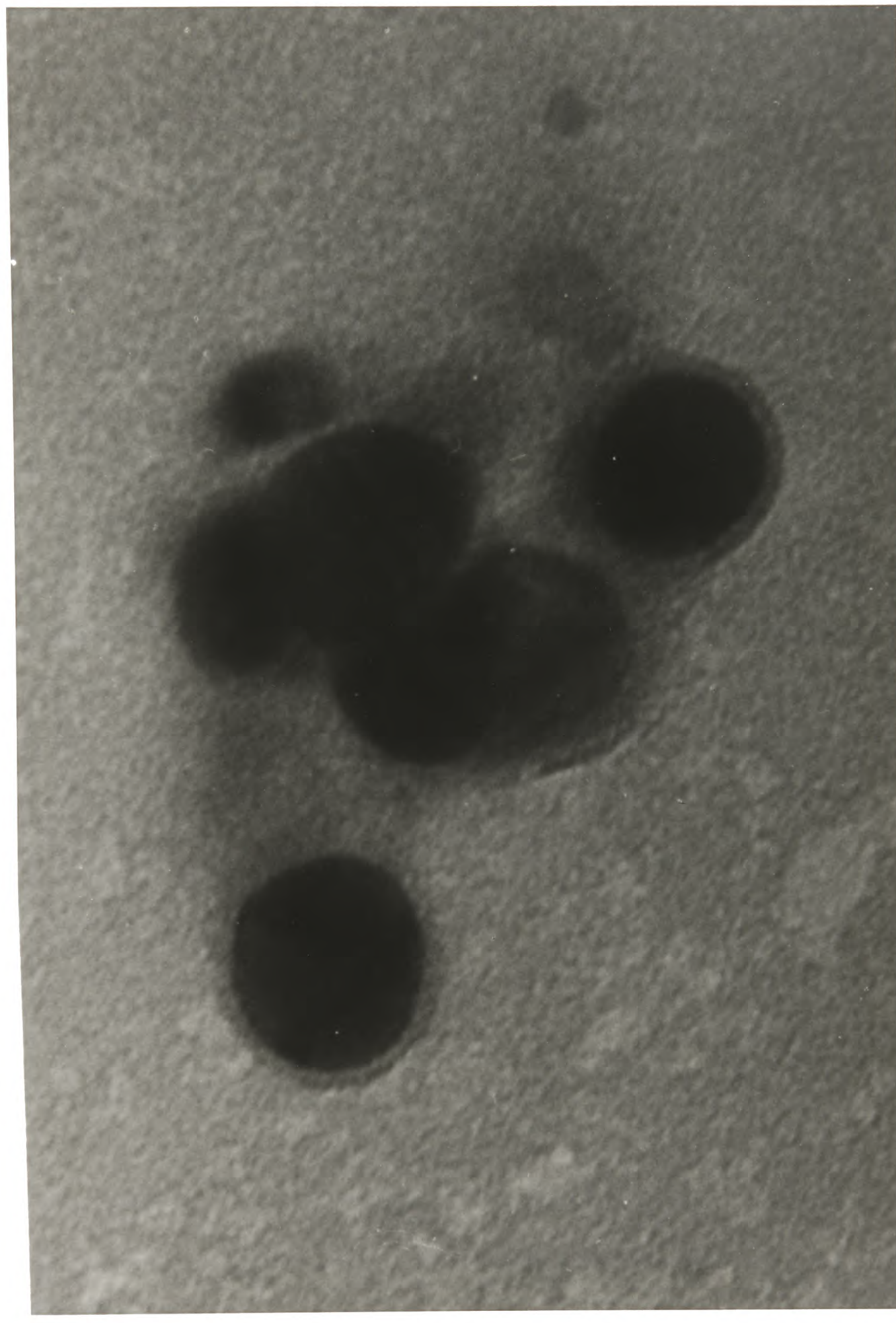

Figure 6.4 Electron micrograph of intravesicular Ag_2SiO_3 particulates x1,100,000.Membrane structures are resolved around two of the particles.

patterns were obtained. These were compared with those recorded from a sample of Ag_2SiO_3 prepared in the absence of lipid (figure 6.5). Spacings were calculated in both cases and were found to be the same for both types of particulates (table 6.2). It is concluded from reference data (1) that the intravesicular deposits are crystalline orthorhombic Ag_2SiO_3.

6.3 Intravesicular Co(II) hydroxide

In chapter 3 the intravesicular precipitation of crystalline Ag_2O was described in detail. In this section a similar process, the preparation of intravesicular $Co(OH)_2$, is described. In section 6.2.1 the intravesicular deposition of amorphous $CoSiO_3$ was reported and included electron micrographs not previously observed for intravesicular deposits. What then would the images of intravesicular $Co(OH)_2$ look like in the electron microscope?

Vesicles containing Co(II) ions (200 mM) were prepared as in section 6.2.1 and extravesicular Co(II) ions removed as before. Intravesicular pH was then raised by the addition of NaOH to a final pH_{OUT} value of 12.5. The vesicle solution was left for 30 minutes before samples were dried onto EM grids.

From chapter 3, (section 3.4, figure 3.8) ^1H n.m.r. spectroscopy has shown that OH^- ions penetrate the membrane removing Co(II) ions from the internal lipid surface. Images of the reaction product in the electron microscope showed very diffuse regions of low contrast (figure 6.6). Several regions appeared to contain circles of an electron dense material (see arrows on figure 6.6). The diameters of these images are difficult to calculate due to their low contrast. They

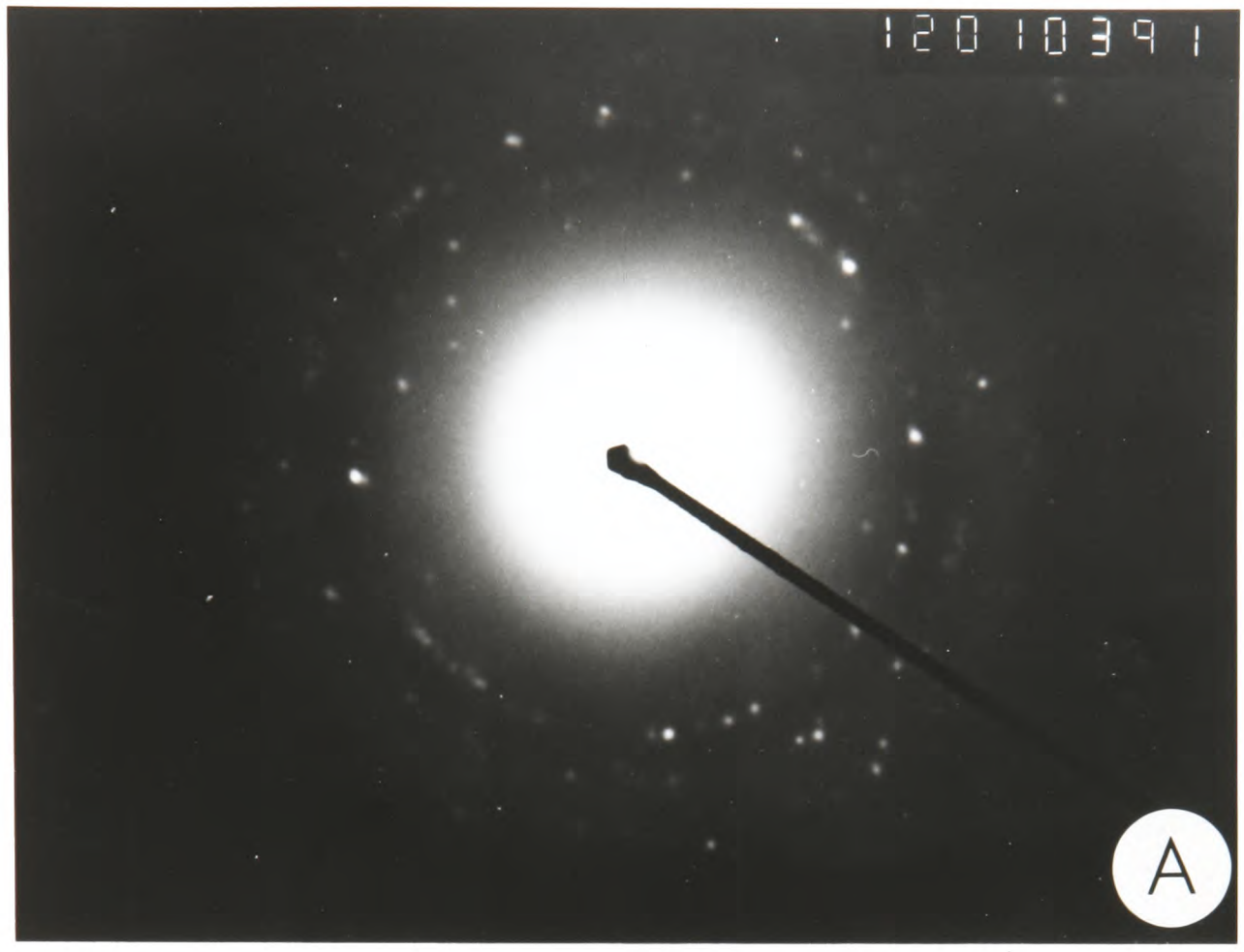

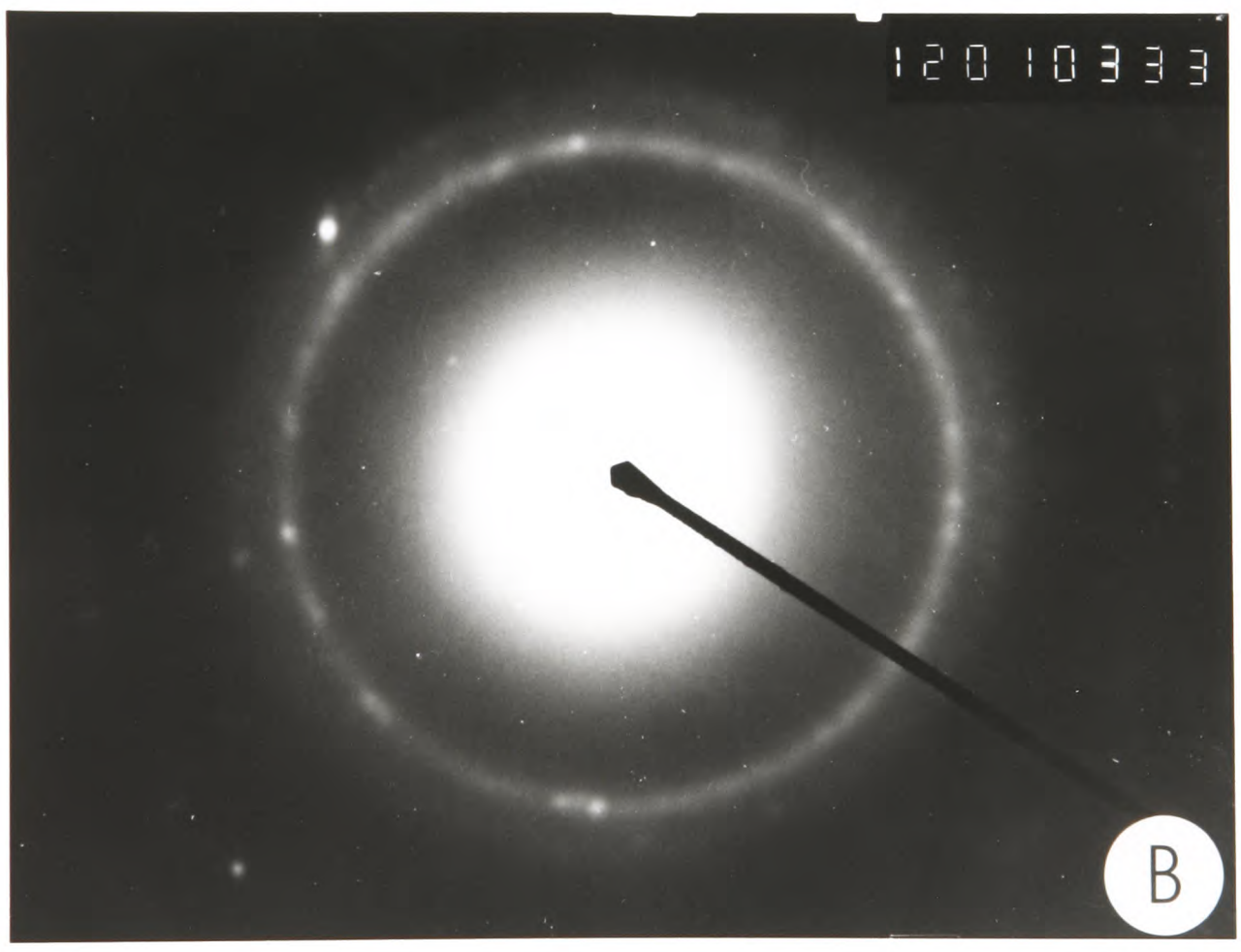

Figure 6.5 Electron diffraction patterns for; a, intravesicular Ag_2SiO_3; b, Ag_2SiO_3 prepared in the absence of lipid. Camera length in both cases, 230 cm.

Table 6.2 Calculated d spacings (Å) for; a, intravesicular Ag_2SiO_3 and b, Ag_2SiO_3 prepared in the absence of lipid

a	b
2.58	
2.20	2.22
1.87	1.87
1.32	1.34
1.14	1.11

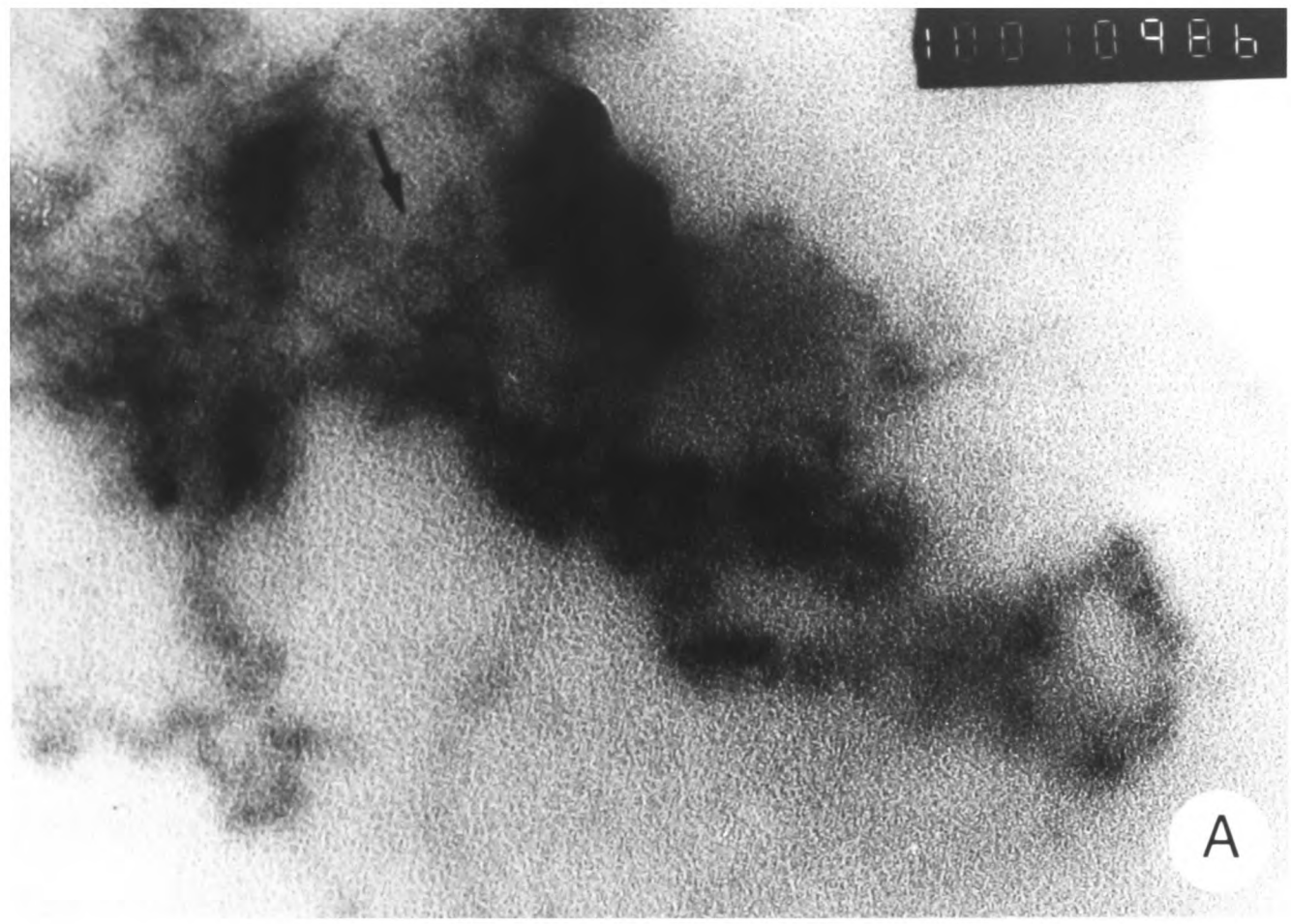

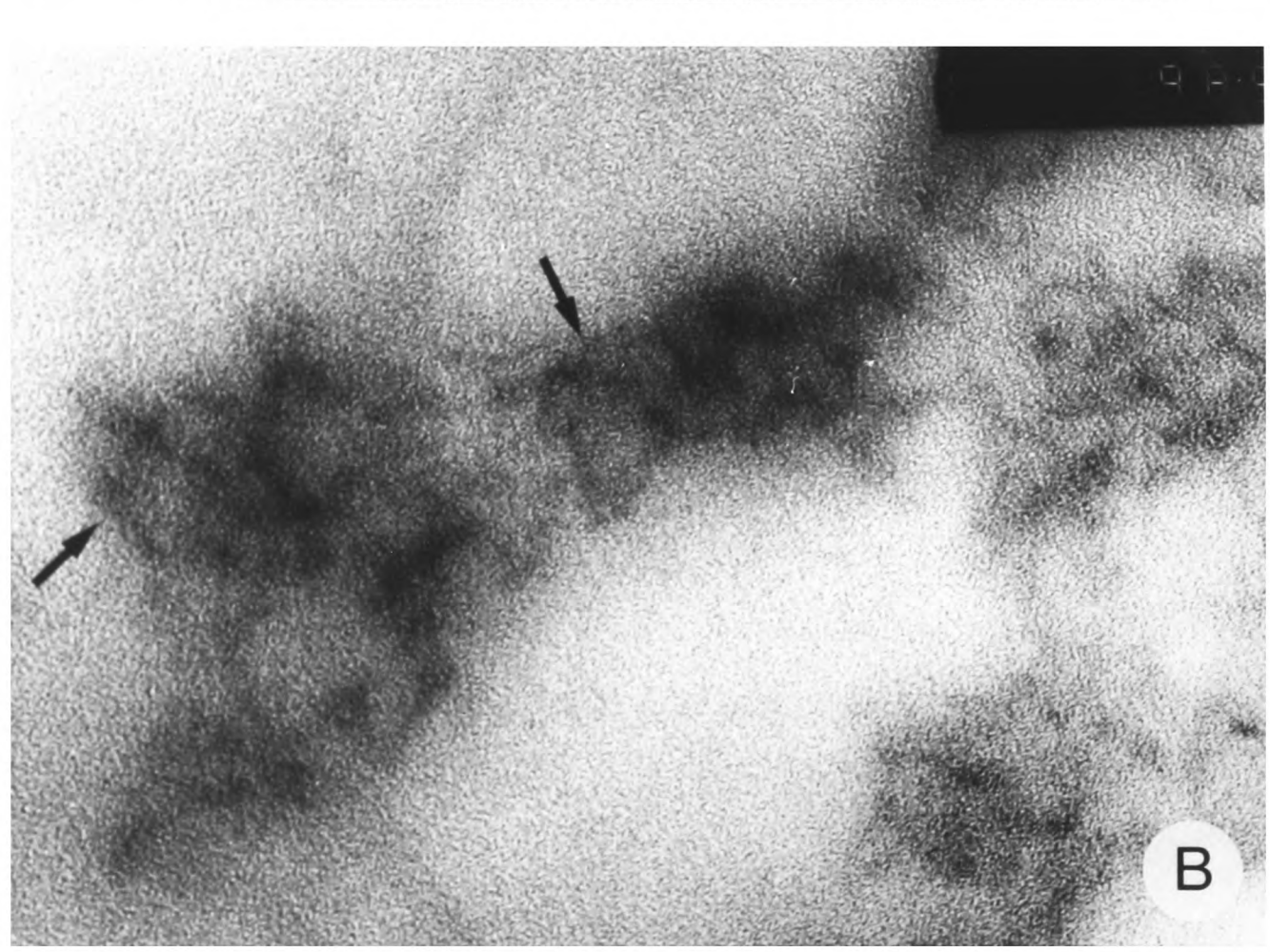

Figure 6.6 Electron micrographs of intravesicular $Co(OH)_2$ particulates; a, x175,000; b, x290,000. Arrows indicate rings of electron-dense material.

are in the range 20-35nm.

X-ray microprobe analysis over these areas detected Si, P, S, Co and Cu (from the grid). Counts for low energy peaks such as P were low above background (figure 6.7). It is not clear from where the Si and S have originated. Background analysis detected these elements but at much lower intensities.

Selected area electron diffraction was performed over many areas of these images and only diffuse rings were observed. The material is then amorphous.

6.4 Intravesicular sulphides

Intravesicular sulphides can be prepared by encapsulation of the metal cation followed by addition of $(NH_4)_2S$ solution. Undissociated H_2S molecules in the $(NH_4)_2S$ solution will penetrate the membrane and react with the cation in the internal compartment (2).

6.4.1 Intravesicular Ag(I) sulphide

17mM PC was sonicated in the presence of 125mM $AgNO_3$ and the extravesicular Ag(I) ions removed by cation ion-exchange chromotography. Addition of one drop of 1% $(NH_4)_2S$ solution gave an immediate colour change to dark-brown/black. The precipitation of Ag_2S is rapid as shown from turbidity measurements (chapter 3, figure 3.17c). Images observed in the electron microscope were electron dense, essentially discrete particulates of diameter 20-30nm (figure 6.8a). X-ray microprobe analysis over these areas detected P, S, Ag and Cu (from the grid) (figure 6.9a and table 6.3).

Electron diffraction patterns were obtained from these

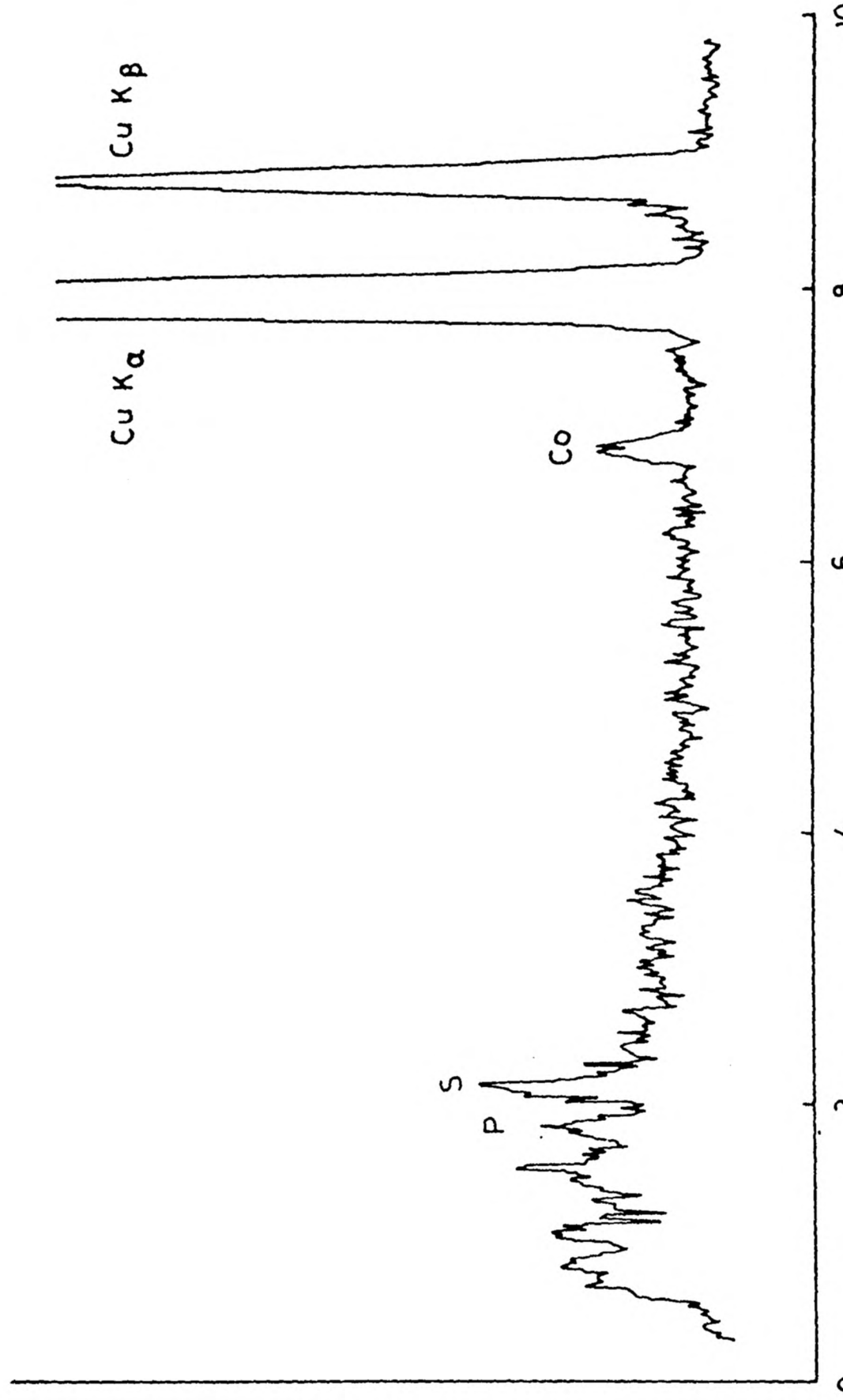

Figure 6.7 X-ray microprobe analysis for intravesicular $Co(OH)_2$ particulates.

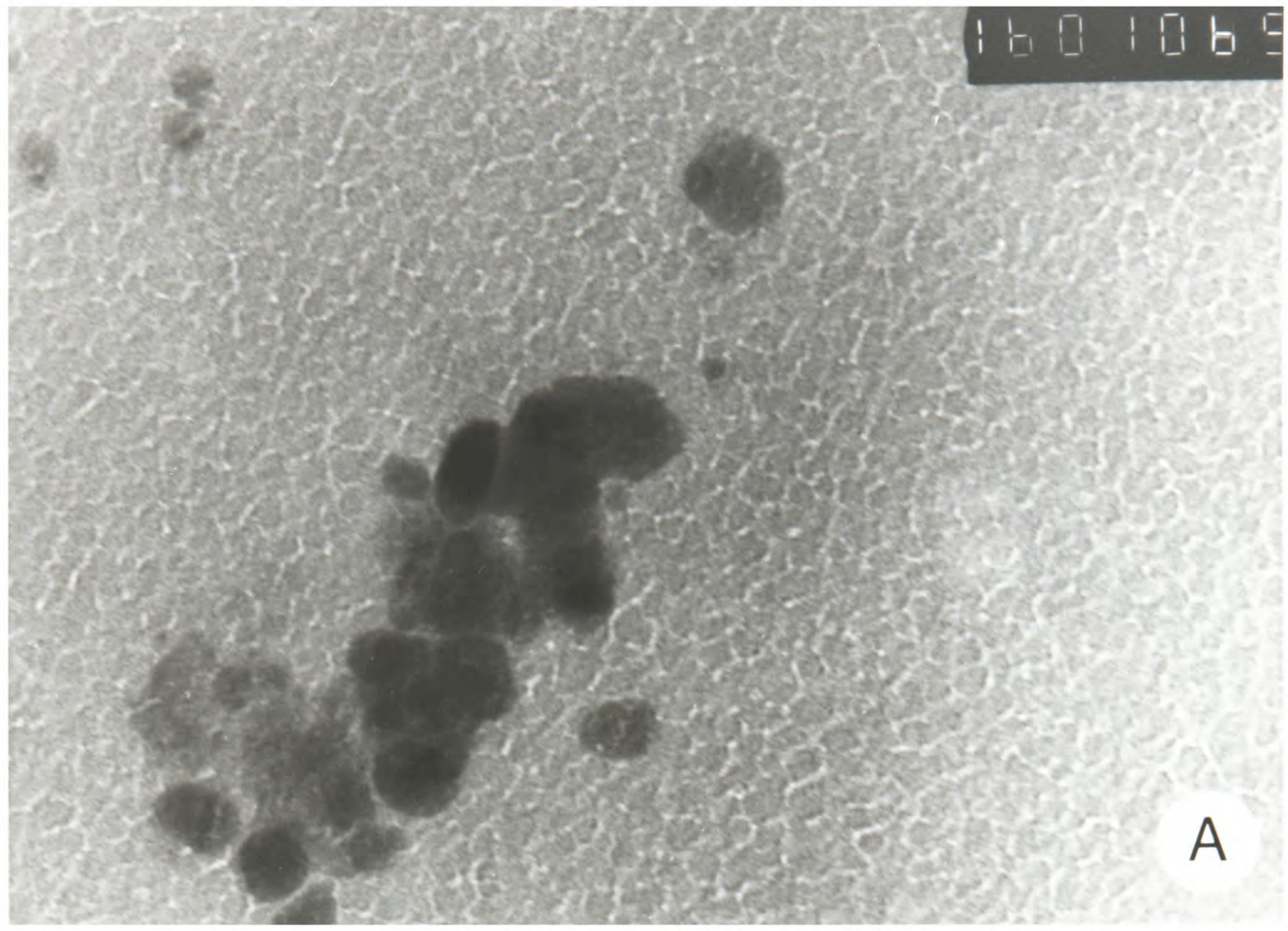

Figure 6.8 Electron micrographs of intravesicular sulphide precipitates; a, Ag_2S x300,000; b, CoS x285,000. Arrows indicate rings of electron-dense material.

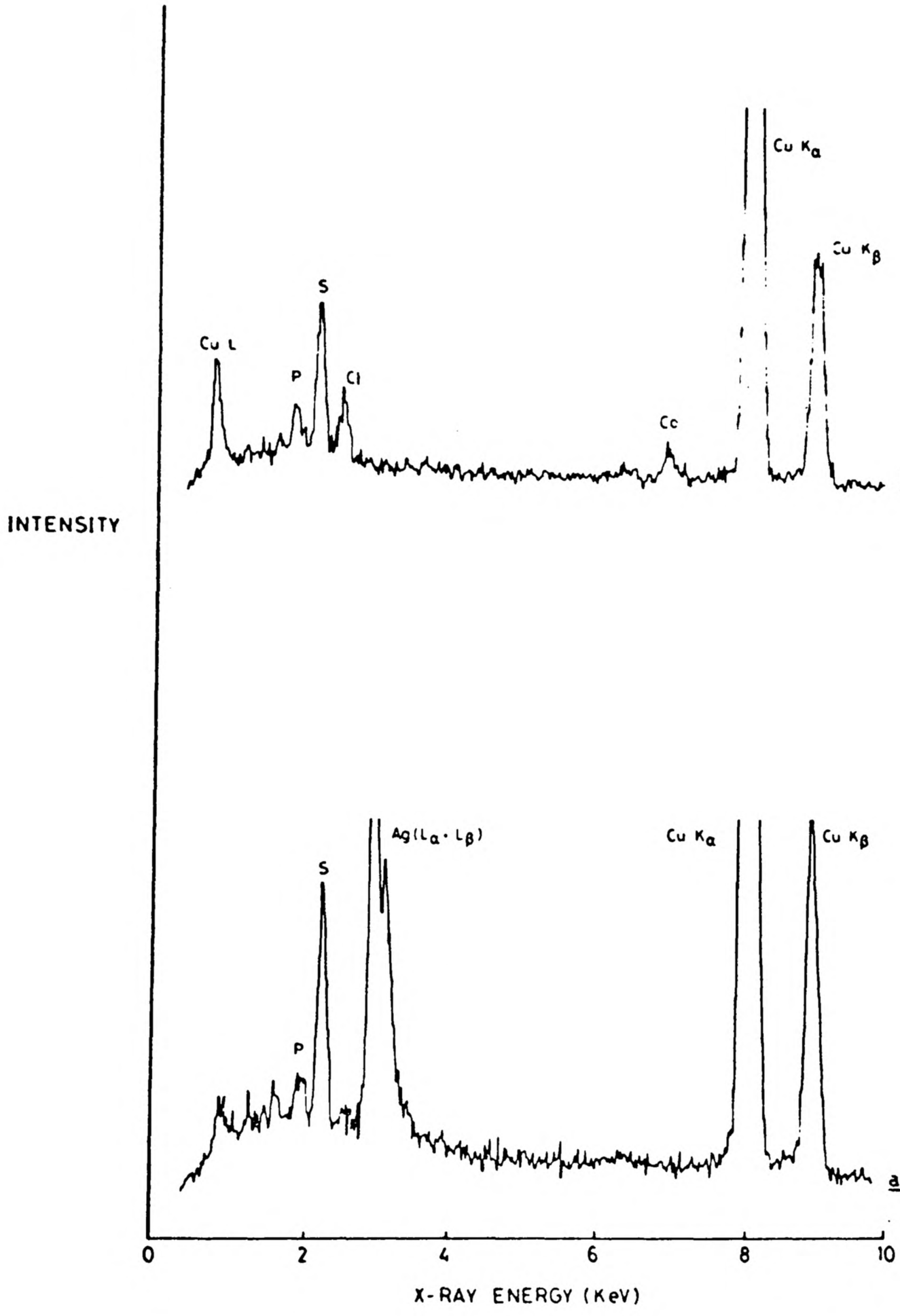

Figure 6.9 X-ray microprobe analysis for intravesicular sulphide precipitates; a, Ag_2S; b, CoS.

Table 6.3 X-ray microprobe analysis data for intravesicular sulphide precipitates

a, Ag_2S; b, CoS

a	Sample	Counts above background/100s			
		P	S	$Ag(L_\alpha + L_\beta)$	Ag/S
	1	126	948	3880	4.1
	2	207	1124	3367	2.99
	3	157	374	1340	3.59
	4	197	2250	8600	3.82
	5	149	905	2050	2.27

b	Sample	Counts above background/100s			
		P	S	$Co(K_\alpha)$	Co/S
	1	183	643	694	1.08
	2	138	812	507	0.63
	3	57	423	137	0.32

areas but were uninterpretable when compared with those obtained from Ag_2S particulates prepared in the absence of lipid (figure 6.10). These ill-defined patterns may arise from the low numbers of intravesicular particles incorporated within the selected area aperture. The patterns, however, do indicate that the intravesicular precipitates are to some degree crystalline.

6.4.2 Intravesicular Co(II) sulphide

Intravesicular CoS can be prepared by the same method as for intravesicular Ag_2S with intravesicular Ag(I) ions replaced by Co(II) ions (100mM) (2). The images obtained in the electron microscope were diffuse, low contrast aggregated particulates, some of which appeared to be in the form of rings (figure 6.8b). X-ray microprobe analysis across these areas detected P, S, Cl, Co and Cu (figure 6.9b and table 6.3). Only diffuse electron diffraction patterns were obtained indicating that the intravesicular material is amorphous.

6.5 Intravesicular Ag(I) iodide

Intravesicular Ag(I) iodide can be prepared by encapsulating Ag(I) ions within the vesicles followed by the addition of 1 drop of KI/I_2 solution. The vesicle solution turns pale yellow within ten minutes. A solution of KI/I_2 was used since it was thought that the presence of I_3^- ions in the equilibrium

$$I^-_{(aq)} + I_{2(s)} \rightleftharpoons I^-_{3(aq)}$$

would be a route to transfering I^- ions into the

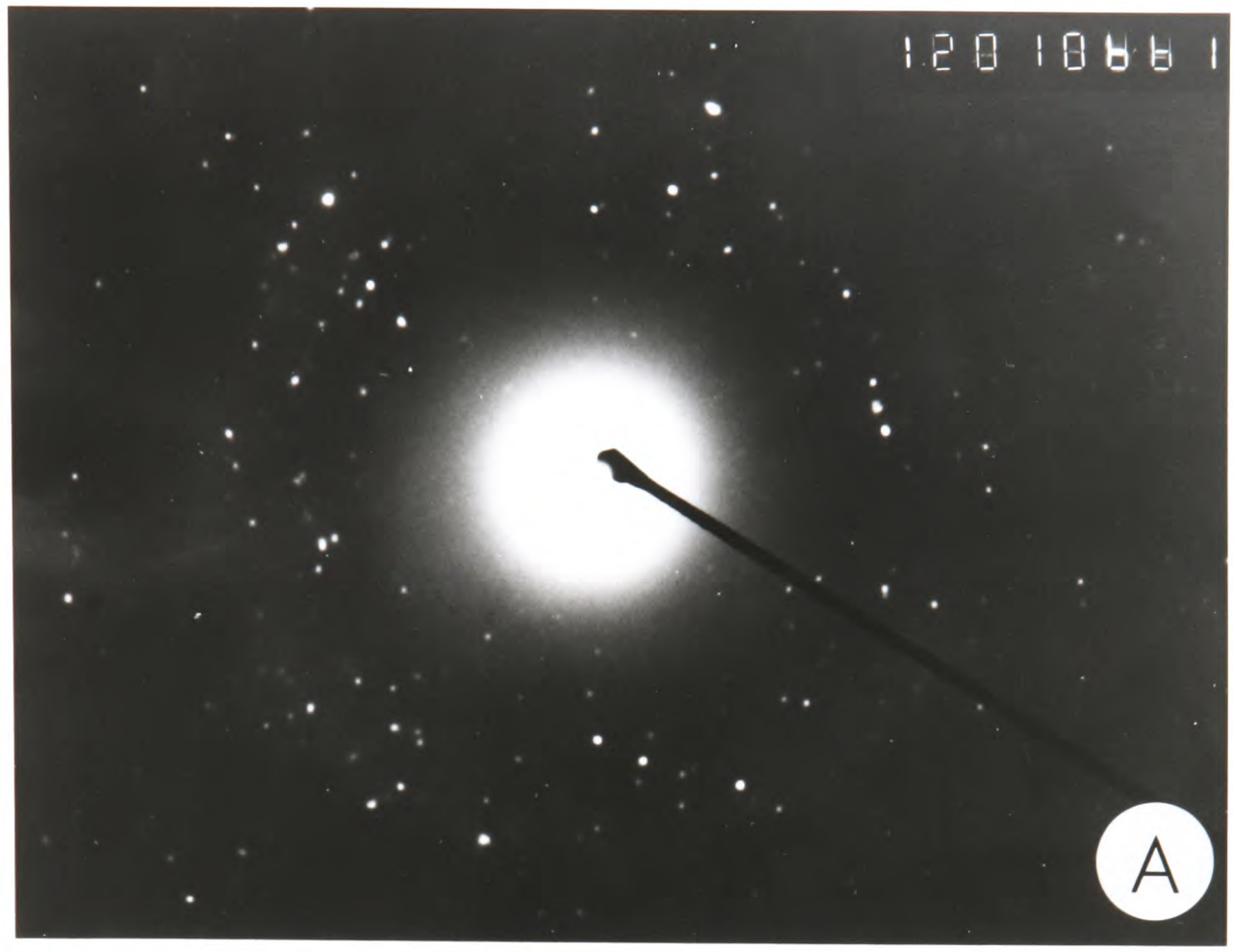

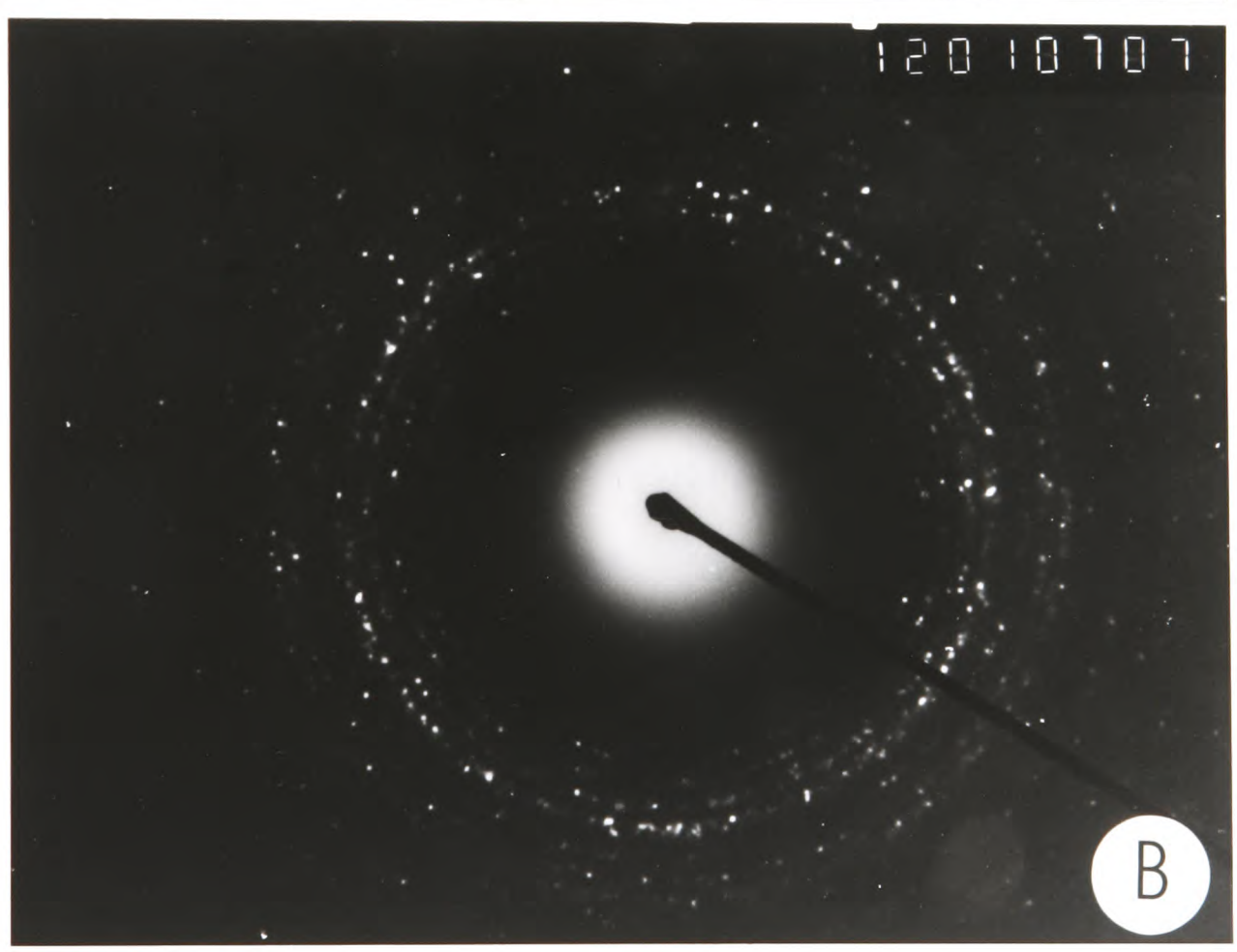

Figure 6.10 Electron diffraction patterns for; a, intravesicular Ag_2S; b, Ag_2S prepared in the absence of lipid. Camera length in both cases, 210 cm.

vesicles. It was speculated that I_3^- ions would penetrate the lipid membrane more easily than I^- ions due to their greater degree of polarisability, and hence the energy barrier to ion-lipid penetration would be lower. However, no evidence has been collected which confirms this hypothesis. It may be that I^- is sufficiently polarisable to cross the membrane energy barrier and being smaller than I_3^- there would be less steric hindrance in its passage through the hydrophobic regions of the membrane.

Well defined electron-dense spheres, diameter 10-30nm were imaged in the electron microscope for intravesicular particulates formed from Ag(I)- encapsulated ions (figure 6.11). X-ray microprobe analysis showed that these particulates contained P, Ag and I (figure 6.12 and table 6.4). The particulates were shown to be crystalline by electron diffraction (figure 6.13a). D spacings were calculated in Å and compared with those values obtained for similar measurements made for AgI particulates precipitated in normal aqueous solution (table 6.5). Diffraction spacings were the same in both cases. Comparison with reference data (3) showed the crystallites to be hexagonal AgI.

6.6 Discussion

Several intravesicular precipitation reactions of Ag(I) and Co(II) have been described in this chapter. There are two main questions to be asked. Firstly, is the intravesicular chemistry different from 'normal' chemistry in the test-tube? Secondly, what determines the crystallographic nature of the particulates formed and what effects does this have on precipitation in vesicles?

Interestingly, the answers to the first question may be

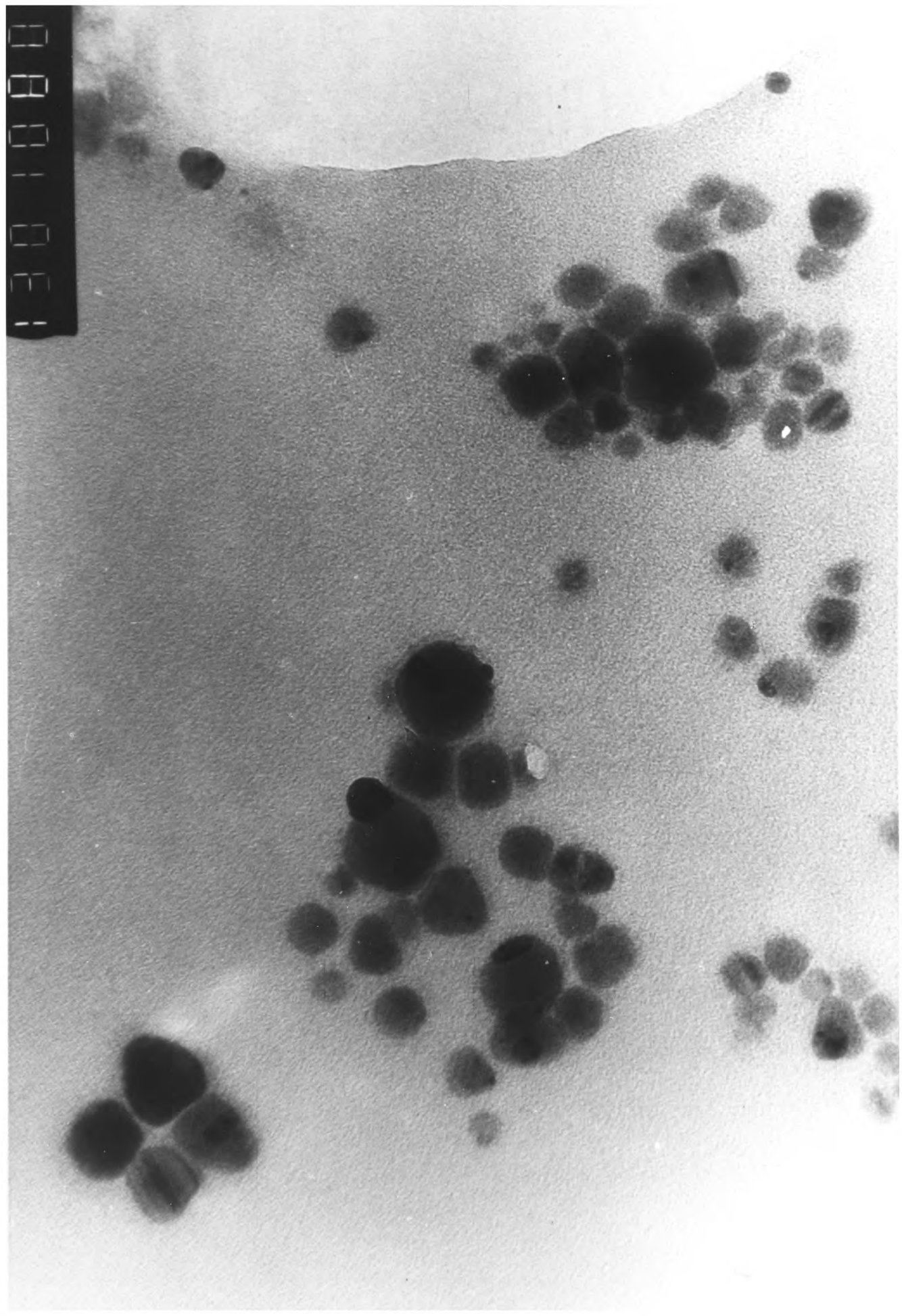

Figure 6.11 Electron micrograph of intravesicular AgI particulates x390,000.

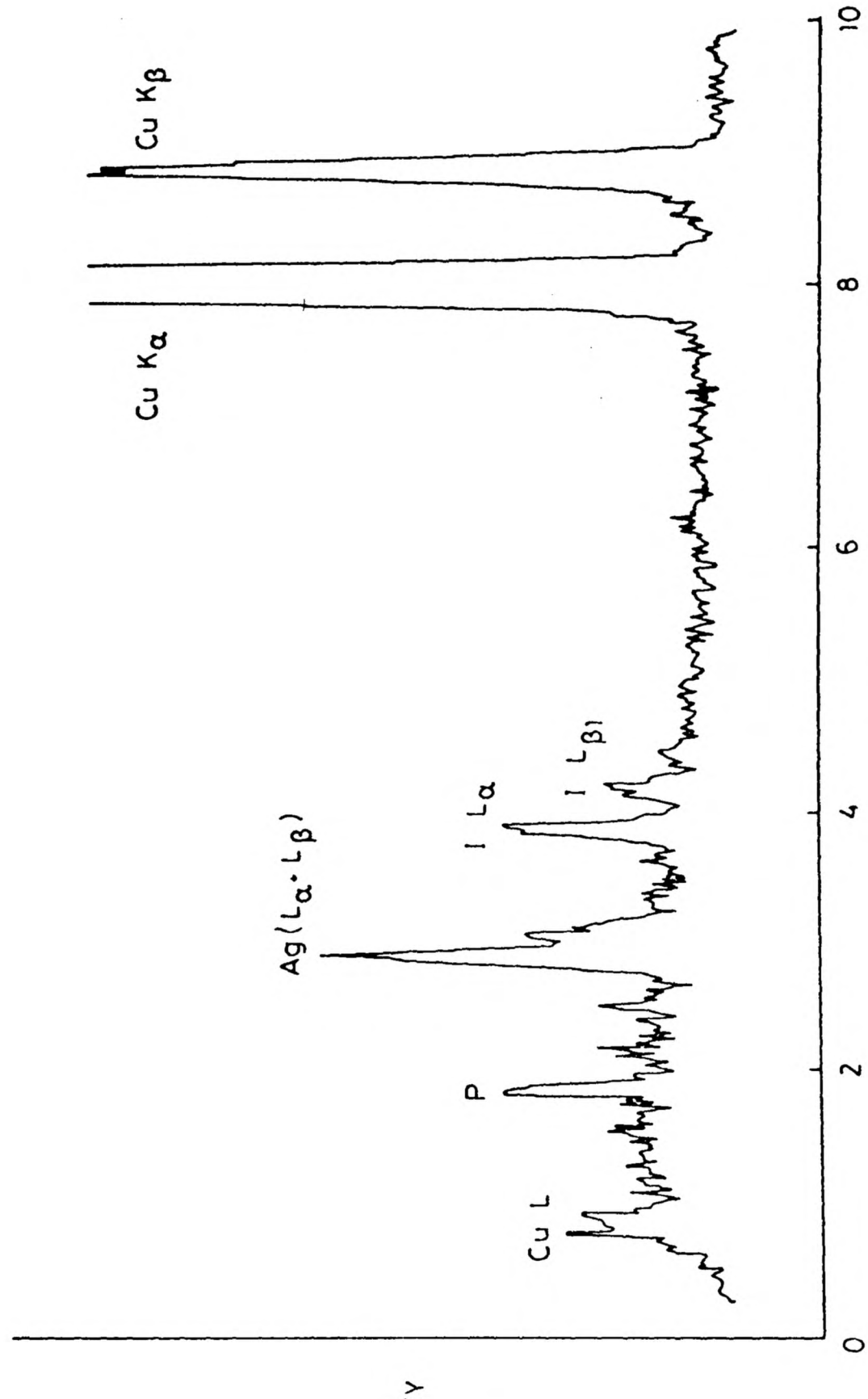

Figure 6.12 X-ray microprobe analysis for intravesicular AgI particulates.

Table 6.4 X-ray microprobe analysis data for intravesicular AgI particulates

Sample	Counts above background/100s				
	P	$Ag(L_\alpha + L_\beta)$	$I(L_\alpha)$	$I(L_\beta)$	$Ag/I(L\alpha)$
1	616	13818	5397	248	2.57
2	427	15400	4790	2016	3.22
3	219	1224	528	199	2.32
4	322	1610	668	385	2.42
5	312	1035	356	234	2.91

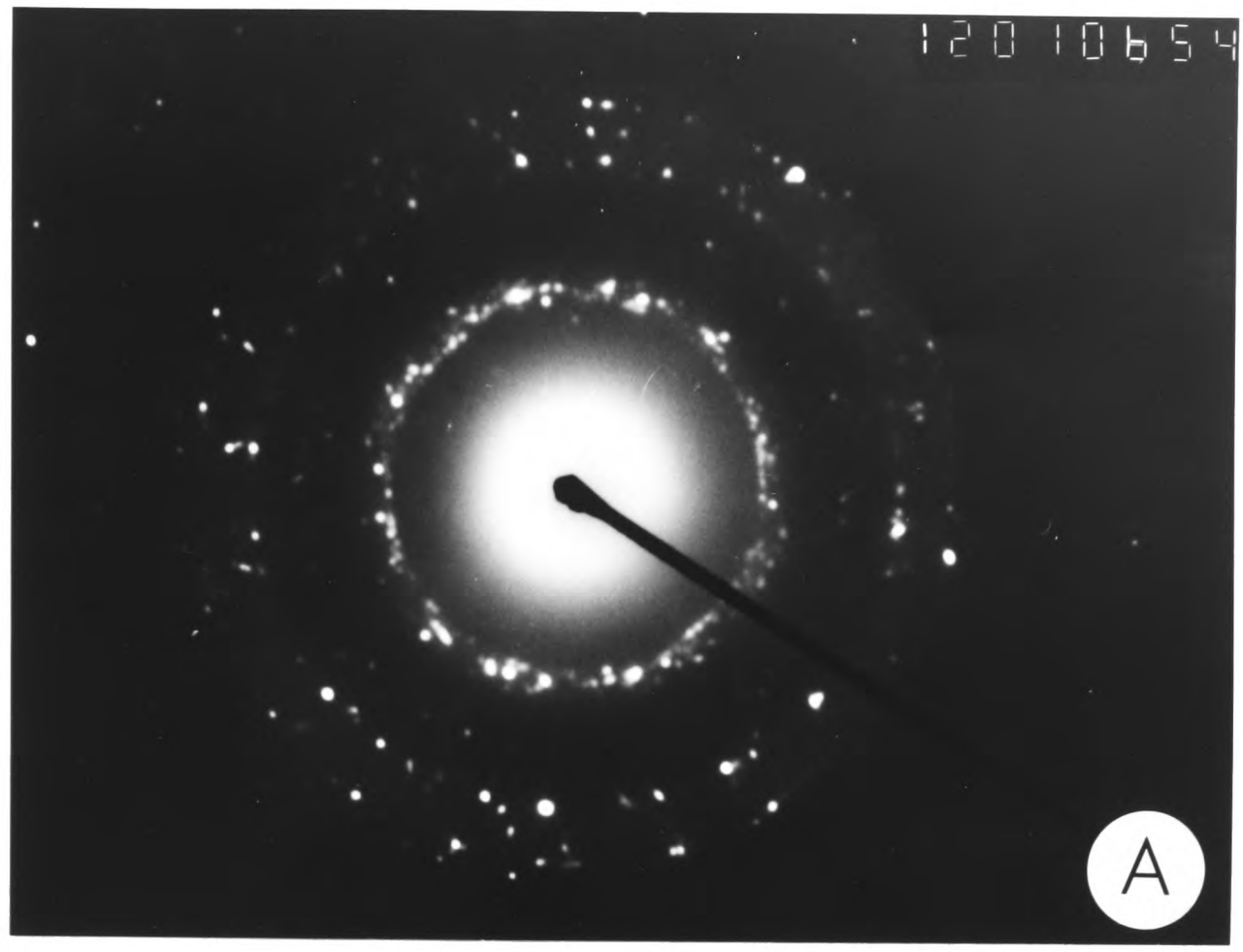

Figure 6.13 Electron diffraction patterns for; a,intravesicular AgI;b,AgI prepared in the absence of lipid.Camera length in both cases,210 cm.

Table 6.5 Calculated d spacings in Å for; a, intravesicular AgI; b, AgI prepared in the absence of lipid.

a	b
3.76	3.68
2.61	
2.16	2.20
1.85	1.84
1.37	1.32
	1.13

'yes' and 'no'. The final reaction product in each case does in fact mirror the same material when prepared in normal aqueous solution. Thus $Co(OH)_2$, $CoSiO_3$ and CoS precipitates are amorphous whether formed within vesicles or in aqueous solution. Similarly precipitates of Ag_2O (chapter 3), Ag_2SiO_3, Ag_2S and AgI are crystalline whether prepared in vesicles or in aqueous solution. However, the mechanism of precipitation may differ in these two systems even though the final reaction product does not, since in the vesicle system the localisation of the cation towards the phosphate headgroups has to be considered in any mechanism of nucleation and crystal/particulate growth.

Non-crystalline solids are always metastable phases in which the free energy excess over the more stable (crystalline) arrangement is 'frozen' or quenched into the system usually by a sudden change of a thermodynamic intensive variable. In liquid-deposited amorphous solids this quenched excess energy occurs due to sudden changes of chemical potential on precipitation. Hence there is often a high activation energy barrier for the transformation from a non-crystalline to crystalline state.

The two general descriptions of a non-crystalline solid are, (a) a continuous random network, and (b) a microcrystalline/ cluster network. In the continuous random network model the amorphous state is described in terms of a random network of small structural units which are related to those found within the unit cell of the crystalline state. These units are attached in a random way subject only to the spatial constraints imposed by the steric hindrance of the environment and the allowable ranges for bond angles. In the microcrystalline

model the amorphous structure is described in terms of a random array of microcrystalline polyhedra (clusters). Clusters of icosahedral symmetry ("amorphons") may be advantageous to the energy of the solid state when only local order contributions to the free energy are taken into account (i.e. neglect long range energy contributions).

The growth of single crystals would be preferred under circumstances of slow thermodynamic change whereas rapid changes would favour polycrystalline and amorphous states. In chapter 3 a model for single crystal formation in vesicles was postulated in which nucleation occurred at one site on the membrane surface followed by slow crystal growth in certain preferential directions. It was also speculated that rapid nucleation at myriad sites on the membrane surface would result in a hollow sphere of material bound to the membrane. It was further postulated that this effect may inhibit further intravesicular precipitation due to the inaccessability of the diffusing anion to cations in the central vesicle space.

The images observed for Co(II) precipitates differ greatly from those of Ag(I). It has also been shown that ring or 'hole' structures of low contrast material can be observed in these images in the electron microscope. It is suggested that in these reactions the strong binding of Co(II) ions to the phosphate headgroups favour nucleation at many sites at the same time resulting in a hollow sphere of precipitate around the inner surface of the vesicles. The material deposited would then surely be amorphous since no periodic array of atomic structure can take place. Amorphous electron dense spheres can also be imaged (figure 6.2b) particularly

if the concentration of encapsulated Co(II) ions is high. A possible mechanism is that clusters of Co(II) X ($X = OH^-$, SiO_3^{2-}, S^{2-}) are formed at the membrane surface which aggregate with random orientation to form the amorphous intravesicular particulates. The whole structure can be thought of as a random array of these microcrystalline clusters with the interstices filled with water molecules. Similar models have been postulated for amorphous calcium phosphate deposition (4). The low density of these hydrated materials may then explain the low contrast and aggregation of such intravesicular solids when imaged in the electron microscope.

In general for simple single oxidation state compounds the material formed in vesicles is the same as that in the absence of lipid. However, this does not seem to be the case for mixed valence state systems (chapter 5).

Silicate vesicles have been described for Ag(I) and Co(II) cations. It is rather surprising that SiO_3^{2-} ions can penetrate the membrane. It may be that $HSiO_3^-$ ions diffuse through rapidly and then hydrolyse to SiO_3^{2-} in the inner phase. However, intravesicular pH will be in the range of 7.0 which implies that OH^- diffusion must also occur for hydrolysis of intravesicular $HSiO_3^-$ ions.

Further experiments which would be of interest would be the intravesicular precipitation of (a) SiO_2, (b) $CaCO_3$, (c) calcium phosphate.

For SiO_2 precipitation a binding mode for $Si(OH)_4$ polymerisation must be first introduced into the vesicles. This could take the form of an inorganic ($Fe_2O_3nH_2O$?) or organic (catechols?) template incorporated into the inner compartment.

Intravesicular $CaCO_3$ deposition is important in relation to the widespread biological occurrence of this solid. The initial problems in this system will be (i) instability of vesicles in the presence of Ca^{2+}(5), and (ii) passage of CO_3^{2-} ions into the vesicles. The second problem may be overcome by the use of a HCO_3^-/OH^- medium although there may be problems of reaching a high enough pH_{IN} for CO_3^{2-} formation. Intravesicular calcium phosphate precipitation is important as a model for hydroxyapatite deposition in matrix vesicles for bone formation (6). PH control of the intravesicular environment will be of vital importance in controlling this precipitation reaction.

6.7 References

(1) ASTM Powder Diffraction File 12-648, 1972.

(2) Skarnulis A.J., Strong P.J., Williams R.J.P. J.C.S. Chem.Comm., 23, 1020-1032, 1978.

(3) ASTM Powder Diffraction File 9-374, 1972.

(4) Betts F., Posner A.S., Symp.Liquid and Amorphous Materials, Vol. 10, 73-84, 1974.

(5) Papahadjopoulos D., Vail W.J., BBA 394, 483-491, 1975.

(6) Anderson H.C., Reynolds J.J., Develop.Biol. 34, 211-227, 1973.

CHAPTER 7

VESICLES AS A MODEL SYSTEM FOR MAPPING ORGANIC MOLECULES IN BIOLOGICAL SPACE

7.1 Introduction

Two methods currently used to map biological systems are electron microscopy and high resolution n.m.r. spectroscopy. Electron microscopy combined with energy dispersive analysis allows the distribution in space of elements heavier than sodium to be defined. It is however, a destructive technique with samples being subjected to high vacuum conditions and intense electron irradiation. In the investigation of biological samples sections often have to be prepared using a procedure which results in a specimen which may bear little resemblance to that in the living system. High resolution n.m.r. spectroscopy however, is a non-destructive method which detects systems in a dynamic state.

In order to combine electron microscopy and n.m.r. spectroscopy in an approach to probe biological systems, probes must be used which perturb the n.m.r. signals and which can be imaged and detected in the electron microscope. In previous chapters it has been shown how intravesicular precipitation reactions can be accomplished in phosphatidylcholine (PC) vesicles. This method can also be used as a system for introducing paramagnetic probes near to the membrane which can then be located by electron microscopy and n.m.r. spectroscopy. The method depends upon the probe being located in particular regions of space so that organic molecules which lie in the vicinity of the probe can be detected.

The development of this approach of combining high resolution n.m.r. spectroscopy with electron microscopy has been discussed for simple paramagnetic probes such as Co(II) and $Fe(CN)_6^{3-}$ using vesicles as a model system for a biological specimen with two compartments (1). In this chapter three new potential membrane probes, $K_5PhGeSiW_{11}O_{39}$, $Gd(fod)_3$ where fod = $CF_3(CF_2)_2COCH_2COCHMe_2$, and t-$BuNH_3[(n\text{-}C_{22}H_{45}PO_3)_2Mo_5O_{15}]$ (I), are described.

The reagent $K_5PhGeSiW_{11}O_{39}$ is an organo-heteropoly tungstate (VI) compound. The anion $[PhGeSiW_{11}O_{39}]^{5-}$ is based on the Keggin structure (2) of the heterpoly anion $[SiW_{12}O_{40}]^{4-}$ in which the Si atom is enshrouded by a cage of WO_6 octahedra and with the PhGe group bound to three O atoms to replace the missing WO group.

The compound is soluble in water and can be reduced to the blue mixed-valence species without loss of structure. The added electrons are thought to be localised on the W atoms (3).

$Gd(fod)_3$ is a paramagnetic Gd(III) complex which is soluble in organic solvents such as chloroform but insoluble in water. It is commercially available.

Compound I is an organo-heteropoly molybdate with a disc-like oxometalate group with the organic residues directed along the axes in opposite directions (4). The preparation of this compound is described elsewhere (5).

Because of the hydrophobic nature of $Gd(fod)_3$ and the lipophilic nature of compound I it was speculated that these reagents could be incorporated into the hydrophobic regions of the vesicle bilayers. Since the existing methods for fixing and staining biological membranes use chemically aggressive reagents such as osmium tetraoxide and lead (IV) citrate these

more gentle lipophilic reagents may be preferable in probing such structures.

To test these three probes, PC vesicles were prepared in the presence of these compounds and the resulting vesicles investigated by electron microscopy and ^{1}H n.m.r. spectroscopy.

7.2 Materials and methods

7.2.1 $K_5PhGeSiW_{11}O_{39}$ vesicles

Since this reagent was soluble in water, PC vesicles (34mM in lipid) were made in D_2O as described previously and n.m.r. spectra recorded of vesicle solutions containing different concentrations of $K_5PhGeSiW_{11}O_{39}$ in the external phase. Spectra were also recorded of vesicle solutions which contained reduced $K_5PhGeSiW_{11}O_{39}$. Reduction was carried out by the addition of a crystal of $Na_2S_2O_4$ to the $K_5PhGeSiW_{11}O_{39}$ solution (initial concentration 17mm) which immediately turned blue on formation of the mixed valence tungsten blue compound. N.m.r. spectra were recorded on a 270MHz Bruker spectrometer as previously described.

For electron microscopy experiments, one drop of the 'blank' vesicle solution was placed onto a formvar coated grid and one drop of 0.8mM $K_5PhGeSiW_{11}O_{39}$ solution added. After 30 seconds surplus solution was removed by filter paper and the grid allowed to dry in the air. The grid was then washed with distilled water to remove excess $K_5PhGeSiW_{11}O_{39}$ particulates from the grid. The electron microscope used was a JEOL 100CX as previously described.

7.2.2 $Gd(fod)_3$ vesicles

Vesicles containing $Gd(fod)_3$ were prepared as follows. 25mg (PC) lipid in chloroform was added to a solution of 10mg $Gd(fod)_3$ in chloroform. The resulting solution was evaporated to dryness *in vacuo* using a rotary evaporator with a liquid nitrogen trap. $4cm^3$ of distilled water (D_2O for n.m.r. experiments) was then added and the milky suspension sonicated at 4^oC as before until the solution was opalescent. Drops of the vesicle solution were put onto electron microscope grids in the normal manner.

7.2.3 $t\text{-}BuNH_3[(n\text{-}C_{22}H_{45}PO_3)_2Mo_5O_{15}]$ vesicles

21mg of compound I dissolved in methanol was added to 25mg of lipid in chloroform. Vesicles containing compound (I) were then prepared following the same procedure as in section 7.2.2.

7.3 Results

7.3.1 $K_5PhGeSiW_{11}O_{39}$ vesicles

^1H n.m.r. spectra of vesicles in the presence of different concentrations of extravesiclar $[PhGeSiW_{11}O_{39}]^{5-}$ are shown in figure 7.1. The external NMe_3^+ headgroup shifted downfield on increasing addition of the heteropoly anion. Addition of 3.2mM (total concentration) $K_5PhGeSiW_{11}O_{39}$ to vesicles (34mM lipid) resulted in a shift of 0.05 ppm from an initial position of 3.41 ppm to 3.46 ppm. The internal NMe_3^+ resonance position remained fixed at 3.41 ppm.

The perturbation of the external NMe_3^+ headgroup shows that the large tungstate anion binds at the membrane surface altering the magnetic environment in these regions of space.

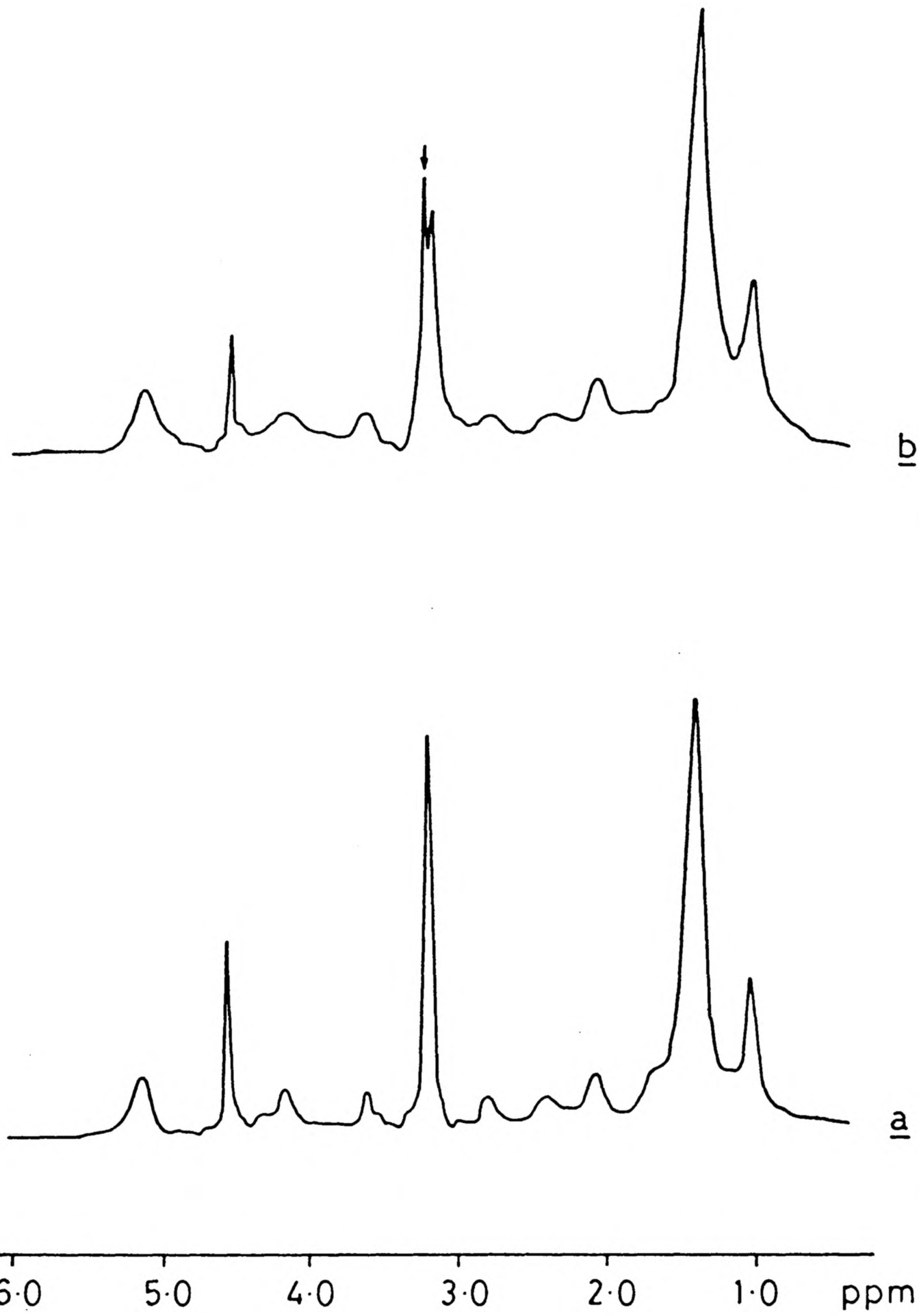

Figure 7.1 ^{1}H n.m.r. spectra of vesicles (34mM lipid) in the presence of extravesicular $K_5PhGeSiW_{11}O_{39}$; a, blank vesicles; b, vesicles in the presence of 3.2mM $K_5PhGeSiW_{11}O_{39}$. Arrow indicates the shifted external NMe_3^+ peak.

Hence such a probe can be used to show the presence of two compartments within the vesicle system.

N.m.r. spectra recorded on vesicle solutions containing the reduced form of the heteropoly anion in the external phase of the vesicle solution had no effect on the magnitude of the NMe_3^+ splitting.

Figure 7.2 shows an electron micrograph of vesicles in the presence of $K_5PhGeSiW_{11}O_{39}$. Circles of electron-dense material (diameter 15-25nm) could be observed, usually aggregated. These images show that the vesicles are 'stained' by the heteropoly tungstate compound with the high electron-scattering W atoms locating the position of the membrane surface.

X-ray microprobe analysis was performed over such areas and the elements Si, P, K, W, Ge and Cu (from the grid) were detected (figure 7.3 and table 7.1). Hence $K_5PhGeSiW_{11}O_{39}$ appeared to be a useful EM/n.m.r. probe for PC vesicles.

7.3.2 $Gd(fod)_3$ vesicles

Vesicles prepared in the presence of $Gd(fod)_3$ showed images in the electron microscope corresponding to hollow spheres of diameter 25-30nm (figure 7.4). The contrast in such electron micrographs occurred due to the Gd within the lipid phase of the vesicles. X-ray microprobe analysis over these areas detected Gd and P (figure 7.5 and table 7.1). Ca and Si was also present in these regions of the electron microscope grid, presumably as impurities since neither were detectable in significant amounts in the background analysis.

Examination of $Gd(fod)_3$ vesicles by ^1H n.m.r. spectroscopy showed that the presence of the Gd(III) entity within the membrane broadened the vesicle spectrum such that the resonance

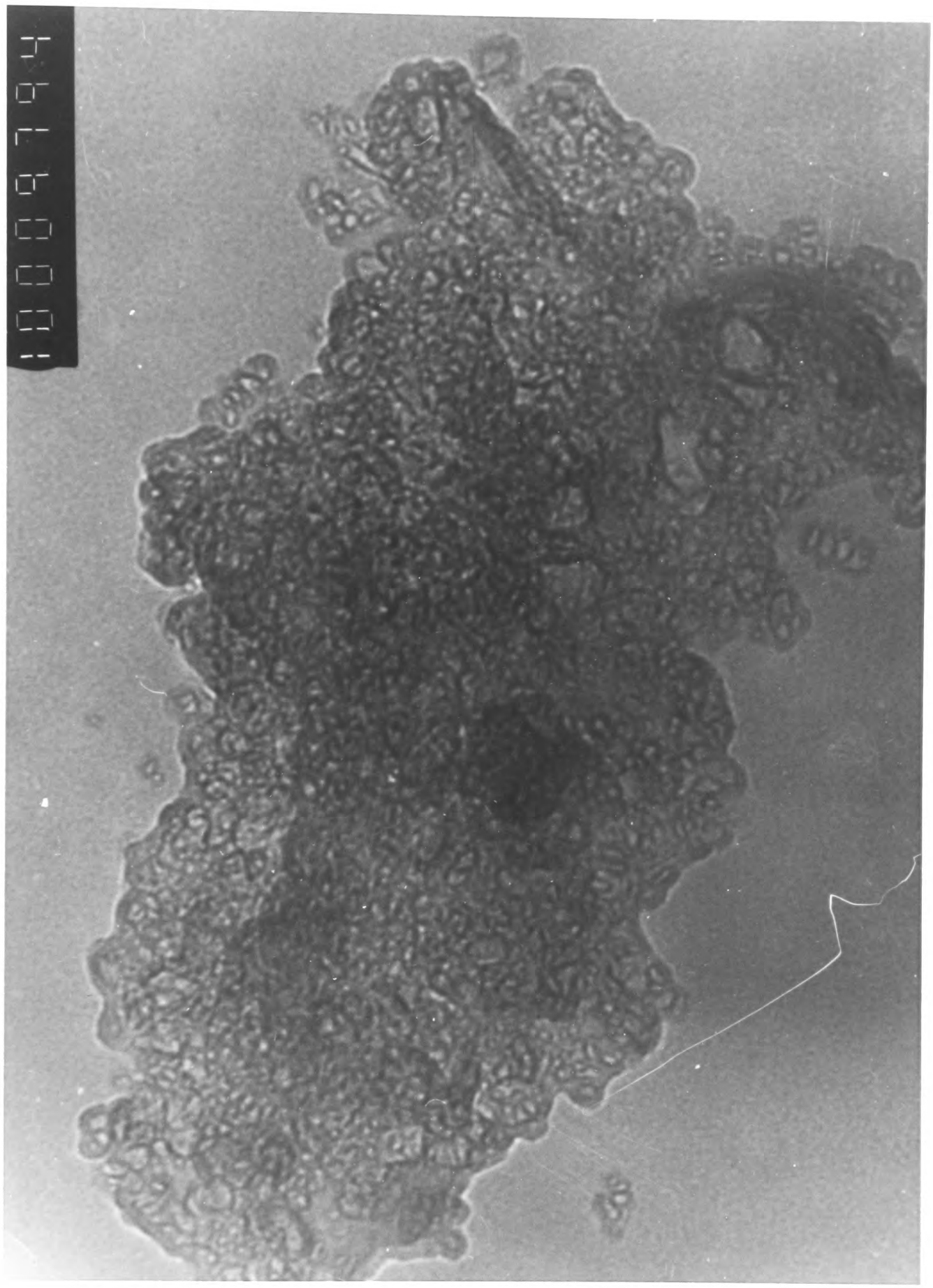

Figure 7.2 Electron micrograph of vesicles 'stained' by $K_5PhGeSiW_{11}O_{39}$ x220,000.

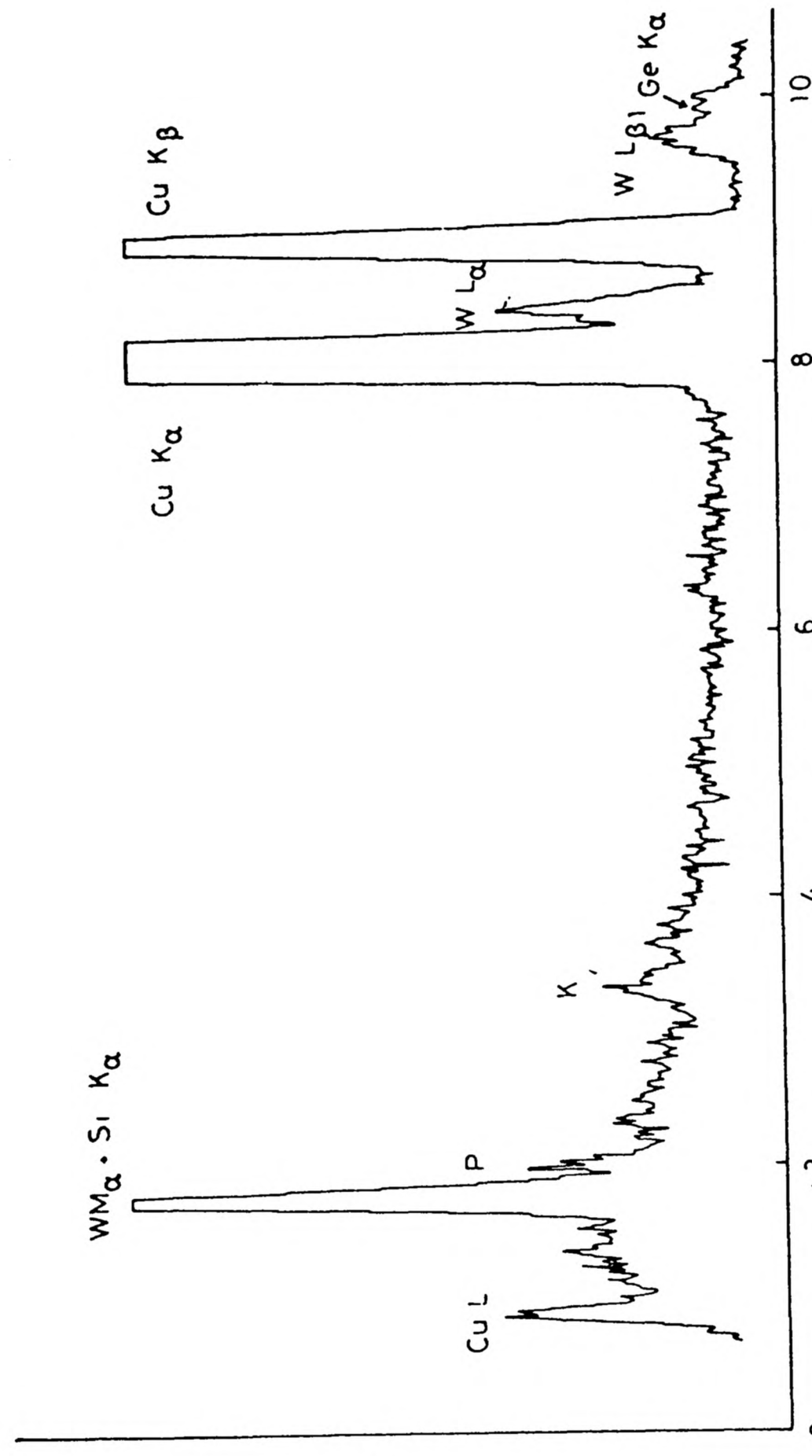

Figure 7.3 X-ray microprobe analysis for $K_5PhGeSiW_{11}O_{39}$ vesicles.

Table 7.1 X-ray microprobe analysis data for vesicles in the presence of, a, $K_5PhGeSiW_{11}O_{39}$; b, $Gd(fod)_3$; c, $t\text{-}BuNH_3[(n\text{-}C_{22}H_{45}PO_3)_2Mo_5O_{15}]$

a, Sample — Counts above background/100s

	W(Mα) + Si(K)	P	K	W(Lα)	Ge(Kα)	W(Lα)/P
1	16772	949	2443	5253	76	5.5
2	1997	378	448	809	116	2.2

b, Sample — Counts above backgroud/100s

	P(K)	Gd(Lα)	P/Gd
1	430	156	2.76
2	578	162	3.57
3	236	155	1.53
4	326	226	2.20

c, Sample — Counts above background/100s

	P(K)	Mo(Kα)	P/Mo
1	575	597	0.97
2	436	526	0.83
3	527	486	1.11
4	429	370	1.16

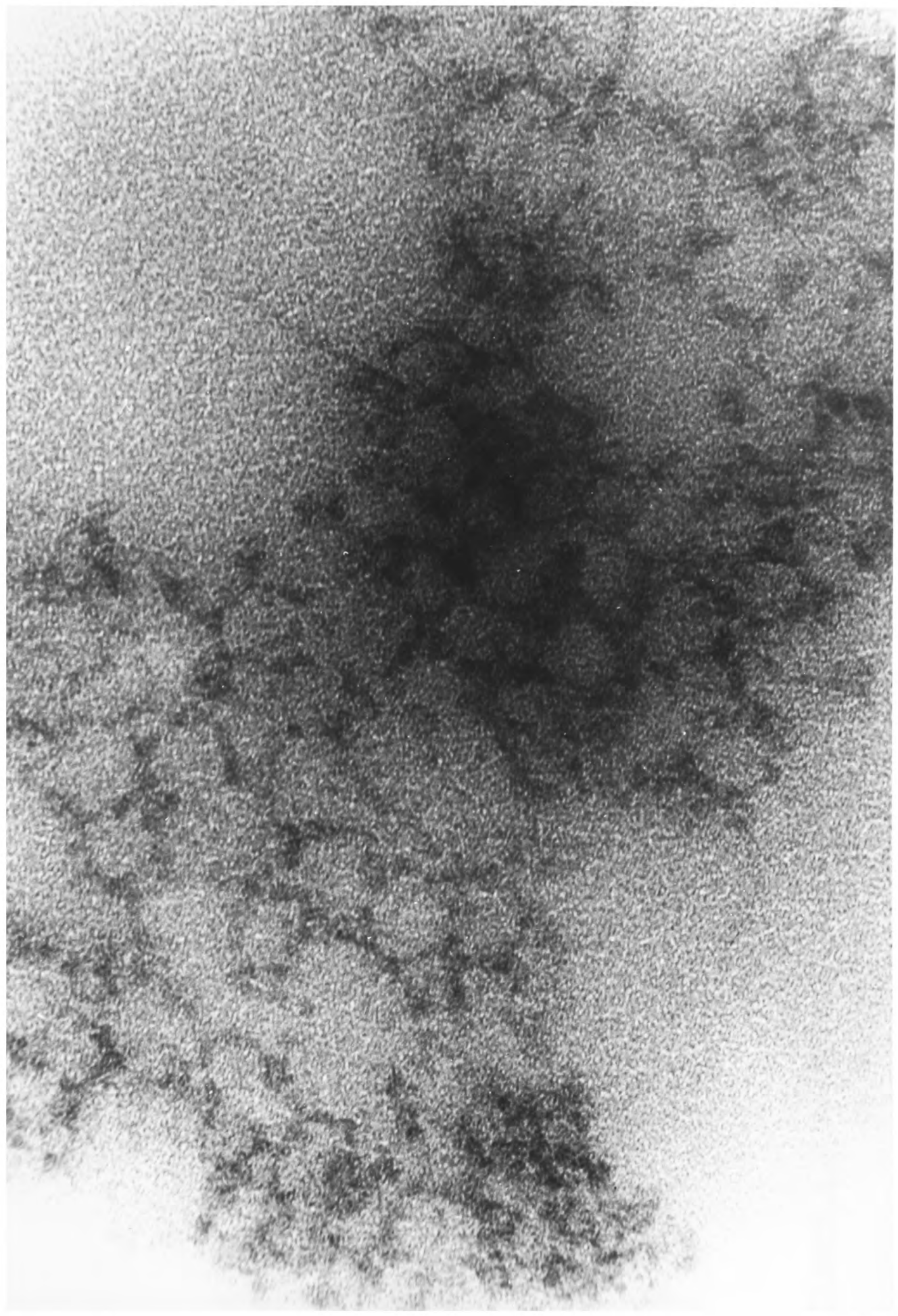

Figure 7.4 Electron micrograph of $Gd(fod)_3$-containing vesicles x455,000.

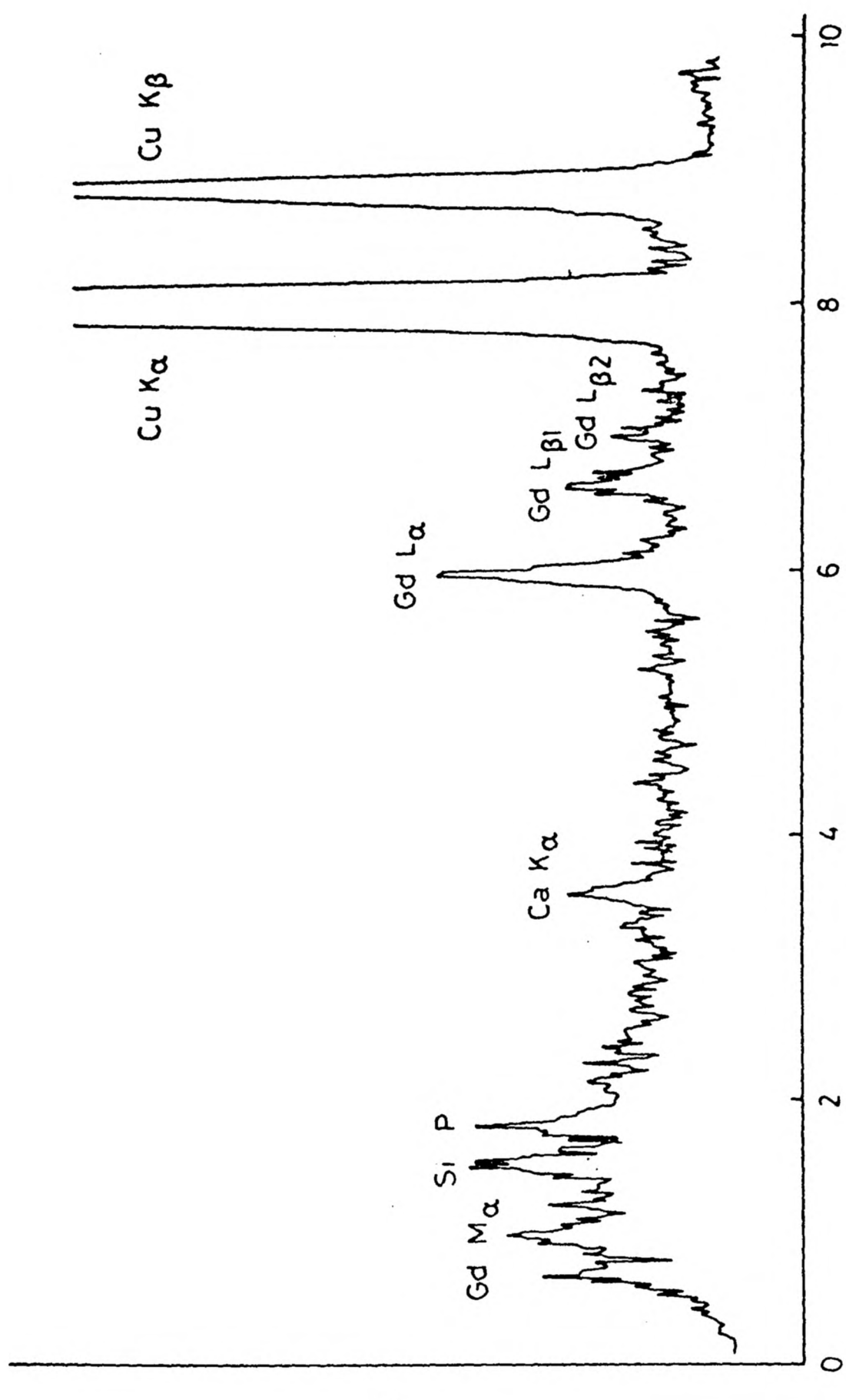

Figure 7.5 X-ray microprobe analysis for $Gd(fod)_3$-containing vesicles. Ca and Si are impurities in the preparation.

positions of the terminal CH_3 and $[CH_2]_n$ chain of the fatty acids were extensively broadened (figure 7.6). The choline headgroup was also broadened but could still be resolved indicating that the probe is located within the hydrophobic regions of the membrane and is thus at some distance from the polar headgroup.

7.3.3 t-$BuNH_3[(n-C_{22}H_{45}PO_3)_2Mo_5O_{15}]$ vesicles

Vesicles prepared in the presence of this probe showed similar images in the electron microscope as observed with $Gd(fod)_3$ - containing vesicles. Hollow spheres of diameter 20nm (arrows on figure) were observed (figure 7.7) but, in general, contrast was low and images diffuse.

X-ray microprobe analysis over these areas detected Mo and P (figure 7.8 and table 7.1) indicating that the images observed were vesicles 'stained' by the organo-heteropoly molybdate compound.

The ^1H n.m.r. spectrum of vesicles in the presence of this probe showed no change in resonance positions when compared with a normal vesicle spectrum.

7.4 Discussion

In this chapter the use of three organometallic reagents located either at the membrane surface or within the lipid bilayer of unilamellar PC vesicles, has been described in terms of their ability to act as n.m.r./EM probes for mapping organic molecules.

Binding of the anion $[PhGeSiW_{11}O_{39}]^{5-}$ to the vesicle surface has been shown to be useful in electron microscopy and n.m.r. spectroscopy experiments in probing lipid membranes.

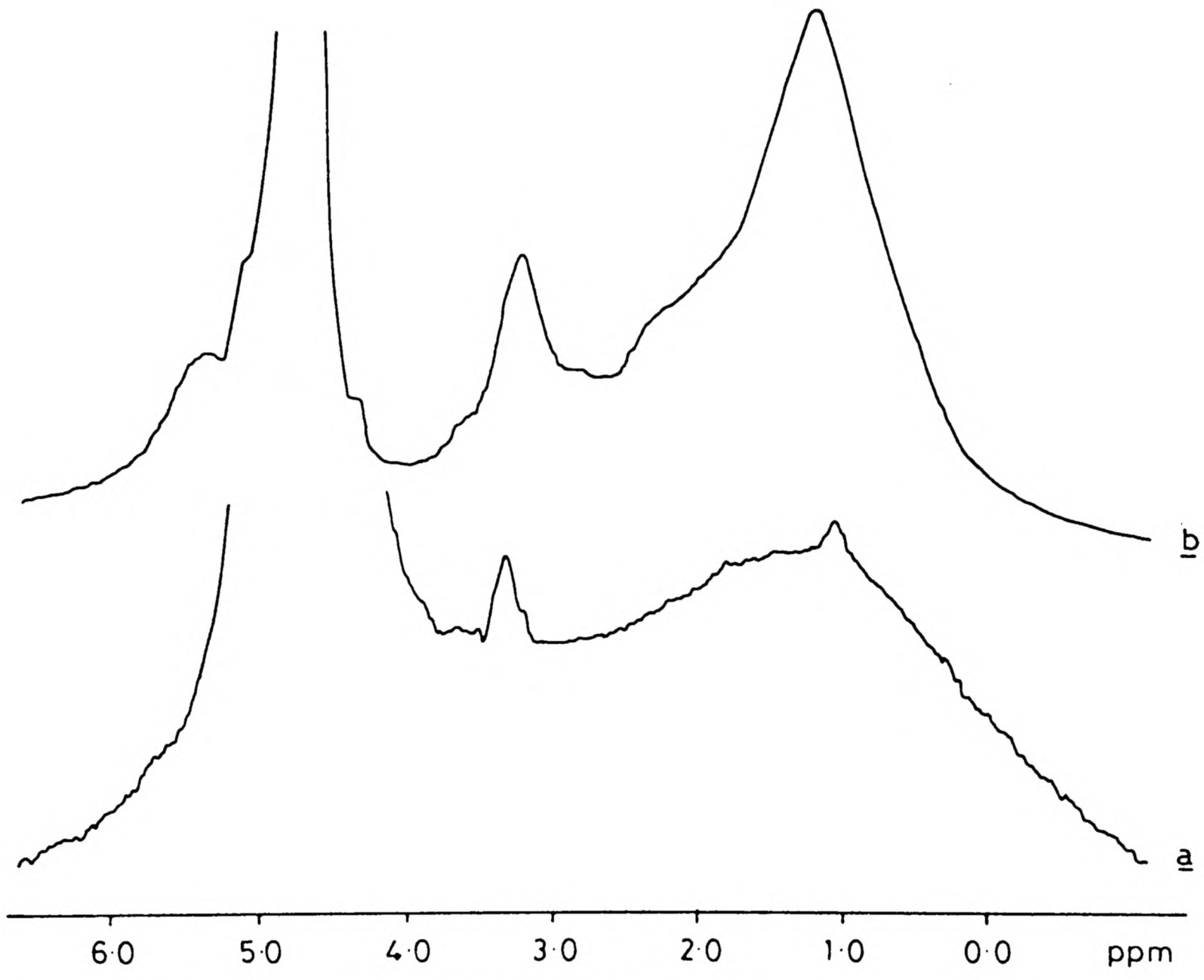

Figure 7.6 ^{1}H n.m.r. spectra of $Gd(fod)_3$- loaded vesicles; a, 25mg lipid/10mg $Gd(fod)_3$ b, 25mg lipid/2mg Gd(fod). Both preparations were made in $4cm^3 D_3O$. Three resonance peaks are observed corresponding to, HOD(4.63 ppm), NMe_3^+ (3.2 ppm), and $[CH_2]_n$ (1.27) ppm.

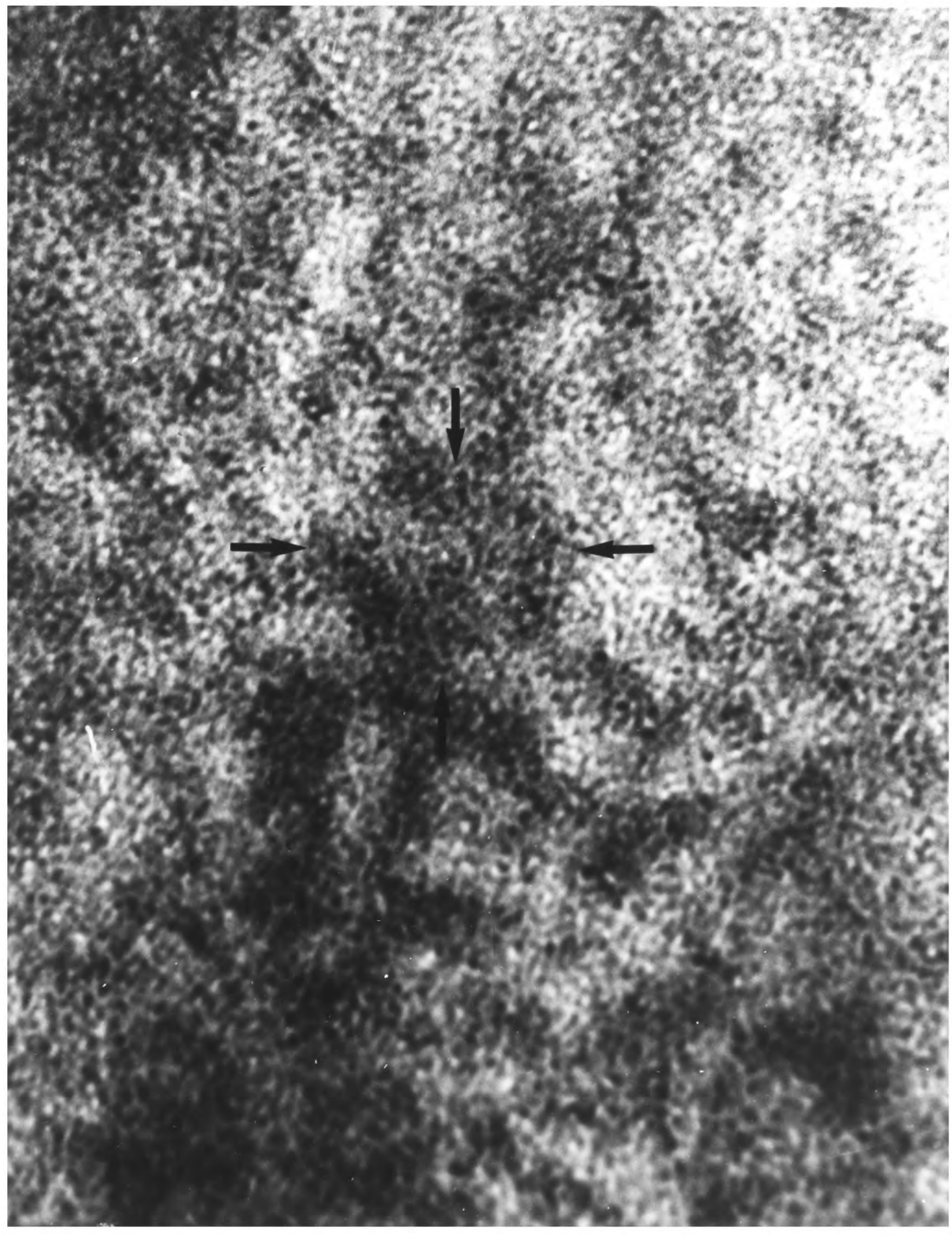

Figure 7.7 Electron micrograph of a 'dense' region of vesicles containing t-$BuNH_3[(n\text{-}C_{22}H_{45}PO_3)_2Mo_5O_{15}]$ x1,190,000.Arrows indicate a vesicle of diameter 20 nm.

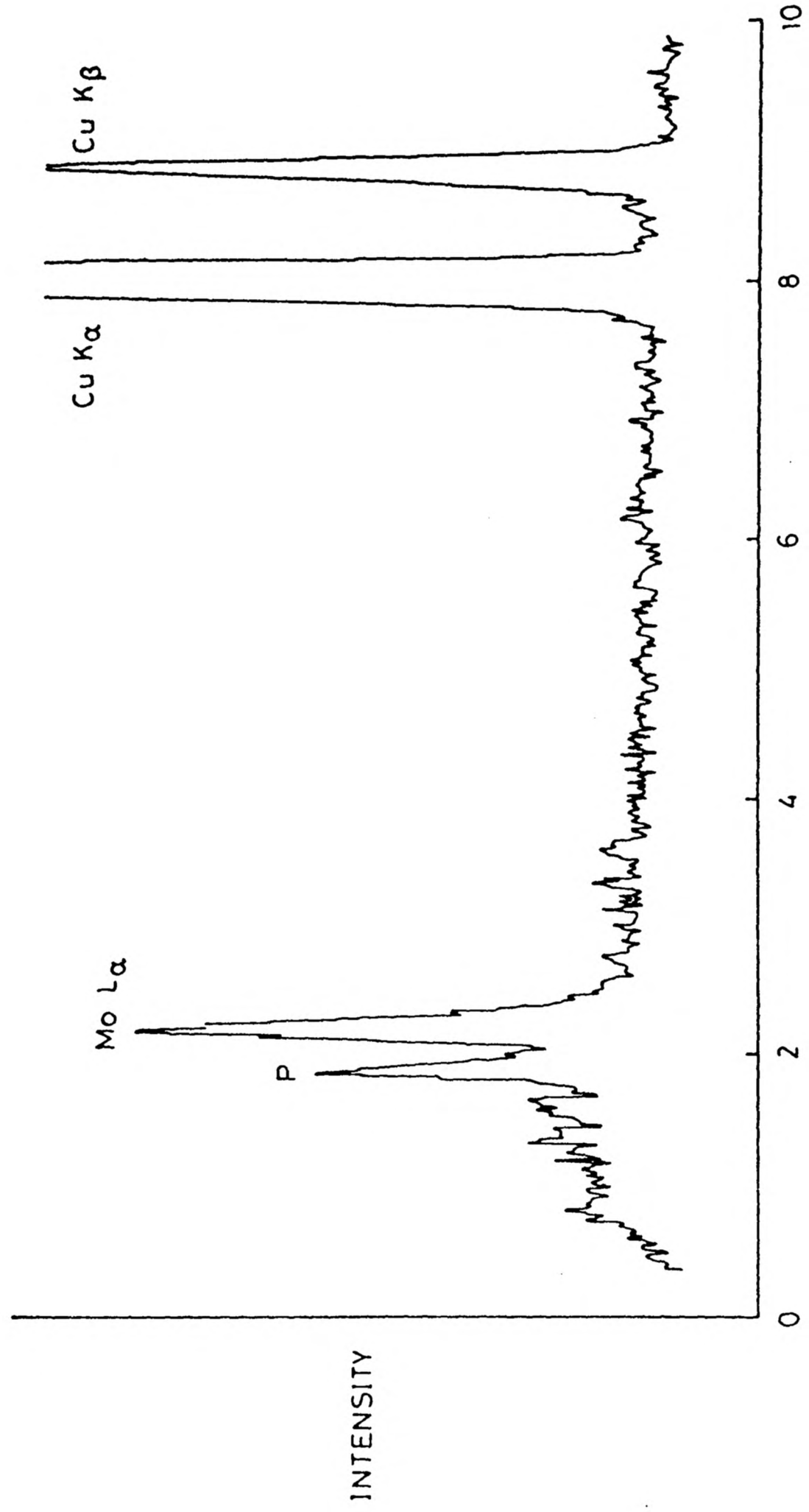

Figure 7.8 X-ray microprobe analysis for t-$BuNH_3[(n-C_{22}H_{45}PO_3)_2Mo_5O_{15}]$ vesicles.

Experiments with $Gd(fod)_3$ and $t\text{-}BuNH_3[(C_{22}H_{45}PO_3)_2Mo_5O_{15}]$ vesicles have shown that these reagents are not very useful as n.m.r. probes since they accumulate within the lipid phase and do not appear to be localised at any particular organic site within the vesicle system. However, they do appear to be potential electron microscopy stains since they penetrate the membrane without altering the integrity of the lipid bilayer (as seen from the possibility of vesicle preparation and n.m.r. spectra). These reagents give very different EM images from those observed by normal uranyl acetate staining processes (figure 7.9).

Another possible use of $Gd(fod)_3$- loaded vesicles is as a paramagnetic probe in studying membrane - protein interactions. For instance, n.m.r. spectroscopy would correlate the perturbations of protein regions close to the binding site at the vesicle surface whilst protein regions further from this binding site would show unchanged resonance positions.

The possibility of preparing tungstates and molybdates having different organic residues would obviously allow further probe experiments to be undertaken.

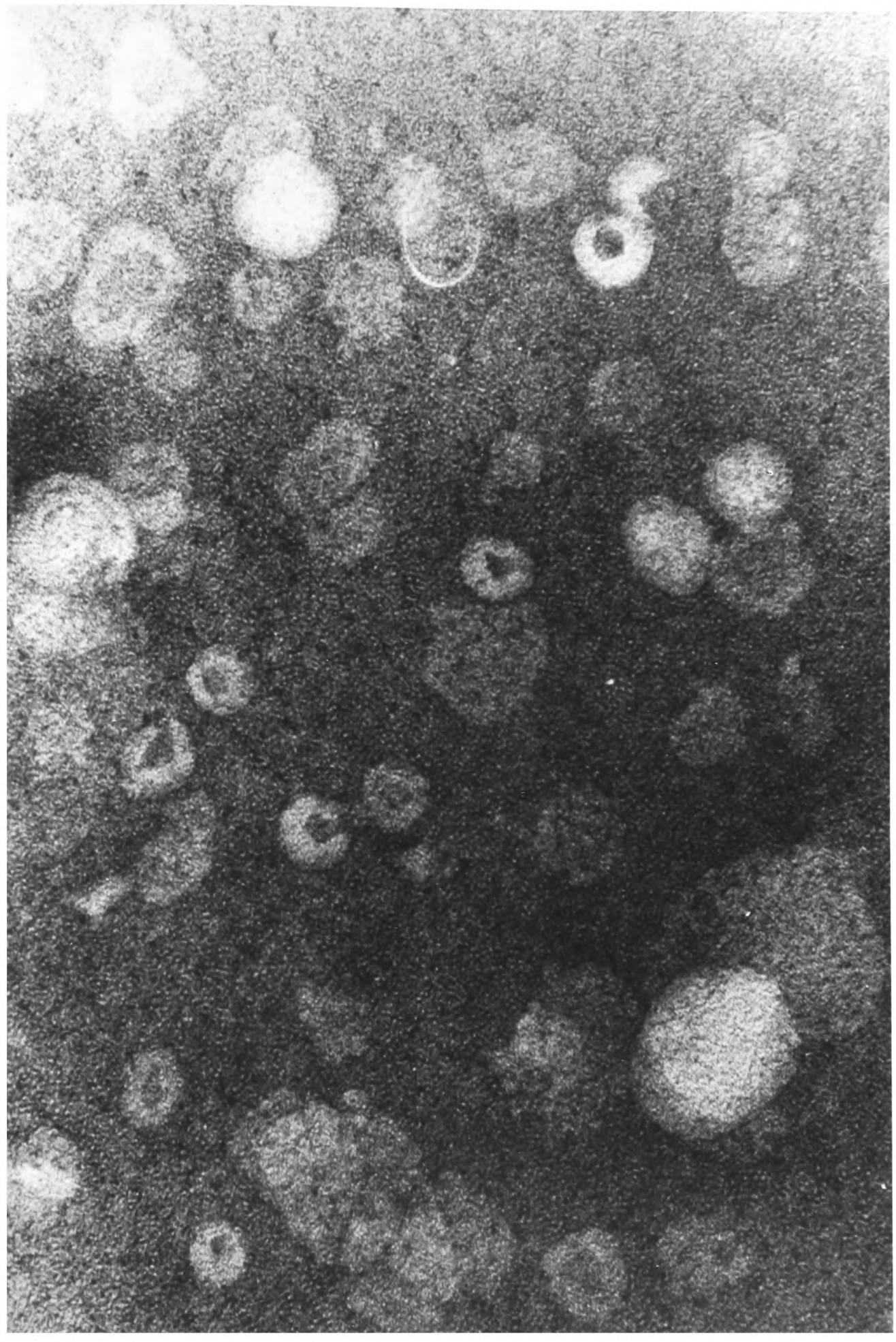

Figure 7.9 PC vesicles stained by 1% uranyl acetate at pH 7.0.The images occur through negative staining of the vesicle regions on the support film x370,000.

7.5 References

(1) Skarnulis A.J., Strong P.J., Williams R.J.P.
JCS Chem.Comm., 1030-1032, 1978

(2) Cotton F.A., Wilkinson G., Advanced Inorganic Chemistry
4th Edition, p858, 1980.

(3) Ibid p 861.

(4) Stalick J.K., Quicksall C.O., Inorg.Chem. 15, 1577-1584
1976.

(5) Mann S., Williams R.J.P., Sethurman P.R., Pope M.T.,
JCS Chem.Comm. 1083-1084, 1981.

CHAPTER 8

SUMMARY

8.1 The formation and nature of intravesicular solids in chemical systems

It is important to study the process of ion precipitation on an organic preformer within a confined micro-environment from a chemical and biological perspective. One such system examined in this thesis was the study of solid state chemistry within the confined space of synthetic phosphatidylcholine vesicles. This system was shown to be a suitable model for simulating biological deposition in small compartments. Several intravesicular solids were prepared and investigated using electron microscopy, n.m.r. spectroscopy and light scattering (for Ag_2O only). Table 8.1 summarises these reaction systems.

In general, the observations were that the chemistry within vesicular space is the same as that in normal aqueous solution so that intravesicular crystallites are formed whenever their aqueous counterparts are also crystalline. In part, this may be a little surprising since intravesicular precipitation takes place in the presence of the lipid bilayer which could have acted as an inhibitor of crystal growth and placed spatial constraints on the growth of crystal faces. The only intravesicular reaction system which was found to be markedly different, in terms of chemical product, from that in aqueous solution was the attempted preparation of intravesicular Fe_3O_4. This preparation gave an amorphous material, presumably hydrated Fe_2O_3, unlike the crystalline inverse-spinel Fe_3O_4 prepared in aqueous solution. Possible mechanisms for preventing intravesicular Fe_3O_4 crystallisation were suggested

Table 8.1 Intravesicular solids studied in model and biological systems

Intravesicular solid	Structure	Chapter (section)
Ag_2O	Crystalline (cubic)	3
SiO_2	Amorphous	4
FeO(OH)[Fe(II)/OH^-]	Crystalline(hexagonal)	5 (5.3.2)
FeO(OH)[Fe(III)/OH^-]	Crystalline but poorly ordered	5 (5.3.1)
FeO(OH)?[Fe(II),Fe-(III)/OH^-]	Amorphous	5 (5.3.3)
Fe_3O_4(preformed)	Crystalline (inverse spinel)	5 (5.2.2)
Ag_2SiO_3	Crystalline (ortho-rhombic)	6 (6.2.2)
$CoSiO_3$	Amorphous	6 (6.2.1)
$Co(OH)_2$	Amorphous	6 (6.3)
Ag_2S	Crystalline (?)	6 (6.4.1)
CoS	Amorphous	6 (6.4.2)
AgI	Crystalline(hexagonal)	6 (6.5)

(chapter 5). These included,(a) differences in binding constants for Fe(II) and Fe(III) at the inner membrane surface result in preferential release of Fe(II) on pH increase followed by oxidation of this species before incorporation into the inverse spinel lattice, and (b) slow intravesicular pH change on raising extravesicular pH results in substantial amorphous Fe_2O_3 precipitation before the pH for magnetite formation can be attained. The presence of the lipid membrane, then markedly affects the chemistry of this system which illustrates that biological precipitation can be very different from the corresponding reaction studied by inorganic chemistry.

The precipitation of Fe-oxides within vesicles requires further study. Mossbaüer spectroscopy appears to be of potential use. The chemistry of these vesicle systems requires further investigation because it is not at all clear how biology mineralises materials such as magnetite in cellular compartments.

Detailed chemical studies were described for intravesicular Ag_2O deposition. Analytical EM showed that particles of different sizes could be prepared by varying the encapsulated Ag(I) concentration. ^1H n.m.r. spectroscopy showed that OH^- diffusion is possible through lipid bilayers, raising pH_{IN} and removing the cation from the inner membrane surface and incorporating it within the solid phase. Electron diffraction and ultra-high resolution EM showed further that the intravesicular particulates so formed were crystalline, cubic Ag_2O. Single-domain crystals were formed as shown from the direct lattice imaging of these crystallites. A single site model for intravesicular nucleation followed by slow crystal growth was postulated on the basis of electron micrographs of crystallites

recorded at early stages of crystal growth and light scattering experiments. The rate-determining step for crystallisation was investigated by light scattering and was shown to be dependent on the rate of crystal growth and not the rate of nucleation. The rate of precipitation was found to be directly proportional to the intravesicular Ag(I) concentration above pH_{OUT} 11.0 but varied with extravesicular hydroxide concentration; below pH_{OUT} 11.0 no precipitation was observed, between pH_{OUT} 11.0-12.0 the rate was shown to be almost directly proportional to $[OH^-]_{OUT}$ and above pH_{OUT} 12.0 the rate became less dependent on $[OH^-]_{OUT}$. These results were explained in terms of the rate of supersaturation within the vesicle; below pH_{OUT} 11.0 supersaturation is not reached due to minimal OH^- influx. Above 11.0 the rate increases with OH^- influx and at very high pH becomes almost independent of $[OH^-]_{OUT}$ as a maximum constant rate of influx is attained. The control of pH_{IN} by the lipid membrane is then crucial in the intravesicular precipitation of hydroxides and oxides and was investigated in more detail by ^{31}P n.m.r. spectroscopy. Results from these experiments showed that the presence of permeable intravesicular anions was vital for raising pH_{IN}, this only occurring when a critical potential gradient across the membrane had been surpassed. Once this potential gradient was overcome then OH^- influx could occur and precipitation within the vesicles took place as in normal aqueous solution, as shown by estimating the percentage of Ag(I) ions incorporated into the solid phase as a function of pH (section 3.5.5 (b)).

The precipitation of Ag_2O crystallites within vesicles may be an excellent system for studying nucleation and crystal growth in general since inhibitors (proteins, sugars) can be

incorporated into the lipid membrane and the effects on crystallisation investigated by EM, n.m.r., and light scattering. The system simulates a biological compartment in that it involves the inclusion of a cation into an organic preformer followed by precipitation which is largely determined by the control of pH_{IN} by the surrounding membrane. Other potential uses of intravesicular Ag_2O particulates were described, notably in colloidal chemistry and catalysis.

The formation of amorphous materials within vesicles was studied in chapter 5. At early stages in particle growth, rings of electron-dense material were imaged in the EM. These images were very different to those for crystalline Ag_2O where continuous small angular particulates were imaged. For amorphous materials it was suggested that nucleation occurs at myriad sites on the inner surface of the membrane resulting in the circular structures observed.

The aim of the chemical investigations was to prepare intravesicular solids in situ. However, preformed solids which are then encapsulated within vesicles have potential use in colloidal chemistry as a method of stabilising sols and, in the case of magnetic solids such as Fe_3O_4 (chapter 5), incorporation of the solid with a water soluble drug may have potential use as magnetic drug-carriers. Magnetic vesicles may also be important in studying the interactions of protein molecules with membranes, using n.m.r. spectroscopy.

8.2. The formation and nature of intravesicular silica in Stephanoeca diplocostata Ellis

Chapter 4 was concerned with silica deposition in the organism Stephanoeca diplocostata Ellis and the nature of the costal strips in the intact loricae. This chapter illustrates the complexity of a biological system of deposition as compared with the model vesicle system of chapter 3.

Ultra-high resolution EM was used to investigate the nature of the siliceous costal strips which were found to be extremely amorphous in structure. The surfaces of costal strips were found to be active to Co(II) and Fe(III) ions, lipids and colloidal silica. An important aspect of the work was in revealing the nature of T-joins between costal strips in intact loricae. These junctions were shown to contain silica centred around a filamentous material of unknown composition and postulated to be formed through initial attachment of the filaments followed by a flow of surface silica onto active binding sites in the filamentous material.

The presence of organic material was shown to be most probable. Sectioned material of nascent strips at early stages of development showed stained filaments within the intracellular vesicles which are thought to represent a hollow cylinder of organic material. Silicification could then initiate on this organic template and a variety of growth mechanisms have been described (section 4.8). The presence of an organic phase in mineralisation seems most likely since, for silica formation to occur solely through concentration changes, a fifty-fold increase in $Si(OH)_4$ concentration above that in sea water would have to be attained.

Investigation of the demineralisation processes of costal

strips further concluded that the presence of a central axis of organic material seemed most likely since demineralisation initially occurs along this central axis. It is interesting to note the implications of demineralisation on the mechanical properties of costal strips. A curved fibre of isotropic material will experience maximum bending stress at its surface and no stress along its neutral axis (central axis of symmetry). For a given mechanical bending moment the stress experienced at the surface of a cylinder of radius R will vary as a function of r, the radius of demineralisation, and is given by, (1),

$$\sigma = A \frac{1}{(R^4 - r^4)}$$

where A is a constant

Thus when r is small, σ does not change appreciably with increasing r; for values of $r > R/2$, σ increases rapidly. Hence costal strips will retain their mechanical strength over a substantial degree of demineralisation until the tubular walls become very thin when fracture and bending could occur. Loricae will then remain intact even though their costal strips have undergone extensive demineralisation. This phenomenon may be important in terms of the evolutionary mechanisms involved in the formation of silica structures such as in costal strips. The mechanical design of biological systems is thus a very important consideration in correlating biological function to the property and structure of biomineralised solids.

8.3 Vesicle systems with n.m.r. probes and EM stains

The imaging of biological materials by means of conventional stains is not satisfactory since the specimen is often coated in dense heavy metal negative stains which are

aggressive chemical reagents. More suitable staining methods would be those using chemically less aggressive reagents which are specific in action, and in which the mechanism of staining was fully understood. In chapter 5 it was shown that Fe(III) ions could bind to the inner membrane surface of vesicles without affecting the integrity of the vesicles. The location of these ions at the membrane surface could also be shown by n.m.r. spectroscopy. Thus paramagnetic probes of this type may be useful for biological systems particularly if the system can be investigated by a combination of EM and n.m.r. techniques.

Other paramagnetic stains such as $K_5SiGePhW_{11}O_{39}$ (chapter 7) seem to have potential EM/n.m.r. applications. Others, such as $Gd(fod)_3$ appeared to be good EM stains but were not located in any specific manner by n.m.r. spectroscopy. However, this paramagnetic vesicle system may be useful in studying the interactions of proteins and lipid membranes in solution by n.m.r. spectroscopy.

8.4 References

(1) Wainwright S.A., Biggs W.D., Currey J.D., Gosline J.M., In, Mechanical Design in Organisms, chapter 6, 1976 (E. Arnold).

APPENDIX I

I.1 Principles of electron microscopy (EM)

Fundamentally and functionally, EM is very similar to optical microscopy, both techniques serve to magnify objects normally invisible to the naked eye. However, the properties of the electron beam are such that a much greater resolution is attained in EM, and that very different technical procedures are required for image formation.

I.1.1 Limit of resolution

The limit of resolution attained in an EM depends on several factors; (a) diffraction effects due to the wave nature of electrons, (b) lens aberrations (chromatic and monochromatic), (c) magnetic field asymmetry (astigmatism) and (d) mechanical, thermal and electronic stability of the instrument.

Due to diffraction effects of electron waves passing through small apertures the intensity profile of an image point is in the form of the Airy disc (figure I.1a). The resolution of such a system is defined as the distance between the intensity maxima of two emitting points of the object when the maximum intensity from one point coincides with the first minimum for the other point (figure I.1b). The separation of the two points (d_D) due to diffraction aberration is given by the relationship,

$$d_D = \frac{0.61\lambda}{n\sin\theta} \qquad \text{I.(1)}$$

where λ is the wavelength of the electrons, n is the refractive index of the material in which the object lies and θ is the angle subtended by the aperture to the lens axis. Since for

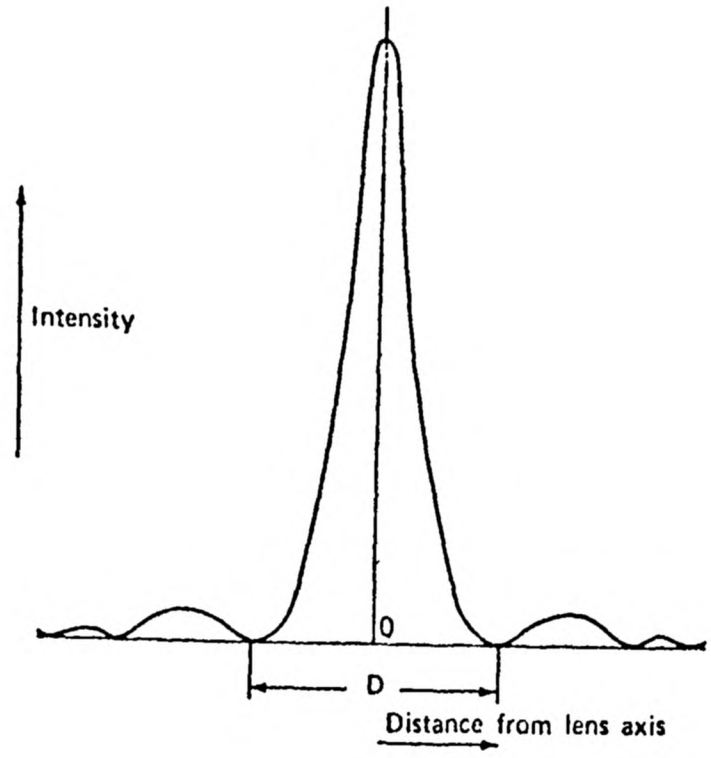

(a)

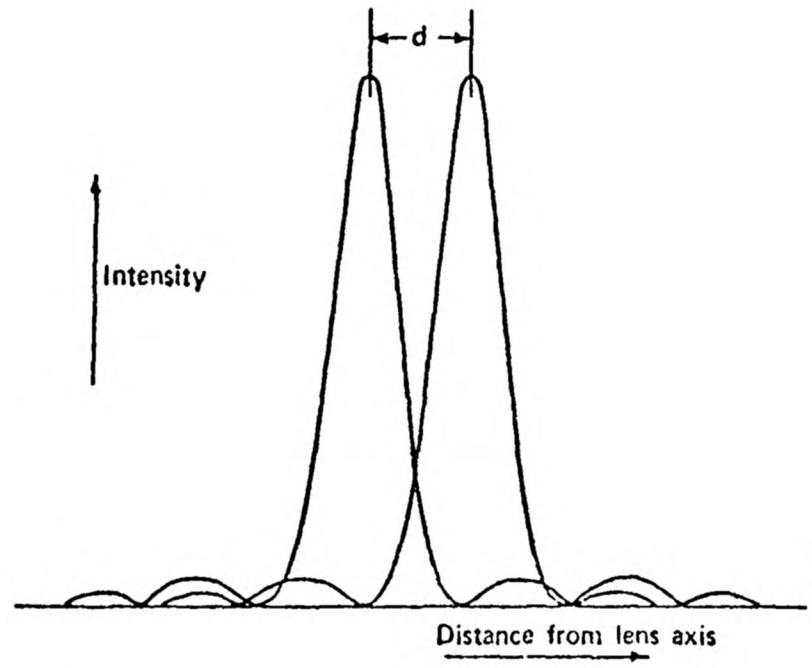

(b)

Figure I.1 a, Intensity profile of the Airy disc at an image point; b, the definition of resolution in terms of Airy disc seperation.

electrons travelling in a vacuum, n = 1, and θ is always small (10^{-2}-10^{-3} radians) such that $\sin\theta = \theta$, equation I.(1) can be written,

$$d_D = \frac{0.61\lambda}{\theta} \qquad \text{I.(2)}$$

Hence diffraction aberration does not depend on any property of the lens except its semi-angular aperture. Increased resolution (smaller d_D) can then be attained by smaller wavelengths and higher θ.

The wavelength of the electrons is related to the accelerating voltage V in the following manner. The kinetic energy of an electron of rest mass m gained by acceleration through a potential V to a velocity u, is

$$\tfrac{1}{2}mu^2 = eV$$

Combining this with the de Broglie equation

$$\lambda = \frac{h}{mu}$$

and substituting for u gives

$$\lambda = \frac{h}{(2meV)^{\frac{1}{2}}} \qquad \text{I.(3)}$$

Hence for high resolution EM, high accelerating voltages are required to minimise diffraction aberrations. At voltages above 50kV relativistic effects will be important since the velocity u of the electrons will be close to that of the speed of light c. A relativistic correction factor is then included in equation I(3) by substituting V for V_r, the relativistic voltage, where

$$V_r = V + (1 + eV/2mc^2)$$

and amounts to 2% for a voltage of 50kV and 10% for 200kV.

In principle, if only diffraction aberrations are considered, the resolution of the EM would be such that atomic structures could be imaged at voltages of 60kV. In practice

this is never achieved due to lens aberrations, astigmatism and mechanical, thermal and electronic instabilities in the instrument.

There are two types of lens aberrations, monochromatic and chromatic. Monochromatic aberrations, namely spherical aberrations, are due to the inability of the lens system to focus incident electrons at large angles to the lens axis exactly at the Gaussian focus of those electrons close to the axis. The result is that the object points are imaged as 'discs' (circles of least confusion), the limiting disc diameter d_s given by

$$d_s = \tfrac{1}{2} C_s \theta^3 \qquad \text{I.(4)}$$

where C_s is the spherical aberration coefficient. Spherical aberration is the most serious lens aberration encountered in the EM. Unlike chromatic aberration and astigmatism (see below) it is practically impossible to eliminate. It can be minimised by using a small objective aperture but from equation I.(2) this will increase diffraction aberration . The optimum value of θ, θ_{opt}, and hence the limit of resolving power d_{min}, have been calculated by combining spherical aberration and diffraction aberration as illustrated in figure I.2. There seems to be some dispute as to the best method of combining equations I.(2) and I.(4). In general the results are in the form,

$$\theta_{opt} = K\lambda^{\frac{1}{4}} C_s^{-\frac{1}{4}}$$
$$d_{min} = BC_s^{\frac{1}{4}} \lambda^{\frac{3}{4}} \qquad \text{I.(5)}$$

where K is a constant with values varying from 0.4 to 1.4 and B is a constant with values varying from 0.56 to 0.43. Equation I.(5) implies that the resolving power of the EM can only be improved substantially by using increased accelerating voltages

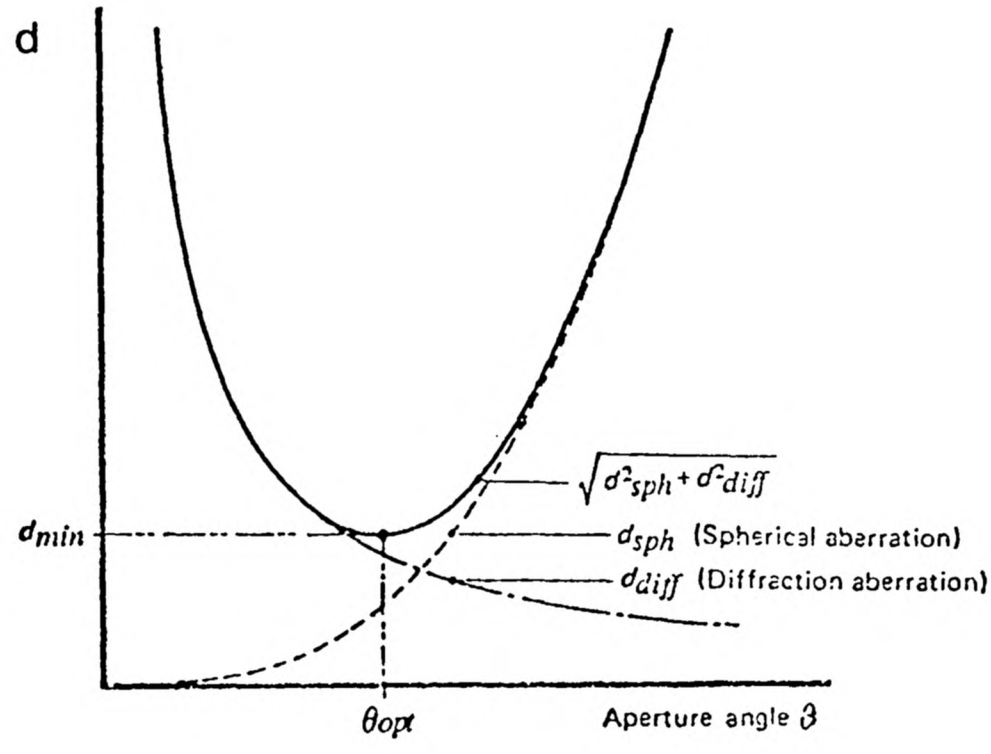

Figure I.2 The limit of resolving power, d, as a function of aperture angle for spherical and diffraction aberration.

but this is offset since C_s increases with the lenses required for these conditions.

Equation I.(5) is predicted on the assumption that only spherical aberration and diffraction aberration exist. Chromatic aberrations occur due to the energy spread of electrons in the electron beam giving rise to a spread of electron wavelengths. Since the focal length of a magnetic-electron lens is determined by the field strength in the lens space and by the accelerating voltage, i.e.

$$f = \frac{KV_r}{(NI)^2}$$

where f is the focal length of the lens, K is a constant, N is the number of turns in the coils, I is the current flowing through the windings, any variation in either V_r or I will cause a change in the effective focal length of the objective lens. The limiting resolution d_c due to chromatic aberration is given by,

$$d_c = \theta C_c \frac{\Delta f}{f}$$

$$d_c = \theta C_c \left(\frac{\Delta V_r}{V_r} - \frac{2\Delta I}{I} \right)$$

where Δf, ΔV, ΔI are the fluctuations in f, V and I, and C_c is the chromatic aberration coefficient. In practice chromatic aberrations arising from fluctuations in accelerating voltage and lens current can be virtually eliminated by providing very stable lens and voltage supplies. However in specimens where there is a high energy loss due to interactions of the electron beam with the sample (inelastic scattering) chromatic aberration may be high. Hence thin samples or higher voltages are required to minimise this effect.

Aberrations due to defects of magnetic field asymmetry

in the objective lens (astigmatism) results in differing lens strength in two directions at right angles. The defect arises from lack of perfection in the machining of the lens pole pieces and inhomogeneities in the iron. Astigmatism can also arise from contamination in the lens pieces. Fortunately it can be corrected by the use of compensating cylindrical lens fields.

For very high resolution imaging, extremely high mechanical and electrical stability must be incorporated into the EM column. Until recently it was these practical factors combined with specimen conditions which had essentially controlled the resolution, and not the theoretical optimum balance between spherical aberration and diffraction broadening as given in equation I.(5). However, recent advances in instrumentation, notably in improved thermal stability of specimen stages, electron guns of high coherence, increased control over contamination and improved electronic stability, have allowed the resolution in the EM to be no longer limited by the incoherent blurring of the image due to electrical and mechanical instabilities. Under these conditions the interpretation of the image depends principally on the phase contrast function (section I.1.3(b)). Specimen conditions are found to markedly effect resolution at high and low magnification. Insulators often charge up in the electron beam resulting in a vibrating image. Contamination of the sample, often by a thin film of carbon resulting from the degradation of residual hydrocarbons (from greases, oils) will also lower the resolution obtained at high magnifications. Similarly, extensive beam damage of the sample will prevent high resolution images from being recorded. Hence for direct lattice imaging,

specimen conditions are of extreme importance given the inherent high resolving power of the instrument. The material must be stable in the electron beam and be sufficiently thin in the direction of the beam in order to minimise chromatic aberrations due to inelastic scattering within the sample. Other factors such as the feasibility of aligning the required lattice planes in crystalline samples parallel to the beam must also be considered.

I.1.2 Image formation in TEM

The image-forming system of the TEM basically consists of,

(i) the electron gun

(ii) a condenser system of magnetic lenses

(iii) a specimen chamber

(iv) a magnification system of lenses

(v) an image recording device.

There are two modes of image formation in the TEM. In the normal magnification mode of operation the intermediate image I_1 formed by the objective lens is the object plane for the first (intermediate) projector lens P1 (figure I.3a). Thereafter the intermediate lens P1 produces a second intermediate image I_2 which is finally magnified and imaged onto the viewing screen by the projector lens P2. The image is focused on the screen by varying the focal length of the objective lens.

In the diffraction mode the strength of lens P1 is so reduced that the back focal plane of the objective lens is projected onto the viewing screen (figure I.3b). Since the diffracted beams leaving the specimen are brought to a focus in the back focal plane of the objective lens, an enlarged

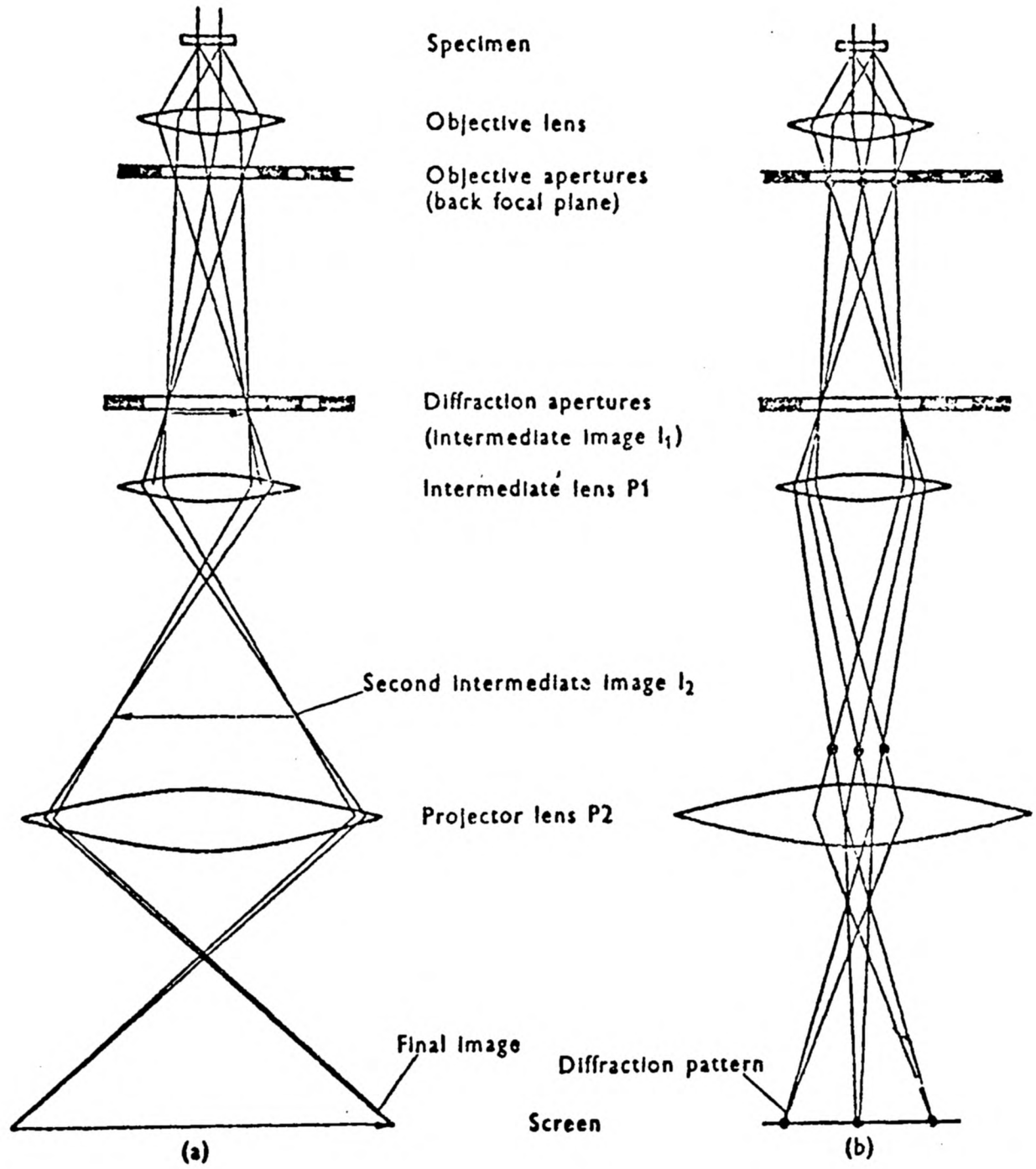

Figure I.3 Ray diagrams for conventional TEM; a, imaging conditions; b, diffraction conditions.

projection of this pattern is observed on the screen.

Thus, rays scattered from the same point in the object are brought to a point-focus in the first image plane, whereas rays scattered in the same direction from the object are brought to focus in the back focal plane. The formation of the image in the normal magnification mode can then be considered as two equivalent stages of diffraction. For coherent illumination the object is related to the diffraction pattern and hence to the image by a Fourier transfer function (FT), i.e.

$$\text{Object} \xrightarrow{\text{FT}} \text{Diffraction pattern} \xrightarrow{\text{FT}} \text{Image}$$

Electron diffraction is discussed in more detail in section I.2.

I.1.3 Image contrast

The possible interactions of an electron beam with a sample in the EM are shown in figure I.4. The mode of image formation and hence image contrast recorded in an EM micrograph depends on the nature of the specimen and on the resolution at which the instrument is operating.

I.1.3(a) Low and medium resolution images

At medium and low resolution, amplitude (or absorption) contrast is understood to arise from the creation of an intensity deficit in regions of large scattering where the scattered electrons are intercepted by the objective aperture. There are two main scattering processes, elastic and non-elastic scattering.

Elastic scattering occurs due to the deflection of electrons by atomic nuclei through relative large angles with-

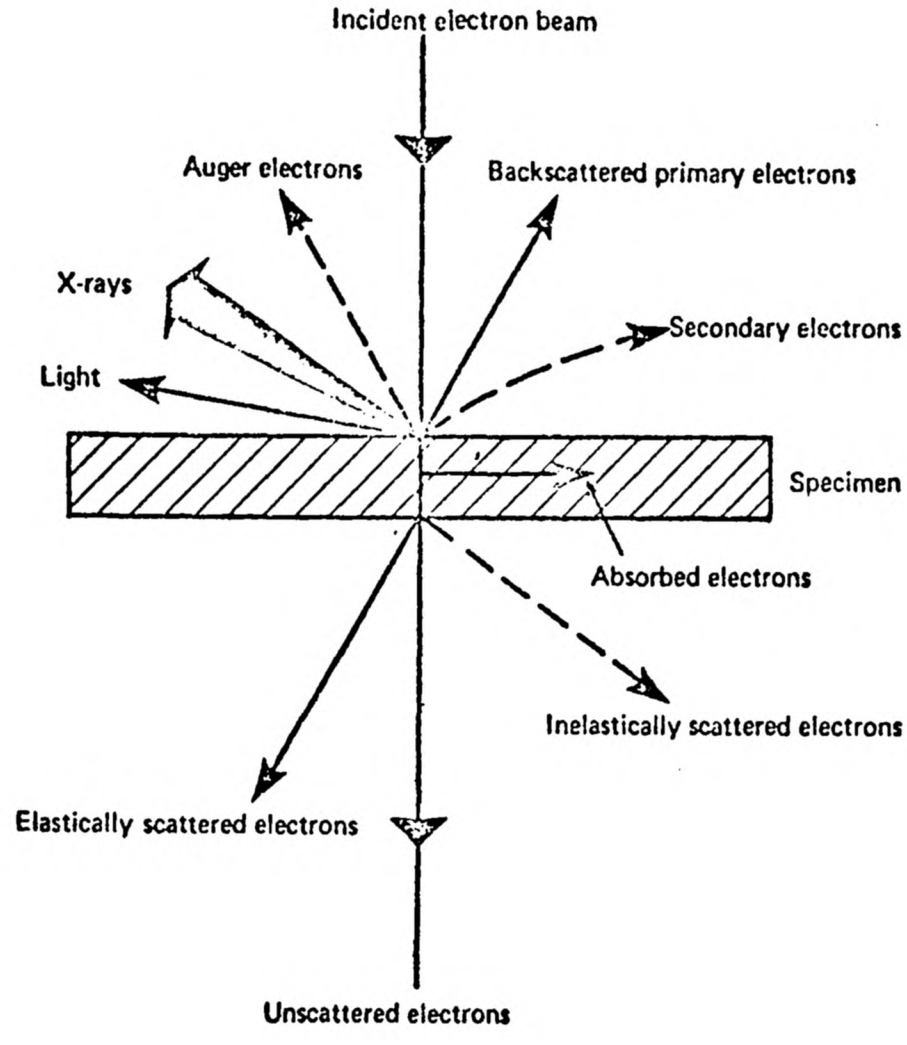

Figure I.4 The various effects of electron-specimen interaction. Light is emitted as visible fluorescence, elastically scattered electrons suffer no energy loss, inelastically scattered electrons lose some energy, and secondary electrons are of much lower energy than the primary backscattered electrons.

out loss of energy. The transmitted intensity I for a specimen of thickness t and density ρ is given by

$$I = I_o \exp(-\mu t)$$

where

$$\mu = \frac{\sigma \rho L}{M}$$

and σ is the effective area of an atom in scattering, L is Avogadro's number, and M the molecular weight of the material.

Since the number of electrons deflected increases with the thickness of the sample and is also proportional to the atomic number, contrast in the TEM at low and medium resolution will occur due to thickness differences or, as in the case of biological staining methods, by the presence of high atomic weight atoms in localised regions of the sample.

Amplitude contrast will be markedly increased by small objective apertures since highly scattered rays will not be recorded at the viewing screen. In practice, a compromise between contrast and resolution effects is made since small aperture sizes markedly increase diffraction aberrations.

For completely amorphous materials elastic scattering will be incoherent, i.e. random and in no way related. Hence, for a disordered material of constant thickness and σ, no contrast within the specimen would be observed at a low level of resolution since all points in the specimen scatter to the same extent. For periodic specimens elastic scattering from the atomic planes gives rise to diffraction contrast; crystals appearing bright if the scattered beams pass through the objective aperture and dark if intercepted.

In thin crystals dark fringes are often observed due to diffraction contrast arising from the bending of the crystal (bend contours) since some crystal planes are orientated so

that the scattered electrons hit the objective aperture and are lost from the image. In wedge-shaped crystals similar diffraction effects can be observed due to the interference of the diffracted beam and transmitted beam within the specimen producing reinforcement and extinction bands (figure I.5a).

Diffraction contrast is also responsible for the formation of Moiré patterns from overlapping crystals whether superimposed parallel to each other or at a small angle about the normal to the two crystal planes (figure I.5.b). The resulting image is formed by the action of double diffraction where the beam diffracted by the top crystal acts as a primary beam to be further diffracted by the second crystal.

I.1.3(b) High resolution images

The theory of amplitude contrast for images at low and medium resolution is not adequate in explaining and interpreting images obtained at high resolution in the EM. For thick specimens the classical case of incoherent imaging is sufficient since any phase relationships due to transmission through the specimen do not contribute significantly to the intensity distribution of the image since they are cancelled out by the summation of intensities for the various incident beam directions. For ultra-high resolution images of atomic lattice planes very thin samples are required since the resolution is markedly degraded by the effects of multiple-elastic and inelastic scattering. Such thin specimens are best described as thin phase objects and thus the incident electron wave undergoes only a phase and not an amplitude change on transmission through the sample. The transmission function is of the form

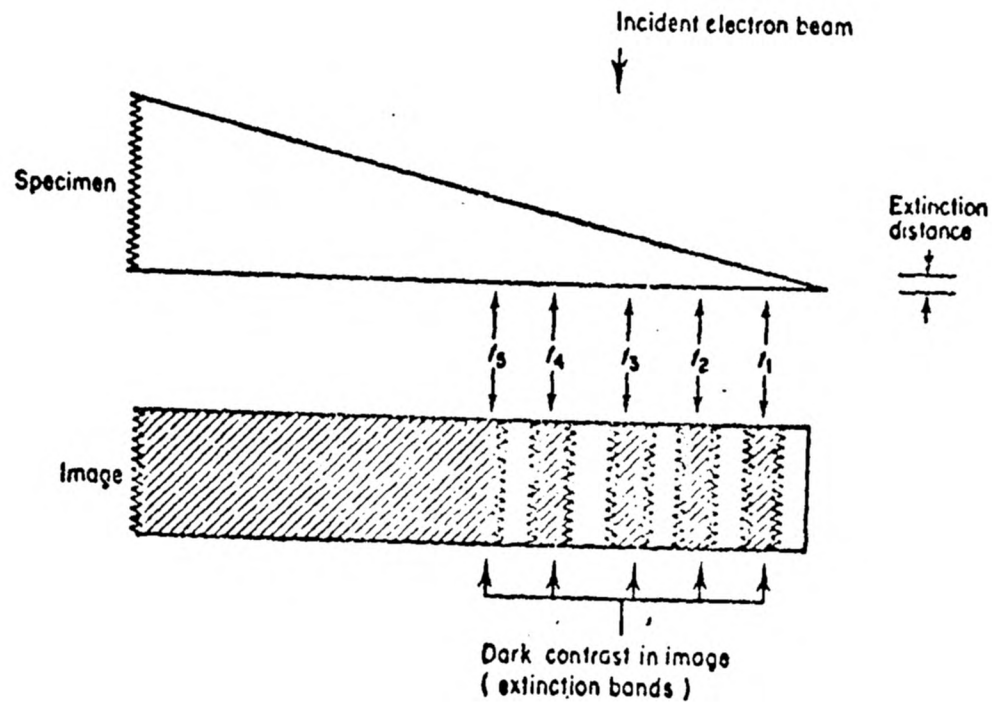

(a)

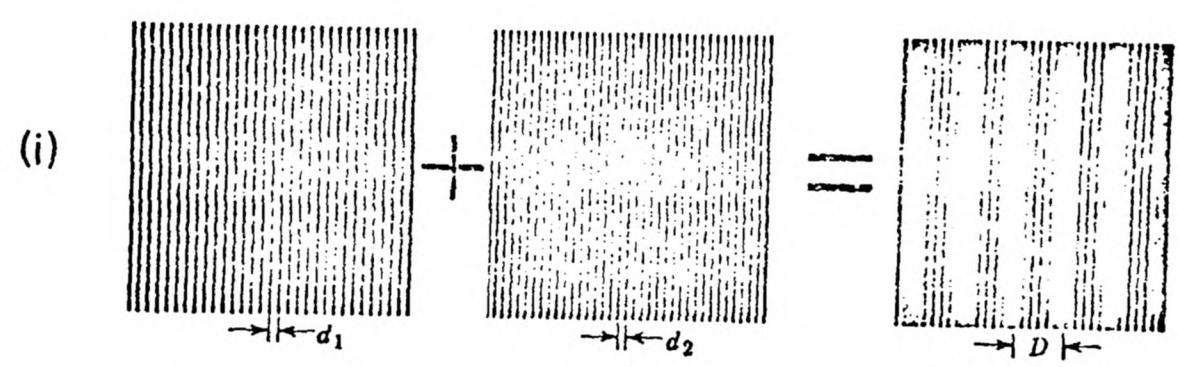

(b)

Figure I.5 Examples of diffraction contrast; a, thickness contrast in a wedge-shaped crystal. Thickness increments t_1-t_5 correspond to integral extinction distances, until at t_5 the crystal is too thick to obtain a resolvable image; b, the formation of two basic types of Moiré patters, (i) parallel Moiré pattern where $D = d_1 d_2/(d_1-d_2)$, (ii) rotational Moiré pattern where $D = d/\varepsilon$

(in one dimension),

$$T(x) = \exp(-i\phi(x)) \qquad I.(7)$$

where the phase change $\phi(x)$ depends on the thickness and refractive index of the material. Thus the theory of phase contrast becomes important when the incoherent instabilities such as electronic and mechanical instabilities no longer limit the resolution of the EM since the details required to be imaged are smaller than the coherence length. Fresnel fringes, lattice fringes and single atomic images are examples of phase contrast in which the image appears as an interference pattern due to phase changes on transmission through the sample. The use of highly coherent electron sources is crucial for successful images since strong interference patterns will only occur when the phase change is the same for all points in the specimen.

It is found experimentally (and can be derived theoretically) that the contrast of phase objects is a maximum for small values of de-focus and reverses when one goes through focus. This is because the constructive interference of diffracted and unscattered beams occurs at a position behind the Gaussian focus. If a plane incident wave of amplitude unity falls on the object, the transmitted intensity is given by $|T(x)|^2$ (from equation I.7). For an ideal lens, the transfer from object to diffraction pattern is given by a Fourier transformation as is the case for the transfer of the amplitude distribution of the diffraction pattern to the distribution in the image. The intensity of the out-of-focus object is found to be

$$I(x) = 1 + \frac{\lambda \Delta F}{2\pi} \phi''(x)$$

and thus the contrast depends on the second differential of the phase function $\phi(x)$, and is reversed when the sign of the defocus, ΔF, is reversed. When $\Delta F = 0$, $I(x) = 1$ and no phase

contrast is observed.

In practice, the transfer of information from object to diffraction pattern to image is not perfect due to the limitations of finite aperture size and lens aberrations. These effects can be represented by changes in amplitude and phase of the electron wave in the back-focal plane of the objective lens. The effect of an insertion of an objective lens aperture is represented by an aperture function $A(\theta)$ equal to unity within the aperture and zero elsewhere. The effect of lens aberrations, notably spherical aberration, may be simulated by introducing a phase change of $\exp[-i\chi(\theta)]$ where

$$\chi(\theta) = \frac{2\pi}{\lambda}\left(\frac{\Delta F\theta^2}{2} - \frac{C_s\theta^4}{4}\right)$$

The back focal plane distribution $F(u)$ referred to points u along the spherical surface of the lens ($u = x/f\lambda$, for points x in the object plane and $u = \theta/\lambda$ for scattering angle θ) is then modified to,

$$F(u)A(\theta)\exp[-i\chi(\theta)] = F_m(u)$$

which is related to the amplitude distribution of the image $F'(u')$ by a Fourier transformation function of $F_m(u)$, the intensity of the image being given by $|F'(u')|^2$.

The contribution to the image contrast of diffracted beam amplitudes for a particular range of u, depends on the value of $\sin\chi(\theta)$, the phase contrast function. Several plots of $\sin\chi(\theta)$ against $u = \theta/\lambda$, or $^1/_d$ where d is the interatomic spacing, for different values of ΔF and $C_s = 1.6$mm are shown in figure I.6. At the Gaussian focus, $\Delta F = 0$, the contributions to image contrast cancel for all values of d. For ΔF values of defocus ca-90nm $\sin\chi(\theta)$ is close to ± 1 for a wide range of d values. All scattered electrons within this 'window' have

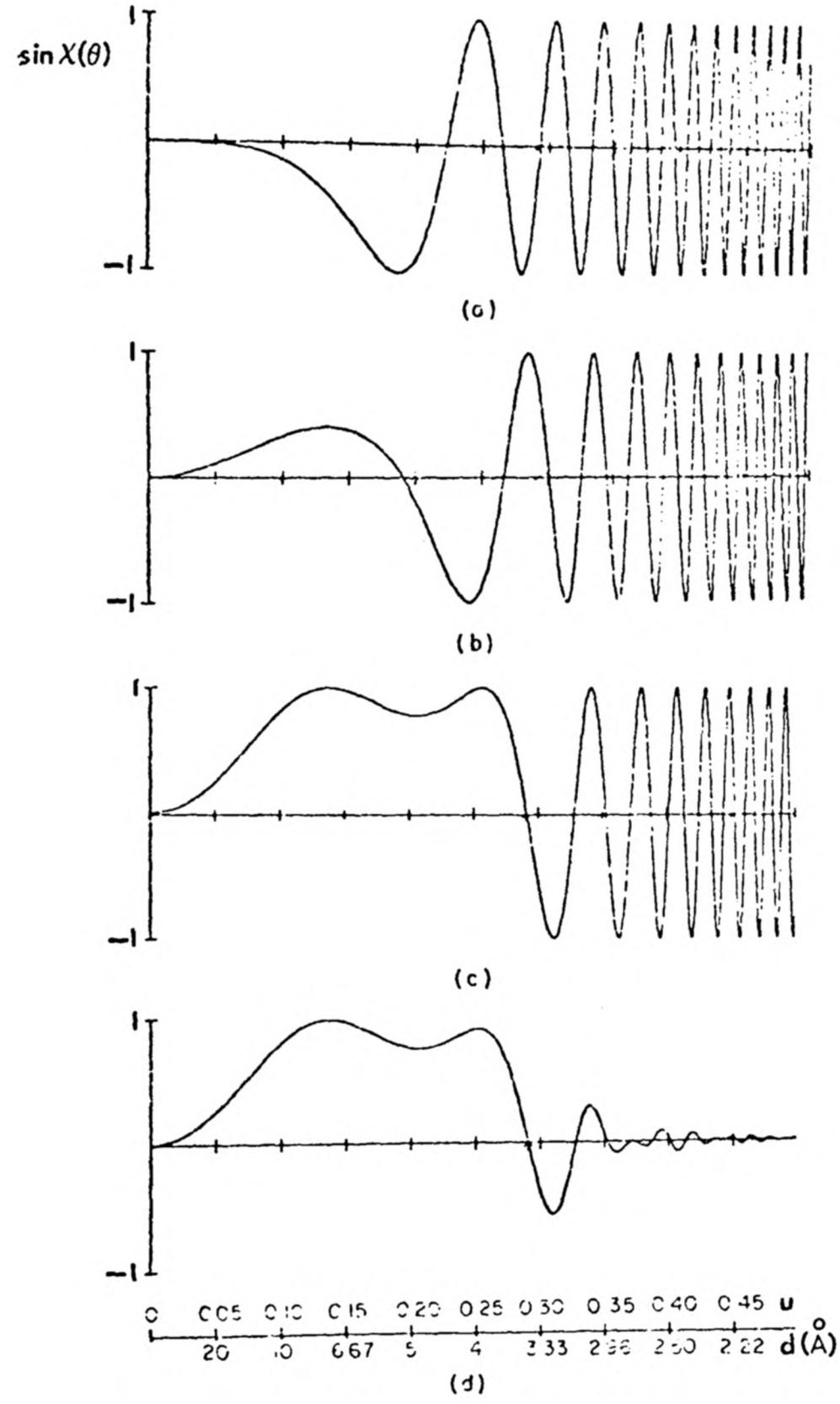

Figure I.6 Typical phase transfer functions, sin $\chi(\theta)$ plotted against spacing d (or u, where $u = {}^{1}/_{d}$) at various values of defocus ΔF; a, $\Delta F = 0$ (Gaussian focus); b $\Delta F = 400\text{Å}$; c $\Delta F = 925\text{Å}$; d $\Delta F = 925\text{Å}$ with sin $\chi(\theta)$ modified by chromatic aberration and spatial coherence envelopes.

approximately an equal phase alteration within the lens and consequently produce strong interference patterns i.e. contrast in the image. The outer limit of this 'window' represents the point-to-point resolution of an EM operating under these conditions. The additional effect of chromatic aberration and finite illumination source size (partial spatial coherence) impose an 'envelope' (figure I.6d) on the calculated transfer function and sets an ultimate limit on resolution. This degree of resolution will only occur under conditions of ultra-thin samples (<15nm) aligned correctly in the electron beam and imaged at the optimum value of defocus. Deviation by more than 20nm in focal length from this optimum value will give images having little or no apparent relationship with the object structure. Thicker samples will give lower resolution due to the effects of multiple scattering.

I.1.3(c) Image simulation

No image simulation methods were used in this thesis. Such techniques are briefly described since they are important in assessing the validity of images taken under conditions of ultra-high resolution.

The interpretation of micrographs recorded under very high resolution conditions is difficult and must be done with care. Despite the elaborate mathematics of wave optics it does not appear possible to find a simple analytical relationship between the high resolution image and the specimen's structure. The reason for the lack of this one to one correspondence between micrograph and object is due to the image being recorded in the form of an intensity distribution and thus does not contain information about beam paths and

scattering angles. Since it is not possible to produce object simulation from the image data recorded, the alternative process, image simulation is undertaken by using advanced computing facilities.

Computer methods will allow exact image calculations to be made for a specimen of known structure, thickness and orientation since all the experimental parameters can be included. The calculated image can then be compared with the experimental images on a trial and error basis. Simulated images of objects of different thickness, defocus and specimen orientation can be compared.

The full n-beam dynamical calculation is the best method of image simulation. In this the amplitude and phases of all diffracted beams are calculated and combined in terms of Fourier transformations. The image is simulated as a projected charge density distribution, after allowing for defocus and lens aberrations. An important development is the multi-slice technique for calculating the complex diffracted amplitudes scattered by a crystal of known structural orientation and thickness. In this method the n-beam dynamical calculation for an electron beam diffracted through a slice thickness ΔZ of the crystal is used for the wave equation entering the next slice of crystal. The total effect of a crystal on an incident wave is then given by the repetition of this process over N slices of the crystal thickness from which the simulated image can be obtained at different values of ΔF.

I.2 Electron diffraction

As has been described earlier, there is a close relationship between electron diffraction patterns and EM images, the diffraction pattern being formed in the back focal plane of the objective lens. The wavelength of the electron at the voltage used in the EM is much shorter than that of an X-ray, such that electron beams interact with substances to a far greater extent and hence have a much greater scattering power. As a result, small samples of less than 50nm in thickness can be effectively studied by electron diffraction. For thicker specimens dynamical effects will occur. In general, results from electron diffraction complement those from other techniques such as X-ray diffraction.

For amorphous materials the diffraction pattern contains no distinct maxima and consists only of diffuse scattering around the bright central spot. Hence since the data recorded is statistical in nature it is not possible to investigate local deviations from the average structure (short range order) and high resolution images must be obtained. For crystalline materials the diffraction pattern contains much information about the structure of the specimen such as the crystallographic space group, lattice parameters, the orientation of the specimen in the EM with respect to the electron beam, the orientation between two or more single crystals, polycrystallinity, preferred orientation within polycrystalline samples, twinning, structure defects such as dislocations, stacking faults and superlattice structures. When combined with X-ray microprobe analysis and utilising data tabulated elsewhere (eg. X-ray diffraction data) electron diffraction can identify the structure and composition of unknown materials.

The formation of the diffraction pattern in the EM is shown in figure I.3b. Discrete diffraction spots or rings only occur when the incident electron wave is diffracted by planes of atoms that lie at an angle θ to the incident beam so that Bragg's law is satisfied. In this case the diffracted beams interfere constructively in the back focal plane of the objective lens. For planes at different angles to the incident beam the electron waves will interfere only weakly or not at all; a small amount of diffuse scattering will be observed around the central spot in the diffraction spot. The pattern observed will depend on the orientation of the crystal to the electron beam, specified by the zone axis [U,V,W] where U, V, W are the Miller indices of the plane perpendicular to the beam, and

$$U = k_1 l_2 - k_2 l_1$$

$$V = l_1 h_2 - l_2 h_1$$

$$W = h_1 k_2 - h_2 k_1$$

For any given zone there will be a number of planes satisfying the Bragg condition, so several spots corresponding to different d spacings will be observed. The angle of planes to the beam will be very small (often $<1^{o}$) so that the reflecting planes are almost parallel to the direction of the electron beam.

The resulting diffraction pattern is formed in reciprocal space where the measured distance of any spot from the central spot (R values) is proportional to $1/d_{hkl}$ where d is the interplanar spacing for plane hkl, and where R is a vector parallel to the normal of plane hkl. This can be seen more clearly from a construction of the Eward sphere as in figure I.7.

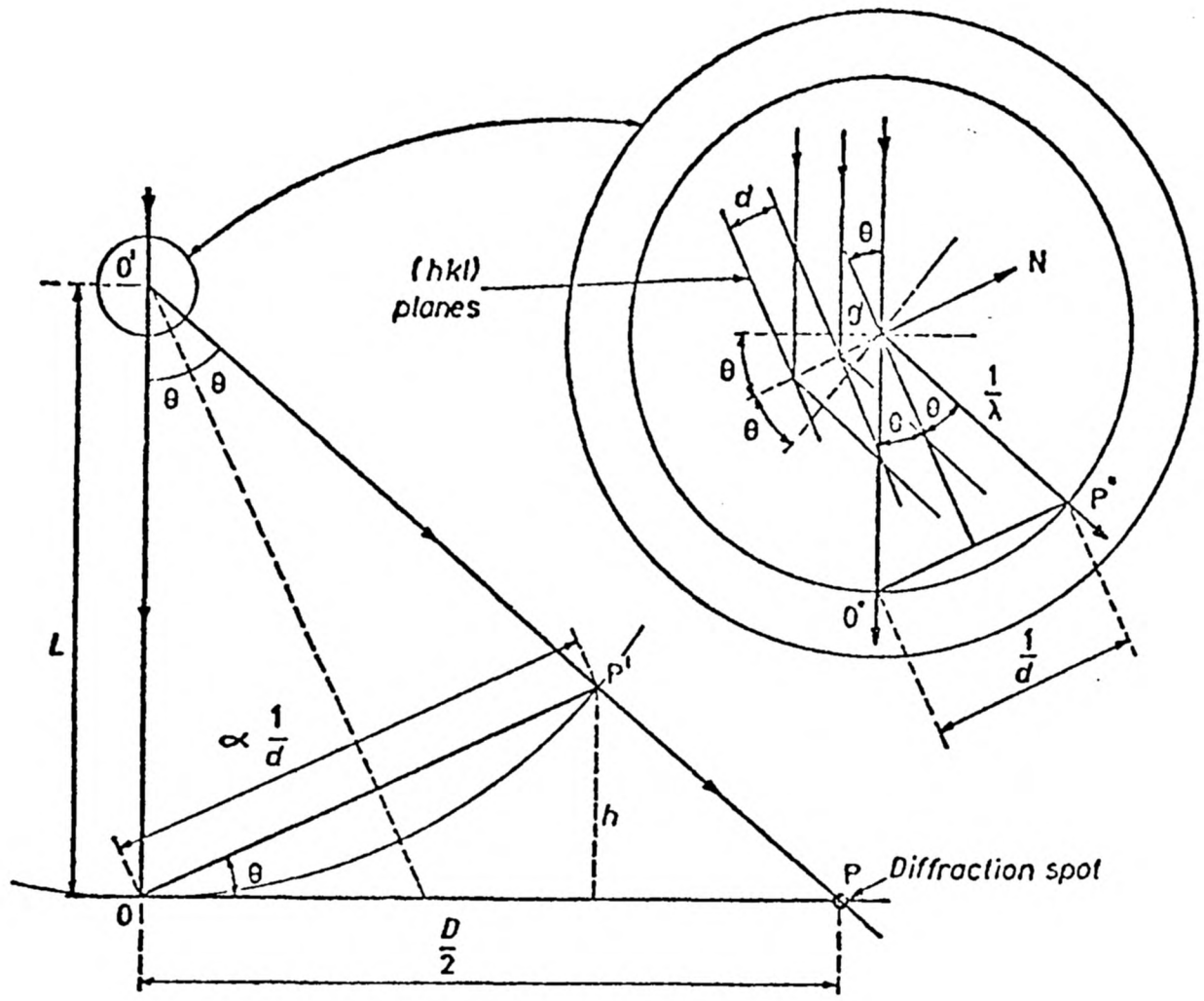

Figure I.7 Construction of the Ewald sphere for electron diffraction. See text for details.

In the circular inset, a coherent beam of electrons impinges on a crystal making an angle of incidence θ with a set of atomic planes, spacing d_{hkl}. Diffraction occurs when the path differences of diffracted rays are an exact number of wavelengths, i.e.

$$n\lambda = 2d_{hkl}\sin\theta \qquad \text{I.(8)}$$

and $\sin\theta = \theta$ for small θ.

A sphere (Ewald sphere), centre at O' of radius $1/\lambda$ intersects the direct beam at O'' and the diffracted beam at P''. The distance O''P'' is then equal to $1/d$ since equation I.(8) can be written

$$R = \frac{1}{d_{hkl}} = 2\,\frac{1}{\lambda}\,\sin\theta$$

and is parallel to the plane hkl. Any point such as that at a distance OP in the diffraction pattern will be proportional to $1/d_{hkl}$ when θ is small since length OP will be almost equal to OP'. If the incident beam is exactly perpendicular to a reciprocal lattice layer a pattern of spots will form because the distance of the layer from the Ewald sphere will be less than the finite size of the diffraction spot. For most specimens orientated on the EM grid with their direction of thinness parallel to the electron beam, diffraction spots will be extended in length in the direction of thinness. The reciprocal lattice points are therefore streaked (rel rods) perpendicular to the photographic plate such that the Ewald sphere will intersect lattice rods far from the central spot extending the appearance of the diffraction pattern. If the specimen is not correctly aligned the pattern will not be symmetrical since spots to one side of the photographic plate will disappear as they fall below the Ewald sphere. Laue zones

may also be observed under these circumstances since the Ewald sphere may intersect other layers in the reciprocal lattice. Such zones are often used as a measure of correct specimen orientation when recording diffraction patterns in the EM.

The diffraction pattern contains three types of information:

(a) Spatial arrangements; d spacings and angles between major crystal axes can be calculated.

(b) Intensities of diffraction spots. There may be extinctions due to the crystal space group, e.g. no {100} spots for a face centred cubic system aligned along the [001] axis. There may be extra spots due to superlattice ordering.

(c) Fine structure: There may be extra reflections in the diffraction pattern which occur as satellite spots around the main reflections. These often indicate the presence of twinning in the specimen. Streak patterns in the plane of the photographic plane arise when the direction of thinness in the crystal is perpendicular to the electron beam. These are often found in stacking faults where a thin slice of the crystal may have planes (hkl) in a different orientation which then act as an isolated crystallite.

Kikuchi patterns are observed in thick (1μm) specimens due to inelastic scattering. The diffraction pattern is obscured by the intense background due to inelastic scattered electrons but has a network of parallel bright and dark bands from diffracted beams rescattered in directions parallel to reflections of different order. Such lines can be used to determine very accurately the orientation of the crystal.

I.3 Scanning electron microscopy (SEM)

A brief outline of SEM and STEM (section I.4) is included since these modes of operation were used for samples investigated by X-ray microprobe analysis (section I.5).

In the SEM a fine beam of electrons is scanned across the specimen by deflector coils while an electron detector counts the number of low energy secondary electrons emitted from each point on the surface. At the same time the spot of a cathode ray tube (c.r.t.) is scanned across its screen. The secondary electrons are converted into a current by the detector which is then amplified and used to control the brightness of the c.r.t. image. The mechanism by which an image is magnified does not involve any lenses but is given by the ratio of the side length of the c.r.t. raster to the side length of the raster on the specimen. The deflector coils allow an electron beam to scan a raster as small as 1μm x 1μm and thus magnifications greater than 100,000 can readily be obtained. However, the resolution of the instrument is determined largely by the diameter of the beam of electrons which is scanning the specimen, often 5-10nm in diamter. Thus the resolution in the SEM is generally much less than in the TEM. A further limiting factor is that as the scanning beam is decreased in size the intensity of the secondary signal falls until no image can be formed in reasonable time. Larger condenser apertures can be used but this increases the spherical aberration of the second condenser lens.

The main advantages of SEM are that the formation of the magnified image is achieved without the use of lenses eliminating lens aberrations, and the image information, being transmitted as electrical impulses, can be amplified and electronically

manipulated; allowing control over contrast and brightness and the possibility of photography. The large depth of field makes SEM an excellent technique for investigating bulk samples. For thin samples, such as many of the intravesicular deposits described in this thesis, SEM was of no use; X-ray microprobe analysis was then performed only in the STEM mode.

I.4 Scanning transmission electron microscopy (STEM)

In the STEM an electron detector is placed below the specimen and collects the electrons transmitted from a raster beam through the sample. The corresponding electrical impulses control the intensity of the c.r.t. raster as in the SEM. STEM has several of the advantages of SEM.

Thicker specimens can be imaged in STEM than in TEM since in the former method all the transmitted electrons can be collected and can contribute to the image whereas in TEM, thin samples are required to prevent a high degree of inelastic scattering which results in chromatic aberration in the lenses.

I.5 X-ray microprobe analysis

The generation of characteristic X-rays from the interaction of the electron beam with the specimen in the electron microscope allows the identification to be made of elements within microvolume regions of the sample. This is a very important technique since a correlation can then be made between the ultrastructural information and the chemical analysis.

X-rays are emitted from a sample in the EM whenever the interaction of the electron beam with the specimen transmits energy greater than the critical excitation potential (absorption

edge) of an electron in particular atomic orbital, resulting in the ionisation of core electrons.

The excited state of the ionised atom reverts to a low energy state by electron transition from higher to lower energy states releasing energy in the form of X-rays. In a large atom several such transitions can occur on a single ionisation event resulting in several X-ray emission frequencies. The permitted transitions vary in intensity, the most intense lines being for transitions to the K(1s) shell (K lines). The relationship between atomic number Z and X-ray frequency γ is given by

$$\gamma = (Z-1)^2 \, R\left(1- \frac{1}{n^2}\right) \qquad \text{I.(8)}$$

for K lines, where R is the Rydberg constant and n the principal quantum number. For other series, L, M,

$$\gamma = a(Z-S)^2$$

where a is a constant and S is the screening constant. For the solid state detector used in this thesis the energies detected lie in the range 3-20keV. Thus from equation I.(8) for elements of high atomic number the critical excitation potential for K lines may lie outside this region and L lines are then used for characterisation of the element. The low limit to detection is due to low X-ray fluorescent yields for low atomic number elements and due to low energy X-rays being absorbed by the Be window of the detector. These factors limit elemental detection to atomic numbers above sodium which is a great disadvantage for biological specimens. The pulse collected in the SSD is integrated and passed to a field-effect transistor (FET) in a pre-amplifier positioned close to the detector to reduce noise. The output voltage is further amplified and passed to a multichannel analyser (MCA) in which the pulses are separated in terms of amplitude and stored in memory

channels corresponding to these amplitudes. The resulting energy spectrum can be displayed on a c.r.t. screen, plotted on paper or recorded by teletype. A schematic diagram of the system is shown in figure I.8.

A major advantage of the solid-state detector (SSD) is that it can be placed very close to the source of X-rays and so accept a wide solid angle of radiation which increases the detector sensitivity. However, if the total intensity of the X-rays is very high, there may be a large 'dead-time' in the collection. Disadvantages include the absorption at the Be window and the operational conditions of liquid N_2 temperatures for the SSD.

The spectra recorded show characteristic lines on a background of 'white' radiation. This white radiation arises when photons are emitted due to inelastic scattering of the electron beam in thick specimens. Peaks must then be integrated with the necessary background subtracted. This can be performed by computer programs or from background analyses performed over empty areas of the grid adjacent to the sample.

Spectra may contain spurious peaks due to 'escape peaks' originating from X-rays entering the detector and causing fluorescence of the detector material resulting in peaks at energy values of $E_x - E_c(Si)$ where E_x is the energy of the entering X-ray and $E_c(Si)$ is the critical ionisation potential of the Si K shell. Other spurious peaks can arise from contaminants on the grid and from electrons scattered from the holder and grid materials. Background analyses are very important in determining the presence of such peaks away from the sample area.

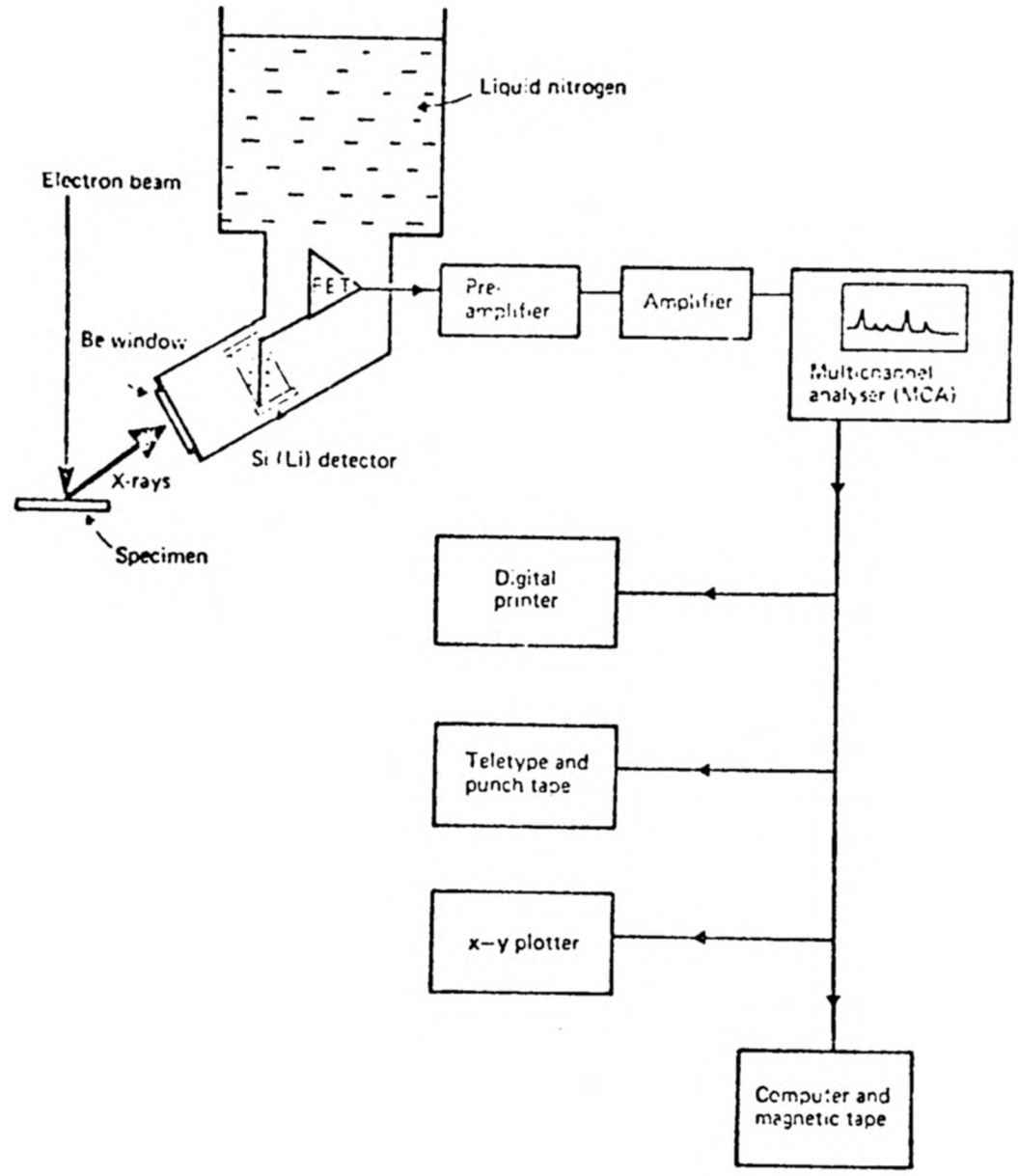

Figure I.8 Schematic diagram of the nucleonics associated with an SSD.

I.6 Bibliography

Andrews K.W., Dyson D.J., Keown S.R. Interpretation of Electron Diffraction Patterns (Hilger) 1971.

Belk J.A. Electron Microscopy and Microanalysis of Crystalline Materials (Applied Science) 1979.

Cowley J.M. Diffraction Physics (North Holland) 1975

Fryer J.R. The Chemical Applications of Transmission Electron Microscopy (Academic Press) 1979.

Glauert A.M. Practical methods in Electron Microscopy. Volumes 1,2,5 (North Holland) 1972, 1974, 1975.

Grundy P.J., Jones G.A. Electron Microscopy in the Study of Materials (E. Arnold) 1976.

Rymer T.B. Electron Diffraction (Methuen) 1970.

Spence J.C.H. Experimental High Resolution Electron Microscopy. (Monographs on the physics and chemistry of materials) Clarendon 1981.

APPENDIX II

II.1 Energetics of nucleation

The change in Gibbs free energy (ΔG) at constant temperature and pressure when a substance is transformed from one phase into another is given by the equation

$$\Delta G = (\mu_2 - \mu_1)\ \Delta n$$

where $(\mu_2 - \mu_1)$ is the change in chemical potential of the phase change and Δn is the change in amount of substance transformed.

The affinity (ϕ) of the phase change is given by

$$\phi = -\frac{\Delta G}{\Delta n} = \mu_1 - \mu_2$$

and is a measure of the driving force of the phase change. If $\phi > 0$ then the process is thermodynamically possible.

The surface layer of a solid phase will have more free energy than the rest of the material since it is in a higher state of potential energy (weaker, unsaturated bonds). Macroscopically, this extra surface free energy is expressed by the surface tension σ (surface free energy per unit surface area).

For very small crystals of area A,

$$A \propto n^{2/3}$$

where n is the number of ions in the crystal. Hence the free energy in forming the crystal from homogeneous solution is given by,

$$\Delta G = -n\phi + \sigma A$$

and

$$\Delta G = -n\phi + n^{2/3}\psi$$

where $\psi = A\sigma/n^{2/3}$ and relates surface free energy to the number

of ions in the crystal. A plot of ΔG against n is shown in figure II.1.

When $\phi<0$, ΔG is always positive. When $\phi>0$ eg. for a supersaturated solution, ΔG will be negative at large n values since n tends to infinity faster than $n^{2/3}$ goes to infinity. Hence at small n, ΔG is > 0 and a critical nucleus n* will be reached below which the crystal seed will dissolve and above which the crystal will grow without limit (thermodynamically) The critical nucleus has been estimated to be about 10Å or 100 molecules or ions (1).

The affinity can be related to the supersaturation ration S (1), where

$$S = c/s$$

and c = concentration of dissolved matter

s = solubility

by the equation

$$\phi = kT \ln S$$

Where k is the Boltzmann's constant and T the temperature in degrees Kelvin.

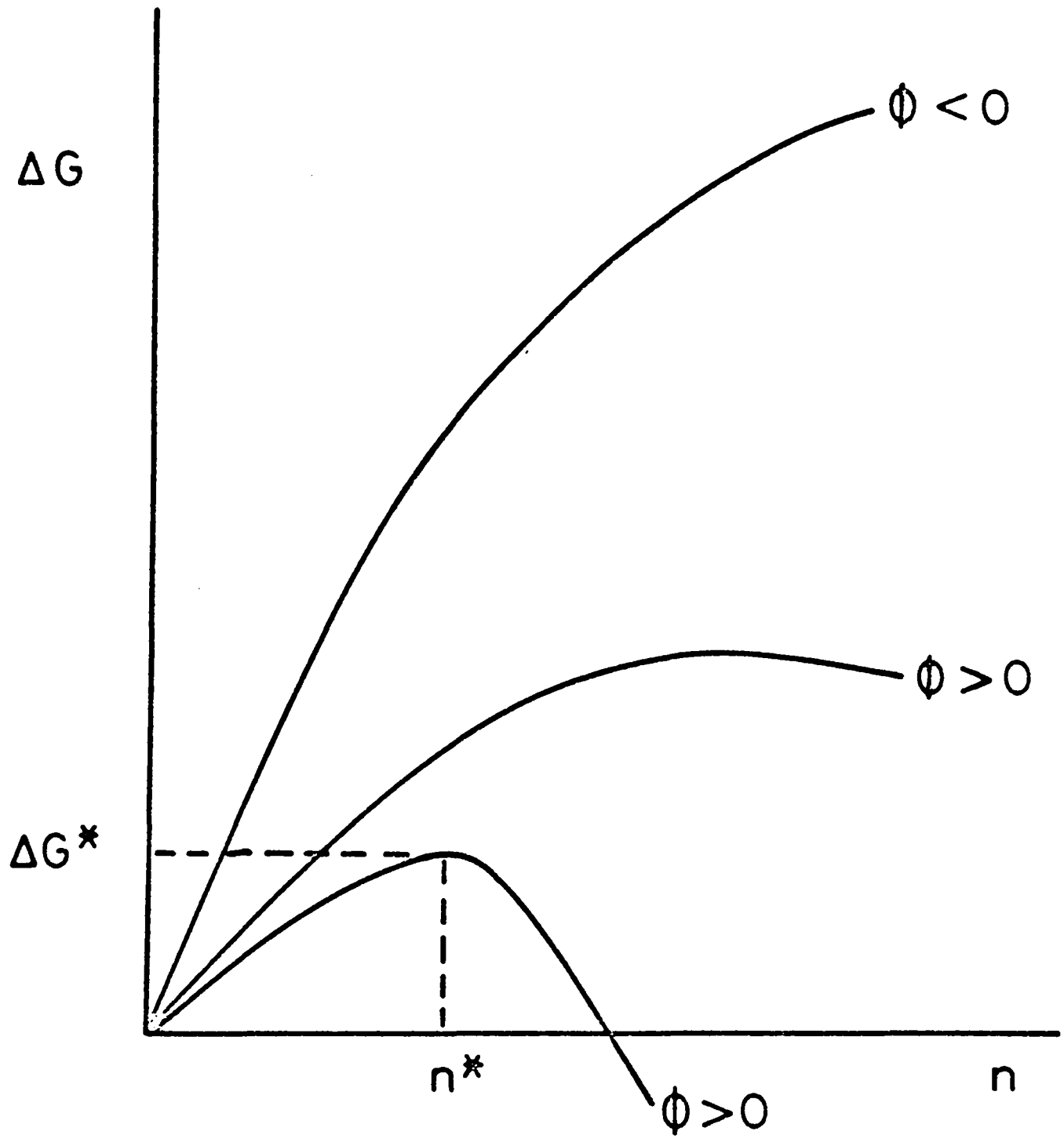

Figure II.1 Plot of ΔG of crystal formation against the number of ions, n, in the crystal.

II. 2 References

(1) Van Hook A., In, Crystallisation, (Reinhold) 1961.